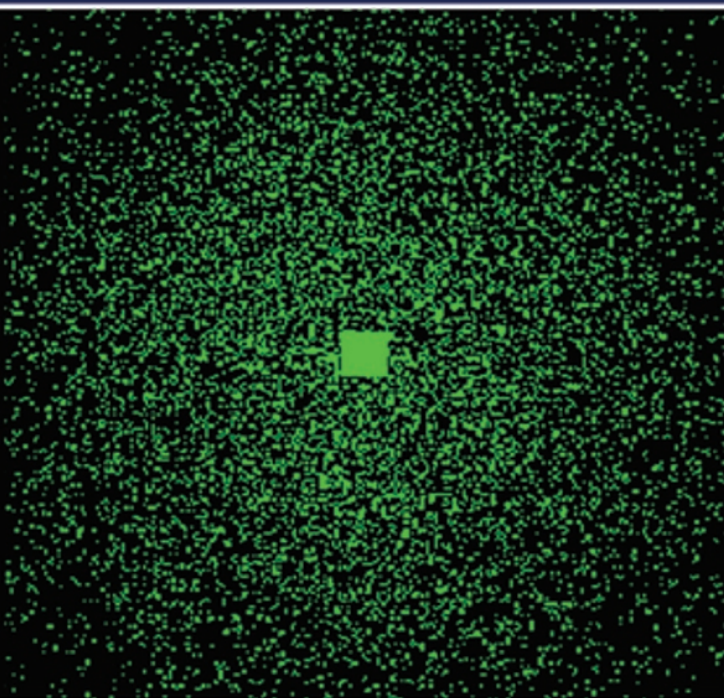


Fourier Optics and Computational Imaging



Kedar Khare



Ane Books
Pvt. Ltd.

WILEY

Fourier Optics and Computational Imaging

Fourier Optics and Computational Imaging

Kedar Khare

*Department of Physics
Indian Institute of Technology Delhi
New Delhi, India*

WILEY
John Wiley & Sons Ltd.



Ane Books Pvt. Ltd.

Fourier Optics and Computational Imaging

© 2016 Kedar Khare

This edition published by

John Wiley & Sons Ltd

The Atrium, Southern Gate
Chichester, West Sussex PO19
8SQ United Kingdom
Tel : +44 (0)1243 779777
Fax : +44 (0)1243 775878
e-mail : customer@wiley.com
Web : www.wiley.com

For distribution in rest of the world other than the Indian sub-continent and Africa.

Under license from:

Ane Books Pvt. Ltd.

4821, Parwana Bhawan, 1st Floor,
24 Ansari Road, Darya Ganj, New Delhi - 110 002, India
Tel.: +91(011) 23276843-44
Fax: +91(011) 23276863
e-mail: kapoor@anebooks.com,
Website: www.anebooks.com

ISBN: 978-11-1890-034-5

All rights reserved. No part of this publication may be reproduced, stored in a retrieval system, or transmitted in any form or by any means, electronic, mechanical, photocopying, recording or otherwise, except as permitted by the U.K. Copyright, Designs and Patents Act 1988, without the prior permission of the publisher.

Designations used by companies to distinguish their products are often claimed as trademarks. All brand names and product names used in this book are trade names, service marks, trademarks or registered trademarks of their respective owners. The publisher is not associated with any product or vendor mentioned in this book.

Library Congress Cataloging-in-Publication Data

A catalogue record for this book is available from the British Library.

Contents

Preface	11
1 Introduction	13
1.1 Organization of the book	16
Part 1: Mathematical preliminaries	
2 Fourier series and transform	21
2.1 Fourier Series	21
2.2 Gibbs phenomenon	23
2.3 Fourier transform as a limiting case of Fourier series	27
2.3.1 Fourier transform of the rectangle distribution	28
2.4 Sampling by averaging, distributions and delta function	30
2.5 Properties of delta function	32
2.6 Fourier transform of unit step and sign functions . .	33
2.7 Fourier transform of a train of delta functions . . .	36
2.8 Fourier transform of a Gaussian	36
2.9 Fourier transform of chirp phase	37
2.10 Properties of Fourier transform	40
2.11 Fourier transform of the 2D circ function	42
2.12 Fourier slice theorem	43
2.13 Wigner distribution	45

3 Sampling Theorem	49
3.1 Poisson summation formula	50
3.2 Sampling theorem as a special case	51
3.3 Additional notes on the sampling formula	52
3.4 Sampling of carrier-frequency signals	53
3.5 Degrees of freedom in a signal: space bandwidth product	55
3.6 Slepian (prolate spheroidal) functions	56
3.6.1 Properties of matrix $A^{(0)}$	59
3.7 Extrapolation of bandlimited functions	63
4 Operational introduction to Fast Fourier Transform	67
4.1 Definition	67
4.2 Usage of 2D Fast Fourier Transform for problems in Optics	69
5 Linear systems formalism and introduction to inverse problems in imaging	75
5.1 Space-invariant impulse response	77
5.2 Ill-posedness of inverse problems	78
5.3 Inverse filter	80
5.4 Wiener filter	82
6 Constrained optimization methods for image recovery	87
6.1 Image denoising	87
6.2 Image de-convolution by optimization	91
6.3 Blind image deconvolution	95
6.4 Compressive Imaging	97
6.4.1 Guidelines for sub-sampled data measurement and image recovery	99
6.4.2 System level implications of compressive imaging philosophy	103
6.5 Topics for further study	104
7 Random processes	107
7.1 Probability and random variables	107
7.1.1 Joint Probabilities	108

7.1.2	Baye's rule	108
7.1.3	Random Variables	109
7.1.4	Expectations and Moments	110
7.1.5	Characteristic function	112
7.1.6	Addition of two random variables	113
7.1.7	Transformation of random variables	113
7.1.8	Gaussian or Normal distribution	114
7.1.9	Central Limit Theorem	115
7.1.10	Gaussian moment theorem	116
7.2	Random Processes	117
7.2.1	Ergodic Process	118
7.2.2	Properties of auto-correlation function	119
7.2.3	Spectral Density: Wiener-Khintchine theorem	119
7.2.4	Orthogonal series representation of random processes	120
7.2.5	Complex Representation of random processes	121
7.2.6	Mandel's theorem on complex representation	123

Part 2: Concepts in optics

8	Geometrical Optics Essentials	127
8.1	Ray transfer matrix	127
8.2	Stops and pupils	130
9	Wave equation and introduction to diffraction of light	133
9.1	Introduction	133
9.2	Review of Maxwell equations	135
9.3	Integral theorem of Helmholtz and Kirchhoff	136
9.4	Diffraction from a planar screen	140
9.4.1	Kirchhoff Solution	141
9.4.2	Rayleigh-Sommerfeld Solution	141
10	The angular spectrum method	145
10.1	Angular spectrum method	145

11 Fresnel and Fraunhoffer diffraction	153
11.1 Fresnel diffraction	153
11.1.1 Computation of Fresnel diffraction patterns .	155
11.1.2 Transport of Intensity Equation	156
11.1.3 Self imaging: Montgomery conditions and Talbot effect	160
11.1.4 Fractional Fourier transform	162
11.2 Fraunhoffer Diffraction	163
12 Coherence of light fields	167
12.1 Spatial and temporal coherence	167
12.1.1 Interference law	169
12.2 van Cittert and Zernike theorem	169
12.3 Space-frequency representation of the coherence func- tion	171
12.4 Intensity interferometry: Hanbury Brown and Twiss effect	173
12.5 Photon counting formula	175
12.6 Speckle phenomenon	177
13 Polarization of light	183
13.1 The Jones matrix formalism	183
13.2 The QHQ geometric phase shifter	185
13.3 Degree of polarization	186
14 Analysis of optical systems	189
14.1 Transmission function for a thin lens	189
14.2 Fourier transforming property of thin lens	191
14.3 Canonical optical processor	193
14.4 Fourier plane filter examples	194
14.4.1 DC block or coronagraph	194
14.4.2 Zernike's phase contrast microscopy	195
14.4.3 Edge enhancement: vortex filter	197
14.4.4 Apodization filters	198
14.5 Frequency response of optical imaging systems: co- herent and incoherent illumination	199

15 Imaging from information point of view	205
15.1 Eigenmodes of a canonical imaging system	206
15.1.1 Eigenfunctions and inverse problems	209
 Part 3: Selected computational imaging systems	
16 Digital Holography	217
16.1 Sampling considerations for recording of digital holograms	220
16.2 Complex field retrieval in hologram plane	221
16.2.1 Off-axis digital holography	222
16.2.2 Phase shifting digital holography	224
16.2.3 Optimization method for complex object wave recovery from digital holography	226
16.3 Digital holographic microscopy	229
16.4 Summary	230
17 Phase retrieval from intensity measurements	235
17.1 Gerchberg-Saxton algorithm	237
17.2 Fienup's hybrid input-output algorithm	238
17.3 Phase retrieval with multiple intensity measurements	
17.3.1 Phase retrieval with defocus diversity	240
17.3.2 Phase retrieval by spiral phase diversity	244
17.4 Gerchberg-Papoulis method for bandlimited extrapolation	247
18 Compact multi-lens imaging systems	253
18.1 Compact form factor computational camera	253
18.2 Lightfield cameras	256
18.2.1 The concept of lightfield	257
18.2.2 Recording the lightfield function with microlens array	259

19 PSF Engineering	267
19.1 Cubic phase mask	267
19.2 Log-asphere lens	271
19.3 Rotating point spread functions	273
20 Structural illumination imaging	277
20.1 Forward model and image reconstruction	279
21 Image reconstruction from projection data	285
21.1 X-ray projection data	286
21.2 Image reconstruction from projection data	287
22 Ghost Imaging	293
22.1 Schematic of a ghost imaging system	293
22.2 A signal processing viewpoint of ghost imaging	297
23 Appendix: Suggested Exercises	301

Preface

This book is an outgrowth of a series of lectures on Fourier Optics and Imaging that I have been teaching to the students at Indian Institute of Technology Delhi for the past few years. There are excellent books and other reference resources on various aspects of Optics, Photonics, Mathematics and Image Processing. However, when I started teaching students from various backgrounds and disciplines at IIT Delhi, I strongly felt the need of a single self-contained volume that covered the fundamental ideas required to appreciate the recent developments in Computational Imaging in a concise manner. The material in this book has been written at a level suitable for advanced undergraduate or post-graduate students who may wish to pursue research and development activities involving imaging systems for their future careers.

I would like to thank the excellent mentors I had at IIT Kharagpur during my undergraduate years, who encouraged me to take up a career in research and academics. I especially thank my Ph.D. supervisor Prof. Nicholas George at Institute of Optics, University of Rochester, USA for introducing me to the exciting world of imaging research. Over the years he has been much more than just a Ph.D. adviser to me and I am sure he will be very happy to see this book getting published. Several years spent at the General Electric Global Research center in Niskayuna, NY, USA further broadened my appreciation and expertise in relation to a wider range of practical imaging systems and I am thankful to my colleagues there for providing a great real-world learning opportunity. During the last few years I have been grateful to have company of several wonderful faculty colleagues at IIT Delhi who have helped me to get started as an independent faculty member. Many thanks are also due to several

12 Fourier Optics and Computational Imaging

enthusiastic students at IIT Delhi who make me think of new ways to understand the material discussed in this book and several allied topics. Finally I wholeheartedly thank my wife Sarita, my daughters Rasika and Sanika, and all other family members in appreciation of their patience, encouragement and constant support over the last few of years while this manuscript was being prepared.

Kedar Khare
New Delhi
June 2015

1. Introduction

Imaging systems form an integral part of our lives. Research and development efforts in diverse areas of science and technology over the last few decades have resulted in practical imaging systems that we often take for granted today. From cell phone cameras to advanced diagnostic imaging systems, from weather prediction based on satellite imagery to night vision devices meant for soldiers guarding our national frontiers, there are numerous examples of imaging systems that touch all aspects of our lives. Further, in current science and technological investigations dealing with sub-nano to astronomical length scales, imaging systems allow researchers to visualize natural phenomena or objects of interest and in effect, directly contribute to new discoveries. Imaging is thus an active interdisciplinary research area that is relevant to a wide range of fundamental and applied problems.

The chart in Fig. 1.1 shows a wide variety of topics where imaging systems have become indispensable. It may not be too much of an exaggeration to say that every current Science and Technology student is very likely to encounter at least one of the topics listed in this chart during his/her career. While it is difficult to describe all the topics listed in Fig. 1.1 in detail in a single book, luckily for us the various imaging modalities share many common principles and mathematical ideas that are useful for design and analysis of imaging systems. The goal of this book is to present these basic tools followed by a discussion of some specific imaging systems so as to provide the reader sufficient background to enter the area of imaging research.

It is possible to describe a variety of imaging systems schematically by a simple model as shown in Fig. 1.2. A source of radiation

14 Fourier Optics and Computational Imaging

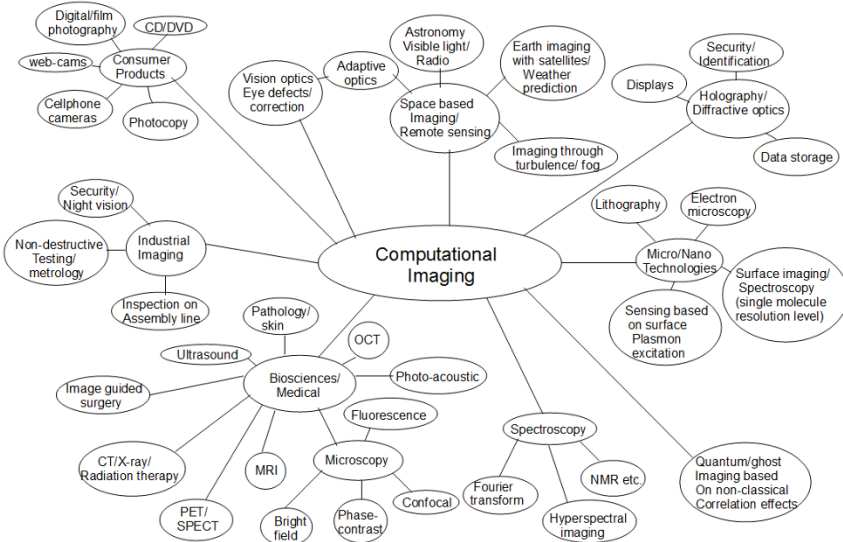


Figure 1.1: Scope of imaging research and development

produces waves (e.g. electromagnetic waves, sound waves) which then interact with the object of interest that is to be imaged. The waves scattered from the object encode the information about the object as space-time variations of intensity, phase, spectrum, polarization, coherence properties, and any other correlations depending on the problem at hand. Note however that this multi-dimensional information in the scattered waves is not available to us directly. The central goal of an imaging system is to derive the maximum possible information that is encoded in the scattered waves so that; a human observer may be able to visualize and interpret this information in the form of an image of the object or its characteristics.

Typically the imaging system hardware (e.g. lens assembly in a camera) is designed so as to modify or manipulate this coded information suitably by applying some transformation to the scattered waves before they are detected at an imaging sensor. Traditional research in imaging systems involved efforts for improving the imaging hardware (e.g. lens design) so as to obtain the best possible visual images at the sensor. With the availability of computer processing power over the last couple of decades, imaging systems (e.g.

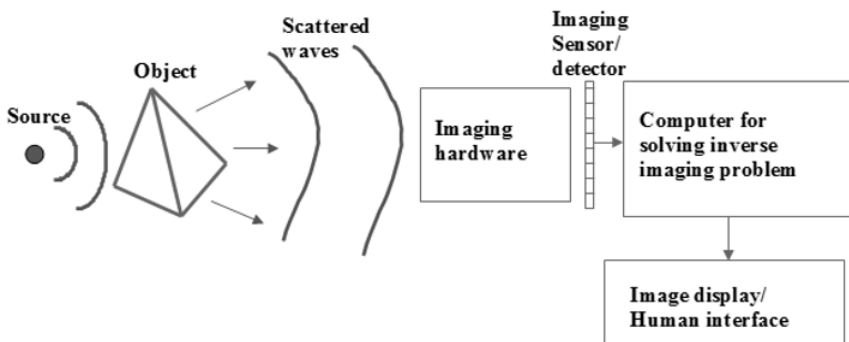


Figure 1.2: Computational imaging model

those in Fig. 1.1) have increasingly become computational in nature. In this new paradigm, the pattern recorded on the sensor may not have any visual similarity to the spatial details of the object of interest to be imaged. The imaging hardware is however designed such that, starting with the digitally recorded data at the imaging sensor, it is possible to solve an inverse or image reconstruction problem and to form an image of the object that is suitable for human interpretation. As imaging systems increasingly become important to scientific investigations and in our daily lives, it is always desirable to have systems with better resolution, faster imaging time, lesser sensitivity to noise, ability to capture multidimensional information (e.g. intensity and spectrum at each pixel) etc. Simple brute force scaling of traditional imaging systems for this purpose may however prove infeasible from technical as well as economic points of view. Computational imaging model has a significant role to play in this context in the future. Computational imaging systems are hybrid in nature as they place equal emphasis on the imaging hardware part and the computational part for solving inverse imaging problems. This opens up new possibilities for obtaining unprecedented imaging performance for years to come. The current trend in various imaging system designs indicates that even the most familiar imaging tools like cameras, microscopes, telescopes, etc. are likely to have a completely different physical form and information gathering capabilities than what we are used to. These developments are exciting because they increase our technological capabilities to

probe the nature to newer space-time scales. Some aspects of computational imaging must therefore form a part of training for every serious Science and Technology student.

1.1 Organization of the book

This book is organized in three parts. The first part deals with the Mathematical Preliminaries that will be found useful later the book. This material has been provided in order to make the book self-contained. The mathematical ideas as presented here have not appeared in any single monograph on imaging to the best of the author's knowledge. Discussing the mathematical ideas at the beginning will also help us in setting up a consistent notation for the rest of the book. In Chapter 2 we discuss the important tools of Fourier analysis that are used throughout the book. In Chapter 3 we present the basic ideas behind Shannon sampling theory and the concept of space-bandwidth product which is useful in quantifying information content in an image. The allied topic of the prolate spheroidal functions is also described and an interesting connection between the sampling theory and the prolate functions is discussed. Having introduced Fourier analysis and sampling theory, the next logical topic is the Fast Fourier Transform (FFT) presented in Chapter 4. FFT is an essential tool in almost all image handling tasks. Instead of discussing the finer aspects of the FFT algorithm itself, we present an operational introduction to this topic which will help a reader to use FFT functions available in several standard numerical software packages effectively for simulating optics and imaging problems. Linear systems theory and associated inverse problems are essential for understanding the basic working principle of computational imaging systems. These topics are described in detail in Chapter 5. Several current computational imaging systems require image reconstruction methods that cannot be described as linear filtering operations but rather as constrained optimization problems. Some basic ideas in constrained optimization are described in Chapter 6. This chapter also includes more advanced topics such as compressive imaging that are likely to play major role in future imaging system designs. The last Chapter of the first part presents a discus-

sion of random processes. Conceptual treatment of imaging systems is often presented by means of deterministic equations. The generation, propagation and detection of light waves are however inherently statistical in nature. The understanding of random processes is therefore essential for taking up any imaging system design problem. The topics discussed here find direct utility in later parts of the book.

The second part of the book discusses some important concepts in Optics that are key to understanding the working of imaging systems and their capabilities or limitations. Unlike many well-known books in Optics, the topics in this part are not covered from a historical perspective but are presented in a way that is more suitable for developing an understanding of imaging phenomena from a systems perspective. We begin this part with description of essential concepts of ray or geometrical optics in Chapter 8 followed by details of wave equation and diffraction phenomena in Chapter 9. Diffraction theory is essential to understand how light waves can carry information from the object of interest to the imaging system. Chapter 10 presents another view of diffraction from a transfer function approach. The exact Rayleigh-Sommerfeld-Smythe relations for description of diffraction problem are also presented in this chapter. Next in Chapter 11 we discuss some useful approximations to the exact diffraction relations, viz. Fresnel and Fraunhofer approximations, that are found to be useful in analysis or design of several common practical system setups. The important ideas related to coherence of light fields are described in Chapter 12. While the reader may not appreciate the reason for discussing this topic at this stage, the author believes that without the knowledge of coherence theory, one's knowledge of Optics is incomplete. This is especially so if someone is interested in designing novel futuristic imaging systems. This discussion is followed by Chapter 13 on polarization of light. Polarization is an additional degree of freedom possessed by light waves, although it has not been utilized to its fullest potential in imaging system design so far. Next in Chapter 14 we use the ideas developed in second part of the book to show the reader how one can model simple optical systems involving free-space propagation, lens elements or other phase masks. After covering the important cases of the optical Fourier transform and the canonical or 4F imag-

ing systems configurations, we discuss several practical systems that utilize these ideas. Concepts that help one evaluate an imaging system performance such as the Optical Transfer Function (OTF) are also discussed. Chapter 15 which is the last chapter of the second part of the book presents a general treatment of imaging phenomena from an information point of view. A simple treatment based on the sampling theorem is used here to provide some interesting insights into information carrying capacity of imaging systems from object to the image space.

The third part of the book builds on the material developed in the first two parts to discuss some specific computational imaging ideas. This part is intended to give the readers a feeling for the current research ideas in computational imaging. In Chapters 16 and 17 we discuss one of the most important computational problem of interferometric and non-interferometric phase imaging. Phase of light waves scattered by an object encodes critical information about the object. The phase information is however not available to us directly and phase can only be inferred computationally. In Chapter 18, we discuss some novel compact multi-lens systems that outperform traditional cameras by combining unconventional design and computational image recovery. In Chapter 19 we describe some phase mask designs that use pupil function engineering for extended depth of field imaging. Microscopic imaging beyond traditional diffraction limit has become essential part of basic Bio-sciences research and we discuss a powerful computational imaging modality that uses structural illumination for super-resolution imaging in Chapter 20. In Chapter 21 we present some basic ideas in image reconstruction from projections - a topic which is of considerable importance to the working of several diagnostic imaging systems. Finally in Chapter 22 we describe a somewhat unusual imaging system setup that uses a single pixel detector for generating high resolution images exploiting the correlations in specially designed optical beams.

While computational imaging systems other than optical imaging systems do exist, the author believes that having studied this material, a reader will have no difficulty in understanding them. The material covered in the first two parts in and some selected topics from the third part, can constitute sufficient material for a semester-long course suitable for academic programs in Optics/Photonics.

Part 1:

Mathematical Preliminaries

2. Fourier series and transform

The ideas of Fourier series and transform play a central role in our mathematical treatment of imaging phenomena and the design of image reconstruction algorithms. While these topics are extensively discussed in excellent monographs on the subject, we cover them here for completeness.

2.1 Fourier Series

A periodic function $g(x)$ with period T such that

$$g(x) = g(x + T), \quad -\infty < x < \infty \quad (2.1)$$

may be represented as a Fourier series:

$$g(x) = \sum_{n=-\infty}^{\infty} G_n \exp(i2\pi nx/T). \quad (2.2)$$

This is a very important idea as we shall see when studying linear systems. The question of when such an expansion exists is addressed in the Dirichlet sufficiency conditions:

1. The function $g(x)$ must be absolutely integrable over one period.
2. The function $g(x)$ must be piecewise continuous. A finite number of finite discontinuities is allowed.

3. The function $g(x)$ must have finite number of extrema in one period. Something like $\sin(1/x)$ near $x = 0$ is not allowed.

The co-efficient G_n may be determined using the following orthogonality relation:

$$\begin{aligned} \int_{-T/2}^{T/2} dx \exp[i2\pi(m-n)x/T] &= \left[\frac{\exp[i2\pi(m-n)x/T]}{i2\pi(m-n)/T} \right]_{x=-T/2}^{T/2} \\ &= T \frac{\sin[\pi(m-n)]}{\pi(m-n)} \\ &= T\delta_{m,n} \end{aligned} \quad (2.3)$$

The coefficients G_n can therefore be obtained as:

$$G_n = \frac{1}{T} \int_{-T/2}^{T/2} dx g(x) \exp(-i2\pi nx/T). \quad (2.4)$$

If $g(x)$ has a (finite) discontinuity at $x = x_0$, the series expansion converges to:

$$g(x_0) = \left[\frac{g(x_{0-}) + g(x_{0+})}{2} \right]. \quad (2.5)$$

Illustration: Consider the Fourier series expansion for a square wave of period T.

$$\begin{aligned} g(x) &= g(x+T), \\ g(x) &= 0, x \in (-T/2, 0) \\ &= 1, x \in (0, T/2). \end{aligned} \quad (2.6)$$

The Fourier coefficients are given by:

$$\begin{aligned} G_n &= \frac{1}{T} \int_0^{T/2} dx \exp(-i2\pi nx/T) \\ &= \frac{1}{T} \left[\frac{\exp(-i2\pi nx/T)}{-i2\pi n/T} \right]_{x=0}^{x=T/2} \\ &= \frac{1 - \exp(-i\pi n)}{i2\pi n}. \end{aligned} \quad (2.7)$$

The Fourier coefficients may be listed as follows:

$$G_0 = \frac{1}{2}. \quad (2.8)$$

$$G_1 = \frac{1}{i\pi}, G_{-1} = \frac{1}{-i\pi}. \quad (2.9)$$

$$G_2 = G_{-2} = 0. \quad (2.10)$$

$$G_3 = \frac{1}{3i\pi}, G_{-3} = \frac{1}{-3i\pi}. \quad (2.11)$$

In general, all odd order terms survive and all even order terms except $n = 0$ term vanish. Using the non-vanishing terms we can write the Fourier series expansion as:

$$g(x) = \frac{1}{2} + \frac{2}{\pi} \sin\left(\frac{2\pi x}{T}\right) + \frac{2}{3\pi} \sin\left(\frac{6\pi x}{T}\right) + \dots \quad (2.12)$$

Plots of the series for the first 11, and 101 terms of Eq. (2.12) are shown in Fig. 2.1. The plots show how the series converges to the square wave as the number of terms in the series representation increase. The numerical value $T = 1$ has been used in this illustration for the period of the square wave.

2.2 Gibbs phenomenon

We note a peculiar phenomenon which arises near the discontinuity of a periodic function that is being represented by means of the Fourier series. We rewrite the Fourier series representation for the square wave considered in the illustration earlier.

$$\begin{aligned} g(x) &= \frac{1}{2} + \frac{2}{\pi} \sin\left(\frac{2\pi x}{T}\right) + \frac{2}{3\pi} \sin\left(\frac{6\pi x}{T}\right) + \dots \\ &= \frac{1}{2} + \frac{2}{\pi} \sum_{n=0}^{\infty} \frac{1}{(2n+1)} \sin\left[\frac{2\pi(2n+1)x}{T}\right] \end{aligned} \quad (2.13)$$

When a finite number of terms is included in the summation above, the left hand side has a discontinuity while the right hand side is a sum of continuous functions. The convergence of the series sum to the periodic square wave is therefore not a point-wise convergence (near the discontinuity one observes undershoot and overshoot) but uniform convergence. In fact the overshoot and undershoot do not die out as the number of terms in the partial series sum increases. This interesting feature is known by the name of Gibbs phenomenon.

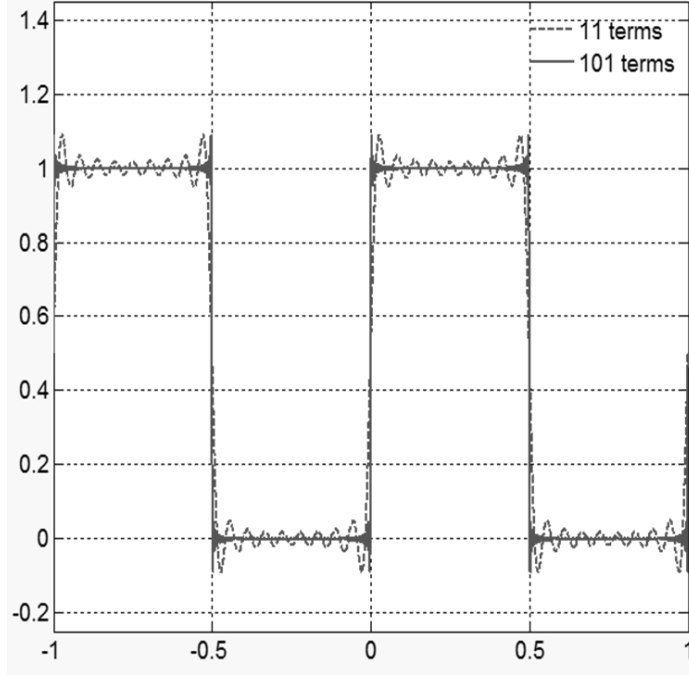


Figure 2.1: Fourier series representation for a square wave with 11 and 101 terms as in Eq. (2.12).

The under and overshoot get closer to the discontinuity with increasing number of terms such that the area under them tends to zero. In other words they do not contribute to the energy in the function. This type of convergence is termed as uniform convergence or “almost everywhere” convergence (convergence everywhere except on sets of measure zero). Figure 2.2 shows a region near the discontinuity of the square wave in Fig. 2.1 to illustrate the behaviour of the Fourier series representation as the number of terms increases. We may express the uniform convergence property as follows:

$$\lim_{N \rightarrow \infty} \left\| g(x) - \frac{1}{2} - \sum_{n=0}^N \frac{1}{(2n+1)} \sin\left[\frac{2\pi(2n+1)x}{T}\right] \right\|^2 = 0. \quad (2.14)$$

The notation above for the L2-norm square is to be understood as:

$$\|g(x)\|^2 = \int_{-\infty}^{\infty} dx |g(x)|^2. \quad (2.15)$$

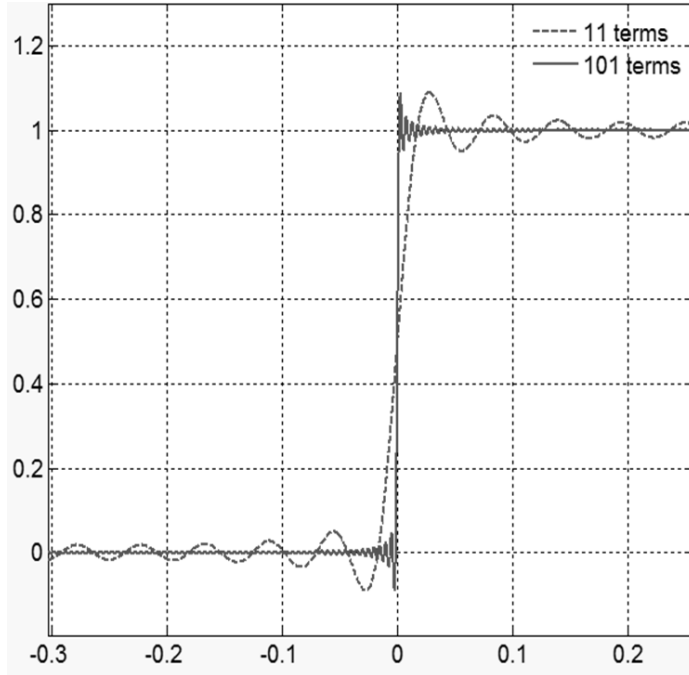


Figure 2.2: Fourier series representation for a square wave with 11 and 101 terms near the discontinuity.

As stated above the uniform convergence implies that $g(x)$ and its approximation need not coincide at every point. The overshoot near the point of discontinuity can be estimated using a Fourier series with finite number of terms. Let us consider the partial sum:

$$S_N(x) = \sum_{n=0}^N \frac{1}{(2n+1)} \sin\left[\frac{2\pi(2n+1)x}{T}\right]. \quad (2.16)$$

Taking a derivative of this partial sum with respect to x gives:

$$S'_N(x) = \frac{2\pi}{T} \sum_{n=0}^N \cos\left[\frac{2\pi(2n+1)x}{T}\right]. \quad (2.17)$$

Summing of this series requires a trick. We note that the consecutive terms of the series have arguments inside the $\cos(\dots)$ function that differ by $(\frac{4\pi x}{T})$ and so we multiply both sides of the equation

by $\sin(\frac{4\pi x}{T})$ and use the relation $[2 \cos(A) \sin(B) = \sin(A + B) - \sin(A - B)]$. Several terms now cancel out in the summation and what remains is:

$$\begin{aligned} S'_N(x) \sin\left(\frac{4\pi x}{T}\right) &= \frac{\pi}{T} \left\{ \sin\left[\frac{2\pi(2N+3)x}{T}\right] + \sin\left[\frac{2\pi(2N+1)x}{T}\right] \right\} \\ &= \frac{2\pi}{T} \sin\left[\frac{2\pi(2N+2)x}{T}\right] \cos\left(\frac{2\pi x}{T}\right). \end{aligned} \quad (2.18)$$

The derivative can thus be expressed as:

$$S'_N(x) = \left(\frac{\pi}{T}\right) \frac{\sin\left[\frac{4\pi(N+1)x}{T}\right]}{\sin\left(\frac{2\pi x}{T}\right)}. \quad (2.19)$$

As we move from the discontinuity at $x = 0$ to right on the x -axis, the first maximum of the partial sum in Eq. (2.16) occurs at the place where the derivative is zero for the first time (one may verify this by going to second derivatives and checking the sign) at the point: $x_0 = \frac{T}{4(N+1)}$. The value of the partial sum at this point gives us an estimate of the value of overshoot.

$$\begin{aligned} S_N(x_0) &= \sum_{n=0}^N \frac{1}{(2n+1)} \sin\left[\frac{\pi(2n+1)}{2(N+1)}\right] \\ &= \frac{\pi}{2} \sum_{n=0}^N \frac{1}{(N+1)} \text{sinc}\left[\frac{n+\frac{1}{2}}{N+1}\right], \end{aligned} \quad (2.20)$$

where we have used the definition:

$$\text{sinc}(x) = \frac{\sin \pi x}{\pi x}. \quad (2.21)$$

For large N the partial sum at $x = x_0$ above is an approximation of the integral of the sinc function on interval $(0, 1)$. We therefore write:

$$S_N\left(\frac{T}{4(N+1)}\right) \approx \frac{\pi}{2} \int_0^1 dx \text{sinc}(x). \quad (2.22)$$

Plugging back into the Fourier series for the square in Eq. (2.13) wave we have:

$$g\left(\frac{T}{4(N+1)}\right) \approx \frac{1}{2} + \int_0^1 dx \text{sinc}(x) \approx 1.0895. \quad (2.23)$$

The graph of function thus shoots above the square wave by approximately 9% even as large number of terms are added to the series. It is to be noted that this maximum occurs closer and closer to zero (at $x = \frac{T}{4(N+1)}$) as the number of terms in the partial sum increases. We shall see later in the book that the Gibbs phenomenon manifests itself in the form of ringing artifacts in images when any filtering operation is performed where the filter has a sharp edge in the frequency space.

2.3 Fourier transform as a limiting case of Fourier series

We will now consider the limiting case of the Fourier series as the period T goes to ∞ . It is clear that the function $g(x)$ is no more periodic. We denote the discrete frequencies as:

$$f_{xn} = \frac{n}{T}, \quad (2.24)$$

The difference between the consecutive discrete frequencies is given by $\Delta f_x = f_{x(n+1)} - f_{xn} = 1/T$. Further we define:

$$G(f_{xn}) = \int_{-\infty}^{\infty} dx g(x) \exp(-i2\pi f_{xn}x). \quad (2.25)$$

We may write the Fourier series expansion as:

$$\begin{aligned} g(x) &= \sum_{n=-\infty}^{\infty} G_n \exp(i2\pi f_{xn}x) \\ &= \sum_{n=-\infty}^{\infty} \left[\frac{1}{T} \int_{-T/2}^{T/2} dx' g(x') \exp(-i2\pi f_{xn}x') \right] \exp(i2\pi f_{xn}x). \end{aligned} \quad (2.26)$$

In the limit $T \rightarrow \infty$ we have:

$$\begin{aligned} g(x) &\rightarrow \sum_{n=-\infty}^{\infty} G(f_{xn}) \exp(i2\pi f_{xn}x) \Delta f_x \\ &\rightarrow \int_{-\infty}^{\infty} df_x G(f_x) \exp(i2\pi f_x x). \end{aligned} \quad (2.27)$$

The functions $g(x)$ and $G(f_x)$ form what is called as the Fourier transform pair.

$$\begin{aligned} G(f_x) &= \int_{-\infty}^{\infty} dx \ g(x) \exp(-i2\pi f_x x), \\ g(x) &= \int_{-\infty}^{\infty} df_x \ G(f_x) \exp(i2\pi f_x x). \end{aligned} \quad (2.28)$$

The Fourier transform pair will often be denoted with the following notation: $G(f_x) = \mathcal{F}\{g(x)\}$ and $g(x) = \mathcal{F}^{-1}\{G(f_x)\}$. Once again this definition of Fourier transform is meaningful under the Dirichlet sufficiency conditions that are similar to those for the Fourier series:

1. $g(x)$ is absolutely integrable. $\int dx |g(x)| < \infty$.
2. $g(x)$ has finite number of finite discontinuities. No infinite discontinuities allowed.
3. $g(x)$ can have only finite number of extrema in a finite interval on x -axis.

What do we mean by $G(f_x)$? We observe from Eq. (2.28) that $g(x)$ is a linear combination of elementary functions of the form $\exp(i2\pi f_x x)$ and $G(f_x)$ is the weight associated with a particular frequency f_x in the expansion for $g(x)$. The description in terms of $G(f_x)$ can thus be considered as an equivalent alternative description for the function $g(x)$. We will now consider a simple example of Fourier transform and introduce some notation along the way.

2.3.1 Fourier transform of the rectangle distribution

Consider the rect function or the rectangle distribution defined as:

$$g(x) = \text{rect}\left(\frac{x}{2L}\right) = \begin{cases} 1 & |x| < L \\ 1/2 & |x| = L \\ 0 & |x| > L \end{cases} \quad (2.29)$$

The Fourier transform of the rect function may be evaluated as:

$$\begin{aligned}
 G(f_x) &= \int_{-L}^L dx \exp(-i2\pi f_x x) \\
 &= \left[\frac{\exp(-i2\pi f_x x)}{-i2\pi f_x} \right]_{-L}^L \\
 &= 2L \frac{\sin(2\pi f_x L)}{(2\pi f_x L)} \\
 &= 2L \operatorname{sinc}(2Lf_x).
 \end{aligned} \tag{2.30}$$

Here the sinc-function is as defined in Eq. (2.21). Note that although $\operatorname{rect}(x)$ has a discontinuity, its transform is continuous. Further it is somewhat surprising to know that $|\operatorname{sinc}(f_x)|$ is not absolutely integrable to have a Fourier transform or Fourier inverse in the conventional sense required by the Dirichlet sufficiency conditions. To show this consider the intervals along f_x axis where $|\sin(\pi f_x)| \geq 0.5$. These intervals are given by $f_x \in [n + 1/6, n + 5/6]$. We therefore have:

$$\int_{-\infty}^{\infty} df_x |\operatorname{sinc}(f_x)| > 2 \frac{1}{2\pi} \sum_{n=0}^{\infty} \frac{2/3}{n + 5/6} \rightarrow \infty. \tag{2.31}$$

The series on the right hand side diverges and as a result the absolute integral of $\operatorname{sinc}(f_x)$ does not exist. Functions such as spikes, steps and even ever extending sines and cosines do not have a Fourier transform in traditional theory. Defining Fourier transforms for such functions is however a practical necessity when representing images as 2D matrices in digital form. In fact edges or spikes contain most important visual information in images. The traditional Fourier transform theory must therefore be extended to take these cases into account. We will study the important case of the Dirac delta function in this context. This class of functions (spikes, steps, etc) with no Fourier transform in conventional theory is known by the name generalized functions. We will not deal with theory of generalized functions in detail but study some specific cases of interest starting with the Dirac delta function.

2.4 Sampling by averaging, distributions and delta function

We will now learn the important idea of the delta function that will be handy later in this book. Sampling a continuous function is a part of every measurement or digitization process. Suppose we have a signal $I(x)$ - say the intensity of ambient light along a line on a screen - that we wish to sample at discrete set of points x_1, x_2, \dots . How do we go about it? Every detector we can possibly use to measure the intensity will have some finite width $2L$ and a sample of $I(x)$ will be an average over this detector area. So we may write the intensity at point $x = 0$, or $I(0)$ as:

$$I(0) \approx \frac{1}{2L} \int_{-\infty}^{\infty} dx I(x) \text{rect}\left(\frac{x}{2L}\right). \quad (2.32)$$

Now how do we improve this approximation so that we go to the ideal $I(0)$? Clearly we have to reduce the size $2L$ over which the average is carried out. We may say that:

$$I(0) = \lim_{2L \rightarrow 0} \frac{1}{2L} \int_{-\infty}^{\infty} dx I(x) \text{rect}\left(\frac{x}{2L}\right). \quad (2.33)$$

Notice that as the length $2L \rightarrow 0$ the width of the function $\frac{1}{2L} \text{rect}\left(\frac{x}{2L}\right)$ keeps reducing whereas its height keeps increasing such that the area under the curve is unity. This limiting process leads us to an impulse which is also commonly known by the name delta function. We may write:

$$\delta(x) = \lim_{2L \rightarrow 0} \frac{1}{2L} \text{rect}\left(\frac{x}{2L}\right). \quad (2.34)$$

Although it is commonly referred to as the “delta function” and we will often call it that way, you will appreciate that it is not a function in the usual sense. When we say $f(x) = x^2$ we are associating a value for every input number x . The impulse or delta distribution is more of an idea that is the result of a limiting process. Anything that is equal to zero everywhere in the limit except at $x = 0$, where it tends to infinity cannot be a function in the sense you may have learnt in your mathematics classes. It is not continuous nor is it

differentiable in the usual way. What can it do? Given a continuous signal $g(x)$, it can sample it at any given point.

$$\int_{-\infty}^{\infty} dx \ g(x) \delta(x - x') = g(x'). \quad (2.35)$$

So unlike a function which takes a number as an input and produces another number as its output, the delta function takes a function as its input and produces a number $g(x')$ as its output. It is in this sense that the terminology “generalized function” for the delta function is to be understood. Another important point to note is that the delta function does make sense when used under the integral sign. For example the sampling property above is a perfectly meaningful result. We will define $\delta(x)$ as:

$$\begin{aligned} \int_{-\infty}^{\infty} dx \ \delta(x) &= 1 \\ \int_{-\infty}^{\infty} dx \ g(x) \delta(x - x') &= g(x'). \end{aligned} \quad (2.36)$$

What is the Fourier transform of $\delta(x)$? We have already seen that:

$$\mathcal{F}\left\{\frac{1}{2L}\text{rect}\left(\frac{x}{2L}\right)\right\} = \text{sinc}(2Lf_x). \quad (2.37)$$

The first zero of the sinc-function is at $2Lf_x = 1$. When $2L \rightarrow 0$ the first zero effectively occurs at infinity meaning that in the Fourier transform space:

$$\mathcal{F}\{\delta(x)\} = 1 \text{ for all } f_x. \quad (2.38)$$

In other words we may write:

$$\delta(x) = \int_{-\infty}^{\infty} df_x \ \exp(i2\pi f_x x). \quad (2.39)$$

Note again that the integral is not valid in the usual sense but is only true in the sense that it represents the idea of an impulse. It should be clear to you now that an impulse requires equal contribution from all the frequencies.

2.5 Properties of delta function

1. **Sampling property** At points of continuity of a function $g(x)$ we have:

$$\int_{-\infty}^{\infty} dx g(x) \delta(x - x') = g(x'). \quad (2.40)$$

If at $x = x'$ the function $g(x)$ has a finite jump discontinuity, the right hand side of the above equation is an average value of the two limits $g(x'_+)$ and $g(x'_-)$.

2. **Derivatives of delta function** All operations with delta function are to be associated with a test function under integral sign. We evaluate the integral below by parts.

$$\begin{aligned} & \int_{-\infty}^{\infty} dx g(x) \frac{d}{dx} \delta(x - x') \\ &= g(x) \delta(x - x')|_{-\infty}^{\infty} - \int_{-\infty}^{\infty} dx \frac{d}{dx} g(x) \delta(x - x') \\ &= -g'(x'). \end{aligned} \quad (2.41)$$

This property applies to multiple order derivatives. So continuing along the lines of above equation we get:

$$\int_{-\infty}^{\infty} dx g(x) \frac{d^n}{dx^n} \delta(x - x') = (-1)^n g^{(n)}(x'), \quad (2.42)$$

where $g^{(n)}(x)$ is the n-th order derivative of $g(x)$.

3. **Delta function with scaling** First of all we note that the delta function is even: $\delta(-x) = \delta(x)$. This leads to:

$$\begin{aligned} \int_{-\infty}^{\infty} dx g(x) \delta(ax) &= \frac{1}{|a|} \int_{-\infty}^{\infty} dx g\left(\frac{x}{a}\right) \delta(x) \\ &= \frac{1}{|a|} g(0). \end{aligned} \quad (2.43)$$

We may therefore write: $\delta(ax) = \frac{1}{|a|} \delta(x)$.

4. **Delta function having another function as an argument** What is the meaning of $\delta(g(x))$? We suppose that $g(x)$ has

a zero at $x = x_1$. If $g(x)$ is a well-behaved test function, it may be expanded near the zero as: $g(x_1) = (x - x_1) g'(x_1)$. (If the first derivative is zero we may use the second or higher derivatives.) The delta function may then be expressed using the scaling property as:

$$\delta(g(x)) = \frac{\delta(x - x_1)}{|g'(x_1)|}. \quad (2.44)$$

This equation may be generalized as a summation of similar terms near all the zeros of the function $g(x)$.

5. **Relation between delta function and unit step** Consider the function: $\int_{-\infty}^x dt \delta(t)$. By inspection we observe that when $x < 0$ the integral is zero when $x > 0$ the values of the integral is equal to 1 for all x . The integral thus represents a step function defined as:

$$u(x) = \begin{cases} 0 & x < 0 \\ 1/2 & x = 0 \\ 1 & x > 0 \end{cases} \quad (2.45)$$

We may now write the integral relation in reverse and observe that the derivative of the unit step is the delta function.

$$\frac{du(x)}{dx} = \delta(x). \quad (2.46)$$

2.6 Fourier transform of unit step and sign functions

The Fourier transform of the unit step function is an interesting case to study. We have already seen that the derivative of a unit step function is the delta function. We will rewrite this more generally as:

$$\frac{d[u(x) + c]}{dx} = \delta(x), \quad (2.47)$$

since the derivative is not affected by the constant c . We will denote the Fourier transform of $u(x)$ by $U(f_x)$ and write the derivative

relation as:

$$\frac{d}{dx} \int_{-\infty}^{\infty} df_x [U(f_x) + c \delta(f_x)] \exp(i2\pi f_x x) = \delta(x). \quad (2.48)$$

Taking the derivative operation inside the integral sign we get:

$$\int_{-\infty}^{\infty} df_x \{(i2\pi f_x)[U(f_x) + c \delta(f_x)] - 1\} \exp(i2\pi f_x x) = 0. \quad (2.49)$$

Since the integral is identically zero for all x we may conclude that:

$$U(f_x) + c \delta(f_x) = \frac{1}{i2\pi f_x}. \quad (2.50)$$

Now all that remains is to determine the constant c . Taking inverse Fourier transform of the above equation gives:

$$u(x) + c = \int_{-\infty}^{\infty} df_x \frac{\exp(i2\pi f_x x)}{i2\pi f_x}. \quad (2.51)$$

The integrand on the right hand side has a pole at $f_x = 0$ on the real line and the integral is to be understood as the Cauchy principal value. The contour used for integration is shown in Fig. 2.3. For $x > 0$ the appropriate semicircle to be selected is in the upper half plane as per Jordan's lemma. For $x > 0$ we have:

$$\int_{-R}^{-\epsilon} + \int_{C1} + \int_{\epsilon}^R + \int_{C2} = 0. \quad (2.52)$$

The integral over C1 gives $(-i\pi)/(i2\pi) = -1/2$ as the curve is traversed clockwise. As $R \rightarrow \infty$ the integral over C2 vanishes for $x > 0$. Thus the principal value of the integral by letting $\epsilon \rightarrow 0$ is given by:

$$P \int_{-\infty}^{\infty} df_x \frac{\exp(i2\pi f_x x)}{i2\pi f_x} = \frac{1}{2}, \quad x > 0. \quad (2.53)$$

In the Eq. (2.51) we may now set $x > 0$ to get:

$$1 + c = \frac{1}{2} \Rightarrow c = -\frac{1}{2}. \quad (2.54)$$

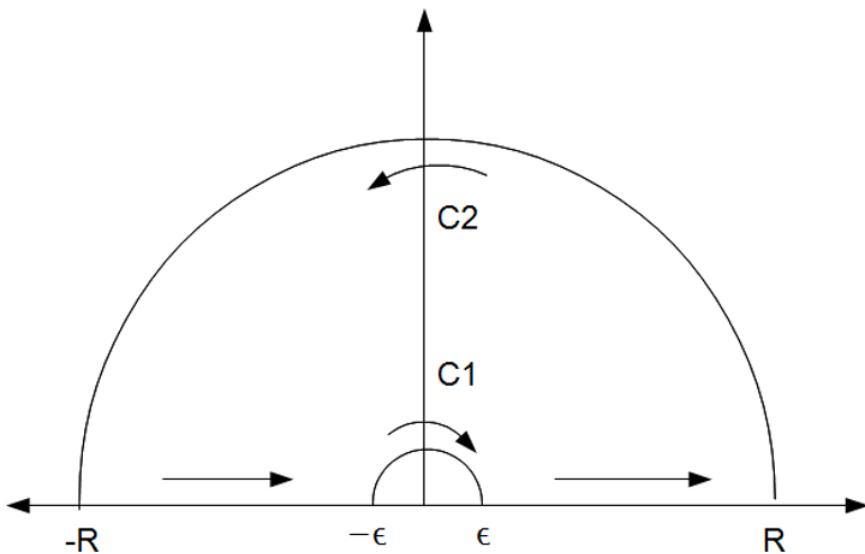


Figure 2.3: Contour used for complex integration in Eq. (2.51) with indent at the origin.

The Fourier transform of the unit step is thus given by:

$$U(f_x) = \frac{1}{i2\pi f_x} + \frac{1}{2} \delta(f_x). \quad (2.55)$$

Once we find the transform of unit step as above, we may evaluate the transform of the sign function $\text{sgn}(x)$ function very easily. We define:

$$\text{sgn}(x) = \begin{cases} -1 & x < 0 \\ 0 & x = 0 \\ 1 & x > 0 \end{cases} \quad (2.56)$$

Note that $\text{sgn}(x) = 2u(x) - 1$ so the transform:

$$\begin{aligned} \mathcal{F}\{\text{sgn}(x)\} &= 2U(f_x) - \delta(f_x) \\ &= \frac{1}{i\pi f_x}. \end{aligned} \quad (2.57)$$

Once again the inverse transform integral is to be understood as the Cauchy principal value.

2.7 Fourier transform of a train of delta functions

We define the comb function or a periodic train of delta functions as:

$$\text{comb}(x) = \sum_{n=-\infty}^{\infty} \delta(x - n). \quad (2.58)$$

The periodicity of the comb function allows us to represent it as a (generalized) Fourier series with period $T = 1$.

$$\text{comb}(x) = \sum_{k=-\infty}^{\infty} c_k \exp(i2\pi kx). \quad (2.59)$$

The series coefficients c_k may be evaluated as:

$$c_k = \int_{-1/2}^{1/2} dx \text{comb}(x) \exp(-i2\pi kx) = 1. \quad (2.60)$$

All the Fourier series coefficients are seen to be identically equal to 1. The Fourier transform of the comb function can now be evaluated in a straightforward manner.

$$\mathcal{F}\{\text{comb}(x)\} = \sum_{k=-\infty}^{\infty} \delta(f_x - k) = \text{comb}(f_x). \quad (2.61)$$

We observe the interesting property that the Fourier transform of a comb function is another comb function. We will now consider another self-Fourier function.

2.8 Fourier transform of a Gaussian

Before evaluating the Fourier transform of the Gaussian we evaluate a useful integral.

$$J = \int_{-\infty}^{\infty} dx \exp(-\pi x^2). \quad (2.62)$$

We note that it is easy to evaluate J^2 in 2D polar co-ordinates.

$$\begin{aligned}
 J^2 &= \int \int dx dy \exp[-\pi(x^2 + y^2)] \\
 &= \int_0^{2\pi} d\theta \int_0^\infty dr r \exp(-\pi r^2) \\
 &= (2\pi) \frac{1}{2\pi} \\
 &= 1.
 \end{aligned} \tag{2.63}$$

This gives an interesting result:

$$\int_{-\infty}^{\infty} dx \exp(-\pi x^2) = 1. \tag{2.64}$$

We will now evaluate the Fourier transform of a Gaussian.

$$\begin{aligned}
 &\int_{-\infty}^{\infty} dx \exp(-\pi x^2 - i2\pi f_x x) \\
 &= \int_{-\infty}^{\infty} dx \exp[-\pi(x + if_x)^2] \exp(-\pi f_x^2) \\
 &= \exp(-\pi f_x^2) \int_{-\infty+if_x}^{\infty+if_x} du \exp(-\pi u^2).
 \end{aligned} \tag{2.65}$$

The contour to be used for evaluating the transform is shown in Fig. 2.4. The contour is in upper half plane for $f_x > 0$ (shown in figure) and in the lower half plane when $f_x < 0$. As $R \rightarrow \infty$ the contribution of the vertical parts of the integration paths vanishes as $\exp(-\pi(\pm R + iy)^2) \rightarrow 0$. The integral over the real line gives -1 (direction from + to -). The integral we want to evaluate is thus equal to +1 since the integrand is analytic on and inside the contour. The result is:

$$\mathcal{F}\{\exp(-\pi x^2)\} = \exp(-\pi f_x^2). \tag{2.66}$$

2.9 Fourier transform of chirp phase

The Fourier transform of quadratic or chirp phase function is an important result as we shall see later in the context of Fresnel diffraction. The function of interest is $g(x) = \exp(i\pi x^2)$ whose Fourier

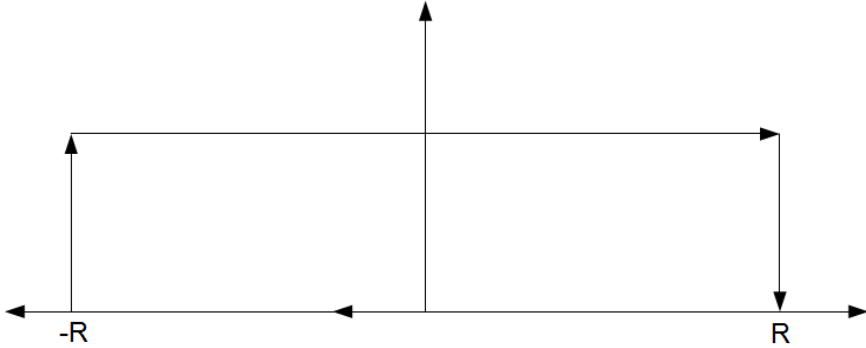


Figure 2.4: Contour used for evaluating Fourier transform of Gaussian.

transform is evaluated as follows.

$$\begin{aligned}
 G(f_x) &= \int_{-\infty}^{\infty} dx \exp(i\pi x^2 - i2\pi f_x x) \\
 &= \exp(-i\pi f_x^2) \int_{-\infty}^{\infty} dx \exp[i\pi(x - f_x)^2] \\
 &= \exp(-i\pi f_x^2) \int_{-\infty}^{\infty} dx \exp(i\pi x^2) \\
 &= 2 \exp(-i\pi f_x^2) \int_0^{\infty} dx \exp(i\pi x^2).
 \end{aligned} \tag{2.67}$$

Since we know the integral of $\exp(-\pi t^2)$ on the real line, let us make a substitution:

$$-\pi z^2 = i\pi x^2 \Rightarrow z = \exp(-i\pi/4)x. \tag{2.68}$$

As x goes from 0 to ∞ , the integration path for z goes along a radial line through the origin at an angle $(-\pi/4)$ with the x-axis. We will now evaluate the integral of $\exp(-\pi z^2)$ along the 45-degree wedge contour shown below. For the integral along the slant line $z = \exp(-i\pi/4)x$, with x increasing along real line from zero to ∞ , we have: $\exp(-\pi z^2) = \exp(i\pi x^2)$ as is required for the Fourier transform that we are evaluating. The integral along the curved part of the contour vanishes as $R \rightarrow \infty$. The integral along the real line is already known as we found in evaluating the Fourier transform of

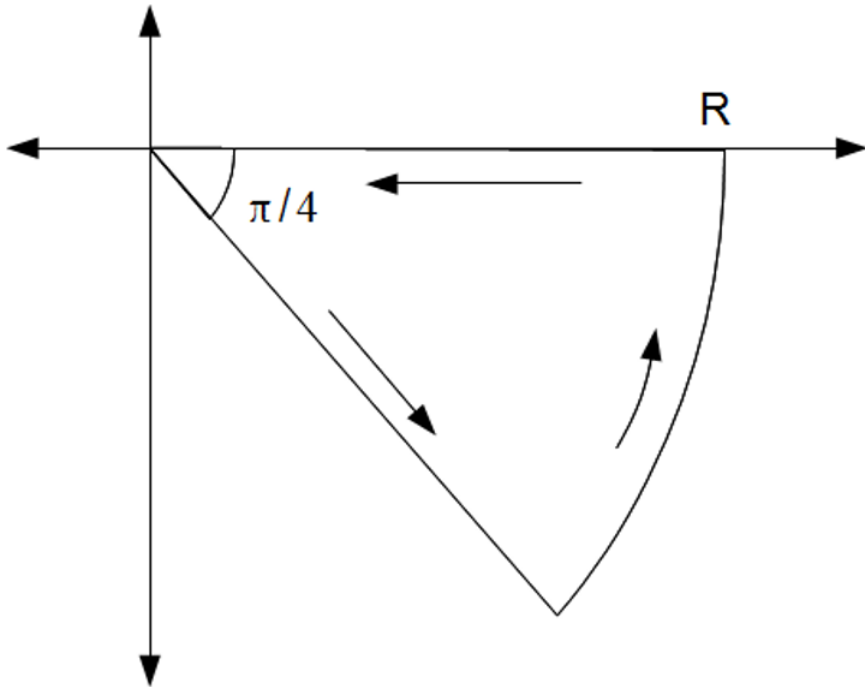


Figure 2.5: Contour used for evaluating Fourier transform of quadratic phase function.

a Gaussian.. The integrand being analytic on and inside the wedge shaped contour, we have the following result:

$$\begin{aligned} \int_0^\infty dx \exp(-i\pi/4) \exp(i\pi x^2) - \int_0^\infty dx \exp(-\pi x^2) &= 0 \\ \Rightarrow \int_0^\infty dx \exp(i\pi x^2) &= \frac{1}{2} \exp(i\pi/4). \end{aligned} \quad (2.69)$$

The Fourier transform of interest is thus given by:

$$\mathcal{F}\{\exp(i\pi x^2)\} = \exp(i\pi/4) \exp(-i\pi f_x^2). \quad (2.70)$$

Note the change of the sign of i in the exponential and the additional phase factor of $\pi/4$.

2.10 Properties of Fourier transform

In this section we will discuss several important properties of Fourier transform that will then be used directly throughout the book.

1. **Linearity** Fourier transform is a linear operation. For two functions $g_1(x)$ and $g_2(x)$ and constants c_1 and c_2 , we have:

$$\mathcal{F}\{c_1 g_1(x) + c_2 g_2(x)\} = c_1 G_1(f_x) + c_2 G_2(f_x). \quad (2.71)$$

2. **Scaling property** If a function is scaled by a constant factor a the Fourier transform is scaled too, but in opposite way. If a function is stretched, its Fourier transform is compressed.

$$\begin{aligned} & \mathcal{F}\left\{g\left(\frac{x}{a}\right)\right\} \\ &= \int_{-\infty}^{\infty} dx g\left(\frac{x}{a}\right) \exp(-i2\pi f_x x) \\ &= |a| \int_{-\infty}^{\infty} d(x/a) g\left(\frac{x}{a}\right) \exp(-i2\pi a f_x x/a) \\ &= |a|G(af_x). \end{aligned} \quad (2.72)$$

3. **Shifting property** The Fourier transform of a shifted function gets an additional phase factor depending on the shift in coordinates.

$$\begin{aligned} \mathcal{F}\{g(x - a)\} &= \int_{-\infty}^{\infty} dx g(x - a) \exp(-i2\pi f_x x) \\ &= \exp(-i2\pi f_x a)G(f_x). \end{aligned} \quad (2.73)$$

4. **Energy (Parseval) theorem** The energy contained in a signal $g(x)$ is equal to the energy in its Fourier transform $G(f_x)$. Here the energy is defined as the squared L2-norm of $g(x)$ or $G(f_x)$ evaluated with respect to x or f_x coordinates respectively.

$$\begin{aligned} & \int_{-\infty}^{\infty} df_x |G(f_x)|^2 \\ &= \int_{-\infty}^{\infty} df_x \left\{ \int_{-\infty}^{\infty} dx g(x) e^{-i2\pi f_x x} \right\} \left\{ \int_{-\infty}^{\infty} dx' g^*(x') e^{i2\pi f_x x'} \right\}. \end{aligned} \quad (2.74)$$

The integration over f_x may now be performed by making use of the Fourier integrgr representation of the delta function to obtain:

$$\begin{aligned} & \int_{-\infty}^{\infty} df_x |G(f_x)|^2 \\ &= \int_{-\infty}^{\infty} dx \int_{-\infty}^{\infty} dx' g(x) g^*(x) \delta(x - x') \\ &= \int_{-\infty}^{\infty} dx |g(x)|^2. \end{aligned} \quad (2.75)$$

5. **Convolution theorem** This is one of the most important results and as you will see later in this book. The Fourier transform of the convolution (defined below) of two functions is given by a product of their Fourier transforms.

$$\begin{aligned} & \mathcal{F}\left\{\int_{-\infty}^{\infty} dx' g(x') h(x - x')\right\} \\ &= \int_{-\infty}^{\infty} dx \exp(-i2\pi f_x x) \int_{-\infty}^{\infty} dx' g(x') h(x - x') \\ &= \int_{-\infty}^{\infty} dx' g(x') H(f_x) \exp(-i2\pi f_x x') \\ &= G(f_x) H(f_x). \end{aligned} \quad (2.76)$$

The convolution operation is often required to model system response in linear systems theory and we will find that the convolution theorem plays an important role. A similar result - the auto-correlation theorem - may be obtained if we use $h(x) = g^*(x)$ giving:

$$\mathcal{F}\left\{\int_{-\infty}^{\infty} dx' g(x') g^*(x - x')\right\} = |G(f_x)|^2. \quad (2.77)$$

As an application of the convolution theorem we consider the transform of a triangle function:

$$\Lambda(x) = \begin{cases} 1 - |x| & |x| \leq 1 \\ 0 & \text{Otherwise.} \end{cases} \quad (2.78)$$

We observe that the triangle function can be obtained by convolving two rectangle distributions:

$$\Lambda(x) = \text{rect}(x) * \text{rect}(x), \quad (2.79)$$

so that, its Fourier transform is given by $\mathcal{F}\{\Lambda(x)\} = \text{sinc}^2(f_x)$. In fact one may repeatedly convolve the rect function with itself and generate a family of interpolation functions known as the Box-splines.

2.11 Fourier transform of the 2D circ function

This is the first inherently 2D case that we will consider here in the study of Fourier transforms. Several optical elements like lenses are often circular in shape and this case is thus important. We define the circ function (or distribution) as:

$$\text{circ}\left(\frac{r}{a}\right) = \begin{cases} 1 & \sqrt{x^2 + y^2} < a \\ 1/2 & \sqrt{x^2 + y^2} = a \\ 0 & \sqrt{x^2 + y^2} > a \end{cases} \quad (2.80)$$

Before evaluating the Fourier transform we make transformations:

$$\begin{aligned} x &= r \cos(\theta) \\ y &= r \sin(\theta) \\ f_x &= \rho \cos(\phi) \\ f_y &= \rho \sin(\phi). \end{aligned} \quad (2.81)$$

We will use this notation throughout the book for 2D polar co-ordinates (spatial and spatial frequency domains). The Fourier integral may now be expressed as:

$$\begin{aligned} \mathcal{F}\{\text{circ}\left(\frac{r}{a}\right)\} \\ = \int_0^{2\pi} d\theta \int_0^a r dr \exp(i2\pi r\rho \cos(\theta - \phi)). \end{aligned} \quad (2.82)$$

The integral over θ can be expressed in term of the Bessel function $J_0(\dots)$ so as to get:

$$\begin{aligned}
 & \mathcal{F}\{\text{circ}(\frac{r}{a})\} \\
 &= 2\pi \int_0^a r dr J_0(2\pi r\rho) \\
 &= 2\pi \frac{1}{(2\pi\rho)^2} \int_0^{2\pi a\rho} u du J_0(u) \\
 &= 2\pi \frac{1}{(2\pi\rho)^2} \int_0^{2\pi a\rho} du \frac{d}{du} [u J_1(u)] \\
 &= \frac{1}{2\pi\rho^2} \left[u J_1(u) \right]_0^{2\pi a\rho} \\
 &= (2\pi a^2) \frac{J_1(2\pi a\rho)}{(2\pi a\rho)} \\
 &= (\pi a^2) \text{jinc}(2a\rho). \tag{2.83}
 \end{aligned}$$

Here $J_n(\dots)$ denotes the Bessel function of the first kind and of order n . In evaluating the integral we have used the property of Bessel functions:

$$\frac{d}{du} [u^n J_n(u)] = u^n J_{n-1}(u). \tag{2.84}$$

Also in analogy with the “sinc” function we define the “jinc” function as:

$$\text{jinc}(u) = 2 \frac{J_1(\pi u)}{(\pi u)}, \tag{2.85}$$

which tends to 1 in the limit $u \rightarrow 0$.

2.12 Fourier slice theorem

Fourier slice theorem is another property of Fourier transforms inherent to two or higher dimensions. The Fourier slice theorem relates the 2D Fourier transform of a function to its projection in a particular direction. We define the projection $p_\theta(t)$ of the image $g(x, y)$ as a line integral through the image $g(x, y)$ along the line L as shown in Fig. 2.6:

$$p_\theta(t) = \int \int_{xy \text{ plane}} dx dy g(x, y) \delta(x \cos \theta + y \sin \theta - t). \tag{2.86}$$

The appearance of the delta function above is due to the fact that the line L is described by equation $x \cos \theta + y \sin \theta = t$.

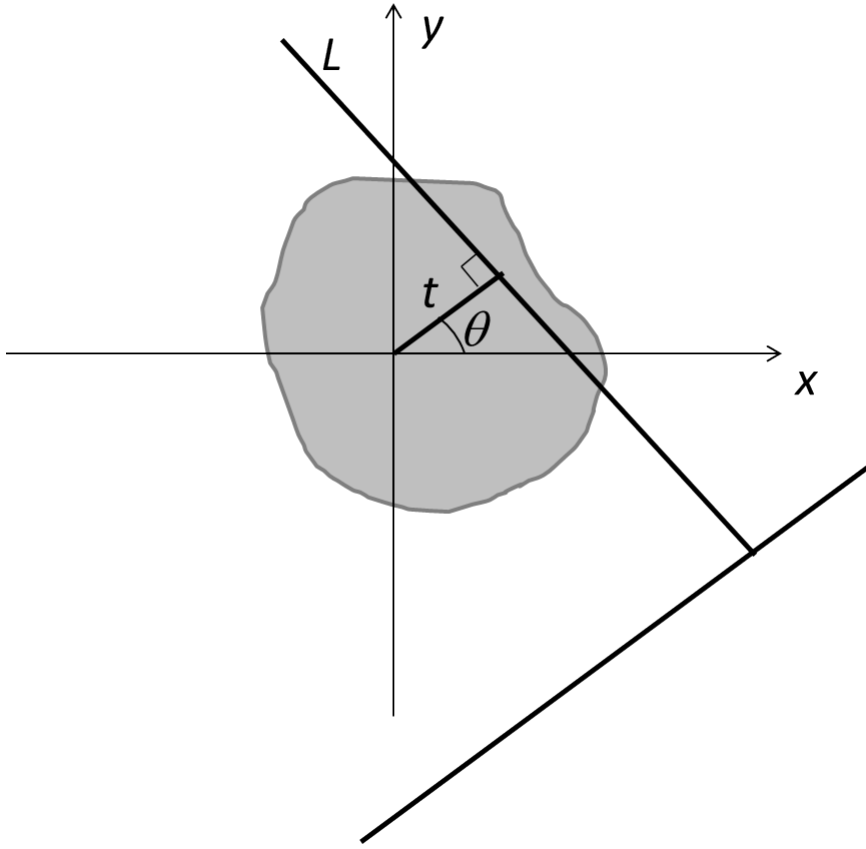


Figure 2.6: Projection $p_\theta(t)$ as a line integral of object $g(x, y)$ along the line L .

The Fourier transform of the projection with respect to the variable t may be related to the 2D Fourier transform $G(f_x, f_y)$ of the function $g(x, y)$ as follows:

$$\begin{aligned} & \mathcal{F}_t\{p_\theta(t)\} \\ &= \int_{-\infty}^{\infty} dt \exp(-i 2\pi \nu t) \int \int dx dy g(x, y) \delta(x \cos \theta + y \sin \theta - t). \end{aligned} \tag{2.87}$$

The integral over t can be evaluated readily using the sampling property of the delta function. We therefore have

$$\begin{aligned} & \mathcal{F}_t\{p_\theta(t)\} \\ &= \int \int dx dy g(x, y) \exp[-i 2\pi\nu(x \cos \theta + y \sin \theta)] \\ &= G(\nu \cos \theta, \nu \sin \theta). \end{aligned} \quad (2.88)$$

The 1D Fourier transform of the projection is thus seen to be equivalent to the 2D Fourier transform $G(f_x, f_y)$ along the line (or slice) passing through the origin which is described by: $f_x = \nu \cos \theta, f_y = \nu \sin \theta$ with $\nu : (-\infty, \infty)$. Projections along various directions θ thus provide information about central slices through the 2D Fourier transform. This principle is central to medical imaging scanners (e.g. X-ray CT scanners) that generate images of the internal organs using projection data along multiple directions over a circle.

2.13 Wigner distribution

The Fourier transform $G(f_x)$ of a signal contains no information about the local behaviour of the corresponding function $g(x)$. However this does not prevent us from giving a simultaneous space-frequency description of the signal. There is a general class - Cohen class - of distribution functions that try to achieve such simultaneous description. It is clear that such description cannot be more precise than that allowed by the uncertainty relations. One of the important space-frequency descriptions was given by Wigner in 1932. For a signal $g(x)$ the Wigner distribution is a function of both x and f_x and is given by:

$$W_g(x, f_x) = \int_{-\infty}^{\infty} d\xi g(x + \xi/2) g^*(x - \xi/2) \exp(-i2\pi f_x \xi). \quad (2.89)$$

For illustration let us consider two special cases:

$$g_1(x) = \exp(i2\pi f_0 x), \quad (2.90)$$

$$g_2(x) = \exp(i2\pi f_0 x^2). \quad (2.91)$$

The first function has a constant spatial frequency at all x whereas the second signal is a chirp signal with linearly increasing local frequency. Evaluating the integral in Eq. (2.89) gives:

$$W_{g_1}(x, f_x) = \delta(f_x - f_0), \quad (2.92)$$

$$W_{g_2}(x, f_x) = \delta(f_x - 2f_0x). \quad (2.93)$$

The Wigner distribution is thus seen to provide information analogous to musical score where the sequence of notes in time is described. The most important property of the Wigner distribution is its projection property. We first integrate the Wigner distribution with respect to the f_x variable to get:

$$\begin{aligned} \int_{-\infty}^{\infty} df_x W_g(x, f_x) &= \int_{-\infty}^{\infty} d\xi g(x + \xi/2) g^*(x - \xi/2) \delta(\xi) \\ &= |g(x)|^2. \end{aligned} \quad (2.94)$$

Further, integrating the Wigner distribution with respect to the variable x gives:

$$\begin{aligned} \int_{-\infty}^{\infty} dx W_g(x, f_x) &= \int_{-\infty}^{\infty} dx \int_{-\infty}^{\infty} d\xi g(x) g^*(x - \xi) \exp(-i2\pi f_x \xi) \\ &= \int_{-\infty}^{\infty} dx \int_{-\infty}^{\infty} du g(x) g^*(u) \exp[-i2\pi f_x(x - u)] \\ &= |G(f_x)|^2. \end{aligned} \quad (2.95)$$

The projection of the Wigner distribution along x or f_x thus gives the complementary energy density $|G(f_x)|^2$ or $|g(x)|^2$ respectively. Wigner distribution is therefore also sometimes called as a quasi-probability distribution. A closely related function called the ambiguity function is also sometimes used, particularly in radar signal processing for simultaneous space-frequency representation. It is defined as:

$$A_g(x, f_x) = \int_{-\infty}^{\infty} dx' g(x' - x/2) g^*(x' + x/2) \exp(i2\pi f_x x'). \quad (2.96)$$

We will see later in this book that these functions have close relation to the incoherent frequency response (or Optical Transfer Function) of imaging systems.

We have discussed several ideas related to Fourier transforms in this chapter that we will use later in this book when discussing propagation of light waves and analysis of imaging systems.

References and suggested reading

1. R. Bracewell, *The Fourier transform and its applications*, 2nd Ed., McGraw Hill (1986).
2. J. W. Goodman, *Introduction to Fourier Optics*, 2nd Ed., McGraw Hill (1996).
3. M. J. Lighthill, *An introduction to Fourier analysis and generalized functions*, Cambridge Univ. Press (1964).
4. B. G. Osgood, The Fourier transform and its applications, Stanford Engineering Everywhere online material. (see.stanford.edu)

3. Sampling Theorem

We often hear or talk about the digital revolution that we see around us today. Our lives have changed so much just in a span of one generation due to the digital equipment we use everyday. A lot of technologies have to get developed and come together for making a gadget like a cell phone possible. But the core idea of why digital representations of signals that we often model as continuous functions is possible lies in the sampling theorem. Before we go there I would like to point out that communication through electromagnetic means became practical in early years of 20th century. It is then that the problem of quantifying the resources required for communicating some particular information became important. The credit for developing a formalism for quantifying information for communication purposes goes to Claude Shannon. His article titled “The Mathematical Theory of Communication” (in *Bell Systems Tech. Journal* 1948) on this topic is a classic. As I have already discussed before, the information of interest to us in imaging or related phenomena is encoded on waves that carry the information from the object to our system. While most of our models for wave phenomena are continuous, the sampling required in any measurement is done at discrete points. How many samples are enough ? Intuitively it appears that the more samples we take is always better. However, it is also clear that if you wanted to sample a speech signal, it may be too much to sample at the rate of say 1 MHz or 1 GHz when the highest audio frequencies of interest may be at most a few kHz. Can we formalize this intuition in some way? Can we establish some bound on what sampling rate is required? We will study this important basic problem in this chapter. Sampling ideas play an important role in computational imaging systems. The discrete samples used to rep-

resent an image signal is often referred to as the pixels in an image.

3.1 Poisson summation formula

We will arrive at the sampling theorem via an interesting result on Fourier transforms - the Poisson summation formula which was known long before sampling theorem became popular. With the knowledge of the Poisson summation formula, it is not very hard to arrive at the sampling theorem. It is just that the result gained significance due to its relevance to communicating information. We will begin by considering a signal $g(x)$ and its Fourier transform

$$G(f_x) = \int_{-\infty}^{\infty} dx g(x) \exp(-i2\pi f_x x). \quad (3.1)$$

As a first step we will construct a periodic function with period Δ by using the Fourier transform $G(f_x)$ that we can then represent as a Fourier series.

$$\sum_{n=-\infty}^{\infty} G(f_x + n\Delta) = \sum_{k=-\infty}^{\infty} g_k \exp(-i2\pi k f_x / \Delta). \quad (3.2)$$

We have defined the Fourier series with negative sign in the exponential since our left hand side is a Fourier transform. This keeps all our definitions consistent. The negative sign does not really matter otherwise since k goes from $-\infty$ to ∞ . We will now determine the coefficients g_k of the Fourier series in Eq. (3.2).

$$\begin{aligned} g_k &= \frac{1}{\Delta} \int_{-\Delta/2}^{\Delta/2} df_x \sum_{n=-\infty}^{\infty} G(f_x + n\Delta) \exp(i2\pi k f_x / \Delta) \\ &= \frac{1}{\Delta} \sum_{n=-\infty}^{\infty} \int_{(n-\frac{1}{2})\Delta}^{(n+\frac{1}{2})\Delta} du G(u) \exp(i2\pi k u / \Delta - i2\pi n k). \end{aligned} \quad (3.3)$$

Since n and k are integers, we have $\exp(-i2\pi nk) = 1$. Further, the summation over n effectively covers the entire u axis and thus we can write:

$$\begin{aligned} g_k &= \frac{1}{\Delta} \int_{-\infty}^{\infty} du G(u) \exp(i2\pi k u / \Delta) \\ &= \frac{1}{\Delta} g(\frac{k}{\Delta}). \end{aligned} \quad (3.4)$$

The above result tells us that when a periodic function is formed by adding regularly shifted versions of Fourier transform $G(f_x)$, the corresponding Fourier series coefficients are simply the periodic samples of $g(x)$ at points $x = k/\Delta$ with integer k .

3.2 Sampling theorem as a special case

In order to establish the sampling theorem, we will define the class of bandlimited signals. We will call a signal $g(x)$ to be bandlimited to the frequencies $f_x : (-B, B)$ if its Fourier transform vanishes outside this frequency interval. Now we will consider a special case of the Poisson summation formula when the signal $g(x)$ is bandlimited as above and $\Delta = 2B$. The shifted versions of the Fourier transform now do not overlap and we may filter out the $n = 0$ term by multiplying both sides of Eq. (3.2) with a rect function.

$$G(f_x) = \frac{1}{2B} \sum_{k=-\infty}^{\infty} g\left(\frac{k}{2B}\right) \exp\left(-i2\pi k \frac{f_x}{2B}\right) \text{rect}\left(\frac{f_x}{2B}\right) \quad (3.5)$$

Taking an inverse Fourier transform now yields the sampling theorem.

$$\begin{aligned} g(x) &= \frac{1}{2B} \sum_{k=-\infty}^{\infty} g\left(\frac{k}{2B}\right) \int_{-\infty}^{\infty} df_x \exp[i2\pi f_x (x - \frac{k}{2B})] \text{rect}\left(\frac{f_x}{2B}\right) \\ &= \sum_{k=-\infty}^{\infty} g\left(\frac{k}{2B}\right) \text{sinc}[2B(x - \frac{k}{2B})]. \end{aligned} \quad (3.6)$$

This is an exciting result. It tells us that the samples of the bandlimited signal $g(x)$ at discrete points separated $1/(2B)$ apart contain the same information as that in the continuous signal. If we know these discrete sample values, the continuous signal can be reconstructed by sinc-interpolation of the samples. This sampling rate is known by the name Nyquist rate to honour the early contributions by H. Nyquist to communication theory.

3.3 Additional notes on the sampling formula

An important point to note regarding the sampling theorem is that the set of shifted sinc functions forms an orthogonal and complete basis for the class of bandlimited functions. This basis is quite different from other common basis sets you may have encountered before (e.g. Hermite-Gauss functions) in that the shifted versions of the same function are here seen to be orthogonal. The origin of advanced signal representation concepts like wavelets may be traced back to this unusual kind of basis. The orthogonality property may be proved as follows:

$$\begin{aligned} & \int_{-\infty}^{\infty} dx \operatorname{sinc}(2Bx - m) \operatorname{sinc}(2Bx - n) \\ &= \mathcal{F}^{-1}\left\{\frac{1}{(2B)^2} \operatorname{rect}^2\left(\frac{f_x}{2B}\right)\right\}|_{x=\frac{m-n}{2B}} \\ &= \frac{1}{2B} \operatorname{sinc}(m - n) \\ &= \frac{1}{2B} \delta_{m,n}. \end{aligned} \tag{3.7}$$

In the calculation above we have made use to the convolution theorem. The sample $g\left(\frac{m}{2B}\right)$ of the bandlimited signal can thus be thought of as a co-efficient of the series expansion in the sinc-basis.

$$g\left(\frac{m}{2B}\right) = \frac{1}{2B} \int_{-\infty}^{\infty} dx g(x) \operatorname{sinc}(2Bx - m). \tag{3.8}$$

The completeness property of the sinc-basis set is simple to prove. We observe that:

$$\sum_{n=-\infty}^{\infty} \operatorname{sinc}(2Bx - m) \operatorname{sinc}(2Bx' - m) = \operatorname{sinc}[2B(x - x')]. \tag{3.9}$$

The identity follows by applying the sampling theorem to the sinc function itself. For every signal $g(x)$ bandlimited to $f_x : (-B, B)$

we have:

$$\begin{aligned} \int_{-\infty}^{\infty} dx' g(x') \operatorname{sinc}[2B(x - x')] &= \mathcal{F}^{-1}[G(f_x) \frac{1}{2B} \operatorname{rect}(\frac{f_x}{2B})] \\ &= \frac{1}{2B} g(x). \end{aligned} \quad (3.10)$$

If we now use the completeness relation for the term $\operatorname{sinc}[2B(x - x')]$ and the relation in Eq. (3.8), we see that we arrive at the sampling theorem. The sinc-basis thus allows representation of every bandlimited function. The expression $\operatorname{sinc}[2B(x - x')]$ may be thought of as the bandlimited version of $\delta(x - x')$.

3.4 Sampling of carrier-frequency signals

The Shannon sampling theorem is sometimes explained simplistically by stating a thumb rule that a sinusoidal signal requires two samples per cycle of the sinusoid. This statement is somewhat misleading, because if one knows that what we are sampling is a sinusoid then it should be possible to specify the waveform only from the knowledge of its frequency, amplitude and initial phase. A similar situation arises in practice for an important class of signals that one encounters in communication, representation of narrowband optical fields and optical interferometric imaging, etc. that are of the form:

$$g(x) = a(x) \exp(i2\pi f_0 x) + a^*(x) \exp(-i2\pi f_0 x). \quad (3.11)$$

Here $a(x)$ is called as the complex envelope of the signal and f_0 is its carrier frequency. In most cases where such signals are studied, the effective bandwidth $2B$ of the complex envelope $a(x)$ is much less than the carrier-frequency f_0 . The magnitude of Fourier spectrum of a typical carrier-frequency signal is as shown in Fig. 3.1. It is clear that while the highest frequency in the signal is $(f_0 + B)$, it is reasonable to expect that the sampling rate required for digitizing such a signal need not be as high as $2(f_0 + B)$ samples per unit interval in x . This is because there is lot of empty region between the two lobes in the Fourier spectrum centered on the carrier frequency $\pm f_0$. It can be shown that if we select a frequency interval $2B_0$ such

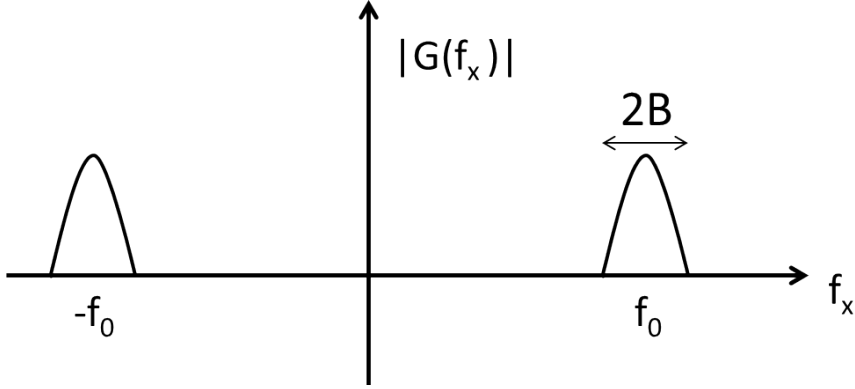


Figure 3.1: Magnitude of Fourier spectrum $|G(f_x)|$ for a carrier-frequency type signal as in Eq. (3.11).

that

$$\frac{f_0}{2B} \geq \frac{f_0}{2B_0} = N + \frac{1}{2}, \quad (3.12)$$

for some integer N (preferably largest possible for given values of f_0 and B), then the signal $g(x)$ can be sampled at intervals $1/(4B_0)$ to get a carrier-frequency form of the sampling theorem:

$$g(x) = \sum_{k=-\infty}^{\infty} g\left(\frac{k}{4B_0}\right) \text{sinc}\left[2B_0\left(x - \frac{k}{4B_0}\right)\right] \cos\left[2\pi f_0\left(x - \frac{k}{4B_0}\right)\right]. \quad (3.13)$$

The above result can be arrived at by similar arguments as the usual low-pass sampling theorem and is sometimes referred to as the band-pass sampling theorem. The central idea in this result is to effectively use the fact that the empty region in Fourier space does not lead to aliasing even if the sampling interval is much larger than $1/2(f_0 + B)$. The cosine term in the equation above can be written as a sum of two exponential terms and the demodulated envelope $a(x)$ can be expressed as a sampling series:

$$a(x) = \sum_{k=-\infty}^{\infty} g\left(\frac{k}{4B_0}\right) \text{sinc}\left[2B_0\left(x - \frac{k}{4B_0}\right)\right] \exp\left(-2\pi f_0 \frac{k}{4B_0}\right). \quad (3.14)$$

The sampling rate is therefore comparable to the fluctuations in the complex envelope rather than the maximum signal bandwidth. The

knowledge of carrier-frequency f_0 is implicitly assumed in the above discussion. This result is important in the context of quantifying the degrees of freedom in a signal as we will discuss in the following section.

3.5 Degrees of freedom in a signal: space bandwidth product

Suppose we have a signal of length $2L$ which we want to store or transmit to someone else. What resources are required? Most practical signals or images are of finite extent and a finite length signal cannot be bandlimited at the same time in exact sense. Its Fourier transform must in principle extend all over the frequency axis. The notion of bandwidth thus needs to be defined carefully. For a signal $g(x)$ in the range $x : (-L, L)$ we define energy concentration ratio within some band of frequencies $f_x : (-B, B)$ as:

$$\alpha = \frac{\int_{-B}^B df_x |G(f_x)|^2}{\int_{-\infty}^{\infty} df_x |G(f_x)|^2}. \quad (3.15)$$

A practical definition of bandwidth is now taken as that interval $f_x : (-B, B)$ for which the energy concentration ratio takes some value close to 1 (e.g. 0.999) as demanded by the application. How many samples of the signal are needed to represent it in a fairly accurate manner? The answer is $(2B)(2L)$. The product $N = 4BL$ is called the space-bandwidth product of a signal and it represents the degrees of freedom in a signal. For a 2D signal or image this number would be N^2 which is the number of pixels required to represent an image.

The space-bandwidth product of a signal and that for a system are two separate concepts. Suppose our object is a biological tissue sample placed in a slide to be observed under a microscope. A living cell is a very complex object and details of interest can be at a molecular or nanometer scale corresponding to spatial frequencies of the order of 10^9 m^{-1} . For a sample of size $1 \text{ mm} \times 1 \text{ mm}$, the space-bandwidth product of the object is then of the order of $(10^{-3})^2(10^9)^2 = 10^{12}$. The system for observing the cell sample may have a much smaller space-bandwidth product. The resolution

size for a microscope using visible light may be $1\mu\text{m}$. For sufficient illuminating light level the space-bandwidth product for the system is thus $(10^{-3})^2(10^6)^2 = 10^6$. So if we want to put a CCD camera as a detector at the back-end of the microscope, a sensor chip with pixel numbers of the order of 1000×1000 pixels should be sufficient. If we are operating under low-light level conditions, the noise will make the signal from each pixel somewhat unreliable. We may have to bin the sensor chip so that an average is performed over say a 2×2 pixel block. The resulting image will thus have 500×500 pixels - resulting in reduction in information that can be retrieved from the system setup. The space-bandwidth product thus depends both on the system parameters and the signal-to-noise considerations.

3.6 Slepian (prolate spheroidal) functions

We have defined the energy concentration ration α in the Eq. (3.15) in order to arrive at a practical definition of what we mean by bandwidth. The problem of finding the functions that achieve the maximum value of α was posed by Shannon in 1950's. The comprehensive analysis of this problem was performed by Slepian, Pollak and Landau in a series of papers in the Bell System Tech. Journal in 1960's. Such functions are now often referred to as the Slepian functions in the honour of D. Slepian. We will study some of their interesting properties and also establish their connection to the Shannon sampling theorem as was first studied in [Khare and George, J. Physics A: Mathematical & General, 36, 10011 (2003)]. The Slepian functions will be found useful later in the book when we discuss issues such as super-resolution and information carrying capacity of imaging systems. For a function $g(x)$ defined over $x : (-L, L)$ we will write the energy concentration ratio α explicitly as:

$$\begin{aligned} \alpha &= \frac{\int_{-B}^B df_x \int_{-L}^L \int_{-L}^L dx dx' g(x)g^*(x') \exp[-i2\pi f_x(x-x')]}{\int_{-\infty}^{\infty} df_x |G(f_x)|^2} \\ &= 2B \frac{\int_{-L}^L \int_{-L}^L dx dx' g(x)g^*(x') \text{sinc}[2B(x-x')]}{\int_{-L}^L dx |g(x)|^2}. \end{aligned} \quad (3.16)$$

We observe that the above expression for α is the Rayleigh-Ritz coefficient for the sinc-kernel and the highest value of α is given by $(2B\lambda_0)$ with λ_0 being the highest eigenvalue of the following eigen-equation:

$$\lambda \phi(x) = \int_{-L}^L dx' \text{sinc}[2B(x - x')] \phi(x'). \quad (3.17)$$

In general the prolate basis functions are numbered in decreasing order of the magnitude of the corresponding eigenvalues. The set of the highest N eigenfunctions may also be treated as a best basis for given values of L and B in the energy concentration sense. In their early work Slepian and co-workers realized that the eigenfunctions of the sinc-kernel are the solutions of the angular part of the prolate spheroidal differential equation:

$$(L^2 - x^2) \frac{d^2\phi}{dx^2} - 2x \frac{d\phi}{dx} + (\chi - \frac{c^2 x^2}{L^2}) = 0, \quad (3.18)$$

for discrete positive values of the function $\chi(c)$. The parameter $c = 2\pi LB$ is now referred to as the Shannon number and is related to the space-bandwidth product. Most of the literature on Slepian functions studies their properties based on the solution of the differential equation (3.18) and its asymptotic solutions depending on the value of c . We will take a different approach based on the sampling theorem. The discussion based on the solution of the differential equation is somewhat *ad hoc* and does not have a simple connection to the ideas such as the space-bandwidth product that are inherently related to the sampling theorem.

We note that the eigenvalue problem in Eq. (3.17) is a homogeneous Fredholm integral equation of the second kind. The kernel of the equation is Hermitian symmetric and square integrable. Further the kernel is positive definite:

$$\begin{aligned} & \int_{-L}^L \int_{-L}^L dx dx' \text{sinc}[2B(x - x')] g(x) g^*(x') \\ &= \frac{1}{2B} \int_{-B}^B df_x |G(f_x)|^2 \\ &\geq 0, \end{aligned} \quad (3.19)$$

for an arbitrary square-integrable function $g(x)$. The equality above holds when $g(x)$ is identically equal to zero and hence the eigenvalues of the sinc-kernel are positive. We will first show that the eigenfunctions of the sinc-kernel satisfy the sampling theorem and are hence bandlimited. We have already note that the sinc-kernel itself is bandlimited and hence has a sampling expansion given by:

$$\text{sinc}[2B(x - x')] = \sum_{m=-\infty}^{\infty} \text{sinc}(2Bx - m) \text{sinc}(2Bx' - m). \quad (3.20)$$

Using this sampling expansion in the Eq. (3.17) gives:

$$\begin{aligned} \lambda \phi(x) &= \int_{-L}^L dx' \sum_{m=-\infty}^{\infty} \text{sinc}(2Bx - m) \text{sinc}(2Bx' - m) \phi(x') \\ &= \lambda \sum_{m=-\infty}^{\infty} \phi\left(\frac{m}{2B}\right) \text{sinc}(2Bx - m). \end{aligned} \quad (3.21)$$

We now write the eigenvalue equation (3.17) as:

$$\begin{aligned} \lambda \phi\left(\frac{m}{2B}\right) &= \int_{-L}^L dx' \text{sinc}(2Bx' - m) \phi(x') \\ &= \int_{-L}^L dx' \text{sinc}(2Bx' - m) \sum_{n=-\infty}^{\infty} \phi\left(\frac{n}{2B}\right) \text{sinc}(2Bx' - n) \\ &= \sum_{n=-\infty}^{\infty} A_{mn}^{(0)} \phi\left(\frac{n}{2B}\right). \end{aligned} \quad (3.22)$$

Here we have defined the matrix $A^{(0)}$ by the matrix elements

$$A_{mn}^{(0)} = \int_{-L}^L dx' \text{sinc}(2Bx' - m) \text{sinc}(2Bx' - n). \quad (3.23)$$

We observe that the continuous eigenvalue problem for the sinc-kernel is thus equivalent to a discrete eigenvalue problem for the matrix $A^{(0)}$. The continuous and discrete problems share the same eigenvalues. Further, the eigenvectors of the matrix $A^{(0)}$ are same as the Nyquist samples of the continuous prolate spheroidal functions. The continuous functions can thus be obtained by sinc-interpolation of the discrete eigenvectors.

3.6.1 Properties of matrix $A^{(0)}$

For brevity we will denote the discrete eigenvectors of the matrix $A^{(0)}$ as

$$u_n = [\dots \phi_n(\frac{m}{2B}) \dots]^T,$$

with “T” denoting the transpose of the row vector. The matrix $A^{(0)}$ is real symmetric so that its eigenvalues and eigenvectors are real. If we normalize the continuous functions $\phi_n(x)$ over $x : (-\infty, \infty)$, it follows that

$$\int_{-\infty}^{\infty} dx \phi_n^2(x) = 1 = \frac{1}{2B} \sum_{m=-\infty}^{\infty} \phi_n^2(\frac{m}{2B}). \quad (3.24)$$

The second equality follows from the fact that $\phi_n(x)$ has a sampling expansion as per Eq. (3.21) and further using the orthogonality of the sinc functions as in Eq. (3.7). The matrix $A^{(0)}$ is centro-symmetric with respect to the element $A_{00}^{(0)}$. It is known that the eigenvectors of such matrices have definite parity - they are either even or odd. The continuous eigenfunctions obtained by sinc-interpolation of the discrete eigenvectors thus also have a definite parity. The matrix $A^{(0)}$ being symmetric can be factored as

$$A^{(0)} = U A_d^{(0)} U^T. \quad (3.25)$$

Here $A_d^{(0)}$ is a diagonal matrix with eigenvalues λ_n along diagonal and the matrix U has the eigenvectors u_n as its columns. Further the eigenvectors being orthogonal have the property that

$$U^T U = 2B \hat{\mathbf{1}} = U U^T. \quad (3.26)$$

These identities may be written explicitly to obtain the following relations: Orthogonality

$$\sum_{m=-\infty}^{\infty} \phi_n(\frac{m}{2B}) \phi_l(\frac{m}{2B}) = 2B \delta_{nl}. \quad (3.27)$$

Completeness

$$\sum_{n=0}^{\infty} \phi_n(\frac{m}{2B}) \phi_n(\frac{k}{2B}) = 2B \delta_{mk}. \quad (3.28)$$

The structure of matrix $A^{(0)}$ is quite interesting. Since the matrix elements are defined as definite integrals over product of shifted sinc-functions, only approximately $(2B)(2L)$ matrix elements along the diagonal of the matrix centered on the matrix element $A_{00}^{(0)}$ are significant. This explains the well-known property of the sinc-kernel that only about $4BL$ highest eigenvalues for the problem are significant. This has interesting implications for signal representation using prolate functions. In Fig.s 3.2 and 3.3 we show the first few prolate functions and their corresponding eigenvalues respectively, computed using the sampling theorem based approach. A 101×101 approximation of the matrix $A^{(0)}$ centered on the element $A_{00}^{(0)}$ is used for this illustration and the matrix elements are computed using standard numerical integration methods as per the definition in Eq. (3.23). The discrete eigenvectors thus obtained are then sinc-interpolated to obtain the continuous eigenfunctions. In general we

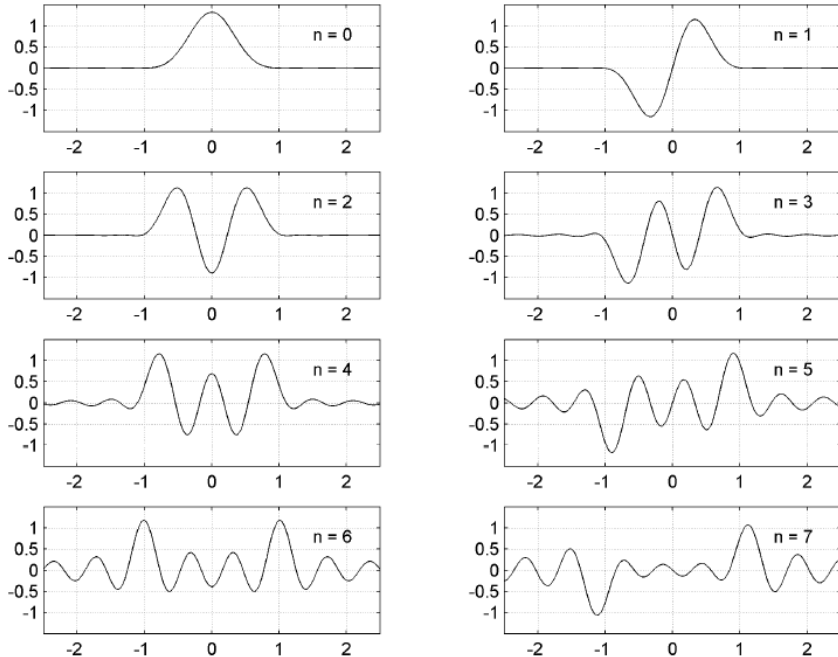


Figure 3.2: First 8 prolate basis functions computed using sampling theorem based approach for $L = 1, B = 5/\pi$

observe that the $n - th$ prolate function has n zero crossings in the interval $x : (-L, L)$. This appears counter-intuitive for functions of order $n > 4BL$ where the number of zero crossings go beyond the space-bandwidth product although the corresponding prolate function is still bandlimited over the infinite interval. Such functions with larger number of zero crossings in a finite interval compared to the space-bandwidth product are referred to as “super-oscillatory” in nature. We further note that as the index n goes above $4BL$, most of the energy in corresponding prolate functions is concentrated beyond the interval $x : (-L, L)$.

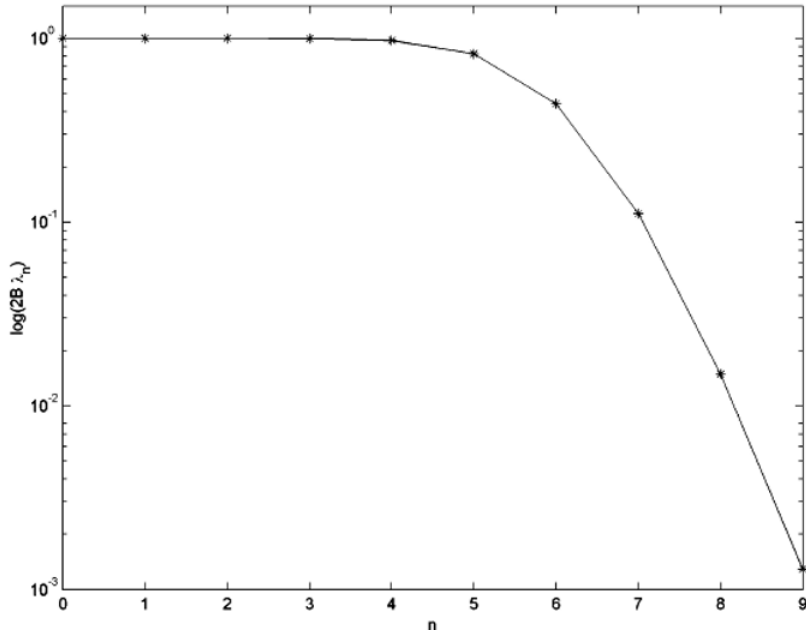


Figure 3.3: First 10 eigenvalues of sinc-kernel computed using sampling theorem based approach for $L = 1, B = 5/\pi$ shown on a log scale.

We will state some of the interesting properties of the prolate functions which can be easily derived from the discrete orthogonality and completeness relations in Eq.s (3.27) and (3.28).

1. **Dual orthogonality** The prolate functions form an orthogonal set over $(-\infty, \infty)$ as well as over the domain $x : (-L, L)$

used for their definition.

$$\int_{-\infty}^{\infty} dx \phi_n(x) \phi_m(x) = \delta_{m,n}, \quad (3.29)$$

$$\int_{-L}^L dx \phi_n(x) \phi_m(x) = (2B\lambda_n) \delta_{m,n}. \quad (3.30)$$

The first of the identity is easy to prove if one uses sampling expansions for both $\phi_n(x)$ and $\phi_m(x)$ followed by the property as per Eq. (3.27). The second orthogonality identity over finite interval can be proved as follows:

$$\begin{aligned} & \int_{-L}^L dx \phi_n(x) \phi_m(x) \\ &= \sum_{k=-\infty}^{\infty} \phi_n\left(\frac{k}{2B}\right) \int_{-L}^L dx \operatorname{sinc}(2Bx - k) \phi_m(x) \\ &= \lambda_m \sum_{k=-\infty}^{\infty} \phi_n\left(\frac{k}{2B}\right) \phi_m\left(\frac{k}{2B}\right) \\ &= 2B\lambda_m \delta_{m,n}. \end{aligned} \quad (3.31)$$

2. **Completeness** The prolate spheroidal functions an orthogonal basis over $(-\infty, \infty)$ for functions bandlimited to $f_x : (-B, B)$ and a complete orthogonal basis for square-integrable functions in $x : (-L, L)$. The completeness properties are not proved here and we refer interested readers to [Khare and George, J. Phys. A: Math. & General 36, 10011 (2003)].

We will use the orthogonality and completeness properties when considering problems such as bandlimited extrapolation. In general, throughout the discussion in this book we will have various occasions to refer to prolate functions when discussing information transmitting capabilities of imaging systems. We remark that the sampling theorem based approach to prolate functions applies equally well to eigenvalue problems associated with bandlimited kernels in general and several interesting mathematical relations similar to the ones for prolate spheroids above can be proved for the general case.

3.7 Extrapolation of bandlimited functions

The dual orthogonality and completeness properties of the prolate spheroidal functions can be utilized for extrapolation of bandlimited functions that are known over a truncated region. Suppose a function $g(x)$ bandlimited to the frequency band $f_x : (-B, B)$ is known over a finite range $x : (-L, L)$ then one may expand it using the prolate spheroidal function set as:

$$g(x) = \sum_n a_n \phi_n(x), \quad (3.32)$$

where the coefficients a_n may be determined using the orthogonality of prolate functions over the region $x : (-L, L)$:

$$a_n = \frac{1}{2B\lambda_n} \int_{-L}^L dx g(x) \phi_n(x). \quad (3.33)$$

Further one may in principle extend the function beyond the range $x : (-L, L)$ by using the same coefficients a_n . The possibility of determining the function beyond the range $x : (-L, L)$ is however practically governed by the accuracy of our knowledge of $g(x)$ over the finite range. If for example, the values of $g(x)$ are determined by some experimental measurement, they will contain some noise which translates to noise on the coefficients a_n . In Eq. (3.33) above, the evaluation of the coefficient a_n involves division by the corresponding eigenvalue λ_n . As we have already seen above, the eigenvalues are typically very small when the index $n >> 4BL$ and the corresponding prolate functions have most of their energy concentrated beyond the range $x : (-L, L)$. So although such higher order prolate functions are capable of recreating the signal beyond the finite range where the function $g(x)$ is known, their inclusion in the series representation involves division of corresponding coefficients a_n by small numbers. Since the coefficients a_n are noisy, such division by small numbers can amplify the noise making the series representation meaningless. One simple way to avoid the amplification of noise is to truncate the series representation to finite number of terms which then amounts effectively to extrapolation over a limited range beyond $(-L, L)$. The extrapolation problem is highly

sensitive to the SNR in the measurement of $g(x)$. Numerical super-resolution imaging techniques usually can be formulated in terms of the extrapolation using the Slepian functions.

We conclude this discussion by noting that the sampling by means of the sinc-series or the Slepian function basis are equivalent to each other. The origins of the important developments in allied areas such as wavelets can be traced to the material covered in this chapter.

References and suggested reading

1. C. E. Shannon, “Mathematical theory of communication”, Bell Syst. Tech. J., vol. 27, pp. 379 (1948).
2. J. R. Higgins *Sampling theory in Fourier and signal analysis*, Oxford Science Publications (1996).
3. D. Slepian, H. O. Pollak, “Prolate spheroidal wavefunctions, Fourier analysis and uncertainty -I”, Bell System Technical Journal vol. 40, pp. 43-64 (1961).
4. H. J. Landau and H. O. Pollak, “Prolate Spheroidal Wave Functions, Fourier Analysis and Uncertainty - II”, Bell System Technical Journal 40, pp. 65-84 (1961).
5. H. J. Landau and H. O. Pollak, “Prolate Spheroidal Wave Functions, Fourier Analysis and Uncertainty – III: The Dimension of the Space of Essentially Time- and Band-Limited Signals”, Bell System Technical Journal 41, pp. 1295-1336 (1962).
6. D. Slepian, “Prolate Spheroidal Wave Functions, Fourier Analysis and Uncertainty - IV: Extensions to Many Dimensions; Generalized Prolate Spheroidal Functions”, Bell System Technical Journal 43, pp. 3009-3057 (1964).
7. Abdul Jerri, “The Shannon sampling theorem - Its various extensions and applications: a tutorial review”, Proceedings of the IEEE, vol. 65, pp. 1565 (1977).
8. M. Unser, “Sampling- 50 years after Shannon”, Proceedings of the IEEE vol. 88, pp. 569 (2000).

9. S. Mallat, *A Wavelet Tour of Signal Processing*, Academic Press USA (2008).
10. A. Kohlenberg “Exact interpolation of band-limited functions”, J. Appl. Phys. 24, 1432-1436 (1953).
11. R. G. Vaughan, N. L. Scott, D. R. White, “Theory of band-pass sampling”, IEEE Trans. Signal Processing 39, 1973-1989 (1991).
12. K. Khare and N. George, “Direct sampling and demodulation of carrier-frequency signals”, Optics Communications 211, 85-94 (2002).
13. K. Khare and N. George, “Sampling theory approach to prolate spheroidal wavefunctions”, J. Phys. A: Math. & Gen. vol. 36, pp. 10011 (2003).

4. Operational introduction to Fast Fourier Transform

4.1 Definition

Fourier transforms will be encountered time and again in this book and it is important for students and practitioners to have a basic operational understanding of numerical routines or functions readily available for implementing Fourier transform on discretely sampled signals and images. This chapter does not by any means discuss the details of the discrete Fourier transform and fast Fourier transform algorithms for which excellent literature is already available. The aim here is to provide sufficient information so that when using standard computational tools or libraries for FFT operation, a user may be able to make sense of the results. A few important aspects regarding the usage of 2D Fourier transform functions for simulating optical imaging systems are also pointed out along the way.

With an introduction to the sampling ideas as discussed in Chapter 3, we may now represent a signal over length $2L$ and an effective bandwidth $2B$ by means of samples $g(0/2B)$, $g(1/2B)$, ..., $g((N - 1)/(2B))$ with $N \approx 4BL$. The discrete Fourier transform (DFT) of the signal is typically defined as:

$$G\left(\frac{m}{2L}\right) = \sum_{n=0}^{N-1} g\left(\frac{n}{2B}\right) \exp(-i2\pi mn/N). \quad (4.1)$$

The corresponding inverse discrete Fourier transform may be de-

fined as:

$$g\left(\frac{n}{2B}\right) = \frac{1}{N} \sum_{m=0}^{N-1} G\left(\frac{m}{2L}\right) \exp(i2\pi mn/N). \quad (4.2)$$

We notice that the discrete Fourier transform operations above are approximations to the continuous integral version of the Fourier transform when the signal is defined only over $x : (-L, L)$ by means of a discrete set of samples. The space domain samples have a periodicity of $1/(2B)$ while the frequency domain periodicity is given by $1/(2L)$. The factors $(2B)$ and $(2L)$ are usually omitted from most standard definitions but we will retain them here explicitly. We observe that the forward and the inverse DFTs are linear transformations which may be written in a matrix form. For example, using the notation

$$\omega = \exp(i2\pi/N), \quad (4.3)$$

for N -th root of 1, the forward transformation may be written as:

$$\mathbf{G} = \mathbf{F}\mathbf{g}, \quad (4.4)$$

or

$$\begin{pmatrix} G\left(\frac{0}{2L}\right) \\ G\left(\frac{1}{2L}\right) \\ \vdots \\ G\left(\frac{N-1}{2L}\right) \end{pmatrix} = \begin{pmatrix} 1 & 1 & \dots & 1 \\ 1 & \omega^{-1} & \dots & \omega^{N-1} \\ \vdots & \vdots & \ddots & \vdots \\ 1 & \omega^{-(N-1)} & \dots & \omega^{-(N-1)^2} \end{pmatrix} \begin{pmatrix} g\left(\frac{0}{2B}\right) \\ g\left(\frac{1}{2B}\right) \\ \vdots \\ g\left(\frac{N-1}{2B}\right) \end{pmatrix} \quad (4.5)$$

We note that ω satisfies the relation:

$$\omega^{(N-m)} = \omega^{-m}. \quad (4.6)$$

As a result the frequencies $0/(2L), 1/(2L), \dots, (N-1)/(2L)$ which form the argument of the discrete Fourier transform G may be re-ordered as positive and negative frequencies. The typical convention used to define positive and negative frequencies is as follows:

1. **Even N case:** $\nu = 0/(2L)$ is the zero frequency or dc term, $\nu = 1/(2L)$ to $\nu = (N/2)/(2L)$ are treated as positive frequencies, and $\nu = (N/2 + 1)/(2L)$ to $\nu = (N - 1)/(2L)$ are treated as negative frequencies.
2. **Odd N case:** $\nu = 0/(2L)$ is the zero frequency or dc term, $\nu = 1/(2L)$ to $\nu = ((N + 1)/2)/(2L)$ are treated as positive frequencies, and $\nu = ((N + 3)/2)/(2L)$ to $\nu = (N - 1)/(2L)$ are treated as negative frequencies.

In defining the negative frequencies, the term $G((N - 1)/(2L))$ is considered equivalent to having frequency component $\nu = -1/(2L)$ and so on as per the property of ω in Eq. (4.6).

4.2 Usage of 2D Fast Fourier Transform for problems in Optics

Without consideration of any properties of the transformation matrix \mathbf{F} , we observe that computing the discrete Fourier transformation would require N^2 multiplication operations. A great advance was made by Cooley and Tukey in 1965 when they published an algorithm that utilized the symmetry properties of the \mathbf{F} matrix and reduced the number of multiplication operations to the order of $N \log N$. The corresponding algorithm for computing the DFT is known as the Fast Fourier Transform (FFT). The idea behind FFT algorithm can be traced back in history to a publication by Gauss, but the significance of this received attention after the Cooley and Tukey work. FFT has now become a benchmark against which other algorithms are often compared in the context of their computational complexity. We will not provide detailed discussion behind the FFT theory but only introduce the readers to operational aspects of using FFT algorithms that are now available in widely used computational tools such as MATLAB, SciLab, NumPy, etc.

As we shall see in later chapters of this book, Fourier transforms occur naturally in study of propagation of light waves, optical information processing methods etc. Digital processing methods used in modeling, analysis and synthesis of optical and other imaging

systems therefore extensively use the FFT algorithm. In these applications it is important to understand the meaning of results that any standard 2-dimensional FFT tool provides and the correct usage of functions such that the results make sense from Physics point of view.

We will provide an illustration of computation of the 2D Fourier transform of the 2D rect function. A rect function of size equal to 11 pixels is defined on a 2D grid of size 255×255 as shown in Fig. 4.1(a).

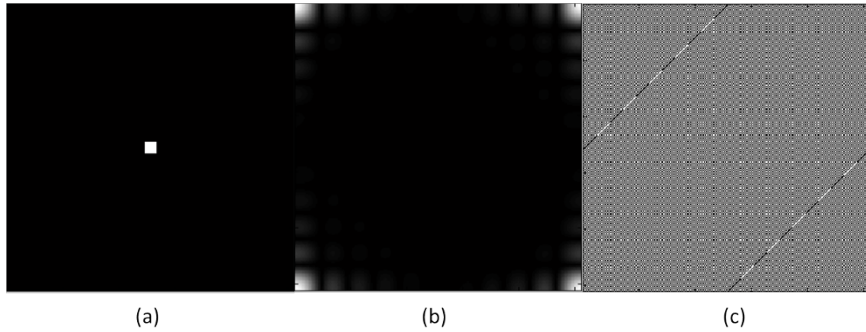


Figure 4.1: Result of applying the function `fft2(...)` on (a) 2D rect-function object, (b) Amplitude and (c) Phase of Fourier transform. The dark and bright pixels in the phase function correspond to phase values of 0 and π respectively.

The amplitude and phase of the images obtained by simple application of the function `fft2` from standard computational tools above is shown in Fig. 4.1 (b) and (c) respectively. The result does not look like the expected 2D sinc-function. We note that the central lobe of the sinc-function is now distributed near the corners of the resultant image. The reason for this is that the standard FFT tools have the zero-frequency component at the beginning of the resultant vector and not at its center. A common remedy for this is to use the `fftshift` function on the result which brings the zero frequency back to the center of the image. Applying the sequence `fftshift(fft2(...))` on the rect-function gives the amplitude and phase as shown in Fig. 4.2 (a) and (b) respectively. The amplitude part here looks sensible but the phase is still not what one would expect for a sinc-function. This

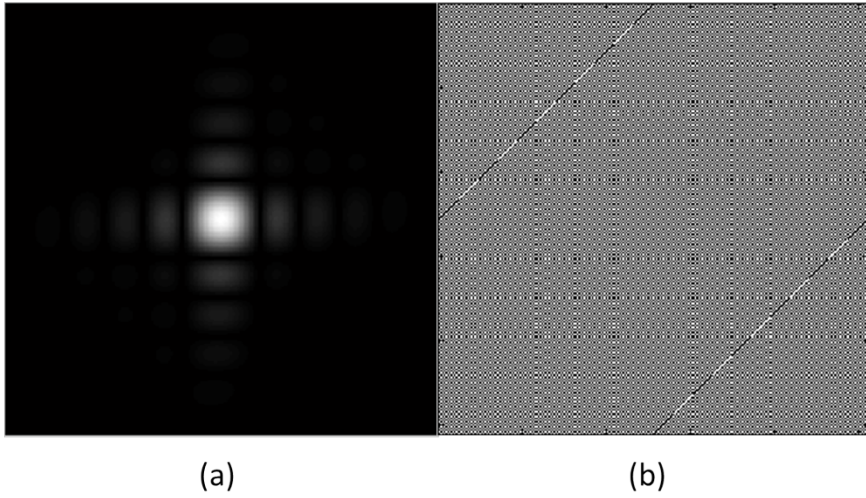


Figure 4.2: Result of applying the sequence `fftshift(fft2(...))` on 2D rect-function object, (a) Amplitude and (b) Phase of Fourier transform. The dark and bright pixels in the phase function correspond to phase values of 0 and π respectively.

unexpected result may be understood as follows. When calculating the Fourier transform as:

$$\int_{-\infty}^{\infty} \int_{-\infty}^{\infty} dx dy \text{rect}\left(\frac{x}{a}, \frac{y}{a}\right) \exp[-i2\pi(f_x x + f_y y)], \quad (4.7)$$

the correct phase value applied to the center of the rect-function corresponds to zero (since $x = 0, y = 0$). However according to the standard FFT convention this phase multiplier is applied at the corner of the image. The initial image to be Fourier transformed must therefore be modified appropriately using the standard `ifftshift` function that takes the center of the image to the corners by swapping the quadrants. The appropriate sequence for 2D FFT in most programming platforms for the result to be meaningful from Physical standpoint (e.g. in describing phenomena like diffraction) is thus given by: `fftshift(fft2(ifftshift(...)))`. The amplitude and phase of the 2D FFT of the rect-function computed with this sequence is shown in Fig. 4.3 (a), (b) respectively. Both the amplitude and phase are now what one desires as per conventions in Optics. We mention that

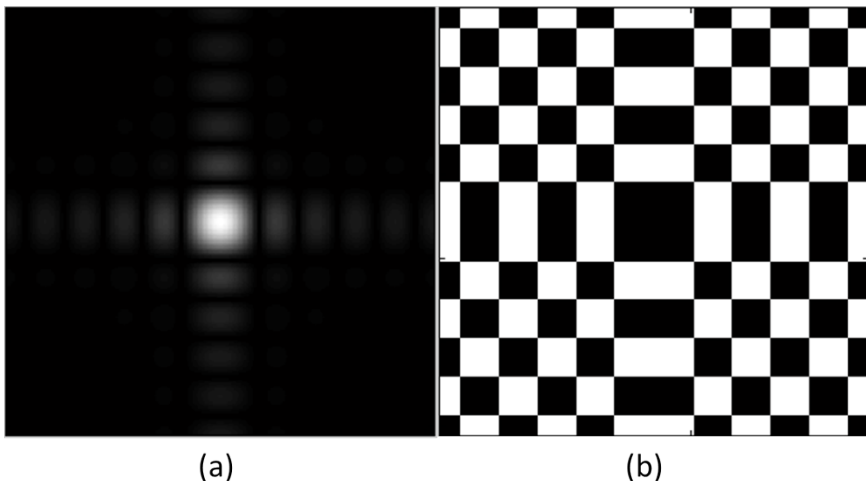


Figure 4.3: Result of applying the sequence `fftshift(fft2(ifftshift(...)))` on 2D rect-function object, (a) Amplitude and (b) Phase of Fourier transform. The dark and bright pixels in the phase function correspond to phase values of 0 and π respectively.

the appropriate usage of functions for the inverse FFT operation is similarly: `fftshift(ifft2(ifftshift(...)))`. The functions `fftshift` and `ifftshift` are typically identical for even dimensional vectors but differ by one pixel shift for odd dimensional vectors. The two sequences for forward and inverse FFT as described above may be used irrespective of whether the dimensions of vectors involved are even or odd to yield the correct phase behaviour as per standard conventions in Optics.

We have provided an operational introduction to FFT routines in computational tools commonly used by researchers. The subtle points regarding the usage of `fftshift` and `ifftshift` functions along with the `fft` routines are illustrated here with examples. These topics have been discussed here since they appear to be common sources of errors when beginning researchers or students start working with FFT based simulations related to Optical imaging and diffraction phenomena.

References and suggested reading

1. J. W. Cooley and J. W. Tukey, “An algorithm for the machine calculation of complex Fourier series”, *Math. Comput.* vol. 19, pp. 297 (1965).
2. M. T. Heideman, D. H. Johnson, C. S. Burrus, “Gauss and the history of the Fast Fourier transform”, *IEEE ASSP Magazine*, vol. 1 (4), pp. 14 (1984).
3. B. G. Osgood, *The Fourier transform and its applications*, Stanford Engineering Everywhere online material. (see.stanford.edu).
4. R. Bracewell, *The Fourier transform and its applications*, 2nd Ed., McGraw Hill (1986).

5. Linear systems formalism and introduction to inverse problems in imaging

With the Fourier transform theory, ideas such as the delta-function (and other generalized functions) and the sampling theorem at our hand we are now in a position to develop the linear systems formalism that will be found useful when studying topics such as diffraction phenomena, imaging systems, optical information processing, to name a few. A schematic diagram of a linear system is shown in Fig. 5.1. Several topics of interest to this book can be cast in terms

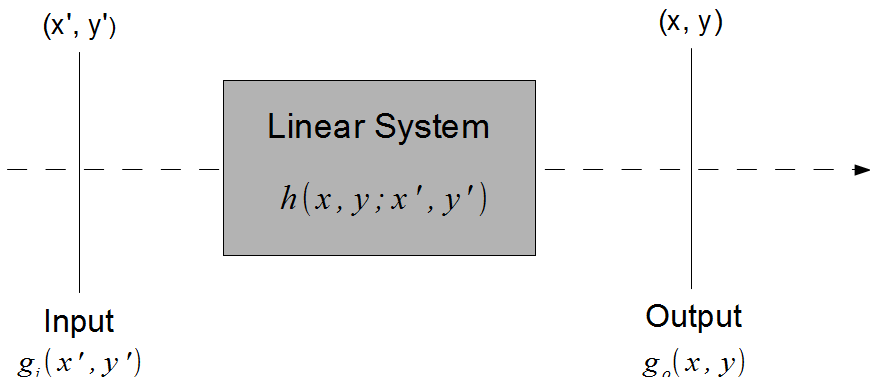


Figure 5.1: Linear system model.

of this picture. We have an input signal $g_i(x', y')$ that can represent complex amplitude or intensity of some wavefield (mostly light waves for topics in this book). This input is acted on by some sys-

tem to give an output $g_o(x, y)$ in another plane. For now we will simply suppose the input and output to be complex valued functions in general without assigning them any physical meaning. The physical meaning will be clear as we study diffraction, imaging, and other related topics. The meaning of linearity here is that if we have two inputs g_{1i} and g_{2i} resulting in individual outputs g_{1o} and g_{2o} respectively, then any linear combination $(\alpha g_{1i} + \beta g_{2i})$ when provided at the input end of the system gives an output: $(\alpha g_{1o} + \beta g_{2o})$. Later in this book we will associate the input and output functions with the light wavefield at the input and output of a system. The Maxwell equations which help describe the propagation of light waves (electromagnetic waves) are linear in nature and the importance of linear system model in imaging applications is therefore not very surprising. The linearity property suggests that instead of working with an arbitrary input function, we may want to work with some elementary set of functions that forms a suitable basis for representing the input signal. Analysis of the system then reduces to studying the response of the system to the basis functions.

An interesting basis set is the set of spikes or delta functions located at each point of the input plane. We can for example represent the input as a sum of delta functions:

$$g_i(x', y') = \int \int du dv g_i(u, v) \delta(x' - u, y' - v). \quad (5.1)$$

In order to find the output of the system $g_o(x, y)$ all we need to do now is to find the response of the system to a delta spike located at each point (u, v) , weight the response by the value of the input $g_i(u, v)$, and then integrate over the (u, v) plane. We will denote the response of the system to the delta spike by $h(x, y; x', y')$. In other words if the input to the system is a delta spike at (x', y') , the response of the system will be given by the function h in the (x, y) plane. Suppose we have a microscope looking at a “point” source, you probably know that the output is some blur (e.g. Airy rings) which in this case is the function h . If we think of the object to be imaged as a collection of point sources, then the resultant image will be a sum of blur functions corresponding to the pair of points (x', y') and (x, y) in the object and image planes respectively. We will call $h(x, y; x', y')$ the impulse response of the system. The output of the

system can therefore be represented in terms of the input as:

$$g_o(x, y) = \int \int du dv g_i(u, v) h(x, y; u, v). \quad (5.2)$$

The idea of impulse response is common in many branches of engineering and sciences and an alternate name for this concept in the Physics literature is the Green's function.

5.1 Space-invariant impulse response

The idea of impulse response is particularly useful when the system has an additional property of space-invariance. A system is space-invariant if the functional form of the impulse response does not depend on where the delta-function is located in the input plane. The result of shifting the delta impulse in the input plane is simply to translate the response function in the output plane - it will not change its form or shape. If the system is space invariant, we can represent the impulse response as:

$$h(x, y; x', y') = h(x - x', y - y'). \quad (5.3)$$

Suppose that a point source of unit strength located at $(x', y') = (0, 0)$ produces an output $h(x, y)$. Space-invariance implies that shifting the input point source to $(x', y') = (a, b)$ will produce an output $h(x - a, y - b)$. For most common optical imaging systems this space-invariance model is a good approximation - the model is however not exact. For a typical imaging system the space-invariance holds near the optical axis. One may observe distortions in the form of h for point far-off from optical axis. For all practical purposes we will assume that the space-invariance approximation is valid as this will allow us to use the Fourier transform theory - particularly the convolution property - and develop a formalism for understanding and analyzing imaging phenomena. With the space-invariance property the input-output relation for linear systems is a convolution relation:

$$g_o(x, y) = \int \int dx' dy' g_i(x', y') h(x - x', y - y'). \quad (5.4)$$

An equivalent relation in Fourier space may be written using the convolution property of the Fourier transforms:

$$G_o(f_x, f_y) = H(f_x, f_y) G_i(f_x, f_y). \quad (5.5)$$

Here G_o , H and G_i denote the 2D The Fourier transforms of the output g_o , the impulse response h and the input g_i respectively. $H(f_x, f_y)$ describes the effect of the system on the input in the spatial frequency space and is commonly referred to as the transfer function of the system. The relation above is very important and central to the study of diffraction and imaging phenomena in general. Note that the multiplication in frequency space is much easier for conceptual understanding than convolution when designing new systems. The transfer function gives the individual spatial frequencies a weight which has in general both an amplitude and a phase. What are the elementary basis functions in this picture ? They are simply the Fourier transforms of the shifted delta function basis - or complex exponentials $\exp[i2\pi(f_x x + f_y y)]$. We can think of the operation of the imaging system as follows - decompose the input and output in terms of the complex exponentials and relate the individual spatial frequency components of the input and output by the numerical value of the transfer function. The final output g_o in (x, y) domain may then be calculated by inverse Fourier transforming the resultant product. When space-invariance approximation cannot be made over the entire field of view, the image may be divided into small patches such that the space-invariance approximately holds over an image patch.

5.2 Ill-posedness of inverse problems

In the previous section we described the commonly used linear systems model that is commonly used in relation to imaging phenomena. With the computational methods forming an integral part of the imaging system, it is very important to discuss some fundamental issues that arise when solving the inverse problem of obtaining the input function g_i using full or partial measurement of the output g_o . We first observe that g_o is typically measured using some detector. If we associate with g_o the output wavefield, then any optical

detector will typically detect the light intensity that is proportional to $|g_o|^2$. For simplicity and for the purpose of discussion here we may assume that g_o is measurable in the laboratory, e.g. by means of an interferometric arrangement. It is important to note that the measurement process is inherently statistical in nature and what is usually available to us is the output function including noise $n(x, y)$ which in its simplest form may be assumed to be additive.

$$\tilde{g}_o(x, y) = \int \int dx' dy' g_i(x', y') h(x - x', y - y') + n(x, y). \quad (5.6)$$

The noise arises out of a combination of statistical nature of detection process as well as due to the fundamental statistical fluctuations associated with light waves themselves. The noise $n(x, y)$ is never ideally zero in any practical system. Let us further consider the nominal form of impulse response $h(x, y)$ associated with a delta-function input. The transfer function $H(f_x, f_y)$ for any practical system extends over a finite range of spatial frequencies and the impulse response function $h(x, y)$ has a spread which is inversely related to the spread of the transfer function in spatial-frequency space. The forward operation of going from object to image space is thus typically a blurring operation.

We observe an important property of the inverse problem of obtaining $g_i(x, y)$ based on the measurement $\tilde{g}_o(x, y)$. Consider a solution $g_i(x, y)$ that would ideally produce $g_o(x, y)$ at the output of the system. Interestingly, any other solution of the form $[g_i(x, y) + A \cos(\omega_x x + \omega_y y)]$ for sufficiently large values of ω_x and ω_y produces an output very close to $g_o(x, y)$ since the highly oscillating additive term averages out to zero as a result of the blurring nature of $h(x, y)$. It is not easy to distinguish between such widely differing solutions since they produce almost the same output within noise limits at the output end. This possibility that widely differing input functions may produce practically indistinguishable outputs as measured in a laboratory setting is commonly referred to as the ill-posedness. The ill-posedness as a general property of practical inverse problems was first discussed formally by Hadamard in 1920's. Careful formulation of the inverse problem is required in order to handle the difficulties due to ill-posedness, so that a meaningful solution to the problem at hand may be obtained for any practical computational imaging sys-

tem. We will illustrate some of the important methods in this regard in the following sections.

5.3 Inverse filter

A simplistic solution to the problem of obtaining the input $g_i(x, y)$ from a measured output \tilde{g}_o is the inverse filter solution. This method is included here as it clearly illustrates the difficulties due to ill-posedness as discussed in the previous section. Disregarding the noise in the output and using Eq. (5.5), one may nominally write the inverse solution as:

$$g_i(x, y) = \mathcal{F}^{-1} \left[\frac{G_o(f_x, f_y)}{H(f_x, f_y)} \right]. \quad (5.7)$$

The function $1/H(f_x, f_y)$ is referred to here as the inverse filter. Unfortunately we do not have access to $G_o(f_x, f_y)$ but only its noisy version $\tilde{G}_o(f_x, f_y) = \mathcal{F}[\tilde{g}_o(x, y)]$. The solution $\tilde{g}_i(x, y)$ estimated using the noisy output may be written as:

$$\tilde{g}_i(x, y) = \mathcal{F}^{-1} \left[\frac{\tilde{G}_o(f_x, f_y)}{H(f_x, f_y)} \right]. \quad (5.8)$$

In numerical computation one may replace any zero value in H with a small constant to avoid dividing by zero. The illustration in Fig. 5.2 shows the effect of a 20×20 pixel square averaging filter (with 1% additive noise) on a picture followed by an attempt at image recovery using the simple inverse filter. The filter $h(x, y)$ and the absolute value of the corresponding transfer function $H(f_x, f_y)$ are shown in Fig. 5.3. The The recovery in Fig. 5.2 (c) appears completely meaningless. The reason for this is that we have simply divided the Fourier transform of the blurred image (b) by the Fourier transform $H(f_x, f_y)$. The function $H(f_x, f_y)$ has zeros (or very small values) over finite regions or isolated lines/points as seen in Fig. 5.3 and dividing by these small values greatly enhances the corresponding frequency components. In particular in presence of noise some of these components may produce completely undesirable large oscillations in the recovery as seen in Fig. 5.2 (c). It

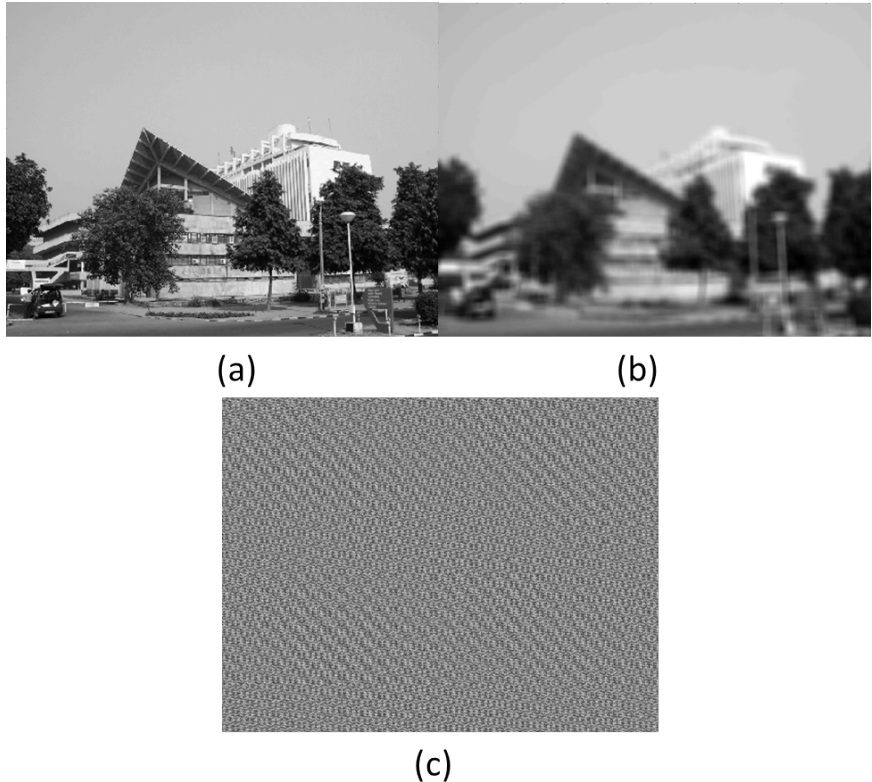


Figure 5.2: Illustration of simple inverse filter: (a) Original image, (b) Image blurred by 20×20 pixel square averaging filter with addition of uniform random noise, (c) Recovery using simple inverse filter.

is important to note that if the averaging filter $h(x, y)$ is applied to this recovery, it produces a result that is almost same as the blurred picture in Fig. 5.2(b). So it is a solution that is consistent with the blurred image data but from a practical standpoint this recovery is not useful at all. This illustration shows the difficulties due to the ill-posedness of the inverse problem. The simplistic solution such as inverse filter is therefore not suitable. A solution must therefore be constructed that gives a visually meaningful result and is reasonably consistent with the blurred image data. We observe that even for a simple looking problem a more involved treatment of the inverse

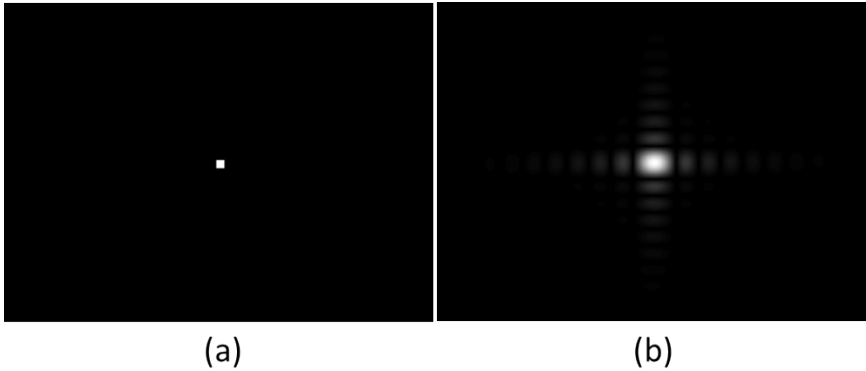


Figure 5.3: (a) 20×20 pixel averaging filter $h(x, y)$ used in illustration in Fig. 5.2 and (b) the absolute value of the corresponding transfer function $H(f_x, f_y)$.

problem is required in order to obtain a useful image recovery.

5.4 Wiener filter

The idea of using the statistical properties of noise to design an appropriate filter for inverse recovery was first proposed by Norbert Wiener. We will assume that a filter $w(x, y)$ is such that when applied to the output $\tilde{g}_o(x, y)$ an estimate of the solution $\tilde{g}_i(x, y)$ given by

$$\tilde{g}_i(x, y) = \int \int dx' dy' \tilde{g}_o(x', y') w(x - x', y - y') \quad (5.9)$$

is obtained that is consistent with the noisy data. Further the solution is such that the expected least square error

$$\epsilon = < \|g_i(x, y) - \tilde{g}_i(x, y)\|^2 > \quad (5.10)$$

is minimized. The notation $\| \dots \|$ here denotes the standard L2 norm and the brackets $< \dots >$ denote the ensemble average. In order to derive the filter we will express the error ϵ in Fourier transform

domain by making use of the Parseval theorem (see Eq. (2.75)).

$$\begin{aligned}\epsilon &= \langle |G_i(f_x, f_y) - \hat{G}_i(f_x, f_y)|^2 \rangle \\ &= \langle |G_i(f_x, f_y) - W(f_x, f_y)[G_i(f_x, f_y)H + N(f_x, f_y)]|^2 \rangle \\ &= \langle |(1 - W H)G_i - W N|^2 \rangle.\end{aligned}\quad (5.11)$$

Here $W(f_x, f_y)$ and $N(f_x, f_y)$ denote the Fourier transforms of the filter $w(x, y)$ and the noise $n(x, y)$ respectively. We will expand the terms in the above expression and equate the cross terms containing

$$\langle G_i(f_x, f_y)N^*(f_x, f_y) \rangle \text{ or its complex conjugate}$$

to zero. This is justified since the noise is not expected to be correlated with the input object function $g_i(x, y)$ that we want to recover. Further we will denote the power spectrum associated with the object and noise as: $S_{obj}(f_x, f_y) = \langle |G_i(f_x, f_y)|^2 \rangle$ and $S_{noise}(f_x, f_y) = \langle |N(f_x, f_y)|^2 \rangle$. The squared error as above may now be written more explicitly as:

$$\begin{aligned}\epsilon &= \int \int df_x df_y [|1 - W(f_x, f_y)H(f_x, f_y)|^2 S_{obj}(f_x, f_y) \\ &\quad + |W(f_x, f_y)|^2 S_{noise}(f_x, f_y)].\end{aligned}\quad (5.12)$$

We note that the error ϵ is a function of both W and W^* . In order to find the appropriate $W(f_x, f_y)$ that minimizes the error, we must equate $\nabla_{W^*}\epsilon$ to zero and the resulting solution for $W(f_x, f_y)$ is given by:

$$W(f_x, f_y) = \frac{H^*(f_x, f_y)}{|H(f_x, f_y)|^2 + \frac{S_{noise}(f_x, f_y)}{S_{object}(f_x, f_y)}}. \quad (5.13)$$

For more details on taking a gradient with respect to the conjugate W^* function for minimization purposes, the reader will have to wait till the next chapter on constrained optimization. The filter contains the object and noise power spectra explicitly. The second term in the denominator above is the inverse of signal-to-noise ratio (SNR) at the particular spatial frequency (f_x, f_y) . For spatial frequencies where the SNR is high, we get an expression close to the inverse filter, whereas, when the SNR is very low the filter effectively blanks out the corresponding spatial frequencies from the recovery. An approximate knowledge of the object and noise power spectra is sufficient for most practical purposes. The estimate of object power

spectrum may be made based on the average Fourier spectrum associated with images of particular class (e.g. natural scenery, faces, text, etc.) that one may be interested in recovering for a particular problem. In Fig. 5.4(a) we show image recovery using the Wiener filter for the same example used in the section 5.3.



Figure 5.4: (a) Image recovery using Wiener filter, (b) Magnified portion of the recovered image.

We notice that the recovery is now meaningful unlike that in Fig. 5.2(c). The filter has recovered the details lost in the blurring process. The result also has somewhat noisy appearance and suffers from some ringing artifacts near sharp edges as shown in Fig. 5.4 (b), which is a magnified view of a small portion of the recovery in Fig. 5.4 (a). These artifacts are typical of the Wiener filter recovery process. While Wiener filter takes into account the noise power spectrum the perceived quality of the recovered image is not necessarily optimal. For example, images with low local noise that still retain sharp edges have better visual quality. This kind of requirement may be incorporated in the reconstruction algorithm by selecting appropriate constraints as we will describe in the next chapter.

Recovery of a reasonable image from its blurred and noisy version as shown here allows us to think of computational optical imaging systems where the recorded raw data is a poor representation of the image we wish to recover. A de-blurring operation (e.g. using Wiener filter) then recovers a more appropriate image. System designs involving controlled blurring for raw data recording followed

by de-blurring of the image offer a lot of flexibility in design and allow interesting applications such as extended depth of field imaging as we shall see later in this book.

References and suggested reading

1. A. V. Opeenheim *Signals and Systems*, Prentice-Hall, USA (1982).
2. R. C. Gonzalez and R. E. Woods, *Digital Image Processing*, Prentice-Hall, USA (2007).
3. A. N. Tikhonov and Y. V. Arsenin, *Solutions of ill-posed problems*, Halsted Press, New York (1977).

6. Constrained optimization methods for image recovery

We have already stated in the first chapter of this book that an integral part of any computational system deals with the solution of some inverse imaging problem using the recorded image sensor data. Increasingly in several computational imaging systems, this inverse problem is now modeled as an optimization problem with appropriate constraints applied to drive the solution of the numerical optimization procedure towards a meaningful image. In this chapter we discuss constrained optimization algorithms and some simple procedures to solve such problems and further provide pointers to more advanced techniques for the interested reader. We will start our discussion with the image denoising problem followed by image deconvolution and finally conclude with introduction to the exciting recent ideas such as compressive imaging. While a variety of constraint choices may be used for inverse imaging problems, we will consider the total variation minimization constraint as a concrete example in this chapter. This choice of constraint has been made here since it has proved to be very powerful from image quality point of view and secondly it does not require any knowledge of topics such as wavelets or allied transforms that are out of the scope of this book.

6.1 Image denoising

Image or video data forms major portion of digital data streams. One of the problems often encountered even with well designed imaging systems is the noisy appearance of recorded images that give a perception of low image quality to the end user. The noise results from

various factors, e.g. electronic readout noise from the sensor, statistical fluctuations in number of photons in the illuminating light beam and the statistical nature of detection process. While one may argue that the noise may be reduced by using sufficient light levels, there are applications such as (i) astronomy where light levels may be inherently low or (ii) medical X-ray imaging where increasing X-ray dose is not desirable. Removing noise from an image is thus an important practical problem. While denoising is not a full fledged inverse problem it is a good starting point for this chapter. Figures

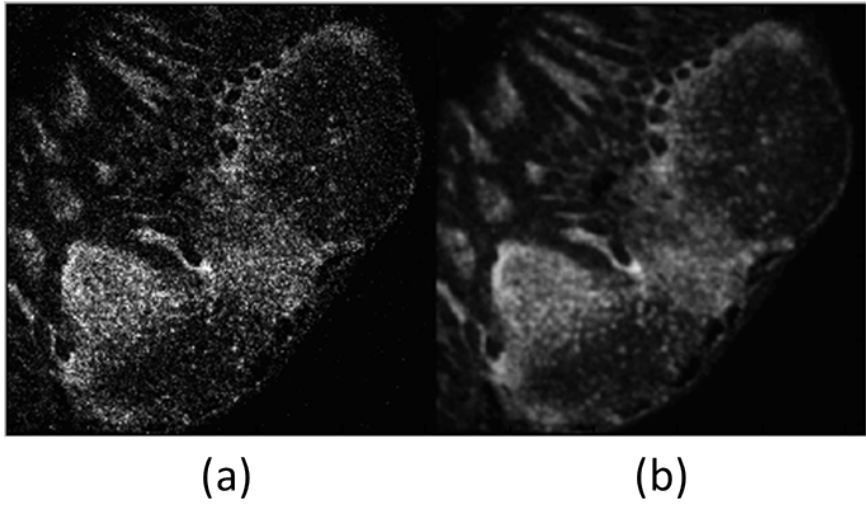


Figure 6.1: (a) Typical image from a fluorescence microscope and (b) its Gaussian filtered version.

6.1 (a), (b) show a typical image obtained from a fluorescence microscope and its Gaussian filtered (filter width = 2 pixels) version respectively. While the filtered image has less noisy appearance the edges in this filtered image appear blurred, indicating that simple averaging over pixels is not sufficient for our purpose. Given a noisy image we would like to obtain another image which has smoother appearance but no loss in sharpness or resolution. It is important to remember that edges in an image play an important role in our perception of the image quality. A scheme must therefore be realized such that the small local noise oscillations are suppressed while

retaining edges at the same time. Given a noisy image $g(x, y)$ we will now attempt to find another image $\hat{g}(x, y)$ which is close to $g(x, y)$ but has the desired properties mentioned above. The problem is modeled here as that of minimization of a cost function $C(\hat{g})$ given by:

$$C(\hat{g}) = \frac{1}{2} \|g(x, y) - \hat{g}(x, y)\|^2 + \alpha \psi(\hat{g}). \quad (6.1)$$

Here the notation $\| \dots \|$ once again denotes the L2-norm, α is a real positive number and ψ is a penalty function or constraint function. The parameter α gives an appropriate weight to the penalty term in relation to the L2-norm squared term. The penalty function is to be designed so that higher magnitudes of gradient at any pixel make larger contribution to the overall cost. A powerful choice for ψ is the total variation (TV) functional:

$$\psi(\hat{g}) = TV(\hat{g}) = \|\nabla \hat{g}\|_1 = \sum_{m,n} |\nabla \hat{g}|_{m,n}. \quad (6.2)$$

The TV functional is seen to be the L1-norm of the gradient which is more explicitly defined in the last term above. The indices (m, n) denote the pixel indices in the image. The contribution of every pixel in the TV of any given image is thus proportional to the magnitude of the gradient at that pixel. A penalty may also be designed such that this contribution is proportional to the L2-norm square of the gradient. Making the penalty in the form of L1-norm, however, gives relatively more weight to the small local oscillations due to noise. Since edges occupy relatively few pixels in a typical image, the contribution of small local oscillations to the penalty function is usually higher compared to that due to edges when using L1-norm penalty. Any numerical procedure for minimizing the cost function in Eq. (6.1) thus gives lot of importance to small local oscillations while preserving edges.

We will now describe a simple method of gradient descent to minimize the cost function in Eq. (6.1). Given a particular guess solution \hat{g} of the problem we wish to consider a small variation $\delta\hat{g}$ in it such that:

$$C(\hat{g} + \delta\hat{g}) < C(\hat{g}). \quad (6.3)$$

This inequality may be achieved if we make $\delta\hat{g}$ proportional to the negative functional gradient of the cost function. The iteration using gradient descent thus progresses as:

$$\hat{g}^{(n+1)} = \hat{g}^{(n)} - t [\nabla_{\hat{g}} C(\hat{g})]_{\hat{g}=\hat{g}^{(n)}}. \quad (6.4)$$

Here t is the step size in direction of negative gradient. The numerical value of t is determined for each iteration to make sure that the cost function does reduce as per Eq. (6.3). For example one may start with some nominal value $t = 1$ and get a test guess for $\hat{g}^{(n+1)}$. If this guess solution does not satisfy Eq. (6.3), t is reduced to (say) $t/2$ and so on till this condition is satisfied.

At this point we present discussion of a general method for optimization of real positive valued cost functions of form:

$$C(\hat{g}) = \int \int dx dy \mathcal{L}(\hat{g}, \nabla_x \hat{g}, \nabla_y \hat{g}). \quad (6.5)$$

The cost function in Eq. (6.1) is already in this form. We will encounter this form more often in this chapter and later in this book. We note that the directional derivative of $C(\hat{g})$ in the direction $\hat{\beta}$ is given by:

$$\begin{aligned} \frac{\partial C(\hat{g})}{\partial \hat{\beta}} &= \lim_{\epsilon \rightarrow 0} \frac{C(\hat{g} + \epsilon \hat{\beta}) - C(\hat{g})}{\epsilon} \\ &= \nabla_{\hat{g}} C \cdot \hat{\beta} \\ &= \int \int dx dy (\nabla_{\hat{g}} C)(x, y) \hat{\beta}(x, y). \end{aligned} \quad (6.6)$$

In accordance with the usual treatment of problems in variational calculus we will assume that the variation $\epsilon \hat{\beta}$ to a solution \hat{g} is zero at the image boundary. Then we have:

$$C(\hat{g} + \epsilon \hat{\beta}) = C(\hat{g}) + \epsilon \nabla_{\hat{g}} C(\hat{g}) \cdot \hat{\beta}, \quad (6.7)$$

upto first order in ϵ . Further, the functional gradient can be expressed in terms of the integrand $\mathcal{L}(\hat{g}, \nabla_x \hat{g}, \nabla_y \hat{g})$ in Eq. (6.5) and has the Euler-Lagrange form:

$$\nabla_{\hat{g}} C(\hat{g}) = \left[\frac{\partial \mathcal{L}}{\partial \hat{g}} - \frac{\partial}{\partial x} \left(\frac{\partial \mathcal{L}}{\partial (\nabla_x \hat{g})} \right) - \frac{\partial}{\partial y} \left(\frac{\partial \mathcal{L}}{\partial (\nabla_y \hat{g})} \right) \right]. \quad (6.8)$$

This formula for functional gradient may be used in general when designing optimization algorithms that use iterative schemes such as the gradient descent scheme described in Eq. (6.4).

When using the TV penalty function as in Eq. (6.1) the functional gradient may be written explicitly as:

$$\nabla_{\hat{g}} C(\hat{g}) = -(g - \hat{g}) - \alpha \nabla \cdot \left(\frac{\nabla \hat{g}}{|\nabla \hat{g}|} \right). \quad (6.9)$$

One implementation detail that is to be noted is that the denominator in the second term of Eq. (6.9) is typically approximated as:

$$|\nabla \hat{g}| \approx \sqrt{|\nabla \hat{g}|^2 + \delta^2}, \quad (6.10)$$

for small positive constant δ , so that, we avoid division by zero in the constant or flat regions of the image. The second term in Eq. (6.9) is seen to have a form of anisotropic diffusion with the diffusion coefficient inversely proportional to the local gradient magnitude which is another way of thinking about the edge preserving property of TV penalty. In the illustration in Fig. 6.2 we show the result of iterative procedure in Eq. (6.4) on Fig. 6.1(a) for two different values of parameter α . Twenty iterations of the algorithm have been used in each case. We observe that when α is set to a small value the solution looks similar to the original noisy image. Further the denoised image in Fig. 6.2(b) retains better edge information and sharpness as compared to the Gaussian filtered image in Fig. 6.1(b) thus demonstrating the advantage of TV based denoising over linear filtering.

6.2 Image de-convolution by optimization

In this section we add some complexity to the denoising problem that was described in the previous section and study the image restoration problem with TV penalty as a constraint term. The data in this case is a blurred image with noise which we will try to recover. The data model is as follows:

$$g_o(x, y) = h(x, y) * g_i(x, y) + n(x, y), \quad (6.11)$$

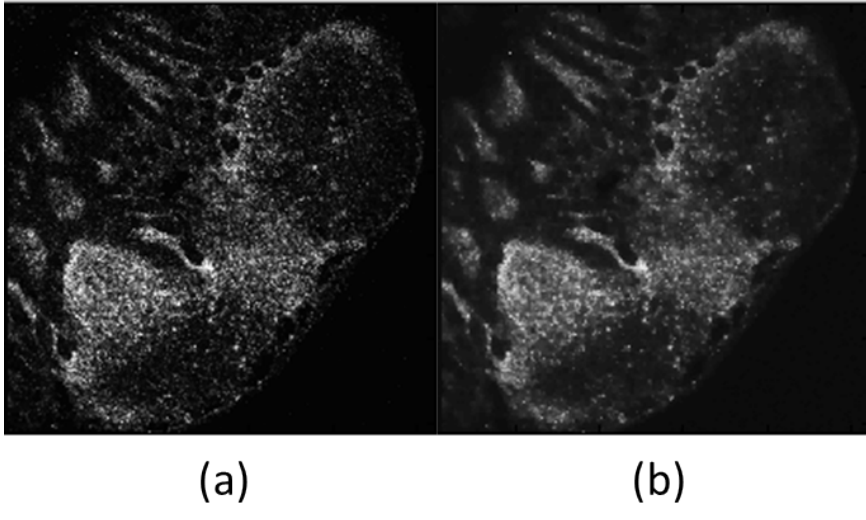


Figure 6.2: Denoising with Total Variation penalty: The values of weight parameter $\alpha = 0.025$, $\alpha = 0.25$ are used in (a) and (b) respectively.

which may also be represented in a matrix operator form as:

$$g_o = Ag_i + n, \quad (6.12)$$

with A denoting the system or blurring linear operator. In a fashion similar to the previous section we model the optimization problem where the cost function is defined as:

$$C(\hat{g}_i) = \frac{1}{2} \|g_o - A\hat{g}_i\|^2 + \alpha TV(\hat{g}_i, \hat{g}_i^*). \quad (6.13)$$

Here we will assume that the image \hat{g}_i is complex in general and the cost function C is a real valued function of both \hat{g}_i and \hat{g}_i^* . The TV function is defined here as:

$$TV(\hat{g}, \hat{g}^*) = \|\nabla g\|_1 = \sum_i \sqrt{(\nabla_x \hat{g}_i)(\nabla_x \hat{g}_i^*) + (\nabla_y \hat{g}_i)(\nabla_y \hat{g}_i^*)}. \quad (6.14)$$

We note that the variation in C can now be represented as:

$$\begin{aligned}\delta C(\hat{g}_i, \hat{g}_i^*) &= \frac{\partial C}{\partial \hat{g}_i} \delta \hat{g}_i + \frac{\partial C}{\partial \hat{g}_i^*} \delta \hat{g}_i^* \\ &= 2Re \left[\frac{\partial C}{\partial \hat{g}_i} \delta \hat{g}_i \right] \\ &= 2Re \left[\left(\frac{\partial C}{\partial \hat{g}_i^*} \right)^* \delta \hat{g}_i \right].\end{aligned}\quad (6.15)$$

The last step above is possible due to the real valued nature of the cost function C . Applying the Cauchy-Schwartz inequality to the term $Re \left[\left(\frac{\partial C}{\partial \hat{g}_i^*} \right)^* \delta \hat{g}_i \right]$ above tells us that the maximum value of δC is achieved when the variation $\delta \hat{g}_i$ is in the direction of $[\partial C / \partial \hat{g}_i^*]$. The iterative solution to the deblurring problem using the gradient descent scheme is thus written as follows:

$$\hat{g}_i^{(n+1)} = \hat{g}_i^{(n)} - t \left[\nabla_{\hat{g}_i^*} C(\hat{g}_i, \hat{g}_i^*) \right]_{\hat{g}_i=\hat{g}_i^{(n)}}. \quad (6.16)$$

We note that when calculating the functional gradient of C with respect to \hat{g}_i^* , \hat{g}_i is to be treated as a constant and vice versa. The functional gradient for this cost function in Eq. (6.13) may be evaluated as:

$$\nabla_{\hat{g}_i} C(\hat{g}_i) = -\frac{1}{2} A^\dagger (g_o - A\hat{g}_i) - \frac{1}{2} \alpha \nabla \cdot \left(\frac{\nabla \hat{g}_i}{|\nabla \hat{g}_i|} \right). \quad (6.17)$$

The factor $1/2$ arises above since both the L2-norm and TV term are now defined in terms of complex quantities as may be verified readily. In order to proceed further, we need to define the adjoint operator A^\dagger explicitly when the system bluring operator A corresponds to convolution by the impulse response $h(x, y)$. We will first define the scalar product of two functions belonging to the output or image space as:

$$(g_{o1}, g_{o2}) = \int \int dx dy g_{o1}^*(x, y) g_{o2}(x, y). \quad (6.18)$$

The adjoint A^\dagger is now defined such that it satisfies the property:

$$(g_{o1}, Ag_{i2}) = (A^\dagger g_{o1}, g_{i2}). \quad (6.19)$$

The function g_{i2} here belongs to the input or object space. When the action of A is equivalent to convolution with impulse response $h(x, y)$, we have:

$$\begin{aligned} & \int \int dx dy g_{o1}^*(x, y) \left[\int \int dx' dy' h(x - x', y - y') g_{i2}(x', y') \right] \\ &= \int \int dx' dy' \left[\int \int dx dy h^*(x - x', y - y') g_{o1}(x, y) \right]^* g_{i1}(x', y'). \end{aligned} \quad (6.20)$$

We observe that the adjoint operator A^\dagger corresponding to the convolution operation is another convolution with the function $h^*(-x, -y)$. This definition may now be used in the functional gradient evaluation as in Eq. (6.17). In the following illustration in Fig. 6.3, we show the recovery of the blurred image in Fig. 5.2 (b) using constrained optimization scheme with TV penalty as in Eq. (6.13). The parameter $\alpha = 1$ is used here along with 10 gradient descent iterations. We observe from the magnified portion of the recovered image that the ringing artifacts have now reduced significantly compared to those in Fig. 5.4 (b) where the Wiener filter was used for image recovery. The Wiener filter solution is however obtained by a single step non-iterative procedure and may be thus used as a first guess for the optimization based iterative solution. The optimiza-

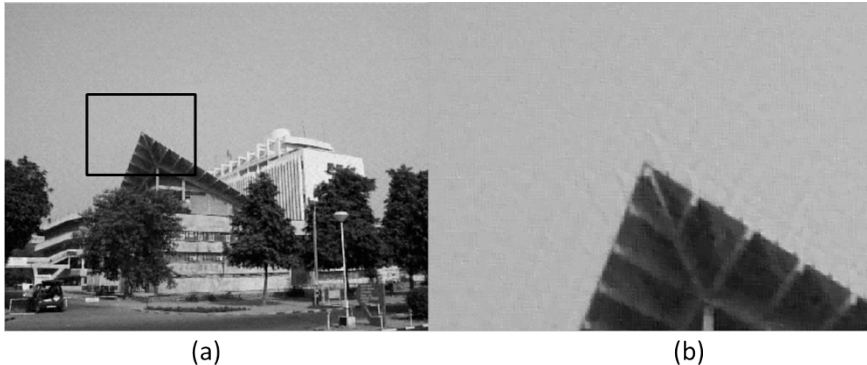


Figure 6.3: (a) Image recovery using constrained optimization with TV penalty, (b) Magnified portion of the recovered image.

tion based solution generally provides significantly improved image quality when the solution is constrained with the appropriate penalty functions. While image quality is a topic beyond the scope of this book, it is important to note that in several applications (e.g. diagnostic imaging) the image quality perceived by the end user plays a very important role in design of image recovery algorithms.

6.3 Blind image deconvolution

In this section we will discuss a somewhat unusual image recovery method - the blind deconvolution method - which allows one to recover blurred images even without the knowledge of the impulse response $h(x, y)$. The problem requires an alternating two-step optimization approach where the deblurred image and the impulse are both updated with appropriate constraints till both the functions converge to appropriate solutions. Two optimization problems as below are solved alternatively as follows:

$$\text{Minimize } \|g_o - h * g_i\|^2 + \alpha_1 \psi_1(g_i) \text{ with } h \text{ held fixed,} \quad (6.21)$$

$$\text{Minimize } \|g_o - h * g_i\|^2 + \alpha_2 \psi_2(h) \text{ with } g_i \text{ held fixed.} \quad (6.22)$$

Here ψ_1 and ψ_2 represents constraints on the image g_i to be recovered and the impulse response h . It is clear that since both the impulse response function h and the input image g_i are unknown, the problem has infinite number of solutions. The constraints on the recovered image and the blur function therefore play a key role in determining a solution for both which is meaningful based on the Physics of the problem. The blind deconvolution process is typically performed iteratively such that at $(n + 1)$ -th iteration, the following steps are used:

1. Start with the blurred image data $g_o(x, y)$ and a guess $h^{(n)}$ for the impulse response.
2. Find a guess solution $g_i^{(n+1)}(x, y)$ for the deblurred image by solving a constrained optimization problem of the form in Eq. (6.13) where $h^{(n)}(x, y)$ is treated as a constant. The constraints in this case will be appropriate constraints on the desired deblurred image.

3. Treating $g_i^{(n+1)}(x, y)$ above as a constant another constrained optimization problem of the type in Eq. (6.13) is solved where now the blur function is updated to a new guess $h^{(n+1)}(x, y)$. The constraint term in optimization now refers to the desired properties of the blur function.

The iteration is initiated with a nominal guess for the blur function $h^{(0)}(x, y)$. It is known that the approximate size or support of the initial guess $h^{(0)}(x, y)$ plays an important role for achieving good convergence of the algorithm in practice. The support of the blur function may be estimated initially from any recognizable features in the blurred image data. In the illustration in Fig. 6.4 we show recovery of a blurred image of a bar-code using the blind deconvolution approach. Here positivity constraint is used for both the deblurred image and the blur function. Additionally a Total Variation penalty is used for the deblurred image. The recovery in blind-deconvolution



Figure 6.4: Illustration of blind deconvolution. (a) Blurred image data, (b) Recovered de-blurred image, (c) Magnified portion of recovered impulse response function.

type approaches critically depends on the constraints used and hence careful consideration of this aspect is required in designing a practical algorithm. Blind deconvolution has found practical applications in astronomical imaging through atmospheric turbulence and the removal of motion blur in digital imaging.

6.4 Compressive Imaging

In this section we turn to an interesting application - compressive imaging - of the constrained optimization framework. The research work on image compression standards over the last two decades has shown that natural images are compressible. In other words the number of degrees of freedom in a typical image is often much less than the number of pixels used to represent it. For example if we visually inspect the image in Fig. 5.2 (a), we observe that there are several flat or smooth regions where the numerical values are locally almost constant or slowly varying from pixel to pixel. These correlations in pixel values may be used efficiently for storage of images as is now done in widely used image compression standards such as JPEG2000. If most images to be recorded in some application are expected to have some structure and hence compressibility, a natural question to ask is:

How many measurements are required to generate an N -pixel image ?

For the imaging model in Eq. (6.12) the simple and conventional answer to this question (disregarding any compressibility in the image g_i) is that we will need approximately N measurements to generate an N pixel image. The argument here is that Eq. (6.12) is a linear system of equations and in order to find N unknown pixel values, we need to have as many equations as the number of unknowns. However if we suppose that the image to be recovered is compressible, then it is conceivable intuitively that number of measurements much less than N should be sufficient. We provide a concrete example of Fourier domain measurements to illustrate this point.

Fourier domain measurements occur commonly in optics, medical imaging modalities such as MRI and X-ray CT, radio astronomy to name a few applications. Consider an image $g(x, y)$ and its Fourier transform $G(f_x, f_y)$ as shown in Fig. 6.5(a), (b) respectively. If the full data is measured in Fourier domain, it is straightforward to invert $G(f_x, f_y)$ using inverse Fourier transformation to get the image $g(x, y)$. However we observe that the image $g(x, y)$ is sparse in the gradient domain. If we inspect the gradient magnitude image as in Fig. 6.5 (c), we observe that the number of pixels with significant gradient magnitude is much less than the total number

of pixels in the image. Can we utilize this gradient domain sparsity in some way ? For example we may measure only $N/4$ Fourier domain samples randomly at locations shown as bright pixels in a binary $(0, 1)$ mask $M(f_x, f_y)$ shown in Fig. (6.6)(a). The corresponding masked Fourier data is shown in Fig. (6.6)(b). The $N/4$ data points in Fourier domain are clearly incomplete in the conventional sense of solving for N unknown pixel values. When the number of data samples is much less than N , we have an incomplete system of equations to solve. In principle such an incomplete system of linear equations has infinite number of solutions. To find an appropriate solution we need some additional criterion to decide on which solution to select. As a first attempt, we consider the minimum L2-norm squared solution by minimizing the cost function:

$$C(g_i, g_i^*) = \frac{1}{2} \| M(f_x, f_y) [G(f_x, f_y) - \mathcal{F}\{g_i(x, y)\}] \|^2. \quad (6.23)$$

Note that here we are looking for the best solution in the least-square sense that has a Fourier transform close to $G(f_x, f_y)$ at the measurement locations in the Fourier domain as per the mask definition. The solution for this minimization problem is shown in Fig. 6.7(a). We observe that the least-square solution is clearly of poor quality and is not useful in any practical application. As discussed above, since we expect the solution to be sparse in gradient domain, we may incorporate this information in the cost function by redefining the cost function as:

$$\begin{aligned} C(g_i, g_i^*) = & \frac{1}{2} \| M(f_x, f_y) [G(f_x, f_y) - \mathcal{F}\{g_i(x, y)\}] \|^2 \\ & + \alpha TV(g_i, g_i^*). \end{aligned} \quad (6.24)$$

The solution to the corresponding problem with TV penalty incorporated is shown in Fig. 6.7(b) where we observe near perfect image recovery with 25% Fourier measurements. Both the optimization problems above are solved using the iteration scheme described in Eq. (6.16) and Eq. (6.17). The adjoint operator A^\dagger in this illustration corresponds to the inverse Fourier transform of the Fourier data restricted by the mask $M(f_x, f_y)$.

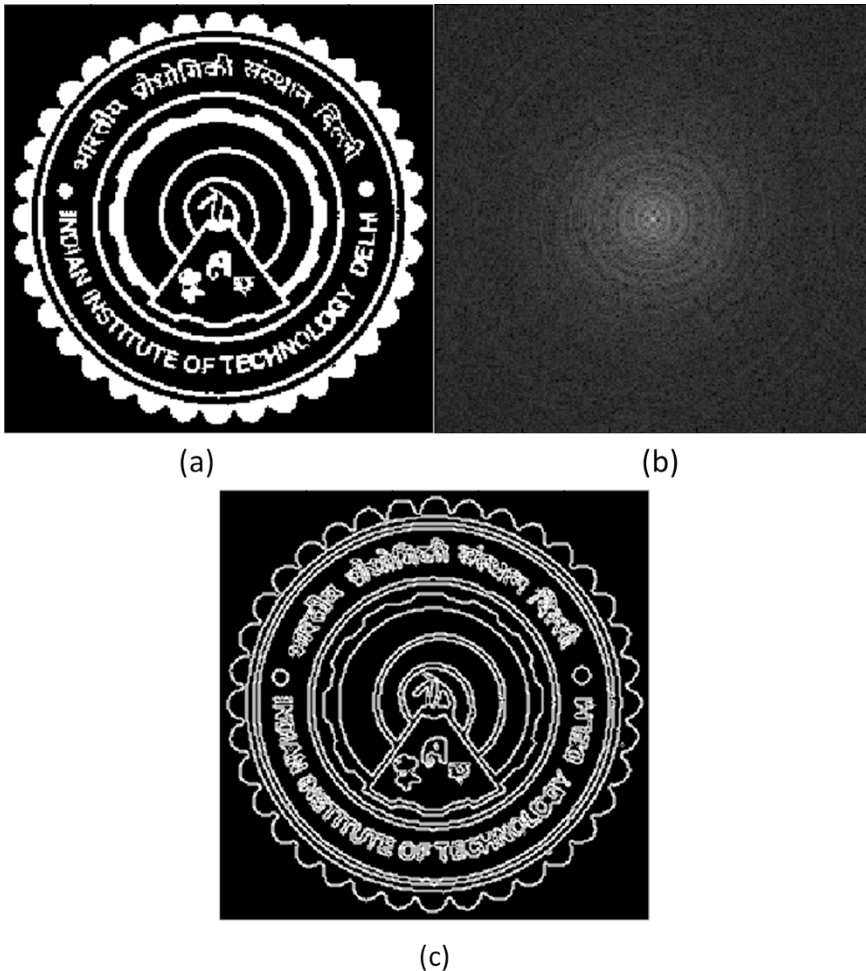


Figure 6.5: (a) Logo image $g(x, y)$, (b) Fourier transform magnitude $|G(f_x, f_y)|$ shown on a log-scale , (c) Gradient magnitude image $|\nabla g(x, y)|$.

6.4.1 Guidelines for sub-sampled data measurement and image recovery

While we have seen excellent image recovery with data that may be considered incomplete in traditional sense, the choice of transform and the measurement scheme need some further discussion. For no-

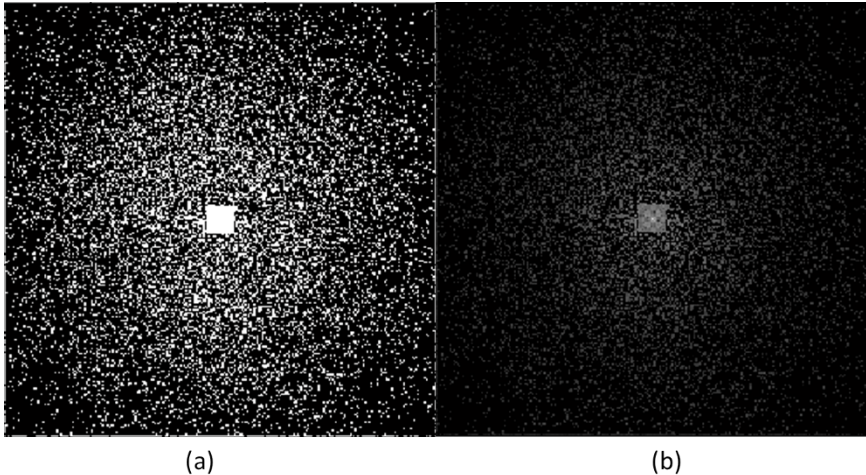


Figure 6.6: (a) Binary mask $M(f_x, f_y)$ showing locations where Fourier data is measured, (b) Fourier transform magnitude $|M(f_x, f_y)G(f_x, f_y)|$ shown on a log-scale.

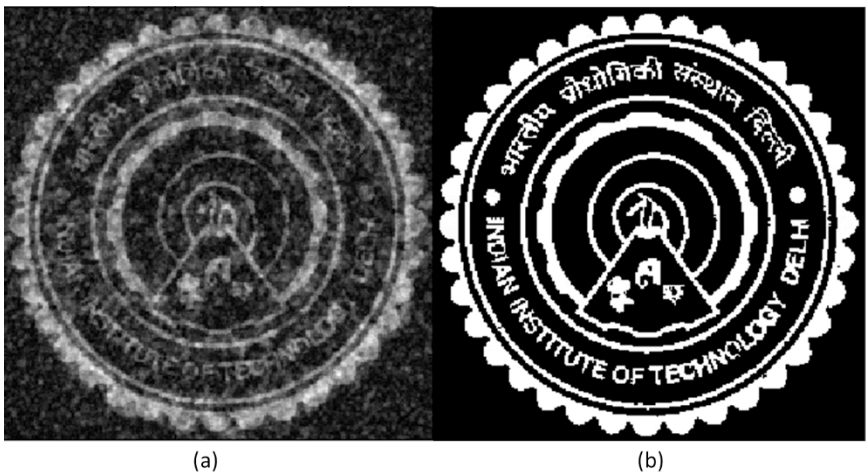


Figure 6.7: Image recovery for (a) minimum squared L2-norm problem as in Eq. (6.23), (b) minimum squared L2-norm problem with TV penalty as in Eq. (6.24).

tational simplicity we will assume that the solution $g(x, y)$ can be expanded in terms of a basis set of functions $\{\phi_n(x, y)\}$:

$$g(x, y) = \sum_n \beta_n \phi_n(x, y). \quad (6.25)$$

Further we assume that the choice of basis is such that the vector β made up of all the coefficients β_n is sparse in nature. In other words a small number of coefficients β_n compared to N are significant. The choice of basis can be typically a scale based basis such as some wavelet family that is known to be efficient for representation of natural images. The imaging model used is as in Eq. (6.12):

$$g_o = A \sum_n \beta_n \phi_n(x, y) + n(x, y). \quad (6.26)$$

The compressive sensing problem refers to recovery of the coefficients β_n under a prior constraint that β is a sparse vector. As shown by Candes, Romberg and Tao (2006), this problem may be modelled as a minimization problem for a cost function given by:

$$C(\beta) = \frac{1}{2} \|g_o - A \sum_n \beta_n \phi_n(x, y)\|^2 + \alpha \|\beta\|_1. \quad (6.27)$$

Here the sparsity in components of β is achieved by imposing an L1-norm penalty. More explicitly $\|\beta\|_1 = \sum_n |\beta_n|$. The TV penalty used for the illustration in Fig. 6.7 is an example of L1-norm penalty as well, except that the image representation is not in terms of a basis set of functions.

Roughly the connection between sparsity and L1-norm is that a sphere in L1 domain is “pointy” (e.g. in 2D a unit sphere with respect to L1-norm is $|x_1| + |x_2| = 1$ rather than $x_1^2 + x_2^2 = 1$). The optimal solution satisfying the data constraint along with L1 penalty is an intersection of the hypersurface denoting the data constraint with an L1-sphere in the large dimensional space whose axes are the coefficients β_n . The “pointy” nature of the L1-sphere suggests that the solution is sparse in the coefficients β_n . The geometrical picture above is not easy to imagine, however, analogy can be drawn to the fact that the TV penalty favors solutions with sparsely located edges along with majority of flat (small gradient) regions in the recovered

image. Finally we would like to mention for completeness that as per the rigorous compressive imaging (or sensing) theory, if an N pixel image is likely to have a representation with $K(<< N)$ significant coefficients in some sparsity basis, then number of measurements of the order of $K \log N$ are required for possibility of the desired image recovery through an appropriate algorithm.

Another important aspect about the compressive imaging methodology is the relation between the measurement scheme and the basis in which the image is likely to be sparse. We will illustrate this with a simple case involving sparsity in pixel basis. Consider a sparse image in pixel basis as shown in Fig. 6.8. Suppose we wish to measure

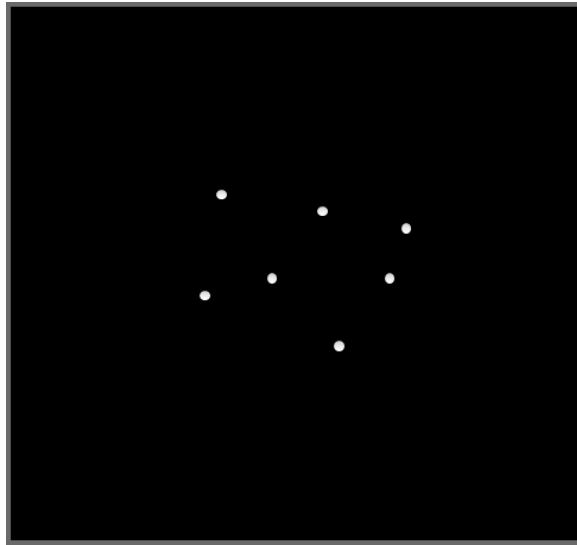


Figure 6.8: A sparse image in pixel basis: Few pixels shown by white dots are non-zero while all other pixels are zero.

an output g_o corresponding to this sparse object as per the model in Eq. (6.26). We notice that each measurement point g_{oj} corresponds to a linear combination

$$g_{oj} = \sum_n \beta_n (A_j, \phi_n) + \text{noise}. \quad (6.28)$$

Here (A_j, ϕ_n) denotes the scalar product between the j -th row of the system matrix A (j -th element of the measurement basis) and the

sparsity basis function ϕ_n . First let us note that the sparsity basis in this case is the pixel basis. The basis function ϕ_n in the case of pixel basis is an image whose n -th pixel has value equal to 1 while all other pixels are zero. If we desire to recover the image $g = \sum_n \beta_n \phi_n$ from number of measurements that are much smaller than the number of total pixels N in the image, we certainly cannot use the pixel basis as the measurement basis. Since the image as shown in Fig. 6.8 is sparse in the pixel basis, choosing the pixel basis once again for measurement will mean that most of the scalar products (A_j, ϕ_n) will be zero and the recovery problem will be meaningless. On the other hand if we choose a Fourier basis for measurement vectors in A , most scalar products are likely to survive making it possible to recover the sparse image with the use of appropriately designed algorithm. Thus an important guideline to follow is that the image to be recovered cannot in general be sparse in both the ϕ_n basis and the measurement basis. This property of the two basis sets is represented more formally in terms of what is known as the restricted isometry property. We will however not discuss this topic further.

6.4.2 System level implications of compressive imaging philosophy

The possibility of solving such “incomplete data” inverse problems has important implications for how imaging systems of tomorrow may be designed. The philosophy behind ideas like compressive imaging is significant to the following classes of problems:

1. **Imaging systems beating conventionally perceived limits**
We now have a new framework for re-examining our notions about imaging system performance metrics such as resolution, sensitivity to noise, etc. and for evolving novel imaging concepts that may outperform traditional imagers in these aspects.
2. **Simpler/leaner imaging systems** High quality imaging performance with less measurements implies simplifying imaging system design with correspondingly reduced cost for imaging technologies in the area of healthcare, security, education, etc. with high social impact.

6.5 Topics for further study

In this chapter we have provided the reader with operational introduction to the important ideas in constrained optimization that are highly valuable for image recovery problems without necessarily providing the most rigorous mathematical treatment to optimization theory for which excellent sources are already available. Starting with the simplest image denoising problem, we added complexity to the problem when discussing the image deblurring (both with known impulse response and unknown impulse response as in case of blind deconvolution) and finally considered the compressive sensing ideas that suggest possibility of image recovery with data that would be considered incomplete in traditional sense. Two major aspects that are left out here are the choice of algorithms and modeling of the cost function. In particular while we have stuck to the simplest gradient descent scheme, many other choices such as steepest descent, conjugate gradient, Nesterov gradient etc. have been studied in the literature with each method having its own advantages or disadvantages. The choice of final algorithm depends on several considerations such as speed, computational load, simplicity of implementation and aspects specific to the system or application under consideration. In terms of cost function modeling there are several statistical approaches such as maximum likelihood, maximum entropy, weighted least squares, etc. that account for the knowledge of statistical nature of signal detection and noise in measurements. Also while TV penalty was used in all the illustrations, a general class of Gibbs prior penalty functions also exists and the choice of penalty function again depends on the application under consideration. We believe that the reader has acquired a sense of the powerful constrained optimization techniques and their importance to computational imaging systems through this chapter. State of the art imaging systems are increasingly based on such optimization algorithms for image recovery from measured data.

References and suggested reading

1. M. Bertero and P. Boccacci, *Introduction to inverse problems in imaging*, IOP, UK (1998).
2. H. H. Barrett and K. J. Myers, *Foundations of imaging science*, Wiley USA (2003).
3. Mallat, *A wavelet tour of signal processing*, Academic Press USA (2000).
4. S. Boyd and L. Vandenberghe, “Convex Optimization”, Cambridge Univ. Press UK (2004).
5. G. R. Ayres and J. C. Dainty, “Blind deconvolution method and its applications”, Optics Letters 13, 547-549 (1988).
6. T. F. Chan and C. K. Wong, “Total variation blind deconvolution”, IEEE Trans. Image Processing 7, 370-375 (1998).
7. D. H. Brandwood, “A complex gradient operator and its applications in adaptive array theory”, Proc. IRE, vol. 30, pp. 11-16 (1983).
8. E. Candes, J. Romberg, T. Tao, “Robust uncertainty principles: exact signal recovery from highly incomplete frequency information”, IEEE Trans. Information Theory, vol. 52, pp. 489-509 (2006). A comprehensive list of resources/articles in Compressive Sensing is available at <http://dsp.rice.edu/cs>
9. S. Geman and D. Geman, “Stochastic relaxation, Gibbs distributions, and the Bayesian restoration of images”, IEEE Trans. Pattern Analysis and Machine Intelligence, vol. 6, pp. 721-741 (1984).

7. Random processes

In this chapter we will introduce several important concepts in theory of random processes that will be useful later when discussing coherence properties of light. When Physical phenomena occur as a result of large number of unknown (almost random) factors, the observations and predictions of experimental results can only be done satisfactorily in statistical terms. The generation, propagation and detection of light that cover most of Optics/Photonics are not deterministic in nature and therefore the study of random processes is essential.

7.1 Probability and random variables

Probability is associated with observable phenomena or events when we do not have sufficient information about the related system under study to predict its precise behaviour. If a particular event has n successes out of N trials then as the number of trials becomes very large, we may associate an average rate of success or probability:

$$p = \frac{n}{N}, \quad N \rightarrow \infty \quad (7.1)$$

In set theoretic terms, we may denote the total event space by Ω . Then $p(\Omega) = 1$ and probability of the null set O is zero. For any subset $A \in \Omega$, $0 \leq p(A) \leq 1$. For two mutually exclusive events A_1 and A_2 in Ω ,

$$p(A_1 + A_2) = p(A_1) + p(A_2). \quad (7.2)$$

7.1.1 Joint Probabilities

When an event is obtained by compounding two events, we have to consider joint probability of events A and B which is denoted by $p(A, B)$ or which is the same as $p(A \cap B)$. It is clear that the joint probability is less than or equal to the probability of one event alone. If M events B_1, B_2, \dots, B_M are mutually exclusive and span the whole of Ω , then

$$\sum_{j=1}^M p(A, B_j) = p(A, \Omega) = p(A). \quad (7.3)$$

For events A and B that are not necessarily mutually exclusive, the probability of their union is:

$$p(A \bigcup B) = p(A) + p(B) - p(A \cap B) \leq p(A) + p(B). \quad (7.4)$$

Condition probability $p(A|B)$ or A given that B has occurred is defined as:

$$p(A|B) = \frac{p(A \cap B)}{p(B)}. \quad (7.5)$$

If the two events are such that $p(A|B) = p(A)$, then as far as A is concerned, it does not matter if B has occurred or not. The two events are then called statistically independent events . From the definition of conditional probability we see in this case that

$$p(A \cap B) = p(A)p(B). \quad (7.6)$$

The above relation may be considered as a necessary and sufficient condition for statistically independent events. If two events are mutually exclusive, they cannot be statistically independent as their joint probability is zero.

7.1.2 Baye's rule

We will now state the Baye's rule on inverse probabilities. This is a relation between the conditional probabilities $p(A|B)$ and $p(B|A)$.

$$p(B|A) = \frac{p(A|B)p(B)}{p(A)}. \quad (7.7)$$

Illustration: A coin is tossed 5 times and produces heads on all five trials. What is the probability that it is a loaded coin?

A = producing H consecutively 5 times

L = coin is loaded, $p(L) = 0.5$

U = coin is fair, $p(U) = 0.5$.

$$\begin{aligned} p(L|A) &= \frac{p(A|L)p(L)}{p(A|L)p(L) + p(A|U)p(U)} \\ &= \frac{(1)(0.5)}{(1)(0.5) + (0.5)^5(0.5)} \\ &= \frac{1}{1 + 1/32} = 32/33. \end{aligned} \quad (7.8)$$

Note that we assigned $p(L)$ and $p(U)$ arbitrarily as we had no more prior information about them. But values other than the assigned ones may be used if data to that effect is available.

7.1.3 Random Variables

The outcome of a complicated experiment is typically some numerical variable x whose value is not deterministic. We will call such variable as a random variable . The variable x may take discrete values or may take any of the (infinite number of) values in some interval. Accordingly the random variable is termed as discrete or continuous random variable. The set of possible outcomes of x is called the ensemble of x . For a discrete random variable we may associate a probability p_i with each of the possible outcomes x_i such that

$$\sum_i p_i = 1. \quad (7.9)$$

When the random variable is continuous, we talk of probability density $p(x)$ such that $p(x)dx$ equals the probability of finding an outcome in the interval $(x - dx/2, x + dx/2)$ and

$$\int dx p(x) = 1. \quad (7.10)$$

The cumulative probability density is defined as

$$P(x \leq X) = \int_{-\infty}^X dx p(x), \quad (7.11)$$

such that,

$$\frac{dP(x \leq X)}{dX} = p(X). \quad (7.12)$$

7.1.4 Expectations and Moments

Behaviour of a random variable can only be described in a statistical sense. In this regard, the important concepts of expectations and moments are useful. For any function $f(x)$ of a random variable with probability density $p(x)$, its expectation value is defined as:

$$\langle f(x) \rangle = \int dx p(x) f(x). \quad (7.13)$$

Among the functions of x , its moments or the expectation values of the powers of x have a special place. The r -th moment of x is defined as:

$$\nu_r = \langle x^r \rangle = \int dx p(x) x^r. \quad (7.14)$$

The mean of the random variable is ν_1 . For discrete case when the random variable takes values 0, 1, 2, ... one may define the r -th moment as:

$$\nu_r = \langle n^r \rangle = \sum_{n=0}^{\infty} p(n) n^r. \quad (7.15)$$

Another useful concept is the factorial moment defined as:

$$\langle n^{(r)} \rangle = \langle n(n-1)(n-2)\dots(n-r+1) \rangle. \quad (7.16)$$

The factorial moments are sometimes easier to evaluate for some common discrete distributions. The moments defined so far have been defined with respect to $x = 0$. If the mean $\langle x \rangle$ is a finite value then one may talk of central moments by converting to a new variable: $\mu = (x - \langle x \rangle)$. The first moment μ_1 in this case will be zero. The second central moment μ_2 is known as the variance of the variable and it represents the spread of the distribution. It must be

noted that the higher order moments like variance may not always exist (or diverge) if the probability distribution has long tails. An example of this is the sinc² probability distribution which describes the probability of arrival of a photon as a result of the single slit diffraction. It is clear that the second moment of this distribution diverges. There are alternative ways to define what we mean by “spread” of such distributions as we have already discussed in Chapter 3 in relation to the energy concentration problem and the Slepian functions. The square root of the variance is often denoted by σ and is called the standard deviation of the distribution. The standard deviation may be used to normalize higher order moments. For example, the skewness of a distribution is defined by: $\alpha_3 = \mu_3/\sigma^3$ and the kurtosis $\alpha_4 = \mu_4/\sigma^4$. Random variables are often expressed in what is called the standard form: $y = (x - \langle x \rangle)/\sigma$. It is easy to show that y has zero mean and unit standard deviation.

Moments of multiple random variables may be evaluated using joint probability distributions. For N real random variables x_j with $j = 1, 2, \dots, N$, we define the covariance matrix μ_{ij} as:

$$\mu_{ij} = \langle \Delta x_i \Delta x_j \rangle. \quad (7.17)$$

The covariance matrix is symmetric with the diagonal elements given by the variances of the individual random variables. By using the Cauchy-Schwartz inequality we can show the following important result. We will assume zero mean random variables for simplicity of notation.

$$\begin{aligned} & \left[\int \int dx_i dx_j p(x_i, x_j) x_i x_j \right]^2 \\ & \leq \left[\int \int dx_i dx_j p(x_i, x_j) x_i^2 \right] \left[\int \int dx_i dx_j p(x_i, x_j) x_j^2 \right] \end{aligned} \quad (7.18)$$

or

$$\mu_{ij}^2 \leq \sigma_i^2 \sigma_j^2. \quad (7.19)$$

The correlation coefficient defined as $\rho_{ij} = \mu_{ij}/\sigma_i \sigma_j$ can therefore take values in the range $[-1, 1]$. If two random variables are statistically independent, the correlation coefficient is equal to zero. This can be shown easily using $p(x_1, x_2) = p(x_1)p(x_2)$ in the definition

of μ_{12} . If the random variables are complex valued, the covariance matrix is made Hermitian symmetric by the following definition:

$$\mu_{ij} = \langle \Delta x_i^* \Delta x_j \rangle. \quad (7.20)$$

The absolute value $|\rho_{ij}|$ here is bounded by 1.

7.1.5 Characteristic function

The characteristic function corresponding to a probability density $p(x)$ is the expected value of $\exp(i\omega x)$ or in other words it is the Fourier transform of the probability density function.

$$C(\omega) = \int_{-\infty}^{\infty} dx p(x) \exp(i\omega x). \quad (7.21)$$

The probability density $p(x)$ is absolutely integrable and hence its Fourier transform always exists. The probability density may be obtained from $C(\omega)$ by inverse Fourier transformation. Some of the properties of the characteristic function are listed as below:

1. $C(0) = 1$.
2. $|C(\omega)| \leq C(0)$.
3. $C(\omega)$ is continuous on real-axis even if $p(x)$ has discontinuities.
4. Since $p(x)$ is real, $C(-\omega) = C^*(\omega)$.
5. $C(\omega)$ is non-negative definite. To show this one may start with:

$$\langle \left| \sum_{j=1}^N a_j \exp(ix\omega_j) \right|^2 \rangle \geq 0. \quad (7.22)$$

Writing the average $\langle \dots \rangle$ in terms of $p(x)$ leads to:

$$\sum_{j=1}^N \sum_{k=1}^N a_j^* a_k C(\omega_k - \omega_j) \geq 0. \quad (7.23)$$

Using a power series expansion for $\exp(i\omega x)$ in the definition of characteristic function in Eq. (7.21) we note that:

$$C(\omega) = \sum_{n=0}^{\infty} \frac{(i\omega)^n}{n!} \langle x^n \rangle \quad (7.24)$$

The moments $\langle x^n \rangle$ of the random variable x are therefore given by:

$$\langle x^n \rangle = \frac{1}{n!} \left[\frac{\partial^n C(\omega)}{\partial \omega^n} \right]_{\omega=0}. \quad (7.25)$$

7.1.6 Addition of two random variables

We will now obtain the probability distribution obtained by adding two random variables. What is the probability distribution of the resultant random variable? We will make use of the characteristic function to prove a useful result. Suppose x_1 and x_2 are statistically independent random variables. We denote their probability densities as $p_1(x)$ and $p_2(x)$ respectively. The addition $y = x_1 + x_2$ has the characteristic function given by:

$$C_y(\omega) = \langle \exp[i(x_1 + x_2)\omega] \rangle = C_1(\omega)C_2(\omega). \quad (7.26)$$

The probability density $p(y)$ is obtained by inverse Fourier transforming of the relation above and is thus equal to the convolution of the two probability distributions.

7.1.7 Transformation of random variables

It is often required to find the probability density associated with a transformed variable y which is a function of the random variable x , i.e. $y = f(x)$. We can get the probability density of y using its characteristic function:

$$\begin{aligned} C_y(\xi) &= \langle \exp(iy\xi) \rangle \\ &= \langle \exp[if(x)\xi] \rangle \\ &= \int dx p(x) \exp[if(x)\xi]. \end{aligned} \quad (7.27)$$

The inverse Fourier transform of $C_y(\xi)$ gives the probability density $p(y)$:

$$\begin{aligned} p(y) &= \frac{1}{2\pi} \int d\xi \int dx p(x) \exp[-i(y - f(x))\xi] \\ &= \int dx p(x) \delta[y - f(x)]. \end{aligned} \quad (7.28)$$

The probability density $p(y)$ is thus obtained by integrating $p(x)$ over all the values of x satisfying the constraint $y = f(x)$. The above relation may be made more explicit in terms of the roots x_i of the equation $y = f(x)$ as below.

$$\begin{aligned} p(y) &= \int dx \delta[y - f(x)]p(x) \\ &= \int dx \sum_i \frac{\delta(x - x_i)}{|f'(x_i)|} p(x) \\ &= \sum_i \frac{p(x_i)}{|f'(x_i)|}. \end{aligned} \quad (7.29)$$

Consider the transformation $y = (x - \langle x \rangle)/\sigma$. The probability density of y denoted by $P(y)$ is given by:

$$\begin{aligned} P(y) &= \int dx p(x) \delta[y - (x - \langle x \rangle)/\sigma] \\ &= \sigma p(y\sigma + \langle x \rangle). \end{aligned} \quad (7.30)$$

7.1.8 Gaussian or Normal distribution

The Gaussian random distribution is defined with a probability distribution function:

$$p(x) = \frac{1}{\sqrt{2\pi}\sigma} \exp[-(x - \langle x \rangle)^2/2\sigma^2]. \quad (7.31)$$

The characteristic function for the Gaussian distribution is:

$$\begin{aligned} C(\xi) &= \frac{1}{\sqrt{2\pi}} \int dx \exp[-(x - \langle x \rangle)^2/2\sigma^2 + i\xi x] \\ &= \exp(i\xi \langle x \rangle + \sigma^2 \xi^2/2). \end{aligned} \quad (7.32)$$

7.1.9 Central Limit Theorem

We have already seen that when random variables are added, their probability density function is a convolution of the respective probability distributions. The central limit theorem states that when a large number of independent random variables are added, the probability distribution of the sum tends to be a Gaussian distribution. As an illustration of this, we can consider multiple random variables each having a rectangle function distribution. The variables are thus equally likely to take values in the range $x : (-1/2, 1/2)$. Convolution of rect with itself produces a triangle function. Convolution of the triangle with another rect for a couple of more times gives the higher order box splines which start looking like a Gaussian distribution. The central limit theorem formalizes this result. For a brief proof of this result, suppose that x_1, x_2, \dots are statistically independent variables in a normal form (mean = 0 and sigma = 1 for each). We construct a variable y as:

$$y = \frac{1}{\sqrt{N}}(x_1 + x_2 + \dots + x_N). \quad (7.33)$$

The mean $\langle y \rangle = 0$ and the variance $\langle y^2 \rangle = 1$. For a random variable x_i in standard form, we can write the characteristic function $C(\omega)$ as a Taylor series around point $\omega = 0$ and using the relation in Eq. (7.25).

$$C(\omega) = 1 - \frac{\omega^2}{2} + O(\omega^3). \quad (7.34)$$

We note that this form is the same for all random variables x_i in normal form irrespective of the probability distribution. The characteristic function $C_y(\omega)$ is therefore given by:

$$C_y(\omega) = [1 - \frac{\omega^2}{2N} + O(\omega^3)]^N. \quad (7.35)$$

For large N we may neglect the terms of order ω^3 and higher to obtain:

$$C_y(\omega) = \lim_{N \rightarrow \infty} [1 - \frac{\omega^2}{2N}]^N = \exp(-\omega^2/2), \quad (7.36)$$

which is a Gaussian. The probability distribution $p(y)$ which is obtained by inverse Fourier transforming $C_y(\omega)$ is therefore also a

Gaussian distribution. The composition of N random variables in standard form for large N thus tends to a Gaussian distribution irrespective of the nature of individual probability distributions.

7.1.10 Gaussian moment theorem

This is a very important property of the Gaussian random variables and we will only state the result here. Suppose x_1, x_2, \dots, x_n are Gaussian random variables. Then their higher order correlations can be expressed in terms of pairwise correlations between them. The result is as follows:

$$\begin{aligned} & \langle \Delta x_1 \Delta x_2 \dots \Delta x_n \rangle \\ &= \sum_{\text{all pairs}} \langle \Delta x_{j_1} \Delta x_{j_2} \rangle \dots \langle \Delta x_{j_{n-1}} \Delta x_j \rangle \quad \text{for even } n, \\ &= 0 \quad \text{for odd } n. \end{aligned} \tag{7.37}$$

The moment theorem has a counterpart for complex valued Gaussian random variables with distribution function given by:

$$p(z) = \frac{1}{\pi\sigma} \exp(-|z|^2/\sigma^2). \tag{7.38}$$

The moment theorem may be stated for complex Gaussian variables $z_{i_1}, z_{i_2}, \dots, z_{i_M}, z_{j_1}, z_{j_2}, \dots, z_{j_N}$ as:

$$\begin{aligned} & \langle \Delta z_{i_1}^* \dots \Delta z_{i_M}^* \Delta z_{j_1} \dots \Delta z_{j_N} \rangle \\ &= \sum_{\text{all pairs}} \langle \Delta x_{i_1}^* \Delta x_{j_1} \rangle \dots \langle \Delta x_{i_M}^* \Delta x_{j_N} \rangle \quad \text{for } M = N, \\ &= 0 \quad \text{for } M \neq N. \end{aligned} \tag{7.39}$$

While we have not provided proof of this result, we mention here that these results may be obtained by differentiating the characteristic function corresponding to the joint probability distribution functions. The moment theorem will be found useful later in this book when intensity correlations (or fourth order field correlations) will be of interest.

7.2 Random Processes

Random process is a concept that builds on that of the random variables. We have been talking of countable variables x_1, x_2, \dots etc. Now suppose that we are thinking of a scalar component of electric field generated by a typical light source. The field is a non-deterministic function of the continuous parameter time and may be denoted as $x(t)$. The samples of $x(t)$ or the values it takes may form a particular probability distribution $p(x, t)$. So at a given time t the value of $x(t)$ may be drawn from the probability distribution. Note that if we integrate over x at any given time t ,

$$\int dx p(x, t) = 1. \quad (7.40)$$

The expectation of x at time t may be defined as:

$$\langle x(t) \rangle = \int dx p(x, t)x. \quad (7.41)$$

Another way of thinking about the mean is that there are a number of realizations of the process under consideration: $x^{(1)}(t), x^{(2)}(t), \dots, x^{(N)}(t), \dots$. The values of the various realizations at time t make the probability distribution $p(x, t)$. The mean or expected value may then be thought of as an average over the possible realizations.

$$\langle x(t) \rangle = \lim_{N \rightarrow \infty} \frac{1}{N} \sum_{r=1}^N x^{(r)}(t). \quad (7.42)$$

The different realizations make what is known as an ensemble and the average above is an ensemble average. The probability density $p(x, t)$ contains information about the possible values taken by x at any time t but has no information about the possible correlations between values of x at different times. That information is contained in joint probability $p(x_1, t_1, x_2, t_2)$ which is the probability density that x takes a value x_1 at t_1 and x_2 at t_2 . Such joint density has more information than $p(x, t)$. In fact by integrating the joint density over x_2 we get $p(x_1, t_1)$. The joint density may be used in particular to define the auto-correlation function or two-time correlation function:

$$\Gamma(t_1, t_2) = \langle x^*(t_1)x(t_2) \rangle. \quad (7.43)$$

The average $\langle \dots \rangle$ above is with respect to the joint density $p(x_1, t_1, x_2, t_2)$. In general the joint densities can be defined up to any order with n -order density having more information than $(n - 1)$ -order density. The exception to this rule is when we have Gaussian density function in which case only second order correlations are sufficient as per the Gaussian moment theorem in Eq. (7.37).

A random process is called stationary if there is no preferred origin for t implying that the statistical nature of the process remains same at all times. Any joint density thus remains same if T is added to all times. For example,

$$p(x_1, t_1, x_2, t_2) = p(x_1, t_1 + T, x_2, t_2 + T), \quad (7.44)$$

and similarly for higher order joint densities. Clearly if we choose $T = -t_1$, the correlation function is seen to be only a function of the time difference $(t_2 - t_1)$.

$$\Gamma(t_1, t_2) \equiv \Gamma(t_2 - t_1). \quad (7.45)$$

We observe that Γ is Hermitian symmetric with respect to $\tau = (t_2 - t_1)$:

$$\Gamma(\tau) = \Gamma^*(-\tau). \quad (7.46)$$

A random process is called stationary in strict sense if joint probability densities of all orders have the stationarity property. A random process is called wide sense stationary if the mean is independent of t and the correlation $\Gamma(t_1, t_2)$ is a function of $(t_2 - t_1)$.

7.2.1 Ergodic Process

A random process is called ergodic if its ensemble average coincides with the time average of one realization.

$$\langle z \rangle = \lim_{T \rightarrow \infty} \int_{-T/2}^{T/2} dt z^{(r)}(t). \quad (7.47)$$

For this to be possible, it is generally required that the correlation $\Gamma(\tau)$ dies out to zero fast for increasing τ . A single realization of the process may then be divided into multiple time intervals that are uncorrelated and may be considered as separate realizations of the process.

7.2.2 Properties of auto-correlation function

Some properties of the auto-correlation function are stated below:

1. $|\Gamma(0)| \geq 0$.
2. $|\Gamma(-\tau)| = |\Gamma^*(\tau)|$.
3. $|\Gamma(\tau)|$ is non-negative definite. For n complex numbers a_1, a_2, \dots, a_n and n real numbers t_1, \dots, t_n ,

$$\begin{aligned} & < \sum_{j=1}^n a_j x(t_j) |^2 > \geq 0 \text{ Or} \\ & \sum_j \sum_k a_j^* a_k R(t_j - t_k) \geq 0. \end{aligned} \quad (7.48)$$

7.2.3 Spectral Density: Wiener-Khintchine theorem

We have encountered the non-negative definiteness property earlier in case of the characteristic function associated with a probability density function. The Fourier transform of such functions is known to be non-negative (Bochner theorem). What is the non-negative quantity that is associated with the correlation function $\Gamma(\tau)$? It is the spectrum of the process - or the spectral density representing the energy density at a given frequency. The Wiener-Khintchine theorem relates the auto-correlation function of a random process with its spectrum. For a random process $z(t)$, we will denote its truncated Fourier transform by:

$$Z(\nu, T) = \int_{-T/2}^{T/2} dt z(t) \exp(-i2\pi\nu t). \quad (7.49)$$

The periodogram or the power density of a single realization may be defined as:

$$S_T(\nu) = \frac{|Z(\nu, T)|^2}{T}. \quad (7.50)$$

The expected value of the power spectral density of the random process is obtained by ensemble averaging the above quantity in the

limit $T \rightarrow \infty$.

$$\begin{aligned}
 S(\nu) &= \lim_{T \rightarrow \infty} \left\langle \frac{|Z(\nu, T)|^2}{T} \right\rangle \\
 &= \lim_{T \rightarrow \infty} \frac{1}{T} \int_{-T/2}^{T/2} \int_{-T/2}^{T/2} dt dt' \langle z^*(t) z(t') \rangle e^{i2\pi\nu(t-t')} \\
 &= \lim_{T \rightarrow \infty} \frac{1}{T} \int_{-\infty}^{\infty} \int_{-\infty}^{\infty} dt dt' \text{rect}\left(\frac{t}{T}\right) \text{rect}\left(\frac{t'}{T}\right) \Gamma(t - t') e^{i2\pi\nu(t-t')} \\
 &= \lim_{T \rightarrow \infty} \frac{1}{T} \int_{-\infty}^{\infty} d\tau \Lambda\left(\frac{\tau}{T}\right) \Gamma(\tau) e^{i2\pi\nu\tau} \\
 &= \int_{-\infty}^{\infty} d\tau \Gamma(\tau) e^{i2\pi\nu\tau}. \tag{7.51}
 \end{aligned}$$

In the above calculation $\Lambda(u)$ is the triangle function defined earlier in Eq. (2.78). The triangle function appears here as a correlation of two rect functions. We observe the important result that the spectral density $S(\nu)$ and the auto-correlation function $R(\tau)$ are related by a Fourier transform. This result is referred to as the Wiener-Khintchine theorem .

7.2.4 Orthogonal series representation of random processes

For a zero mean wide sense stationary random process $z(t)$ we may consider an expansion over $t : (-T/2, T/2)$ in terms of an orthonormal set $\{\psi_n(t)\}$.

$$z(t) = \sum_n c_n \psi_n(t), \tag{7.52}$$

with the expansion coefficients following a Kronecker-delta correlation:

$$\langle c_m^* c_n \rangle = \delta_{m,n}. \tag{7.53}$$

When such an expansion exists, we note that:

$$R(t_1 - t_2) = \sum_n \lambda_n \psi_n^*(t_1) \psi_n(t_2). \tag{7.54}$$

Further due to the orthonormality of the basis functions we have:

$$\int_{-T/2}^{T/2} dt_1 R(t_1 - t_2) \psi_n(t_1) = \lambda_n \psi_n(t_2). \tag{7.55}$$

We therefore see that the orthonormal basis functions are the eigenfunctions of the integral kernel given by the correlation function. This orthonormal expansion is referred to as the Kosambi-Karhunen-Loeve expansion .

7.2.5 Complex Representation of random processes

The quantities such as charges and currents that produce electromagnetic fields are real quantities but it is often required to represent the the electromagnetic fields as complex numbers. For a real random process $x(t)$ we denote the Fourier transform by:

$$X(\nu) = \int_{-\infty}^{\infty} dt x(t) \exp(i2\pi\nu t). \quad (7.56)$$

Since $x(t)$ is real, the transform satisfies the relation $X(-\nu) = X^*(\nu)$. The negative frequencies do not contain any additional information and we may suppress them to define a complex signal associated with the real process $x(t)$ as follows:

$$z(t) = \int_0^{\infty} d\nu X(\nu) \exp(-i2\pi\nu t). \quad (7.57)$$

We will express the above relation as:

$$\begin{aligned} z(t) &= \frac{1}{2} \int_{-\infty}^{\infty} d\nu X(\nu) \exp(-i2\pi\nu t) [1 + \text{sgn}(\nu)] \\ &= \frac{1}{2}[x(t) + iy(t)]. \end{aligned} \quad (7.58)$$

Where $y(t)$ is the Hilbert transform:

$$y(t) = \frac{1}{\pi} P \int_{-\infty}^{\infty} dt' \frac{x(t')}{t - t'}, \quad (7.59)$$

and P denotes the Cauchy principal value. The signal $x(t)$ has a similar representation in terms of $y(t)$.

$$x(t) = -\frac{1}{\pi} P \int_{-\infty}^{\infty} dt' \frac{y(t')}{t - t'}. \quad (7.60)$$

Such relations (or Hilbert transform pair) are often found in Physics in frequency domain and are known as dispersion relations. For example the real and imaginary parts of refractive index obey such relationship (Kramers-Kronig relation) due to causality of material response. In the above discussion this relation occurs in time domain since we have suppressed the negative frequencies in the signal. Finally we observe that:

$$\int dt x^2(t) = \int dy^2(t) = 2 \int dt |z(t)|^2. \quad (7.61)$$

and

$$\int dt x(t)y(t) = 0. \quad (7.62)$$

The concept of complex signal representation plays an important role in many branches of Physics and Electrical Engineering. The analytic signal representation was first introduced in this form by Dennis Gabor. In optics and particularly in this book we will often encounter narrowband fields such that the Fourier transform of the signal is effectively concentrated in a small frequency band $\Delta\nu$ centered on some carrier frequency ν_0 . We may typically express such signal as:

$$x(t) = A(t) \cos[2\pi\nu_0 t + \Phi(t)]. \quad (7.63)$$

The Hilbert transform of the above equation for slowly varying envelope gives:

$$y(t) = A(t) \sin[2\pi\nu_0 t + \Phi(t)] \quad (7.64)$$

If $z(t)$ is the corresponding complex signal, then denoting the Fourier transform of $z(t)$ by $Z(\nu)$, we have the following expression for the complex envelope:

$$z_0(t) = A(t) \exp[i\Phi(t)] = \int d\nu Z(\nu) \exp[i2\pi(\nu - \nu_0)]. \quad (7.65)$$

We see that in the definition of the complex envelope, we are using two functions $A(t)$ and $\Phi(t)$ to represent one function and as a result there could be infinite number of choices for how we define the complex envelope. Is there any unique choice that is in some sense optimal? There is a theorem in this regard by Mandel (1967).

7.2.6 Mandel's theorem on complex representation

Suppose that corresponding to a narrowband real stationary random process $x(t)$, we generate another process $y(t)$ by convolution of $x(t)$ with a filter function $k(t)$

$$y(t) = \int dt' k(t - t') x(t'), \quad (7.66)$$

and represent the corresponding complex signal as

$$z(t) = z_0(t) \exp(i2\pi\nu_0 t). \quad (7.67)$$

Here ν_0 may be considered as the carrier frequency of the narrowband process. A measure of fluctuation in the complex envelope may then be defined as follows:

$$\rho = \left\langle \left| \frac{dz_0(t)}{dt} \right|^2 \right\rangle. \quad (7.68)$$

It is the ensemble average of the absolute squared derivative of the complex envelope. The problem posed by Mandel is to find an appropriate filter $k(t)$ that minimizes this fluctuation. The solution to this problem is formulated as an optimization problem and the answer is that the filter $k(t)$ corresponds to the Hilbert transform. The sine and cosine representation is thus optimal in the sense that it produces signal with least fluctuation in the envelope or an envelope with least redundancy. Finally we note that the spectrum of the complex signal is given by:

$$S_z(\nu) = \frac{1}{4} |1 + \text{sgn}(\nu)|^2 S_r(\nu), \quad (7.69)$$

which vanishes for negative frequencies.

A two dimensional analogue to this theorem exists and has been studied in detail by the present author. The solution of the 2D problem is that the analogue of Hilbert transform in 1D is provided by the spiral phase transform. For an image signal $g_1(x, y)$ the quadrature signal as per this result is given by:

$$g_2(x, y) = \mathcal{F}^{-1}[\exp(i\phi) G_1(f_x, f_y)],$$

where ϕ is the polar angle in the 2D Fourier frequency plane and $G_1(f_x, f_y)$ denotes the 2D Fourier transform of the image $g_1(x, y)$. We will not discuss this topic here any further.

References and suggested reading

1. W. B. Davenport and W. I. Root, *An Introduction to the Theory of Random Signals and Noise*, Wiley-IEEE Press (1987).
2. L. Mandel and E. Wolf, *Coherence and Quantum Optics*, Cambridge Univ. Press (1995).
3. J. W. Goodman, *Statistical Optics*, Wiley-Interscience (2000).
4. A. M. Yaglom, *Correlation Theory of Stationary and Related Random Functions*, Springer-Verlag (1987).
5. B. R. Frieden, *Probability, Statistical Optics, and Data Testing: A Problem Solving Approach*, Springer-Verlag (1991).
6. D. Gabor, “Theory of communications”, J. Inst. Electr. Eng. vol. 93, pp. 429-457 (1946).
7. I. Reed, “On a moment theorem for complex Gaussian processes”, IRE Trans. Information Theory, vol. 8, pp. 194-195 (1962).
8. L. Mandel, “Complex representation of optical fields in coherence theory”, J. Opt. Soc. Am., vol. 57, pp. 613-617 (1967).
9. K. G. Larkin, D. J. Bone, M. A. Oldfield, “Natural demodulation of two-dimensional fringe patterns I: General background of the spiral phase quadrature transform”, J. Opt. Soc. Am. A, vol. 18, pp. 1862-1870 (2001).
10. K. Khare, “Complex signal representation, Mandel’s theorem and spiral phase quadrature transform”, Applied Optics, vol. 47(22), pp. E8-E12 (2008). (Special issue on phase space representations in Optics).

Part 2:

Concepts in Optics

8. Geometrical Optics Essentials

Geometrical optics is a ray based model for describing propagation of light in small wavelength limit. While geometrical optics involves several topics in optical modelling and system design problems that demand detailed discussion, we will introduce a few basic notions as a useful reference when studying imaging systems later in this book.

The basic guideline for tracing rays through an optical system is the Fermat's principle which states that the optical path length along a ray between two fixed points is an extremum (minimum or maximum) when compared to the neighboring paths. The optical path length along a ray joining the two points P_1 and P_2 is given by:

$$S = \int_{P_1}^{P_2} ds n(x, y, z), \quad (8.1)$$

where $n(x, y, z)$ is the refractive index of the medium at the location (x, y, z) along the elemental pathlength ds . For a given distribution of the refractive index the ray path is derived such that the first variation δS of the integral above vanishes. The basic laws such as reflection and refraction governing ray propagation may be obtained using this principle. The ray path in this formalism is obtained by solving the corresponding Euler-Lagrange equation.

8.1 Ray transfer matrix

The first order transfer matrix (or ABCD matrix) formalism aims at connecting the position and direction of a light ray between two

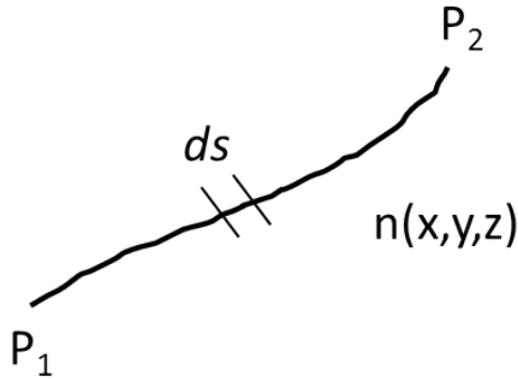


Figure 8.1: The path taken by a light ray through an inhomogeneous medium a described by a position dependent refractive index. The optical path length is an integral of nds .

planes connected by free space or by an optical system, e.g. an imaging system (see Fig. 8.2). The relation between the output and input parameters of the ray is typically expressed as the ABCD matrix. This representation is an approximation that is typically valid for para-axial rays.

$$\begin{pmatrix} \vec{r}' \\ n'\vec{u}' \end{pmatrix} = \begin{pmatrix} A & B \\ C & D \end{pmatrix} \begin{pmatrix} \vec{r} \\ n\vec{u} \end{pmatrix} \quad (8.2)$$

The vectors denoting the position of intersection of a ray \vec{r} at a plane and its direction have two components and thus the ABCD matrix must contain 16 numbers in general. However for optical systems that are symmetric about the yz plane, it can be shown that only two numbers - the coordinate along y -axis and the corresponding direction cosine are relevant. The ABCD matrix for a 2D rotationally symmetric system thus consists of only 4 numbers. This representation of the ray transfer matrix is often referred to as the first order approximation as the matrix elements A, B, C, D may be considered as resulting from first order Taylor series expansion about the axial

ray.

$$\begin{aligned} A &= \frac{\partial y'}{\partial y} \Big|_{y=0, nu_y=0}, \quad B = \frac{\partial y'}{\partial (nu_y)} \Big|_{y=0, nu_y=0}, \\ C &= \frac{\partial (n' u_{y'})}{\partial y} \Big|_{y=0, nu_y=0}, \quad D = \frac{\partial (n' u_{y'})}{\partial (nu_y)} \Big|_{y=0, nu_y=0}. \end{aligned} \quad (8.3)$$

Using the definitions of the matrix elements A, B, C, D as in Eq.

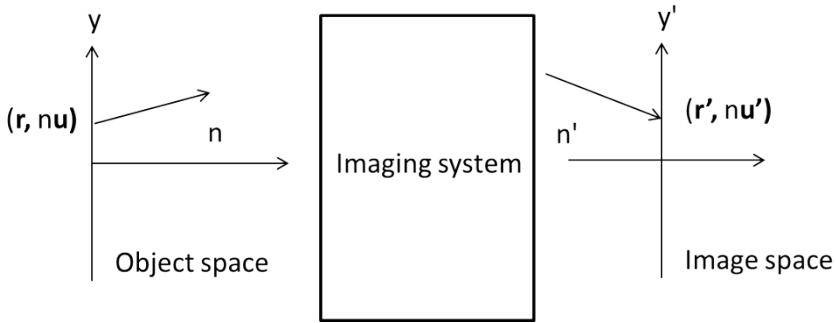


Figure 8.2: The transfer matrix formalism connects the position and direction vectors corresponding to a ray between two planes connected by free space or by an optical system.

(8.3) we observe that the transfer matrices for simple cases of propagation through homogeneous medium and bending of rays at a spherical surface of radius R may be described by the following matrices. For Homogeneous medium, the transfer matrix is given by:

$$T = \begin{pmatrix} 1 & d/n \\ 0 & 1 \end{pmatrix}, \quad (8.4)$$

Here d is the distance of propagation along z -axis and n is the index of the medium. For a curved spherical surface,

$$T = \begin{pmatrix} 1 & 0 \\ -\frac{\Delta n}{R} & 1 \end{pmatrix}. \quad (8.5)$$

Here $\Delta n = (n' - n)$ is the difference between the refractive index of the media on the two sides of the spherical surface. In the convention

where propagation direction is from left to right, the radius R of curvature is assigned a positive sign if the center of curvature is to the right of the surface. For a thin lens in free space, with curvatures of two surfaces equal to R_1 and R_2 we therefore have a transfer matrix that is a product of two matrices corresponding to curved surfaces:

$$T = \begin{pmatrix} 1 & 0 \\ -(n-1)\left(\frac{1}{R_1} - \frac{1}{R_2}\right) & 1 \end{pmatrix}. \quad (8.6)$$

The transfer matrix formalism is suitable to describe the behaviour of a light ray as it passes through a cascade of systems. For example, if the transfer matrices T_1 and T_2 represent the ABCD matrices between planes I - II and planes II-III respectively, then the transfer matrix between planes I-III is given by the matrix product $T_1 T_2$. This simple idea can be used to describe ray propagation through complex optical systems. In principle the transfer matrix formalism has a close link to the Fourier optics description where a plane wave Fourier component is associated in the ray direction ($n\vec{u}$) with an appropriate weight.

8.2 Stops and pupils

The aperture stop is a physical aperture that limits the size of the cone of rays originating from an axial object point that pass through an optical system. We will consider two subsystems S_1 and S_2 as shown in Fig. 8.3. The image of an aperture stop formed in subsys-

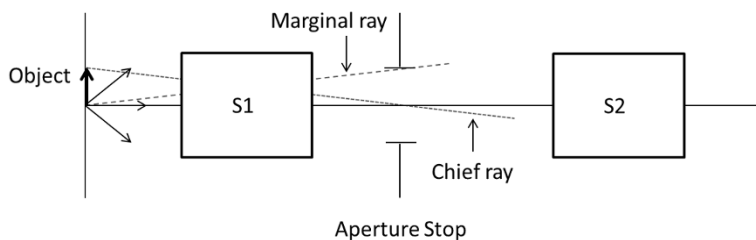


Figure 8.3: Schematic diagram illustrating the idea of an aperture stop. Also shown are the chief ray and the marginal ray.

tem S_1 in object space is referred to as the entrance pupil while the image of the aperture stop formed by the subsystem S_2 in the image space is known as the exit pupil. The distance between the exit pupil and the image plane is an important parameter as it decides the spatial frequency scaling as we will see later when studying Fourier optical analysis of optical systems. The angular range of the cone of rays allowed by the aperture stop also decides the diffraction limited resolution of the system. In tracing rays for understanding image formation, typically two rays are considered to be of utmost importance. The *marginal ray* originates from the axial object point and passes through the edge of the aperture stop, while the *chief ray* originates from the edge of the object and passes through the axial point of the aperture stop. The two parameter column vectors $\begin{pmatrix} y \\ nu \end{pmatrix}$ corresponding to the marginal and chief rays are linearly independent and any other ray passing through the system can be thought as a linear combination of these two rays up to the first order approximation that is used here.

The treatment of geometrical optics as presented here is very brief and is just supposed to provide some reference material to common terms that will be used later. The interested reader may refer to standard detailed texts on this subject. Ray-tracing through complex optical assemblies is an important technical problem relevant to optics industry and several dedicated software packages are now used for this purpose by optical designers.

References and suggested reading

1. M. Born and E. Wolf, *Principles of Optics: Electromagnetic Theory of Propagation, Interference and Diffraction of Light*, (Ed. 7) Cambridge Univ. Press (1999).
2. W. Smith, *Modern Optical Engineering*, SPIE Press (2007).

9. Wave equation and introduction to diffraction of light

9.1 Introduction

In the first part of this book we studied Fourier transform theory, generalized functions, linear systems formalism, sampling theorem, the important idea of degrees of freedom or space bandwidth product and provided introduction to inverse problem in imaging . We are now ready to apply these ideas to problems in Optics. In the previous chapter we briefly discussed some important ideas in geometrical optics or the ray picture of light. For example, you know that a parallel set of rays are focused at the back-focal plane of a lens. Is the physical focus truly a point? How well does geometrical optics work? For answering this type of questions, we need to treat light as a wave phenomenon. Diffraction of light is the fundamental problem of interest here. What is diffraction ? Diffraction refers to any bending or spreading of light waves that cannot be attributed to reflection or refraction at a boundary between two materials. Why do waves diffract ? They do so due to confinement in transverse direction and the spread of the waves may therefore be associated with a form of the uncertainty relation. Another viewpoint that is important as we study imaging and other allied topics is what we have already mentioned in the introductory chapter. When light waves interact with obstacles or objects of interest, the scattered waves carry information about the object with them. When designing any imaging system that is usually at some distance from the object to be imaged,

we should have a model for describing the waves that reach our system. As we shall see in this and the next chapter, diffraction theory provides a rigorous way to understand how information about features of different length scales (relative to illumination wavelength) in the object of interest is propagated to the imaging system. In the context of computational imaging systems diffraction formalism provides a guideline for design of appropriate imaging hardware and image reconstruction algorithms.

Historically the earliest known record of observation of diffraction phenomenon is found in Grimaldi's experiments published in 1665. He observed that transition of intensity from bright to dark at the edge of a shadow region is not sharp but gradual. This observation was contradictory to the corpuscular theory of light which suggested propagation of light in a straight line. Huygens in 1698 proposed a picture for propagation of light waves. He put forth the idea of what we now call the wavefront. In this picture, every point on the wavefront is a secondary source of spherical waves. The envelope of a collection of spherical wavefronts gives the corresponding wavefront at a future time. This qualitative intuitive picture is useful but it does not allow us to actually calculate how waves diffract when they encounter obstacles. This wave picture of light was not worked on for almost 100 years when in 1804 Thomas Young performed the two-slit experiment to put forth the idea of interference of light waves. The credit of developing a first quantitative picture for diffraction goes to Fresnel. In his 1818 paper presented to French academy of sciences, he combined Young's idea of interference and the Huygen's picture of secondary waves to present a theory for diffraction. The wave theory of light was still suspect at this point of time. Poisson who was heading the committee that examined the submitted papers ridiculed Fresnel's idea. He showed that if Fresnel's theory was true then an opaque circular disc obstacle should have a bright point on axis. F. Arago who was a committee member at the academy went to the laboratory and performed this experiment to observe the bright spot! The experimental observation confirmed Fresnel's theory and also to a large extent the wave nature of light. Without going further into interesting historical details we will begin our analysis of the diffraction phenomena with a review of Maxwell equations.

9.2 Review of Maxwell equations

We will start by writing the Maxwell equations that govern the behaviour of \vec{E} and \vec{B} fields in terms of total charges and currents. The four equations in the MKS system take the form:

$$\begin{aligned}\nabla \times \vec{E} &= -\frac{\partial \vec{B}}{\partial t}, \\ \nabla \times \vec{B} &= \mu_0 \vec{J} + \mu_0 \epsilon_0 \frac{\partial \vec{E}}{\partial t}, \\ \nabla \cdot \vec{E} &= \frac{\rho}{\epsilon_0}, \\ \nabla \cdot \vec{B} &= 0.\end{aligned}\tag{9.1}$$

Along with the continuity relation:

$$\nabla \cdot \vec{J} + \frac{\partial \rho}{\partial t} = 0,\tag{9.2}$$

and suitable boundary conditions one may, at least in principle, solve any problem involving electromagnetic fields. We will consider the case of EM fields in region of space where there are no charges and currents thus reducing the Maxwell equations to a simpler form:

$$\begin{aligned}\nabla \times \vec{E} &= -\frac{\partial \vec{B}}{\partial t}, \\ \nabla \times \vec{B} &= \mu_0 \epsilon_0 \frac{\partial \vec{E}}{\partial t}, \\ \nabla \cdot \vec{E} &= 0, \\ \nabla \cdot \vec{B} &= 0.\end{aligned}\tag{9.3}$$

Since we are interested in understanding how \vec{E} or \vec{B} fields behave as they propagate in free space, we will now proceed to obtain the wave equation. Taking the curl of the first equation gives:

$$\nabla(\nabla \cdot \vec{E}) - \nabla^2 \vec{E} = -\frac{\partial(\nabla \times \vec{B})}{\partial t},\tag{9.4}$$

and further substitution of the curl \vec{B} equation gives the wave equation:

$$\nabla^2 \vec{E} = \frac{1}{c^2} \frac{\partial^2 \vec{E}}{\partial t^2}. \quad (9.5)$$

Here we have used the relation $c = 1/\sqrt{\epsilon_0 \mu_0}$ to denote the speed of light in vacuum. The magnetic field obeys the same wave equation as you probably already know very well.

Any time dependence of the \vec{E} field may be modeled by Fourier decomposition and it is therefore customary to analyze the wave equation by a monochromatic or steady state representation. In this approach the time dependence of the solution at each frequency is purely periodic. We will represent the fields with the $\exp(-i2\pi\nu t)$ representation as:

$$\vec{E}(\vec{r}, t) = \text{Re}\{\vec{E}_\nu(\vec{r}) \exp(-i2\pi\nu t)\}. \quad (9.6)$$

In this representation, the wave equation for the space-part \vec{E}_ν at the frequency ν takes the form:

$$(\nabla^2 + k^2) \vec{E}_\nu(\vec{r}) = 0, \quad (9.7)$$

which is known as the homogeneous (source-free) Helmholtz equation and k stands for the magnitude of the wave vector $k = (2\pi\nu)/c$. The scalar diffraction theory that we will study first, deals with the single component of the \vec{E}_ν field, in effect, disregarding the coupling of other field components through Maxwell equations. Our initial treatment of the diffraction problem with only one scalar component will require us to first study the integral theorem of Helmholtz and Kirchhoff (1882). We will denote the scalar field by the symbol $U(\vec{r})$ and ignore the polarization of light in this treatment.

9.3 Integral theorem of Helmholtz and Kirchhoff

The integral theorem of Helmholtz and Kirchhoff aims at expressing the value of the scalar field at a point in volume V as an integral of the value of the field or its derivative on the surface S that bounds the volume. The starting point for arriving at this important result is

another theorem in vector calculus, viz., the Green's theorem. Suppose that $U(\vec{r})$ and $G(\vec{r})$ are two functions that are continuous with continuous first and second order partial derivatives within volume V and on the bounding surface S. Then we have the following identities:

$$\begin{aligned}\nabla \cdot (U \nabla G) &= (\nabla U) \cdot (\nabla G) + U \nabla^2 G, \\ \nabla \cdot (G \nabla U) &= (\nabla G) \cdot (\nabla U) + G \nabla^2 U.\end{aligned}\quad (9.8)$$

Subtracting the two relations above and applying the Gauss divergence theorem gives:

$$\int_V dV (U \nabla^2 G - G \nabla^2 U) = \int_S dS \hat{n} \cdot (U \nabla G - G \nabla U). \quad (9.9)$$

Here \hat{n} denotes an outward normal at the surface S. This is known as the Green's theorem . It is not necessarily very obvious how to proceed from here. The appearance of the ∇^2 operator on the left hand side and also in the Helmholtz equation (9.7) provides a hint. We know that the scalar field U we are seeking satisfies the Helmholtz equation. Now suppose we make a judicious choice such that G satisfies the Helmholtz equation in the volume V as well. It is now easy to see that under this assumption, the left hand side of the Green's theorem vanishes and we are left with:

$$\int_S dS \hat{n} \cdot (U \nabla G - G \nabla U) = 0. \quad (9.10)$$

This relation may be treated as a starting point for the Kirchhoff and Rayleigh-Sommerfeld diffraction theories. The choice made by Kirchhoff for G is the Green's function corresponding to the Helmholtz equation. The Green's function is a solution of the problem:

$$(\nabla^2 + k^2)G(\vec{r}) = -\delta(\vec{r}). \quad (9.11)$$

For $r \neq 0$ the relation can be easily verified by substitution $G(\vec{r}) = A \frac{\exp(ikr)}{r}$. To find the value of the constant A we have to integrate both sides of the equation (9.11) over a small sphere of radius ϵ that we make zero in a limiting process. The integration over the delta

function gives 1. The integration of the k^2 term vanishes since

$$\begin{aligned} \int_0^\epsilon 4\pi r^2 dr \frac{\exp(ikr)}{r} &= 4\pi \left[r \frac{\exp(ikr)}{ik} \right]_0^\epsilon - \int_0^\epsilon dr \exp(ikr) \\ &= 0 \quad \text{in the limit } \epsilon \rightarrow 0. \end{aligned} \quad (9.12)$$

The ∇^2 term may be integrated using Gauss divergence theorem.

$$\begin{aligned} \int dv \nabla^2 \left(\frac{\exp(ikr)}{r} \right) &= \lim_{\epsilon \rightarrow 0} 4\pi \epsilon^2 \frac{\partial}{\partial r} \left. \frac{\exp(ikr)}{r} \right|_{r=\epsilon} \\ &= \lim_{\epsilon \rightarrow 0} 4\pi [\epsilon ik \exp(ikr) - \exp(ik\epsilon)] = -4\pi. \end{aligned} \quad (9.13)$$

The constant A is thus equal to $-1/(4\pi)$.

Suppose we are interested in the value of the field at some point P_0 as shown in Fig. 9.1. At any point \vec{r}_1 in volume V , G is selected as:

$$G = \frac{\exp(ikr_{01})}{r_{01}} \quad \text{where } r_{01} = |\vec{r}_0 - \vec{r}_1|, \quad (9.14)$$

which is a spherical wave centered on P_0 . This choice of G satisfies the Helmholtz equation everywhere in volume V except at P_0 . We can exclude the point P_0 by forming a sphere of radius ϵ around it which we omit from the region of interest. Remember that the outward normal for this small spherical region points towards the point P_0 as seen in Fig. 9.1. Going back to equation (9.10) we now have:

$$\int_{S+S_\epsilon} dS \hat{n} \cdot [U \nabla \left(\frac{\exp(ikr_{01})}{r_{01}} \right) - \left(\frac{\exp(ikr_{01})}{r_{01}} \right) \nabla U] = 0. \quad (9.15)$$

The integral over the small sphere S_ϵ may be evaluated as follows. The unit normal is directed radially inward $\hat{n} = -\hat{r}$ so that only the radial derivative in the gradient operation is of interest. In the limit $\epsilon \rightarrow 0$ we have:

$$\begin{aligned} &\int_{S_\epsilon} dS \hat{n} \cdot (U \nabla G - G \nabla U) \\ &= \lim_{\epsilon \rightarrow 0} 4\pi \epsilon^2 \left[U \frac{(1 - ik\epsilon) \exp(ik\epsilon)}{\epsilon^2} - \frac{\exp(ik\epsilon)}{\epsilon} (-1) \left(\frac{\partial U}{\partial r} \right)_{r=\epsilon} \right] \\ &= 4\pi U(P_0). \end{aligned} \quad (9.16)$$

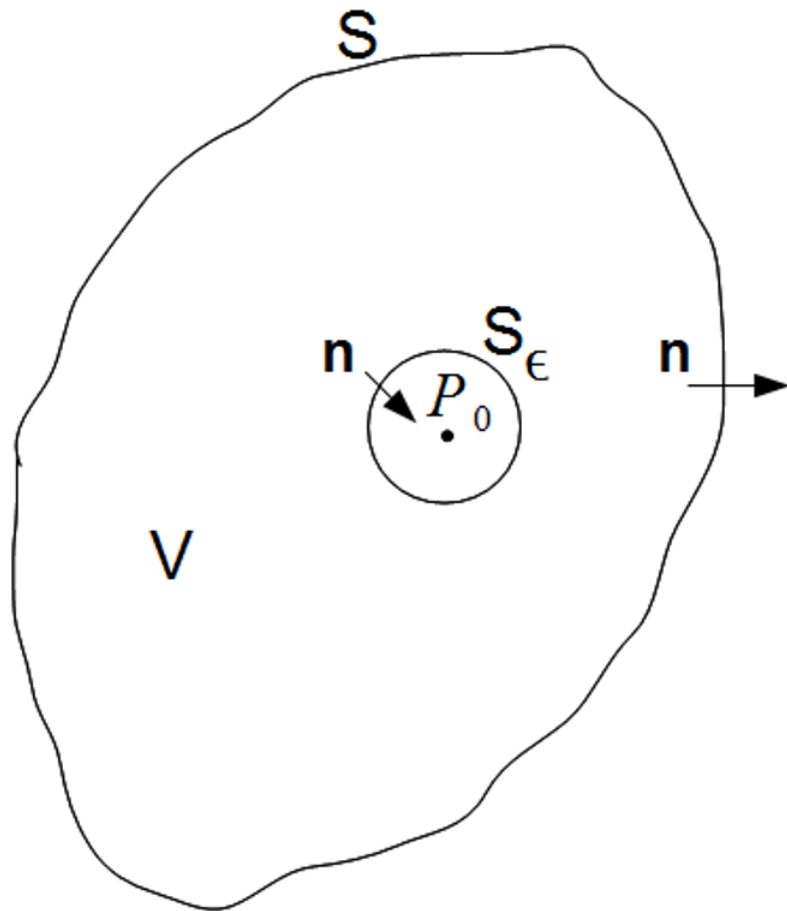


Figure 9.1: Integral theorem of Helmholtz and Kirchhoff: The scalar field at point P_0 in volume V is expressed in terms of the field and its normal derivative on the closed surface S that encloses the volume V .

The second term in the integral is zero since the derivative of U is assumed to be continuous at P_0 and is therefore finite, making the term zero in the limit. We may now write the integral theorem of

Helmholtz and Krichhoff as:

$$U(P_0) = \frac{1}{4\pi} \int_S dS \hat{n} \cdot \left[\frac{\exp(ikr_{01})}{r_{01}} \nabla U - U \nabla \left(\frac{\exp(ikr_{01})}{r_{01}} \right) \right]. \quad (9.17)$$

We observe that this relation is exact for scalar fields and allows us to express diffraction field at a point in terms of the boundary values of the field on some closed surface. What are these boundary values and how do we relate this to diffraction from apertures? We have to make some assumptions for this purpose. The approximations may not always hold but as long as we understand (and verify experimentally) when they give us reasonably accurate results, these approximations are perfectly justified.

9.4 Diffraction from a planar screen

We now apply the integral theorem of Helmholtz and Kirchhoff to the important problem of diffraction from a thin planar perfectly conducting screen. The choice of closed surface is shown in Fig. 9.2. It is composed of two surfaces S_1 and S_2 . The surface S_1 is just to the right of the plane $z = 0$ where the planar screen with an aperture is located. The surface S_2 is a spherical surface of radius R centered on P_0 . If the radius R of the spherical surface is made very large ($R \rightarrow \infty$), we hope to have vanishing contribution from the spherical surface S_2 . Appropriately selecting the boundary condition for the field on the surface S_1 will then provide us a formula for the field at P_0 .

The integral over the large spherical surface S_2 needs some more attention. From the integral theorem in Eq. (9.17) we see that for large R , the integral over S_2 takes the form:

$$\int_{S_2} G \left[\frac{\partial U}{\partial R} - (ik - \frac{1}{R})U \right] R^2 d\Omega, \quad (9.18)$$

where $d\Omega$ stands for the element of solid angle. The function G falls off as $1/R$ and the solution U of any radiation problem is also expected to fall off as $1/R$. The last term $(1/R)U$ in the square brackets already integrates to zero as R is made large. As a result

the integral over S_2 can uniformly vanish for all angles only if the solution U satisfies the following condition:

$$\lim_{R \rightarrow \infty} R \left(\frac{\partial U}{\partial R} - ikU \right) = 0. \quad (9.19)$$

This condition was first introduced by Sommerfeld in 1912 for a general class of exterior boundary value problems and is commonly referred to as the Sommerfeld radiation condition.

9.4.1 Kirchhoff Solution

The Kirchhoff solution refers to a particular choice for U and its normal derivative on the surface S_1 . The surface S_1 is divided in two parts - one consisting of the aperture S_A and its complement. The Kirchhoff solution makes the simplifying assumption that inside the aperture S_A , the field U and its normal derivative $\hat{n} \cdot \nabla U$ have the same value as that for the incident field. Further both the field and the normal derivative are identically zero on the part of S_1 outside the aperture. With this boundary condition and the vanishing of the surface integral over S_2 due to Sommerfeld radiation condition, the resultant Kirchhoff formula for field at point P_0 may be written as:

$$U(P_0) = \frac{1}{4\pi} \int_{S_A} dS \hat{n} \cdot \left[\frac{\exp(ikr_{01})}{r_{01}} \nabla U_i - U_i \nabla \left(\frac{\exp(ikr_{01})}{r_{01}} \right) \right], \quad (9.20)$$

where U_i stands for the incident field from left half space. It is clear from the simplifying assumption that the Kirchhoff's assumption will hold approximately only for apertures that are much larger than wavelength λ of illumination. Further no well-behaved function U can have both its numerical value as well as its normal derivative identically equal to zero over a region of a plane, e.g. the complement of aperture S_A as per the Kirchhoff boundary condition. These inconsistencies are resolved using an alternate form of Green's function as we shall see in the next section.

9.4.2 Rayleigh-Sommerfeld Solution

In order to avoid the difficulties posed by the Kirchhoff boundary conditions, Sommerfeld suggested two alternate choices for the Green's

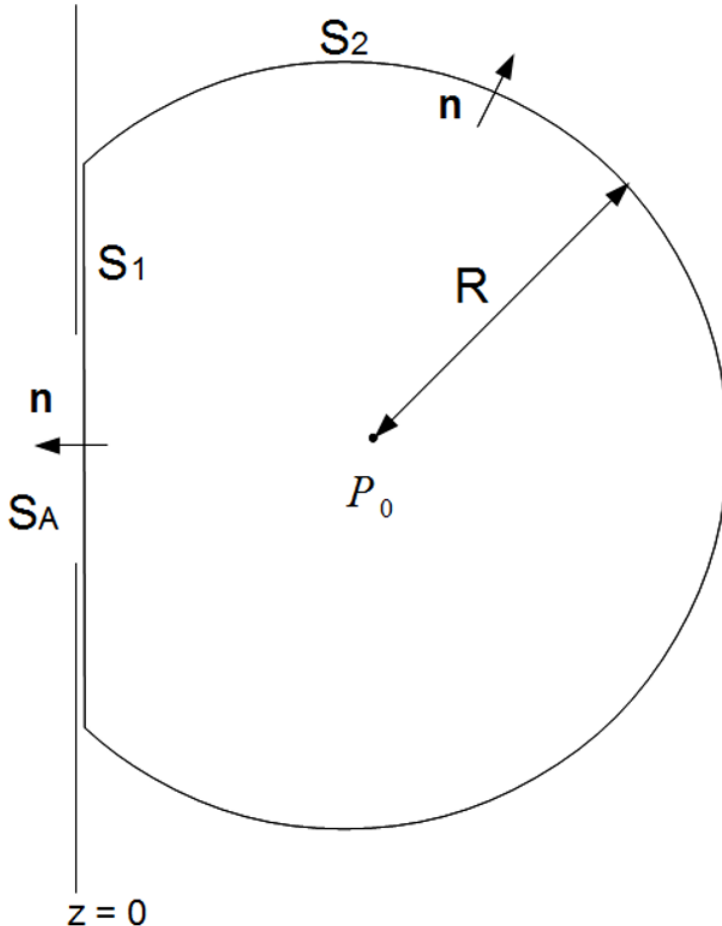


Figure 9.2: Diffraction from a planar screen: choice of closed surface composed of S_1 and S_2 .

function. Referring to Fig. 9.3, we define an image point P_1 that corresponds to a mirror reflection of the point P_0 in the plane $z = 0$. The two possible Green's functions are:

$$G_{\pm} = \frac{\exp(ikr_{0A})}{r_{0A}} \pm \frac{\exp(ikr_{1A})}{r_{1A}}. \quad (9.21)$$

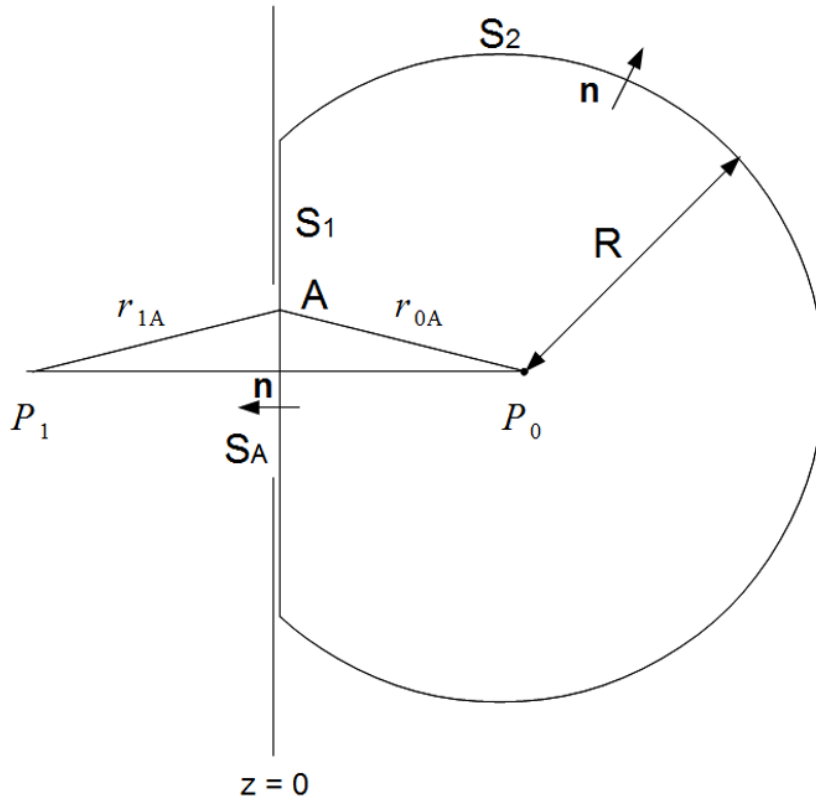


Figure 9.3: Rayleigh-Sommerfeld theory: choice of Green's function using image point P_1 .

The distances r_{0A} and r_{1A} are as shown in Fig. 9.3. We note that the second term added to the Green's function is also a solution of the Helmholtz equation and is well-behaved in the right half space ($z > 0$). As a result, following our derivation of the integral theorem of Helmholtz and Kirchhoff, we observe that this additional term does not contribute to the integral over surface S_ϵ enclosing the point P_0 in the limit $\epsilon \rightarrow 0$. We can therefore use the relation in Eq. (9.17) directly for the modified Green's functions above. The normal derivative used at the surface S_1 is along $-\hat{z}$ direction. For the choice G_- we have $G_- = 0$ and the normal deriva-

tive $\hat{n} \cdot \nabla G_- = 2\hat{n} \cdot \nabla G$ on the plane $z = 0$, with G being the Green's function used in the Kirchhoff theory. The resultant solution is known as the first Raleigh-Sommerfeld solution.

$$U_{RS1}(P_0) = -\frac{1}{2\pi} \int_{S_1} dS \hat{n} \cdot \left[U \nabla \left(\frac{\exp(ikr_{0A})}{r_{0A}} \right) \right]. \quad (9.22)$$

For the choice G_+ we have $G_+ = 2G$ and the normal derivative $\hat{n} \cdot \nabla G_+ = 0$ on the plane $z = 0$, with G being the Green's function used in the Kirchhoff theory. The resultant solution is known as the second Raleigh-Sommerfeld solution.

$$U_{RS2}(P_0) = \frac{1}{2\pi} \int_{S_1} dS \hat{n} \cdot \left[\frac{\exp(ikr_{0A})}{r_{0A}} \nabla U \right]. \quad (9.23)$$

For aperture dimension much larger than the wavelength of illumination one may now make an approximation that either the field or its normal derivative vanish on surface S_1 outside the aperture S_A without the mathematical inconsistency problem in Kirchhoff theory. An interesting point to note is that the Kirchhoff solution is actually nothing but an average of the two Raleigh-Sommerfeld solutions . In the next couple of chapters we will arrive at the first Raleigh-Sommerfeld solution using the angular spectrum method and further explain the Fresnel and Fraunhoffer approximations that are commonly used to describe the diffraction phenomena.

References and suggested reading

1. M. Born and E. Wolf, *Principles of Optics: Electromagnetic Theory of Propagation, Interference and Diffraction of Light*, (Ed. 7) Cambridge Univ. Press (1999).
2. B. B. Baker and E. T. Copson, *The Mathematical Theory of Huygens' Principle*, AMS Chelsea Press (2000).
3. A. Sommerfeld, *Optics (Lectures on Theoretical Physics)*, Academic Press (1954).
4. J. W. Goodman, *Introduction to Fourier Optics*, (Ed. 2), McGraw-Hill (1996).

10. The angular spectrum method

10.1 Angular spectrum method

With the historical introduction to diffraction problem and discussion of the Kirchhoff model and the Rayleigh-Sommerfeld model, we will now introduce an interesting approach to the diffraction problem that is more consistent with the linear systems theory and obtain the corresponding transfer function in spatial frequency space. We will also show that the solution thus obtained is the same as the first Rayleigh-Sommerfeld solution that we discussed in the last chapter. The present approach is called as the angular spectrum method for description of the diffraction problem.

Once again we will start with the Helmholtz equation for a transverse component of the E-field, say, E_x :

$$(\nabla^2 + k^2) E_x(x, y, z) = 0. \quad (10.1)$$

Our aim here is to determine the field $E_x(x, y, z)$ as a function of $E_x(x, y, 0)$. We begin by expressing E_x as a two-dimensional Fourier transform in the x and y co-ordinates. The z co-ordinate is treated as special as this is the direction in which we want to find the propagated fields. The 2D Fourier representation of the field component E_x is given by:

$$E_x(x, y, z) = \int \int df_x df_y \tilde{E}_x(f_x, f_y; z) \exp[i2\pi(f_x x + f_y y)]. \quad (10.2)$$

Applying the Helmholtz operator and equating the integrand in the resultant Fourier expansion to zero (since the integral is identically

zero for all x and y) gives us a differential equation for \tilde{E}_x in variable z :

$$\frac{d^2}{dz^2} \tilde{E}_x(f_x, f_y; z) = -[k^2 - 4\pi^2(f_x^2 + f_y^2)] \tilde{E}_x(f_x, f_y; z). \quad (10.3)$$

Denoting $\alpha = \sqrt{k^2 - 4\pi^2(f_x^2 + f_y^2)}$ we can write the solution of this equation as:

$$\tilde{E}_x(f_x, f_y; z) = A(f_x, f_y) \exp(i\alpha z) + B(f_x, f_y) \exp(-i\alpha z). \quad (10.4)$$

We now need to make a careful choice of the functions $A(f_x, f_y)$ and $B(f_x, f_y)$ to satisfy the boundary conditions of the problem at hand. First of all we note that the Fourier spectrum of the field in $z = 0$ plane is given by:

$$\tilde{E}_x(f_x, f_y; 0) = A(f_x, f_y) + B(f_x, f_y). \quad (10.5)$$

It is important to note the behaviour of α as we move away from origin in the (f_x, f_y) plane. We note that α is a real number for $k^2 \geq 4\pi^2(f_x^2 + f_y^2)$ and we will choose to take the positive value of the square root. However, α becomes imaginary when $k^2 < 4\pi^2(f_x^2 + f_y^2)$. We will use the following convention:

$$\begin{aligned} \alpha &= +\sqrt{k^2 - 4\pi^2(f_x^2 + f_y^2)}, & k^2 \geq 4\pi^2(f_x^2 + f_y^2) \\ &= i\sqrt{4\pi^2(f_x^2 + f_y^2) - k^2}, & k^2 < 4\pi^2(f_x^2 + f_y^2) \end{aligned} \quad (10.6)$$

Note that we now have an explicit connection between the wavelength (since $k = 2\pi/\lambda$) and the spatial frequencies f_x and f_y . This connection will be useful for us throughout this course when we study diffraction and imaging problems. We notice that when $k^2 < 4\pi^2(f_x^2 + f_y^2)$ or for spatial frequencies greater than $1/\lambda$, the A term decays exponentially whereas the B term increases exponentially as we go in the positive z direction. To have a physically meaningful solution as $z \rightarrow \infty$, we must set $B(f_x, f_y) = 0$. Notice that the B term corresponds to an incoming wave solution. Since we are interested in the outward propagating solutions, this condition

on $B(f_x, f_y)$ is in some sense equivalent to the Sommerfeld radiation condition. This choice of $B(f_x, f_y)$ along with Eq. (10.5) gives $A(f_x, f_y) = \tilde{E}_x(f_x, f_y; 0)$ and we have for the propagation problem:

$$\tilde{E}_x(f_x, f_y; z > 0) = \tilde{E}_x(f_x, f_y; 0) \exp(i\alpha z). \quad (10.7)$$

The inverse Fourier transform of the term $\exp(i\alpha z)$ is now needed for obtaining the field $E_x(x, y, z)$ in terms of $E_x(x, y, 0)$. In order to evaluate the inverse transform we observe that:

$$\begin{aligned} & \int_{-\infty}^{\infty} \int_{-\infty}^{\infty} df_x df_y \exp(i\alpha z) \exp[i2\pi(f_x x + f_y y)] \\ &= -\frac{\partial}{\partial z} \left\{ \int_{-\infty}^{\infty} \int_{-\infty}^{\infty} df_x df_y \frac{i}{\alpha} \exp(i\alpha z) \exp[i2\pi(f_x x + f_y y)] \right\}. \end{aligned} \quad (10.8)$$

We note that the quantity included in the curly brackets above is nothing but the Weyl representation for a spherical wave. We may therefore write:

$$\mathcal{F}^{-1}\{\exp(i\alpha z)\} = \frac{\exp(ikr)}{2\pi r} \left(-ik + \frac{1}{r}\right) \frac{z}{r}, \quad (10.9)$$

with $r = \sqrt{x^2 + y^2 + z^2}$. The inversion of Eq. (10.7) may now be represented as a convolution integral given by:

$$E_x(x, y, z) = \int \int dx' dy' E_x(x', y', 0) \frac{\exp(ikR)}{2\pi R} \left(-ik + \frac{1}{R}\right) \frac{z}{R}, \quad (10.10)$$

where the distance R is defined as:

$$R = \sqrt{(x - x')^2 + (y - y')^2 + (z - 0)^2}.$$

This relation is in fact the same as the first Rayleigh-Sommerfeld solution that we discussed in the last chapter and may also be written in terms of a partial derivative with respect to the z coordinate as:

$$E_x(x, y, z) = -\frac{\partial}{\partial z} \int \int dx' dy' E_x(x', y', 0) \frac{\exp(ikR)}{2\pi R}. \quad (10.11)$$

We could have solved the identical problem in a co-ordinate system rotated 90 degrees with respect to the z axis and so we get a similar relation for the y -component of the field.

$$E_y(x, y, z) = -\frac{\partial}{\partial z} \int \int dx' dy' E_y(x', y', 0) \frac{\exp(ikR)}{2\pi R}. \quad (10.12)$$

Notice that the diffraction fields also have a z -component that may be obtained easily by observing that both E_x and E_y in Eq.s (10.11) and (10.12) are represented in terms of partial derivatives with respect to z . Further using the coupling of E_z component to the x and y components through the relation $\nabla \cdot \vec{E} = 0$ in the right half space, we have

$$\begin{aligned} & \frac{\partial}{\partial z} E_z(x, y, z) \\ &= -\frac{\partial}{\partial x} E_x - \frac{\partial}{\partial y} E_y. \end{aligned} \quad (10.13)$$

Finally noting that E_z cannot have a non-zero z -independent additive term (in order to make the field vanish at infinity), the $E_z(x, y, z)$ component may be represented as:

$$E_z(x, y, z) = \int \int dx' dy' \{ E_x(x', y', 0) \frac{(x - x')}{R} + \\ E_y(x', y', 0) \frac{(y - y')}{R} \} \frac{\exp(ikR)}{2\pi R} (-ik + \frac{1}{R}). \quad (10.14)$$

The results in Eq.s (10.11), (10.12), (10.14) may be written in a compact form as first suggested by W. R. Smythe:

$$\vec{E}(x, y, z) = \frac{1}{2\pi} \nabla \times \int \int dx' dy' \hat{n} \times \vec{E}(x', y', 0) \frac{\exp(ikR)}{R}, \quad (10.15)$$

and are referred to as the Rayleigh-Sommerfeld-Smythe relations. These relations are exact solutions of Maxwell equation for the electromagnetic diffraction problem. We observe that all the three components of the \vec{E} field at any point $(x, y, z > 0)$ in the right half space are therefore completely determined by specifying the tangential components $E_x(x, y, 0)$ and $E_y(x, y, 0)$ in the $z = 0$ plane. This may be considered as a starting point for holography. As long as we can specify or generate the required tangential fields in the hologram plane, the hologram on replay will give us an impression as if the fields entering our eye actually originated from a 3D object placed appropriately. The z -component of the field is usually ignored in many problems in para-axial regime where $(x - x')/R$

or $(y - y')/R$ are much smaller than z/R . However this component may become significant particularly in case of fields for high numerical aperture systems near the focus.

While noting the exact nature of the solution as above when the tangential fields in the $z = 0$ plane are known, it is important to observe that the Rayleigh-Sommerfeld-Smythe relations are not sufficient to determine the tangential fields in the aperture plane. Determination of aperture fields that may be used for calculating diffraction fields in $z > 0$ space is a separate problem in itself and needs a careful treatment particularly when the aperture size is comparable or smaller than the wavelength λ of illumination used. This interesting topic is not within the scope of this book and will not be discussed here.

Some consequences that follow readily in the angular spectrum description are as illustrated in Fig. 10.1

1. Propagating waves We note that Fourier components of the input field $E_x(x, y, 0)$ (or $E_y(x, y, 0)$) corresponding to spatial frequencies with $(f_x^2 + f_y^2) < 1/\lambda^2$, get assigned a phase factor $\exp(i\alpha z)$ due to propagation in $+z$ direction. Their Fourier magnitude stays the same. These components are therefore called the propagating components. They carry detectable information about the obstacle/aperture/object even to large distances ($R \gg \lambda$) from the aperture. If we write out the inverse Fourier transform relation:

$$\begin{aligned} E_x(x, y, z) \\ = \int \int df_x df_y \tilde{E}_x(f_x, f_y; 0) \exp[i2\pi(f_x x + f_y y) + i\alpha z]. \end{aligned} \quad (10.16)$$

The component corresponding to spatial frequencies (f_x, f_y) can be considered as a plane wave of weight $\tilde{E}_x(f_x, f_y; 0)$ that makes angles

$$\cos^{-1}(\lambda f_x), \cos^{-1}(\lambda f_y) \text{ and } \cos^{-1}(\sqrt{1 - \lambda^2(f_x^2 + f_y^2)})$$

with the $+x$, $+y$, $+z$ axes respectively and this is the justification for the name “angular spectrum”. Note that zero

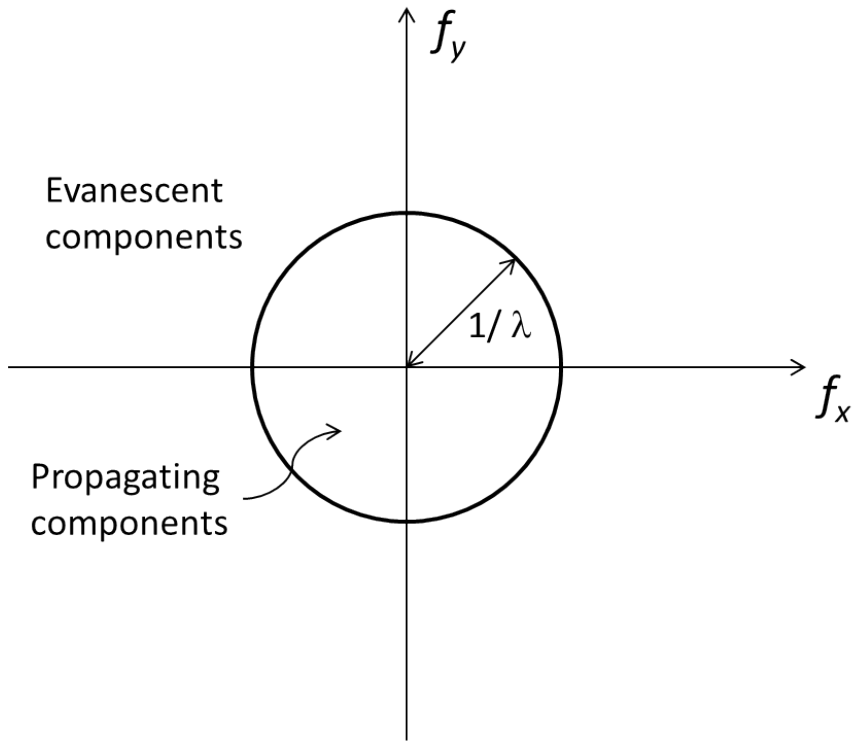


Figure 10.1: 2D Fourier space showing the propagating and evanescent components in the angular spectrum method.

spatial frequency $(f_x, f_y) = (0, 0)$ corresponds to a plane wave propagating in the $+z$ direction. The spatial frequencies $\lambda^2(f_x^2 + f_y^2) = 1$ correspond to plane waves propagating at 90-degrees to the $+z$ axis. As the details in the aperture plane become finer, their diffraction corresponds to plane waves making larger angles with the $+z$ axis.

2. **Evanescent waves** The Fourier components of the input field $E_x(x, y, 0)$ (or $E_y(x, y, 0)$) corresponding to spatial frequencies with $(f_x^2 + f_y^2) > 1/\lambda^2$, get assigned a decaying factor $\exp(-|\alpha|z)$. These wave components decay exponentially as we move in $+z$ direction from the aperture. The decaying components are typically negligible in magnitude as soon as

we are several wavelengths away from the aperture when considering the problem of diffraction in the right half space.

In our discussion of diffraction problem so far this is the first time that the wavelength λ appears explicitly in relation to the scale of features in the aperture. The behaviour of the diffraction field for feature sizes larger and smaller than the wavelengths is seen to be completely different. The information about the sub-wavelength features is not available (for all practical purposes) unless we are in a region that is few wavelengths from the aperture plane. Probing structures such as sharp metal coated optical fiber tips can however pick up this information when placed very close to the aperture plane as is done in near field scanning optical microscopes. Sub-wavelength structures placed very close to the aperture can also convert some of the evanescent components into propagating components resulting in possibility of detecting information about sub-wavelength features in the far-field.

References and suggested reading

1. P. C. Clemmow, *The plane wave spectrum representation of electromagnetic fields*, Wiley-IEEE Press (1996).
2. L. Mandel and E. Wolf, *Coherence and Quantum Optics*, Cambridge Univ. Press (1995).
3. J. W. Goodman, *Introduction to Fourier Optics*, (ed. 2) McGraw-Hill (1996).
4. W. R. Smythe, “The double current sheet in diffraction”, Phys. Rev. vol. 72, pp. 1067-1070 (1947).
5. L. Novotny and B. Hecht, *Principles of Nano-Optics*, Cambridge Univ. Press (2012).
6. G. Lerosey, J. De Rosny, A. Tourin and M. Fink, “Focusing beyond diffraction limit with a far-field time reversal”, Science 315, 1120-1122 (2007).

11. Fresnel and Fraunhoffer diffraction

In this chapter we will discuss two important approximations to the exact Rayleigh-Sommerfeld diffraction formula obtained in the last chapter. The two approximate models are valid depending on the distance of the observation point relative to the aperture location, the aperture size and the wavelength λ of illumination. The approximations are widely used in analysis of most optical systems in typical laboratory settings.

11.1 Fresnel diffraction

We will start with the exact Rayleigh-Sommerfeld solution in Eq. (10.10) for one scalar component of the diffraction field and perform simplifying approximation to arrive at the Fresnel diffraction formula. The x -component E_x of the scalar field may be given by:

$$E_x(x, y, z) = \int \int_{S_A} dx' dy' E_x(x', y', 0) \frac{\exp(ikR)}{2\pi R} \left(-ik + \frac{1}{R}\right) \frac{z}{R}. \quad (11.1)$$

We note that for a finite aperture S_A , all the terms in the integral need not be included at distances much larger than the wavelength λ of illumination. For example, we note that for optical wavelengths $|k| \gg 1/R$ as in typical tabletop experimental settings. The wide-field form of Fresnel diffraction formula may then be stated as:

$$E_x(x, y, z) = \frac{1}{i\lambda} \int \int_{S_A} dx' dy' E_x(x', y', 0) \frac{\exp(ikR)}{2\pi R} \frac{z}{R}, \quad (11.2)$$

Further in the para-axial (or near-axis) region we may assume $z/R \approx 1$ and also the approximation $1/R \approx 1/z$ may be used. The term $\exp(ikR)$ needs to be handled carefully. In the para-axial region we use binomial expansion for the distance R .

$$\begin{aligned} R &= \sqrt{(x - x')^2 + (y - y')^2 + z^2} \\ &\approx z \left[1 + \frac{(x - x')^2 + (y - y')^2}{2z^2} - \frac{1}{8} \left(\frac{(x - x')^2 + (y - y')^2}{z^2} \right)^2 + \dots \right]. \end{aligned} \quad (11.3)$$

We may neglect the third term in the binomial expansion above if it is much less than 1 radian. This condition may be stated explicitly as:

$$z^3 >> \frac{k}{8} [(x - x')^2 + (y - y')^2]_{\max}^2, \quad (11.4)$$

We will refer to the region of right half space satisfying this condition as the Fresnel zone. The para-axial form of the Fresnel zone diffraction formula thus may be written explicitly as:

$$\begin{aligned} E_x(x, y, z) &= \frac{e^{ikz}}{i\lambda z} \int \int_{S_A} dx' dy' E_x(x', y', 0) e^{\frac{i\pi}{\lambda z} [(x - x')^2 + (y - y')^2]}. \end{aligned} \quad (11.5)$$

We note that the above formula is a 2D convolution of the field distribution in the $z = 0$ plane with the Fresnel impulse response $h_F(x, y; z)$ given by:

$$h_F(x, y; z) = \frac{\exp(ikz)}{i\lambda z} \exp \left[\frac{i\pi}{\lambda z} (x^2 + y^2) \right]. \quad (11.6)$$

The corresponding transfer function has already been evaluated in Chapter 2, Section 2.9. Using this result we may write the transfer function for Fresnel diffraction as:

$$H_F(f_x, f_y; z) = \exp(ikz) \exp[-i\pi\lambda z(f_x^2 + f_y^2)], \quad (11.7)$$

so that, the Fresnel diffraction formula may be written in Fourier transform domain as:

$$\hat{E}_x(f_x, f_y; z) = \hat{E}_x(f_x, f_y; 0) H_F(f_x, f_y; z). \quad (11.8)$$

We note that this result may also be obtained by approximating the transfer function in the angular spectrum approach for the para-axial region of right half space. Particularly we do not need to consider the evanescent part in this case and further:

$$\exp(iz\sqrt{k^2 - 4\pi^2(f_x^2 + f_y^2)}) \approx \exp[ikz(1 - 2\pi^2(f_x^2 + f_y^2)/k^2)], \quad (11.9)$$

which is the same as the Fresnel diffraction transfer function in Eq. (11.7).

11.1.1 Computation of Fresnel diffraction patterns

The computation of Fresnel diffraction involves convolving the 2D input field with the Fresnel impulse response $h_F(x, y; z)$ given in Eq. (11.6). The convolution operation is typically implemented in a computer using the 2-dimensional Fast Fourier Transform (FFT) operation denoted below by the symbol \mathcal{F} . The diffraction field may be computed as:

$$E(x, y; z) = \mathcal{F}^{-1}\{\mathcal{F}\{E(x, y; 0)\}\mathcal{F}\{h_F(x, y; z)\}\}. \quad (11.10)$$

The most important aspect of the FFT implementation above is the sampling consideration for the digital representation of the Fresnel impulse response. Suppose that the computation in Eq. (11.10) is to be carried out over a square window of size a^2 centered at origin $(0, 0)$ with pixel sizes Δx and Δy in x and y directions respectively. We will assume $\Delta x = \Delta y$ for simplicity. The rate of change of phase of the Fresnel impulse response is maximum at the edge of the computation window. The phase change in adjacent pixels near the edge $x = a/2$ is given by:

$$\left(\frac{\partial\phi}{\partial x}\right)_{x=a/2} \Delta x = \left(\frac{\pi a}{\lambda z}\right) \Delta x. \quad (11.11)$$

The sampling requirement as per Nyquist criterion demands that the maximum phase change in two adjacent pixels be less than or equal to π , giving the condition $\Delta x \leq (\lambda z)/a$. The sampling interval $(\lambda z)/a$ has been called as the ideal sampling interval by Voelz and

Roggemann (2009). The 2D FFT operation thus needs to be performed over N^2 pixels with $N = a^2/(\lambda z)$ as per the ideal sampling criterion.

As an illustration, suppose we want to compute the Fresnel diffraction pattern for a square aperture of side 2.4 cm at a distance of $z = 10$ m. Assuming plane wave illumination, a square computation window of side $a = 5$ cm, a wavelength of $\lambda = 0.5\mu\text{m}$, the sampling intervals in x and y directions as per the sampling criterion in Eq. (11.11) is given by $\Delta x = \Delta y = 10^{-4}\text{m}$ or a sampling grid of (500×500) points. To implement the Fresnel computation as per Eq. (11.10) we start by sampling both the square aperture and the Fresnel impulse response on the grid as above, perform two FFT operations, one pixel-by-pixel multiplication of the two FFTs, followed by an inverse FFT operation. The result of this process is shown in Fig. 11.1(a),(b) which show the amplitude and the phase of the diffraction field respectively. If we were to use a sampling grid with twice the sampling interval $\Delta x_1 = \Delta y_1 = 2 \times 10^{-4} \text{ m}$, keeping the same computation window size of 5 cm, and repeat the FFT-based procedure above the result is corrupted by aliasing artifacts as shown by the amplitude and phase of the field in Fig.s 11.2 (a),(b) respectively. The aliasing is caused here due to the sub-sampling of the Fresnel impulse response.

Another way of looking at the aliasing problem above is that for a given pixel size Δx (or Δy) aliasing will occur if the distance $z < (a\Delta x)/\lambda$. For such distances the quadratic phase function in the Fresnel impulse response is not appropriately sampled. In case computation is to be made for closer distances, the Fresnel impulse response may be low-pass filtered appropriately to avoid aliasing problems to get an approximate estimate of the diffraction field.

11.1.2 Transport of Intensity Equation

An interesting property satisfied by the Fresnel diffraction field as above is the relation between the z -intensity derivative of the field and the transverse gradient of the phase of the field. Suppose we represent the diffraction field as:

$$u(x, y, z) = \sqrt{I(x, y, z)} \exp[i\theta(x, y, z)]. \quad (11.12)$$

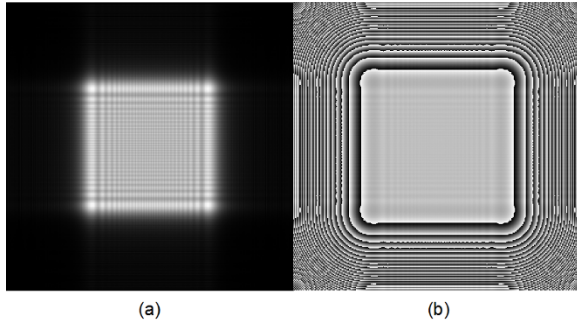


Figure 11.1: Fresnel diffraction computation for a 2.4 cm square aperture with wavelength $\lambda = 0.5 \times 10^{-6}$ m and propagation distance of $z = 10$ m. Computation window is a square of side $a = 5$ cm. The sampling interval $\Delta x = \Delta y = (\lambda z)/a = 10^{-4}$ m is used. The figures (a) and (b) show the amplitude and phase of the diffraction field respectively. The object and the Fresnel impulse response have been sampled on a (500×500) point grid.

Here the intensity and phase of the field $u(x, y, z)$ are denoted by $I(x, y, z) = |u(x, y, z)|^2$ ignoring any additional constant factors and $\theta(x, y, z)$ respectively. We will first obtain an approximate wave equation satisfied by the para-axial Fresnel diffraction field $u(x, y, z)$. Using the transfer function for Fresnel diffraction in Eq. (11.7) we may represent the field $u(x, y, z)$ as:

$$\begin{aligned} u(x, y, z) \\ = e^{ikz} \int \int df_x df_y U(f_x, f_y, 0) e^{-i\pi\lambda z(f_x^2 + f_y^2) + i2\pi(f_x x + f_y y)}. \end{aligned} \quad (11.13)$$

Using this Fourier representation, it is easy to verify that $u(x, y, z)$ satisfies the following differential equation:

$$\left[i \frac{\partial}{\partial z} + \frac{1}{2k} \frac{\partial^2}{\partial x^2} + \frac{1}{2k} \frac{\partial^2}{\partial y^2} + k \right] u(x, y, z) = 0. \quad (11.14)$$

This equation is referred to as the para-axial or parabolic form of wave equation. If Eq. (11.14) is multiplied on the left by $u^*(x, y, z)$ and the conjugate equation is multiplied on the left by $u(x, y, z)$,

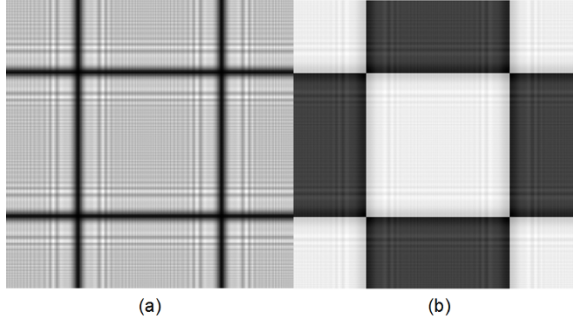


Figure 11.2: Aliasing artifacts in Fresnel diffraction computation for sub-sampled grid. The sampling interval $\Delta x_1 = \Delta y_1 = 2(\lambda z)/a = 2 \times 10^{-4}$ m is used. (a) and (b) show the amplitude and phase of the diffraction field respectively. The object and the Fresnel impulse response have been sampled on a (250×250) point grid.

then the two resultant equations on subtraction give:

$$-\frac{2\pi}{\lambda} \frac{\partial I(x, y, z)}{\partial z} = \nabla_{\perp} \cdot [I(x, y, z) \nabla_{\perp} \theta(x, y, z)], \quad (11.15)$$

where ∇_{\perp} refers to the transverse vector operator $(\partial/\partial x, \partial/\partial y)$. This equation is known as the transport of intensity equation (TIE). From an experimental point of view this equation implies that in the Fresnel diffraction approximation, the z intensity derivative may be used to determine the phase $\theta(x, y, z)$ of a wavefront if the differential equation above can be solved. The intensity derivative can be obtained for example by recording two intensity images $I(x, y, z)$ and $I(x, y, z + \Delta z)$ with longitudinal translation of an area detector. In order to obtain the phase $\theta(x, y, z)$ we first introduce an auxiliary function $\psi(x, y, z)$ such that:

$$\nabla_{\perp} \psi = I \nabla_{\perp} \theta, \quad (11.16)$$

giving

$$-\frac{2\pi}{\lambda} \frac{\partial I}{\partial z} = \nabla_{\perp}^2 \psi, \quad (11.17)$$

which can be solved as:

$$\psi = -\frac{2\pi}{\lambda} \nabla_{\perp}^{-2} \frac{\partial I}{\partial z}. \quad (11.18)$$

Further using the definition of the auxiliary function ψ above and taking transverse gradient gives:

$$\nabla_{\perp}\psi = I\nabla_{\perp}\theta = -\frac{2\pi}{\lambda}\nabla_{\perp}\nabla_{\perp}^{-2}\frac{\partial I}{\partial z}. \quad (11.19)$$

The same idea used for obtaining ψ as in Eq. (11.18) can now be followed for getting the phase function $\theta(x, y, z)$. The final result can be expressed as:

$$\theta(x, y, z) = -\frac{2\pi}{\lambda}\nabla_{\perp}^{-2}\nabla_{\perp} \cdot \left[\frac{1}{I}\nabla_{\perp}\nabla_{\perp}^{-2}\left(\frac{\partial I}{\partial z}\right) \right]. \quad (11.20)$$

The inverse Laplacian operator ∇_{\perp}^{-2} demands a brief discussion. In a manner similar to the Laplacian, the operator can be defined easily in the Fourier domain as:

$$\nabla_{\perp}^{-2}g(x, y) = \mathcal{F}^{-1} \left[\frac{G(f_x, f_y)}{-4\pi^2(f_x^2 + f_y^2)} \right]. \quad (11.21)$$

Further in order to avoid division by zero, the operator may be practically implemented as:

$$\nabla_{\perp}^{-2}g(x, y) \approx \mathcal{F}^{-1} \left\{ \frac{-4\pi^2(f_x^2 + f_y^2)G(f_x, f_y)}{[-4\pi^2(f_x^2 + f_y^2)]^2 + \epsilon^2} \right\}, \quad (11.22)$$

for small positive constant ϵ^2 . The operator can thus be readily implemented using the 2D Fast Fourier Transform routines available in most numerical computation softwares. We will illustrate the numerical method above with an illustration for a constant amplitude quadratic phase function. The intensity derivative shown in Fig. 11.3(a) is obtained by first computing Fresnel diffraction corresponding to the test function by small distances of +0.5 mm and -0.5 mm. The recovered phase is shown as a 3D surface in Fig. 11.3(b) and a plot of the phase profile along the x-axis is shown for both the test and recovered phase functions. The RMS error between the test phase and the recovered phase is less than 0.3% in this illustration. We also selected the test phase to range from 0 to several multiples of 2π to illustrate that for smooth functions the transport of intensity solution directly provides the unwrapped phase profile.

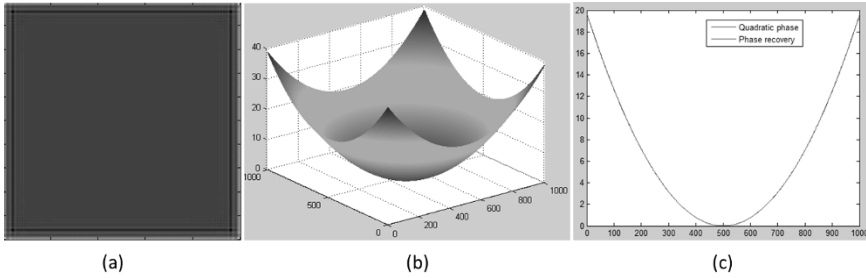


Figure 11.3: Illustration of phase recovery for a constant amplitude quadratic phase function using the transport of intensity equation. (a) Longitudinal intensity derivative, (b) Recovered phase, (c) Comparison of recovered phase and the test phase using plot of the phase values along a central line through the phase function. The RMS error is less than 0.3% in this illustration.

11.1.3 Self imaging: Montgomery conditions and Talbott effect

Self-imaging is a curious phenomenon in which an object with certain spatial frequency content on illumination with a coherent beam produces intensity distribution at a distance that is similar to the object itself. We will first look at self-imaging from the full angular spectrum considerations. As we have studied in the last chapter, the diffraction problem may be described in the Fourier transform domain using the angular spectrum transfer function as:

$$U(f_x, f_y; z) = \exp[iz\sqrt{k^2 - 4\pi^2(f_x^2 + f_y^2)}] U(f_x, f_y; 0). \quad (11.23)$$

It is clear that self-imaging will occur if the phase factor in the transfer function (assuming we are restricting ourselves to propagating components) is an integral multiple of 2π . We may denote the corresponding distances as z_m such that:

$$z_m \sqrt{k^2 - 4\pi^2(f_x^2 + f_y^2)} = 2\pi m, \quad (11.24)$$

where m is an integer. The condition can be stated by further simplification as:

$$\left(\frac{m}{z_m}\right)^2 = \left(\frac{1}{\lambda}\right)^2 - (f_x^2 + f_y^2). \quad (11.25)$$

Objects whose spatial frequency content is restricted to the spatial frequencies (circles in Fourier transform space) as per the above condition will show self-imaging at distances z_m from the aperture. It is to be noted that the above restriction in spatial frequency space implies that such objects are inherently infinite in extent. The condition for self-imaging above is due to Montgomery. The para-axial version of this general result is the Talbott effect in which self-imaging is demonstrated by periodic structures. Consider an amplitude grating described by a transmission function:

$$t(x, y) = \frac{1}{2}[1 + \cos(2\pi f_0 x)]. \quad (11.26)$$

Fourier transform of this transmission function is given by:

$$T(f_x, f_y) = \frac{1}{2}[\delta(f_x, f_y) + \frac{1}{2}\delta(f_x - f_0, f_y) + \frac{1}{2}\delta(f_x + f_0, f_y)]. \quad (11.27)$$

On plane wave illumination of this grating, the Fresnel diffraction field at distance z from the grating may be expressed in Fourier domain as:

$$\begin{aligned} U(f_x, f_y; z) &= T(f_x, f_y) \exp[ikz - i\lambda z(f_x^2 + f_y^2)] \\ &= \frac{1}{2} \exp(ikz) \{\delta(f_x, f_y) + \\ &\quad \frac{1}{2} \exp(-i\pi\lambda z f_0^2) [\delta(f_x - f_0, f_y) + \delta(f_x + f_0, f_y)]\}. \end{aligned} \quad (11.28)$$

We observe that for distances z_n for positive integer values of n such that

$$z_n = \frac{2n}{\lambda f_0^2} = \frac{2np^2}{\lambda}, \quad (11.29)$$

with $p = 1/f_0$ denoting the grating period, the exponential factor $e^{-i\pi\lambda f_0^2}$ is equal to $\exp(-i2\pi n)$ and thus the Fourier transform $U(f_x, f_y; z)$ and the transfer function $T(f_x, f_y)$ are proportional to each other. Fresnel propagation of periodic structures therefore leads to a self-imaging effect at specific distances given by z_n . For a more general periodic object the same conclusion can be made by noting that such periodic functions may be expressed as a Fourier series.

Further it is easy to see that at distances $z_n/2$ the grating function reverses its contrast and the self-imaging with contrast reversal is observed. This effect is termed as the fractional Talbott effect.

11.1.4 Fractional Fourier transform

The Fresnel diffraction can also be viewed as a fractional order Fourier transform. It is well-known that the Hermite Gauss functions denoted by

$$\phi_n(x) = \frac{2^{1/4}}{\sqrt{2^n n!}} \exp(-\pi x^2) H_n(\sqrt{2\pi}x), \quad (11.30)$$

are eigenfunctions of the Fourier transform operator. Here $H_n(x)$ denote the Hermite polynomials given by:

$$H_n(x) = (-1)^n \exp(x^2) \frac{d^n}{dx^n} \exp(-x^2). \quad (11.31)$$

The Hermite Gauss functions on Fourier transforming reproduce themselves such that:

$$\mathcal{F}\{\phi_n(x)\} = (-i)^n \phi_n(f_x). \quad (11.32)$$

Suppose we expand any finite energy function $g(x)$ as a linear combination of $\psi_n(x)$ as:

$$g(x) = \sum_{n=0}^{\infty} a_n \phi_n(x), \quad (11.33)$$

where

$$a_n = \int_{-\infty}^{\infty} dx g(x) \phi_n(x). \quad (11.34)$$

The Fourier transform of $g(x)$ can be obtained using the Fourier transform property of the Hermite Gauss functions as:

$$\begin{aligned} G(f_x) &= \sum_{n=0}^{\infty} a_n (-i)^n \phi_n(f_x) \\ &= \int_{-\infty}^{\infty} dx g(x) \sum_{n=0}^{\infty} (-i)^n \phi_n(x) \phi_n(f_x). \end{aligned} \quad (11.35)$$

The fractional order Fourier transform of order α may now be introduced as:

$$\mathcal{F}^\alpha\{g(x)\} = \sum_{n=0}^{\infty} a_n (-i)^{n\alpha} \phi_n(f_x). \quad (11.36)$$

We note that the transform is linear and additive in index α . Two successive operations \mathcal{F}^α and \mathcal{F}^β are equivalent to $\mathcal{F}^{\alpha+\beta}$. Using the Mehler's identity for Hermite functions the transformation above may be expressed as:

$$\mathcal{F}^\alpha\{g(x)\} = \int_{-\infty}^{\infty} dx g(x) K(x, f_x, \alpha), \quad (11.37)$$

where

$$K(x, f_x, \alpha) = \sqrt{1 - i \cot(\alpha\pi/2)} \times \\ \exp\{i\pi[(x^2 + f_x^2) \cot(\alpha\pi/2) - 2xf_x \csc(\alpha\pi/2)]\}. \quad (11.38)$$

The form of this kernel is similar to the Fresnel kernel and as $\alpha \rightarrow 1$ we observe that the Fresnel diffraction goes over to Fraunhoffer diffraction. Fractional Fourier transform has found application in describing propagation of light through GRIN lenses, in image/signal coding, noise separation etc.

11.2 Fraunhoffer Diffraction

Fraunhoffer diffraction model further approximates the Fresnel diffraction. We write the Fresnel diffraction relation in Eq. (11.5) in a slightly modified form:

$$u(x, y, z) = \frac{e^{ikz} e^{\frac{i\pi}{\lambda z}(x^2+y^2)}}{i\lambda z} \int \int_{S_A} dx' dy' u(x', y', 0) e^{\frac{i\pi}{\lambda z}(x'^2+y'^2)} e^{-i\frac{2\pi}{\lambda z}(xx'+yy')}, \quad (11.39)$$

and observe that the Fresnel diffraction is thus equivalent to a 2D Fourier transform of the input field $u(x', y', 0)$ multiplied by a quadratic

phase factor. For distances z and the aperture sizes such that the quadratic phase factor is small:

$$\frac{\pi(x'^2 + y'^2)_{\max}}{\lambda} \ll z, \quad (11.40)$$

the Fresnel diffraction relation may be modified as:

$$\begin{aligned} u(x, y, z) \\ = \frac{e^{ikz} e^{\frac{i\pi}{\lambda z}(x^2+y^2)}}{i\lambda z} \int \int_{S_A} dx' dy' u(x', y', 0) \exp\left[\frac{-i2\pi}{\lambda z}(xx' + yy')\right]. \end{aligned} \quad (11.41)$$

This relation is known as the Fraunhofer diffraction formula and we observe that the input and output fields in this case are related by a Fourier transform relationship (apart from a quadratic phase factor). The coordinates (x, y) in the observation plane may be related to spatial frequency components

$$f_x = \frac{x}{\lambda z}, f_y = \frac{y}{\lambda z}. \quad (11.42)$$

We observe that the Fourier transform relationship implies that the

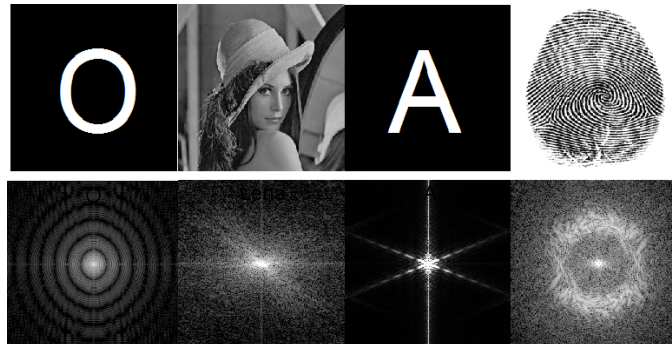


Figure 11.4: Illustration of several objects and their corresponding Fraunhofer diffraction intensity patterns.

Fraunhofer diffraction cannot be associated with a convolution. Lateral shift of the input object therefore simply adds an overall phase

factor to the diffraction pattern. A few examples of Fraunhoffer diffraction patterns are shown in Fig. 11.4 where the diffraction pattern intensity is displayed on a log-scale. It is interesting to observe some characteristic features that are typical of 2D Fourier transforms. For an object like the letter ‘A’, there is a streak perpendicular to each of the three main edge directions. The diffraction pattern for letter ‘O’ shows circular symmetry for the same reason. For a more realistic object like the ‘Lena’ image, it is difficult to assign any feature in the transform with the features in the picture. The energy concentration near zero frequency may however be noted. The fingerprint object is very interesting in that there is a local carrier-frequency at every point in the picture which is oriented in different directions. The result is that the diffraction pattern has energy concentration near zero frequency as well as on an annular ring.

We conclude this chapter by noting that the Fresnel and Fraunhoffer diffraction approximations described in this chapter are very useful for describing most of the typical laboratory experiments and imaging systems and we will use these models extensively in further chapters.

References and suggested reading

1. J. W. Goodman, *Introduction to Fourier Optics*, (Ed. 2), McGraw-Hill (1996).
2. K. Iizuka, *Elements of Photonics*, (vol. 1 and 2), John Wiley & Sons (2002).
3. H. M. Ozaktas, Z. Zalevsky, M. Alper Kutay, *The Fractional Fourier Transform: With Applications in Optics and Signal Processing*, Wiley 2001.
4. D. G. Voelz and M. C. Roggemann, “Digital simulation of scalar optical diffraction: revisiting chirp function sampling criteria and consequences”, *Appl. Opt.* 48, 6132-6142 (2009).
5. M. R. Teague, “Deterministic phase retrieval: a Green’s function solution”, *J. Opt. Soc. Am.* 73, 1434-1441 (1983).

12. Coherence of light fields

The concepts in Optics so far have been treated in a deterministic manner. In particular we have solved the problems on wave propagation and diffraction starting with Maxwell equations which describe the relation between the \vec{E} and \vec{B} fields associated with the light waves. The generation of light waves in a realistic light source occurs from electronic transitions in a large number of atoms. As a result the description of light fields is necessarily statistical in nature. As we shall see later in this chapter, due to the effects of source bandwidth and propagation of light waves, there exist correlations between fields at two space-time points (\vec{r}_1, t_1) and (\vec{r}_2, t_2) . In Chapter 7 we have developed several key concepts in theory of random processes that will be directly utilized in the following analysis.

12.1 Spatial and temporal coherence

We begin by defining important properties of optical fields, viz. the spatial and the temporal coherence, which will be understood in terms of the correlation function introduced in Eq. (7.43). We will introduce these concepts here for a single scalar component of the E-field of light waves, however, these concepts can be generalized to include vectorial fields in a straightforward manner. Given an arbitrary source of light we will define the complex degree of coherence to be the correlation function:

$$\Gamma(\vec{r}_1, \vec{r}_2, \tau) = \langle E^*(\vec{r}_1, t + \tau) E(\vec{r}_2, t) \rangle. \quad (12.1)$$

Here $E(\vec{r}, t)$ denotes the scalar field due to the source which we assume to be a stationary random process in time. We note that

the observed intensity of light is proportional to the equi-space and equi-time correlation function $\Gamma(\vec{r}, \vec{r}, 0)$. The correlation function is typically normalized as follows:

$$\gamma(\vec{r}_1, \vec{r}_2, \tau) = \frac{\Gamma(\vec{r}_1, \vec{r}_2, \tau)}{\sqrt{\Gamma(\vec{r}_1, \vec{r}_1, 0)\Gamma(\vec{r}_2, \vec{r}_2, 0)}}, \quad (12.2)$$

so that the normalized degree of coherence satisfies

$$0 \leq |\gamma(\vec{r}_1, \vec{r}_2, \tau)| \leq 1.$$

The equi-time degree of coherence $\gamma(\vec{r}_1, \vec{r}_2, 0)$ is commonly associated with the spatial coherence of the source while the equi-space degree of coherence $\gamma(\vec{r}_1, \vec{r}_1, \tau)$ is associated with the temporal coherence of the source. Two typical optical experiments - Young's double slit experiment and the Michelson interferometer are shown in Fig. 12.1. In Young's double slit experiment, any near-axis interference fringes observed on the screen can be associated with the equi-time correlation between the field at the two slits. In the Michelson interferometer on the other hand, the two arms of the interferometer can be varied in length to study the field correlation at the same point in space but delayed in time. We will express these relations more formally in the following section.

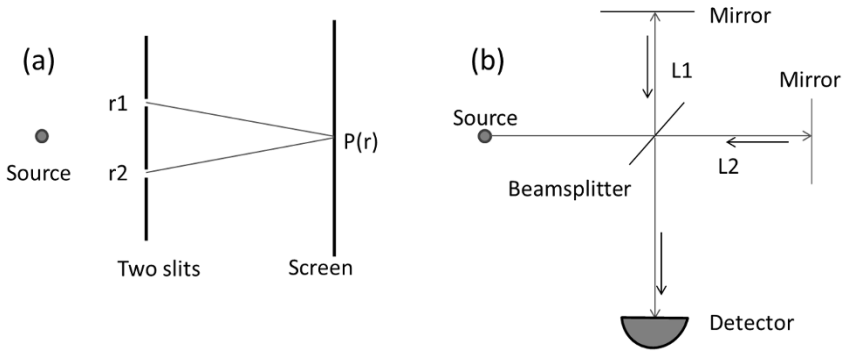


Figure 12.1: Typical experiments illustrating spatial and temporal coherence: (a) Young's double slit experiment, (b) Michelson interferometer.

12.1.1 Interference law

In reference to Fig. 12.1(a) we write the intensity observed at point P due to two point sources at \vec{r}_1 and \vec{r}_2 as:

$$I(P) = < |k_1 E(\vec{r}_1, t - R_1/c) + k_2 E(\vec{r}_2, t - R_2/c)|^2 > \quad (12.3)$$

Here k_1, k_2 are geometrical factors and the field at point P at time t is sum of the fields from the two point sources with the effect of time delay included. The distances R_1 and R_2 are defined as: $R_1 = |\vec{r}_1 - \vec{r}|$ and $R_2 = |\vec{r}_2 - \vec{r}|$. Assuming stationarity condition and defining $I_n = |k_n|^2 < |E(\vec{r}_n, t)|^2 >$ for $n = 1, 2$ gives:

$$I(P) = I_1 + I_2 + 2\text{Re}\{k_1^* k_2 \Gamma(\vec{r}_1, \vec{r}_2, \tau = |\vec{r}_1 - \vec{r}_2|/c)\}. \quad (12.4)$$

When the observation screen is located sufficiently far away from the two pinholes, as per the diffraction formulation developed earlier the constants k_1 and k_2 are purely imaginary and equal to:

$$k_{1,2} \approx \frac{-i}{\bar{\lambda} R_{1,2}}. \quad (12.5)$$

Here $\bar{\lambda}$ is the mean wavelength of the spectrum of the incident light (assuming a narrowband source). In terms of the normalized coherence function $\gamma(\vec{r}_1, \vec{r}_2, \tau)$ the interference law can therefore be written as:

$$I(P) = I_1 + I_2 + 2\sqrt{I_1 I_2} \text{Re}[\gamma(\vec{r}_1, \vec{r}_2, \tau)]. \quad (12.6)$$

The fringe contrast or visibility near the observation point P is given by:

$$V = \frac{I(P)_{max} - I(P)_{min}}{I(P)_{max} + I(P)_{min}} = |\gamma(\vec{r}_1, \vec{r}_2, \tau)|. \quad (12.7)$$

Interference fringes with good contrast can therefore be observed only over the region where the coherence function is not negligible.

12.2 van Cittert and Zernike theorem

In this section we will describe a very important result concerning the propagation of the correlation functions. We will consider

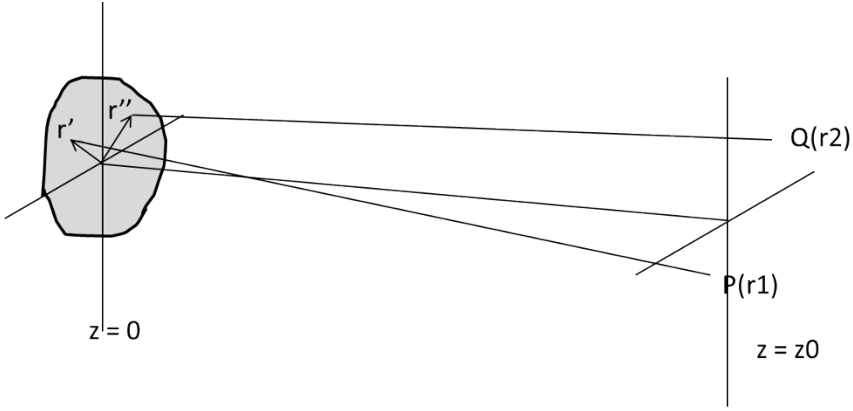


Figure 12.2: van-Cittert and Zernike theorem

a source in plane $z = 0$ and evaluate the equi-time correlation function at a plane $z = z_0$. If the plane $z = z_0$ is sufficiently far away from the source plane, we may simply express the field at point P due to a point source at $\vec{r} = \vec{r}'$ as a spherical wave. The equi-time correlation function of fields at points $P(\vec{r}_1)$ and $Q(\vec{r}_2)$ is given by:

$$\begin{aligned} & \Gamma(\vec{r}_1, \vec{r}_2, 0) \\ &= \int \int d^2\vec{r}' d^2\vec{r}'' \Gamma(\vec{r}', \vec{r}'', 0) \frac{k^2 e^{-ik|\vec{r}_1 - \vec{r}'|} e^{ik|\vec{r}_2 - \vec{r}''|}}{(4\pi)^2 |\vec{r}_1 - \vec{r}'| |\vec{r}_2 - \vec{r}''|}. \end{aligned} \quad (12.8)$$

When the observation plane is in the far field relative to the source, several approximations may be made. For example, $|\vec{r}_1| \gg |\vec{r}'|$ and $|\vec{r}_2| \gg |\vec{r}''|$, so that,

$$|\vec{r}_1 - \vec{r}'| \approx |\vec{r}_1| - \frac{\vec{r}_1 \cdot \vec{r}'}{|\vec{r}_1|}.$$

and

$$|\vec{r}_2 - \vec{r}''| \approx |\vec{r}_2| - \frac{\vec{r}_2 \cdot \vec{r}''}{|\vec{r}_2|}.$$

Also the distances in the denominator of the integrand in Eq. (12.8) may be replaced by z_0 . We will consider the important case of spatially incoherent source for which

$$\Gamma(\vec{r}', \vec{r}'', 0) = I_0(\vec{r}_1) \delta(\vec{r}' - \vec{r}''). \quad (12.9)$$

With these approximations the correlation function in the observation plane as in Eq. (12.8) may be expressed as:

$$\begin{aligned} & \Gamma(\vec{r}_1, \vec{r}_2, 0) \\ & \approx \frac{k^2 e^{-ik(|\vec{r}_1| - |\vec{r}_2|)}}{(4\pi z_0)^2} \int d^2 \vec{r}' I_0(\vec{r}') \exp[-ik\vec{r}' \cdot (\hat{r}_1 - \hat{r}_2)]. \end{aligned} \quad (12.10)$$

This is a statement of the far-zone form of the van Cittert and Zernike theorem. In the above equation, \hat{r}_1 and \hat{r}_2 denote unit vectors along \vec{r}_1 and \vec{r}_2 respectively. We note an important result that the far zone correlation function for a spatially incoherent source is proportional to the 2D Fourier transform of the source intensity pattern. The correlation is to be understood in the following manner. Suppose two pinholes were placed at points \vec{r}_1 and \vec{r}_2 , then the interference fringes on a screen downstream will have visibility or contrast proportional to the magnitude $|\Gamma(\vec{r}_1, \vec{r}_2, 0)|$. Further the Fourier transform relation implies that the extent where $|\Gamma(\vec{r}_1, \vec{r}_2, 0)|$ is significant is inversely proportional to the angular size of the source as seen in plane $z = z_0$.

An important experiment - Michelson's stellar interferometer - is essentially based on the van Cittert Zernike theorem. As shown in Fig. 12.3, starlight from two collection mirrors $M1, M4$ with a baseline d is brought together and the visibility of fringes is observed on a screen as the baseline d is changed. Assuming a circular disk shape for the star, its angular diameter can be related to the baseline d for which the fringes show zero contrast (no fringe pattern). Michelson was able to measure the angular diameter of the star Betelgeuse to be 0.02 arc-seconds using a baseline d approximately equal to 6 m which is much larger than a typical telescope diameter. This principle is also used in radio-astronomical telescopes that involve large antenna arrays spread over several kilometers.

12.3 Space-frequency representation of the coherence function

From the definition of the coherence function in Eq. (12.1) it is clear that the coherence function satisfies the wave equations in the form:

$$(\nabla_i^2 - \frac{1}{c^2} \frac{\partial^2}{\partial \tau^2}) \Gamma(\vec{r}_1, \vec{r}_2, \tau) = 0 \quad \text{for } i = 1, 2. \quad (12.11)$$

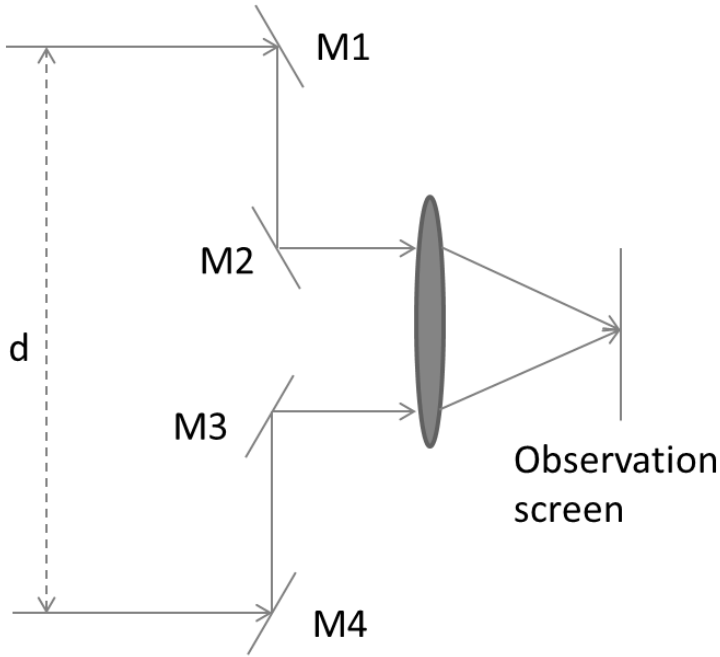


Figure 12.3: Schematic diagram of Michelson stellar interferometer.

Here the operator ∇_i for $i = 1, 2$ is with respect to the coordinates \vec{r}_1 and \vec{r}_2 . The behaviour of the coherence function can also be studied in the frequency domain using the cross-spectral density function defined through a Fourier transform relationship as:

$$W(\vec{r}_1, \vec{r}_2, \nu) = \int_{-\infty}^{\infty} d\tau \Gamma(\vec{r}_1, \vec{r}_2, \tau) \exp(-i2\pi\nu\tau). \quad (12.12)$$

The cross-spectral density is typically normalized as:

$$\mu(\vec{r}_1, \vec{r}_2, \nu) = \frac{W(\vec{r}_1, \vec{r}_2, \nu)}{\sqrt{S(\vec{r}_1, \vec{r}_1, \nu) S(\vec{r}_2, \vec{r}_2, \nu)}}, \quad (12.13)$$

where $S(\vec{r}_i, \vec{r}_i, \nu)$ for $i = 1, 2$ represent the spectral density (or spectrum). The normalized quantity $\mu(\vec{r}_1, \vec{r}_2, \nu)$ is referred to as the spectral degree of coherence and has the property:

$$0 \leq |\mu(\vec{r}_1, \vec{r}_2, \nu)| \leq 1. \quad (12.14)$$

It was noted by Wolf (1982) that the cross spectral density can be thought of as a correlation function obtained from an ensemble of monochromatic realizations of the field. The cross spectral density is Hermitian with respect to variables \vec{r}_1 and \vec{r}_2 and non-negative definite. Further assuming that the cross-spectral density is square integrable over domain of interest, we may represent it as a Mercer expansion:

$$W(\vec{r}_1, \vec{r}_2, \nu) = \sum_n \lambda_n(\nu) \phi_n^*(\vec{r}_1, \nu) \phi_n(\vec{r}_2, \nu). \quad (12.15)$$

This is known as the coherent mode representation of the spectral density function. The parameters $\lambda_n(\nu)$ are the eigenvalues (positive due to non-negative definite property of W) in the homogeneous integral euuation:

$$\int d^2 \vec{r}_1 W(\vec{r}_1, \vec{r}_2, \nu) \phi_n(\vec{r}_1, \nu) = \lambda_n(\nu) \phi_n(\vec{r}_2, \nu). \quad (12.16)$$

We may now introduce an ensemble of fields in frequency domain (in a manner analogous to the Karhunen-Loeve expansion):

$$u(\vec{r}, \nu) = \sum_n a_n(\nu) \phi_n(\vec{r}, \nu). \quad (12.17)$$

where a_n are random variables satisfying

$$\langle a_n^*(\nu) a_m(\omega) \rangle = \delta_{m,n}. \quad (12.18)$$

The individual realizations $u(\vec{r}, \nu)$ satisfy the Helmholtz equation and further lead to the representation

$$W(\vec{r}_1, \vec{r}_2, \nu) = \langle u^*(\vec{r}_1, \nu) u(\vec{r}_2, \nu) \rangle_\nu, \quad (12.19)$$

where $\langle \dots \rangle_\nu$ represents an ensemble in the frequency domain.

12.4 Intensity interferometry: Hanbury Brown and Twiss effect

We will now turn to a somewhat surprising interference effect - the intensity interference. So far in the discussions in this chapter we

have talked about interference in terms of the second order field correlations. However, there is interesting information to be gained from fourth-order or intensity correlations as well. We will be particularly interested in thermal sources. Due to large number of atoms radiating independently in a thermal source, the probability distribution for the real and imaginary parts of the field of light from a thermal source may be assumed to have Gaussian distribution.

$$p(E) = \frac{1}{\pi|E_0|} \exp\left[-\frac{(E_r^2 + E_i^2)}{E_0^2}\right]. \quad (12.20)$$

Here E_r and E_i denote the real and imaginary parts of the light field respectively. Using the complex form of Gaussian moment theorem (7.1.10) we may calculate the intensity correlation at the two space-time points.

$$\begin{aligned} & \langle E^*(\vec{r}_1, t_1)E(\vec{r}_1, t_1)E^*(\vec{r}_2, t_2)E(\vec{r}_2, t_2) \rangle \\ &= \langle E^*(\vec{r}_1, t_1)E(\vec{r}_1, t_1) \rangle \langle E^*(\vec{r}_2, t_2)E(\vec{r}_2, t_2) \rangle \\ &+ \langle E^*(\vec{r}_1, t_1)E(\vec{r}_2, t_2) \rangle \langle E^*(\vec{r}_2, t_2)E(\vec{r}_1, t_1) \rangle \\ &= \langle I(\vec{r}_1) \rangle \langle I(\vec{r}_2) \rangle + |\Gamma(\vec{r}_1, \vec{r}_2, t_1 - t_2)|^2. \end{aligned} \quad (12.21)$$

We notice that in the space-time region where $\Gamma(\vec{r}_1, \vec{r}_2, t_1 - t_2)$ is significant, the fourth order correlation is in excess of $\langle I(\vec{r}_1) \rangle \langle I(\vec{r}_2) \rangle$. This was first observed by R. Hanbury Brown and Twiss. Their experiment was first performed with radio antennas and later with optical sources. The optical version of the experiment is shown schematically in Fig. 12.4. The radiation from a light source is split in two and the photo-currents from the two detectors are correlated. Detector 2 can be translated in transverse and longitudinal directions in order to study intensity correlations wherever $\Gamma(\vec{r}_1, \vec{r}_2, t_1 - t_2)$ is significant so that excess correlation in intensity can be observed. This effect of intensity correlation is surprising as traditionally interference is understood only as a second order correlation effect. The excess intensity correlation effect is a manifestation of statistical property of thermal or Gaussian light fields. Such excess correlation is not observed for light from well-stabilized single mode laser thus providing a possibility of distinguishing light sources based on

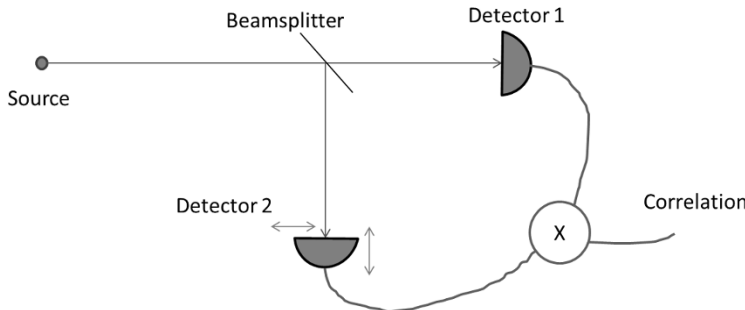


Figure 12.4: Schematic diagram of Hanbury Brown and Twiss intensity interferometer.

their statistical properties. The Hanbury Brown and Twiss experiment was largely responsible for emergence of what we now call ‘Quantum Optics’.

12.5 Photon counting formula

In the previous section we assumed that the photo-current in the detector is proportional to the average light intensity falling on the detector. When photon counting statistics for a given state of lightfield is of interest, the statistical distribution of number of photons can be determined correctly by considering two statistical processes, viz. the fluctuations in the light intensity and the statistical nature of the detection process itself. Suppose that a beam of light falls on a photon counting detector with mean intensity $I(x, y, t)$ (in units of number of photons), the integrated intensity over the detector area is given by:

$$W = \eta \int_0^T dt \int_A dx dy I(x, y, t). \quad (12.22)$$

Here η represents the detector quantum efficiency. When the light field is fluctuating with some statistical distribution $p(W)$ for the integrated intensity W , the distribution $p(n)$ of number of photon counts registered in series of trials each with integration time T is

given by:

$$p(n) = \int_0^\infty dW p(n|W) p(W). \quad (12.23)$$

The probability is determined as sum of all conditional probabilities so that the statistical fluctuation in the integrated intensity is accounted for. The conditional probability $p(n|W)$ is the standard Poisson distribution.

$$p(n|W) = \frac{\exp(-W)W^n}{n!}. \quad (12.24)$$

The photon counting distribution is therefore what is known as the Poisson transform of the distribution $p(W)$:

$$p(n) = \int_0^\infty dW \frac{\exp(-W)W^n}{n!} p(W). \quad (12.25)$$

This is the well-known photon counting formula due to Mandel. Some special cases of this formula are of interest. While discussing the statistics of light from a thermal source we assumed a complex Gaussian distribution for the E-field. The corresponding intensity has an exponential distribution:

$$p(I) = \frac{1}{\langle I \rangle} \exp\left(-\frac{I}{\langle I \rangle}\right). \quad (12.26)$$

If the measurement time T used in the definition of integrated intensity W is much smaller than the coherence time of the source, the intensity $I(t)$ is essentially a constant during the measurement interval. Further assuming a small-area detector, we can use the following approximation:

$$W \approx \eta AIT. \quad (12.27)$$

Since W and I are now related by a proportionality constant, the probability density for W is also an exponential distribution.

$$p(W) = \frac{1}{\langle W \rangle} \exp\left(-\frac{W}{\langle W \rangle}\right). \quad (12.28)$$

The corresponding photon counting distribution is a geometric or Bose-Einstein distribution.

$$p(n) = \frac{(\langle W \rangle)^n}{(1 + \langle W \rangle)^{(n+1)}}. \quad (12.29)$$

The variance corresponding to this distribution is:

$$(\Delta n)^2 = \langle W \rangle (1 + \langle W \rangle). \quad (12.30)$$

Another special case is that of well-stabilized single mode laser where the distribution $p(W)$ can be approximated as:

$$p(W) = \delta(W - \langle W \rangle). \quad (12.31)$$

The resultant photon count distribution is Poissonian in nature.

$$p(n) = \frac{\exp(-\langle W \rangle) \langle W \rangle^n}{n!} \quad (12.32)$$

The variance for this distribution is given by:

$$(\Delta n)^2 = \langle W \rangle. \quad (12.33)$$

The excess fluctuation in the case of thermal light over Poisson distribution is often referred to as the bunching of photons, since the photon counts are seen to be more clustered together in time (due to excess variance). The photon counting distribution therefore provides an interesting way to distinguish light from different sources even when other properties of the light beam such as intensity, polarization, spectrum are same. For completeness we mention here that there are certain states of light that show sub-Poissonian nature of fluctuation. Description of such states requires a full quantum mechanical treatment.

12.6 Speckle phenomenon

Speckle is a complex interference phenomenon commonly observed in the laboratory when a coherent laser beam scatters off a rough surface with surface features that induce almost uniformly random phase shifts in the range $[0, 2\pi]$ to the light beam at different locations. The observed scattered field at any point in space is therefore a superposition of a large number of randomly oriented phasors. Figure 12.5 shows a laser beam focused on a rough diffuser. The resultant diffraction pattern has blob-like bright regions which are known as speckles. The complex speckle field has interesting

structure in that the zeros of real and imaginary parts are along continuous curves in the observation plane. The zeros of intensity pattern are therefore typically located at isolated points as shown in Fig. 12.6.

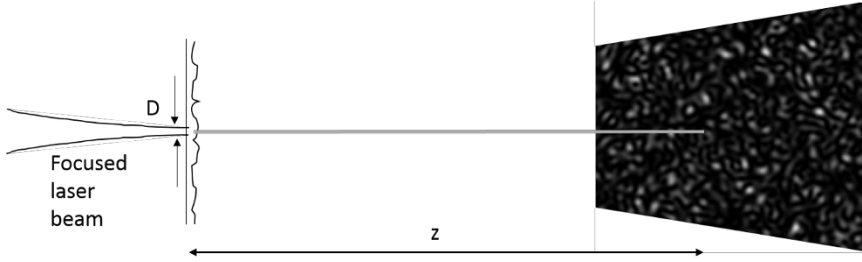


Figure 12.5: Schematic diagram showing formation of speckle pattern.

When the laser spot size on the rough surface is given by D then on a plane which is at a distance z from the scattering surface, the average size of individual speckles is same as the diffraction limited spot size which is of the order of:

$$d_{\perp} \approx \frac{\lambda z}{D}. \quad (12.34)$$

Individual speckles are 3D structures like jelly-beans and the average longitudinal size of speckles is given by:

$$d_{\parallel} \approx \lambda \left(\frac{z}{D}\right)^2. \quad (12.35)$$

The lateral and longitudinal size is thus effectively given by $\lambda/(NA)$ and $\lambda/(NA)^2$ with the numerical aperture of the system given by $NA = D/z$. The number of speckles in a single image frame is thus seen to be of the same order as the space-bandwidth product of the system and is also equal to the number of isolated intensity zeros. The phase of speckle field near an intensity zero is also known to have a vortex-like structure and this fact has been used recently in studies on small motion displacement detection on nanometric scale.

Since speckle has a non-deterministic structure due to the randomness in the rough surface, speckle is often studied statistically.

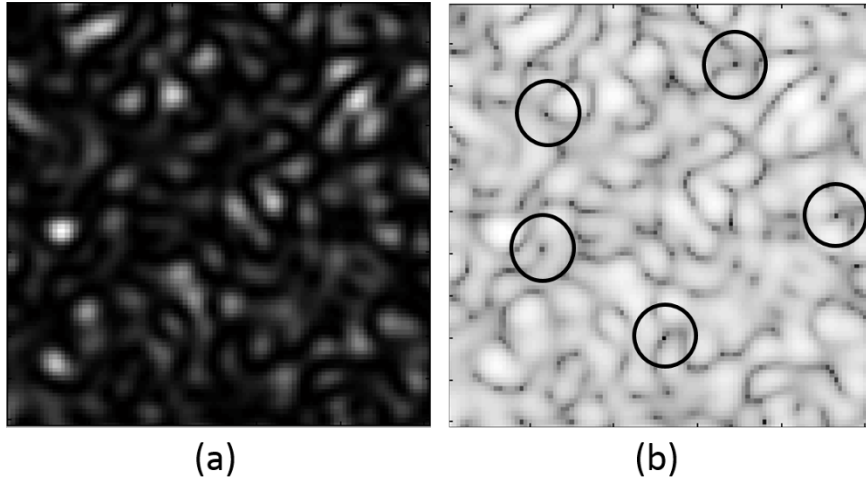


Figure 12.6: (a) A typical speckle intensity pattern, (b) The same pattern shown on log-scale with circles showing some of the isolated intensity zeros.

In particular we will assume that for performing ensemble averages the diffuser is being moved along the transverse direction so that the total field at a given observation point arises due to a different set of scattering centers in each realization of the speckle pattern. As the resultant field is a sum of large number of contributions from various scattering centers with phases distributed uniformly in $[0, 2\pi]$, the resultant field obeys complex Gaussian statistics (as per the central limit theorem). The probability distribution for the real and imaginary parts of scalar E -field denoted by E_r and E_i respectively is thus given by:

$$p(E_{r,i}) = \frac{1}{\sqrt{2\pi}E_0} \exp\left(-\frac{E_{r,i}^2}{2E_0^2}\right). \quad (12.36)$$

The intensity of the speckle field $I = E_r^2 + E_i^2$ therefore follows an exponential statistics given by:

$$p(I) = \frac{1}{I_0} \exp\left(-\frac{I}{I_0}\right), \quad (12.37)$$

where $I_0 = E_0^2$. The spatial statistics of a speckle is thus similar

to the temporal statistics of thermal light. If the speckle pattern is generated by unpolarized laser, the resultant speckle intensity distribution may be obtained by convolution of two exponential distributions which gives the following probability distribution:

$$\begin{aligned} p(I) &= \int_0^I dI' \frac{1}{\langle I \rangle^2} \exp[-(I - I')/\langle I \rangle] \exp(-I'/\langle I \rangle) \\ &= \frac{I}{\langle I \rangle} \exp\left(-\frac{I}{\langle I \rangle}\right). \end{aligned} \quad (12.38)$$

The limits of integration are selected as above since the exponential distribution is valid only in the region where the intensity is non-negative. Note that by adding two polarized speckles, the probability distribution has changed drastically near $I = 0$. Care must be taken if the above statistical distributions are to be applied to a single speckle pattern image as in Fig. 12.6(a) where individual speckles are spread over large number of pixels of an array detector. The distribution of intensity values of all pixels in such an image is certainly not exponential as pixel intensity values within a single speckle are correlated. The statistics will turn out to be exponential only if intensity values at a set of pixels that are mutually separated by a distance more than individual speckle size are selected for histogramming purpose.

An important laboratory tool in the study of speckle is the moving (or rotating) glass diffuser which on illumination by a laser spot produces a thermal-like source statistics. As the glass diffuser translates, a new set of scattering centers keeps appearing in the laser spot. The speckle pattern at an observation point thus keeps fluctuating on temporal scale of the time required for a point on the diffuser to cross the laser spot. The coherence time of such a source is thus given by:

$$\tau_c = a/v, \quad (12.39)$$

where a is the laser spot size on the diffuser and v is the diffuser velocity. From the earlier discussion in this section, it is easy to see that the source statistics at a given observation point resembles that of a thermal source. The coherence time of the source is guided by diffuser motion and the transverse spatial coherence length near the observation point is same as the average size of the speckles.

Such source can give rise to excess intensity correlations as in Hanbury Brown Twiss experiment. Further such source is much brighter compared to a typical narrowband thermal source obtained by filtering a small spectrum window from a thermal lamp. The rotating diffuser source may be used for averaging out the undesirable effect of speckles in imaging systems by making the coherence time τ_c much smaller than the exposure time. The moving diffuser thermal-like source has other more recent applications as we shall see later in case of ghost imaging.

References and suggested reading

1. L. Mandel and E. Wolf, *Coherence and Quantum Optics*, Cambridge Univ. Press (1995).
2. J. W. Goodman, *Statistical Optics*, Wiley-Interscience (2000).
3. J. C. Dainty (Ed.), *Laser speckle and related phenomena*, Topics in Applied Physics, Vol. 9, Springer (1975).
4. N. George and A. Jain, “Space and wavelength dependence of speckle intensity”, *Appl. Phys. A* 4, 201-212 (1974).
5. J. W. Goodman, *Speckle phenomena in Optics: Theory and Applications*, Roberts and Company (2010).
6. W. Martienssen and E. Spiller, “Coherence and fluctuations in light beams”, *Am. J. Phys.* 32, 919-926 (1964).
7. J. F. Nye and M. V. Berry, “Dislocations in wavetrains”, *Proc. Royal Soc. London A* 336, 165-190 (1974).
8. N. B. Baranova and B. Ya. Zel'dovich, “Dislocations of the wave-front surface and zeros of the amplitude”, *Sov. Phys. JETP* 53, 925-929 (1982).
9. W. Wang, T. Yokozeki, R. Ishijima, A. Wada, Y. Miyamoto, M. Takeda and S. G. Hanson, “Optical vortex metrology for nanometric speckle displacement measurement”, *Opt. Express* 14, 120-127 (2006).

13. Polarization of light

Our analysis of light fields so far has been mostly in terms of a single scalar component of the E-field of light waves. In this chapter we present a brief discussion on polarization of light for completeness. The vector nature of the diffraction field was briefly discussed in relation to the exact Rayleigh-Sommerfeld theory. For the purpose of discussion we will assume the light field to be monochromatic in nature. Polarization and related topics such as propagation of light in anisotropic crystals are described well in several books. The material in this chapter is only meant to introduce the reader to some standard notation.

13.1 The Jones matrix formalism

For a linearly polarized plane electromagnetic wave traveling in z -direction, the **E** and **B** fields are perpendicular to each other in transverse direction. The **E** field can thus have two independent components in the transverse plane that we may denote by:

$$\vec{E}_1 = \hat{x}E_{10} \exp[i(kz - \omega t)], \quad (13.1)$$

and

$$\vec{E}_2 = \hat{y}E_{20} \exp[i(kz - \omega t)]. \quad (13.2)$$

These two polarizations can be considered as basis states. Further, assuming that E_{10} and E_{20} are complex valued allows us to describe a general state of the transverse electromagnetic field. The polarization may thus be denoted as a 2-element column vector:

$$\vec{E} = \frac{1}{\sqrt{|E_{10}|^2 + |E_{20}|^2}} \begin{pmatrix} E_{10} \\ E_{20} \end{pmatrix} \quad (13.3)$$

The special cases of linear polarization in x and y directions are denoted by column vectors

$$\begin{pmatrix} 1 \\ 0 \end{pmatrix} \quad \text{and} \quad \begin{pmatrix} 0 \\ 1 \end{pmatrix}$$

respectively. In the same notation right and left circularly polarized light is denoted as:

$$\frac{1}{\sqrt{2}} \begin{pmatrix} 1 \\ -i \end{pmatrix} \quad \text{and} \quad \frac{1}{\sqrt{2}} \begin{pmatrix} 1 \\ i \end{pmatrix}$$

The elliptically polarized light is represented in a manner similar to the circularly polarized light with the magnitudes of the two components of the vector being unequal. The effect of a polarization sensitive device is typically represented by a 2×2 matrix known as the Jones matrix.

Birefringent materials make some of the most important polarization sensitive devices. Suppose that a linearly polarized beam passes through sheet of a material where the x and y components of the polarization vector suffer different phase delays as a result of the polarization dependent refractive index in these two directions. The Jones matrix for such an element may be given as:

$$J = \begin{pmatrix} \exp(i\delta_x) & 0 \\ 0 & \exp(i\delta_y) \end{pmatrix} \quad (13.4)$$

If the thickness of the material is given by L then the two phase differences δ_x and δ_y are given as:

$$\delta_x = \frac{2\pi}{\lambda}(n_x - 1)L, \quad (13.5)$$

and

$$\delta_y = \frac{2\pi}{\lambda}(n_y - 1)L. \quad (13.6)$$

Waveplates are commonly used polarization sensitive devices. When a linearly polarized light with polarization vector oriented at 45 degrees to x -axis passes through the above material of thickness such that the two components exiting the material have a phase shift $|\delta_x -$

δ_y equal to $\pi/2$ or π , then such a device is called a quarter or half-wave plate respectively. It is readily seen that a quarter wave plate (QWP) can convert a linearly polarized light (at 45 degrees) into a left or right circularly polarized light depending on the sign of $(\delta_x - \delta_y)$.

In the Jones matrix formalism a polarization rotator device is readily described by a rotation matrix. The matrix for rotation by angle α (counter-clockwise) is given by:

$$R(\alpha) = \begin{pmatrix} \cos(\alpha) & -\sin(\alpha) \\ \sin(\alpha) & \cos(\alpha) \end{pmatrix} \quad (13.7)$$

A polarizer is a device which passes either x or y polarized light through it while blocking the other component. The x and y polarizers may be described by:

$$P_x = \begin{pmatrix} 1 & 0 \\ 0 & 0 \end{pmatrix}, \quad (13.8)$$

and

$$P_y = \begin{pmatrix} 0 & 0 \\ 0 & 1 \end{pmatrix} \quad (13.9)$$

respectively. When the incident linear polarization is tilted by angle θ to the x -axis, the effect of polarizer is given by:

$$R(\theta)P_xR(-\theta) = \begin{pmatrix} \cos^2(\theta) & \cos(\theta)\sin(\theta) \\ \cos(\theta)\sin(\theta) & \sin^2(\theta) \end{pmatrix} \quad (13.10)$$

The sequence of operations above may be understood as follows. The incident polarization undergoes a basis change followed by action of polarizer in the new basis and finally transforming back to the original basis.

13.2 The QHQ geometric phase shifter

The geometric phase shifter is an interesting device which consists of a combination QHQ where Q stands for a quarter wave plate and H stands for a half wave plate. We assume a configuration where the fast axes of the quarter wave plates are aligned and that of the half

wave plate is rotated by an angle θ with respect to the quarter wave plates. For an incident linear polarization that is 45-degrees with respect to the fast axis of the quarter wave plate, the output field is given by the product:

$$J_{\pi/2}R(\theta)J_\pi R(-\theta)J_{\pi/2}\begin{pmatrix} 1 \\ 1 \end{pmatrix} = \exp(2i\theta)\frac{1}{\sqrt{2}}\begin{pmatrix} 1 \\ 1 \end{pmatrix}. \quad (13.11)$$

For relative rotation of the half-wave plate by angle θ the incident linearly polarized wave thus gets phase shifted by an angle 2θ . This phase shift can be understood as the geometric phase shift. The QHQ device is an interesting method to introduce phase change in a beam without introducing additional path delay, e.g. in a phase shifting interferometer.

13.3 Degree of polarization

The state of polarization of a beam of light can be described by a 2×2 coherence matrix:

$$J = \begin{pmatrix} < E_x^* E_x > & < E_x^* E_y > \\ < E_y^* E_x > & < E_y^* E_y > \end{pmatrix}, \quad (13.12)$$

where E_x and E_y denote the x and y components of the E-field. For example, for unit amplitude x -polarized light,

$$J = \begin{pmatrix} 1 & 0 \\ 0 & 0 \end{pmatrix}, \quad (13.13)$$

and for right circularly polarized light, we have

$$J = \frac{1}{2} \begin{pmatrix} 1 & i \\ -i & 1 \end{pmatrix}. \quad (13.14)$$

Since the matrix J is Hermitian it may be diagonalized by a unitary transformation as:

$$U J U^\dagger = \begin{pmatrix} \alpha_1 & 0 \\ 0 & \alpha_2 \end{pmatrix} \quad (13.15)$$

Assuming $\alpha_1 > \alpha_2$, the degree of polarization of the light beam is defined as:

$$\mathcal{P} = \frac{\alpha_1 - \alpha_2}{\alpha_1 + \alpha_2}. \quad (13.16)$$

Since the eigenvalues of J are determined by solving the equation:

$$\det[J - \alpha I] = 0, \quad (13.17)$$

the degree of polarization can be further expressed as:

$$\mathcal{P} = \sqrt{1 - 4 \frac{\det(J)}{[\text{tr}(J)]^2}}. \quad (13.18)$$

Here $\det(\dots)$ and $\text{tr}(\dots)$ stand for the determinant and the trace of the concerned matrix respectively. The important point to note is that when $\alpha_2 = 0$ we have fully polarized light whereas when $\alpha_1 = \alpha_2$ the light is fully unpolarized.

References and suggested reading

1. M. Born and E. Wolf, *Principles of Optics: Electromagnetic Theory of Propagation, Interference and Diffraction of Light*, (Ed. 7) Cambridge Univ. Press (1999).
2. L. Mandel and E. Wolf, *Coherence and Quantum Optics*, Cambridge Univ. Press (1995).
3. J. W. Goodman, *Statistical Optics*, Wiley-Interscience (2000).

14. Analysis of optical systems

In this chapter we will use the topics covered so far to provide wave optical model of simple optical system arrangements consisting of lenses and free space. The important cases of Fourier transforming property of a convex lens and the canonical or 4F optical processor will be described in detail and a few interesting cases of Fourier plane filters will be discussed.

14.1 Transmission function for a thin lens

Lens elements are commonly used for the purpose of imaging. Starting with human eye, lens system is the most important part of commonly used imaging systems such as cameras, microscopes, etc. We will consider thin lenses for the present discussion. In the ray optical model, a thin lens refers to a lens for which a ray parallel to optic axis entering one surface of the lens exits the other surface at approximately the same height from the optic axis. This is a useful approximation in determining the transmission function of a typical lens. We assume the radii of curvatures for the two lens surfaces to be R_1 and R_2 respectively.

Denoting by n the refractive index of the lens material, the optical path difference encountered along a line at height h parallel to the optic axis and between the two surfaces bounding the lens is given by:

$$OPD(x, y) = \frac{2\pi}{\lambda} [(L_0 - L(x, y)) + nL(x, y)]. \quad (14.1)$$

Here $(L_0 - L(x, y))$ denotes the air path length and the corresponding refractive index has been assumed to be equal to 1. Our goal is

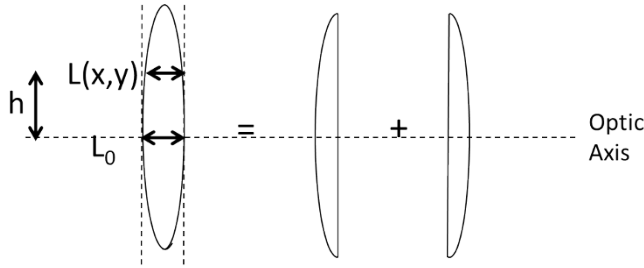


Figure 14.1: Determination of the transmission function for a thin lens. L_0 and $L(x, y)$ denote the thickness of glass material on optic axis and at height h above the optic axis. The radii of curvatures of the two lens surfaces are R_1 and R_2 respectively.

to express $L(x, y)$ in terms of the radii of curvature R_1 and R_2 of the two lens surfaces. As shown in Fig. 14.1 we divide the thin lens in two parts for convenience. The glass length $L(x, y)$ can now be expressed as:

$$L(x, y) = L_0 - \left[R_1 - \sqrt{R_1^2 - (x^2 + y^2)} \right] - \left[-R_2 - \sqrt{R_2^2 - (x^2 + y^2)} \right]. \quad (14.2)$$

Note that here we have used the usual geometrical optics convention that the second surface with its center of curvature to the left has negative radius of curvature. Further if we approximate the square roots in Eq. (14.1) by assuming that R_1 and $-R_2$ are much larger than (x, y) dimensions in the problem, the length $L(x, y)$ can be expressed as:

$$L(x, y) = L_0 - \frac{(x^2 + y^2)}{2} \left(\frac{1}{R_1} - \frac{1}{R_2} \right). \quad (14.3)$$

Substituting back in Eq. (14.1) gives:

$$OPD(x, y) = \frac{2\pi}{\lambda} \left[nL_0 - (n-1) \left(\frac{1}{R_1} - \frac{1}{R_2} \right) \frac{(x^2 + y^2)}{2} \right]. \quad (14.4)$$

Finally recognizing the expression $(n-1)(1/R_1 - 1/R_2)$ as the inverse focal length $1/F$ of the lens we get the transmission function

for a thin lens as follows:

$$t(x, y) = \exp[iOPD(x, y)] = \exp\left[-\frac{i\pi}{\lambda F}(x^2 + y^2)\right]. \quad (14.5)$$

In the above expression we have omitted the constant phase factor involving the lens thickness L_0 along the optical axis as it is inconsequential.

14.2 Fourier transforming property of thin lens

In this section we will discuss the very important 2D Fourier transforming property of a lens which is key to several imaging and optical processing applications. We will consider a configuration involving a lens and free space propagation as shown in Fig. 14.2. An object transparency with transmittance $t(x', y')$ is placed a distance d behind the lens. The output field is observed at the back focal plane of the lens. Assuming illumination of the object by a

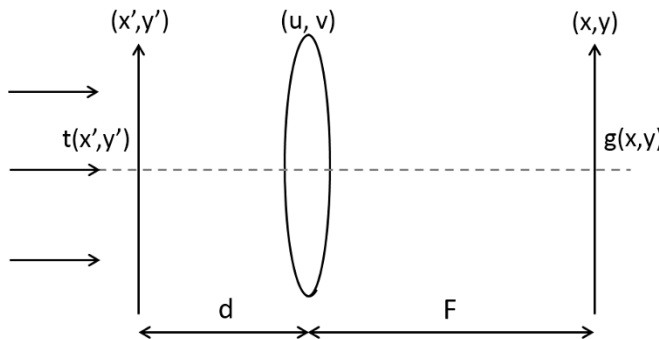


Figure 14.2: Fourier transforming property of a lens.

plane wave propagating along the optic axis, the calculation of the output $g(x, y)$ in terms of the input $t(x', y')$ involves the following steps:

1. Fresnel propagation from input plane to the lens.

2. Multiplication by lens transmission function.
3. Fresnel propagation from lens to output plane.

The Fresnel propagation formula developed in Chapter 11 and the lens transmission function obtained in the previous section may be used for the above steps and the result is stated below directly:

$$g(x, y) = \frac{e^{\frac{i\pi}{\lambda F}(1-\frac{d}{F})(x^2+y^2)}}{i\lambda F} \int \int dx' dy' t(x', y') e^{\frac{-i2\pi}{\lambda F}(xx'+yy')}.$$
(14.6)

We observe that the input-output have a Fourier transform relation with an additional quadratic phase factor in front. Further if we choose $d = F$, the quadratic phase factor vanishes and the Fourier transform relationship is exact. As per the definition in this book, the (x, y) coordinates in the output plane may be associated with the spatial frequencies in the input as:

$$f_x = \frac{x}{\lambda F}, f_y = \frac{y}{\lambda F}.$$
(14.7)

The two dimensional Fourier transforming property makes the lens a very important tool for two-dimensional optical signal processing. The Fourier transforming property may be understood easily in terms of the angular spectrum picture for diffraction. The input $t(x', y')$ when illuminated by a plane wave of wavelength λ will result in an angular spectrum of plane waves. Each plane wave is focused in its back focal plane to a spot (ideally) representing the delta function. The location of this focal spot for a particular plane wave indexed by (f_x, f_y) is at the location $x = \lambda F f_x$ and $y = \lambda F f_y$ in the output plane. The output pattern is an interference of all the plane waves accepted by the lens aperture. Finally we would like to mention that due to the dependence of the spatial frequency scaling on focal length F of the lens the extent of the Fourier transform pattern may be controlled so that it is sampled well by a pixelized detector in the output plane. The results here indicate that the Fraunhofer diffraction pattern of an object may be readily observed with appropriate scaling in the back focal plane of a lens.

14.3 Canonical optical processor

Having derived the Fourier transforming property of a convex lens, we will now consider an important imaging system - the canonical or 4F optical processor. This is a general imaging system model which may be used to describe a large number of imaging systems with minor modifications. The system of interest is as shown in Fig. 14.3. Continuing from previous section, we observe that the canonical op-

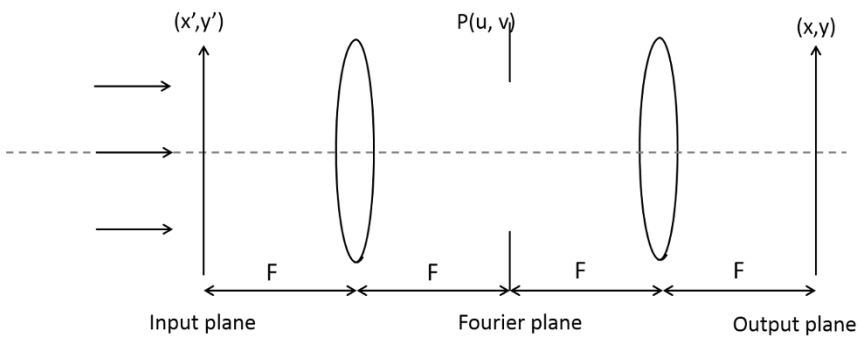


Figure 14.3: Canonical Optical Processor system layout: the focal lengths of the two lenses are given by F , input plane coordinates are (x', y') , output plane coordinates are (x, y) and the intermediate or Fourier plane coordinates are (u, v) .

tical system consists of two Fourier transform systems placed one after the other. When an object $g_{in}(x', y')$ in the input plane is illuminated with a plane wave illumination of wavelength λ , the field in the the intermediate plane is the scaled Fourier transform $G(f_x, f_y)$. For this reason we will call this intermediate plane as the Fourier plane. The spatial frequencies are scaled in terms of coordinates (u, v) in this plane as: $f_x = u/(\lambda F)$ and $f_y = v/(\lambda F)$. An aperture mask $P(u, v)$ which may in general have both amplitude and phase variations, controls the behaviour of the spatial frequencies in the sense that it either blocks or passes a particular spatial frequency (f_x, f_y) or modifies the Fourier component $G(f_x, f_y)$ with both amplitude and phase weight. $P(u, v)$ can thus be understood as

a Fourier plane filter. The output plane field is described by:

$$\begin{aligned} g_{out}(x, y) &= \mathcal{F}^{-1}\left\{G\left(\frac{u}{\lambda F}, \frac{v}{\lambda F}\right)P(u, v)\right\} \\ &= \int \int dx' dy' g_{in}(x', y') p(x + x', y + y') \\ &= g_{in}(x, y) * p(-x, -y). \end{aligned} \quad (14.8)$$

Here $p(x, y)$ is the response of the system and has a Fourier transform relationship with the aperture $P(u, v)$ of the system as given by:

$$p(x, y) = \frac{e^{ik(4F)}}{i\lambda F} \int \int du dv P(u, v) \exp\left[-i\frac{2\pi}{\lambda F}(ux + vy)\right]. \quad (14.9)$$

In the last step $*$ denotes the convolution operation and the negative sign for arguments of p is a result of two successive Fourier transforming operations and results in an inverted image of the object. In the further discussion we will usually omit the effect of this inversion of co-ordinates. We remark that the 4F system model may be used in describing a large number of imaging and diffraction phenomena. For example, in describing diffraction phenomena using the angular spectrum approach, one may consider an effective aperture $P(u, v)$ to be the free space transfer function that defines how the spatial frequencies in the input object are modified. We will use this system for study of several imaging phenomena as illustrated with specialty filters in the next section.

14.4 Fourier plane filter examples

14.4.1 DC block or coronagraph

DC blocking is an important technique that allows one to observe details in an image that would otherwise be hard to detect in presence of strong background. An example is the detection of planets near bright stars or the problem of imaging of solar atmosphere. A filter that blocks the dc component of light in Fourier plane of the 4F system and passes the high frequency components may achieve this. We illustrate this technique with example of a high intensity

2D Gaussian object to mimic a bright star and a small weak intensity object present in the Gaussian tail (see Fig. 14.4). By blocking

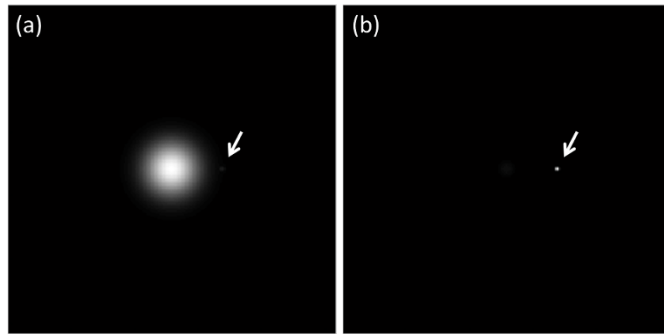


Figure 14.4: Effect of dc blocking on a simulated bright star image with weak planet object nearby: (a) test object, (b) resultant image after dc blocking.

the frequencies near the point $(f_x, f_y) = (0, 0)$ in the Fourier plane, the bright background has been removed as seen in Fig. 14.4(b). The overall dynamic range of the image intensity is therefore significantly modified and as a result the faint object is now visible. A similar approach is also used frequently in the dark-field mode in microscopes. In this and the following illustrations we have used fast Fourier transform based algorithm for demonstrating the various Fourier plane filters.

14.4.2 Zernike's phase contrast microscopy

Phase contrast microscopy is an important Fourier filtering technique first described by F. Zernike in 1942. Commonly studied biological cell specimens are transparent in nature and so their contrast is very poor when observed under a brightfield illumination. The dc blocking technique may be used here but it has one disadvantage that it blocks most of the light. Zernike suggested the use of a quarter wave phase shifting element that significantly enhances the image contrast. The working of the Zernike method can be understood as follows. Suppose that the incident light undergoes a phase change of $\psi(x, y)$ after passing through a transparent cell specimen.

For a weak phase object we may approximate:

$$\exp[i\psi(x, y)] \approx 1 + i\psi(x, y). \quad (14.10)$$

The intensity $I(x, y)$ corresponding to this wavefront observed on an imaging sensor is given by:

$$I(x, y) \approx |1 + i\psi(x, y)|^2 = 1 + [\psi(x, y)]^2. \quad (14.11)$$

For a weak phase object the first term dominates over the square of the second term and reduces the overall image contrast. Blocking the dc-component here amounts to effectively eliminating the first term and the image intensity is proportional to the square of the phase imparted by the object. However if a small quarter wave phase shifting element is placed near the zero frequency in the Fourier plane, the resultant image intensity is given by

$$I(x, y) \approx |i(1 + \psi(x, y))|^2 = 1 + 2\psi(x, y) + \psi(x, y)^2. \quad (14.12)$$

For a weak phase object the image intensity is thus approximately linearly related to the phase change instead of square of the square of the phase function and resultant images have significantly improved contrast. Commercial phase contrast microscopes typically use annular or ring illumination and a corresponding annular quarter wave phase shifter in the Fourier plane. This arrangement has advantage that it has good light throughput and further that from a user perspective aligning the ring image when inserting the Zernike phase plate is much easier. In the illustration in Fig. 14.5 we simulate a weak phase object that is assumed to be imaged by a 4F system. The phase function is shown in Fig. 14.5(a), and the intensity in the image plane without any filter in the Fourier plane is shown in Fig. 14.5(b). Figure 14.5(c) shows the effect of the Zernike's phase contrast filter clearly illustrating the contrast enhancement. The phase contrast mechanism provides significantly enhanced images for Bio-science researchers when transparent cells are to be visualized using a microscope. While phase contrast is a powerful technique we remark that it is a qualitative imaging method. This modality does not provide any quantitative phase information about the sample object under consideration.

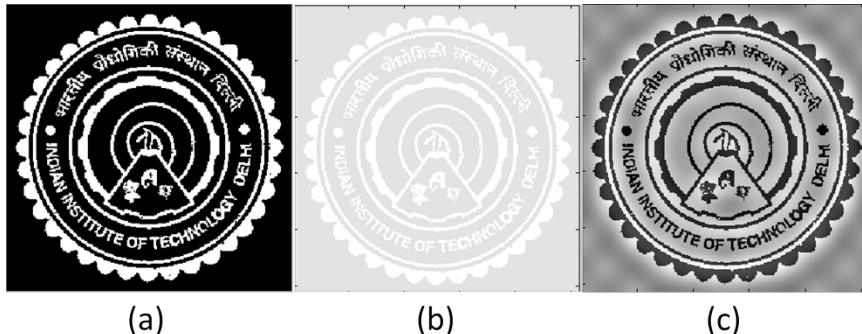


Figure 14.5: Simulation of Zernike phase contrast: (a) simulated phase map of weak phase object, (b) brightfield intensity image, (c) phase contrast image.

14.4.3 Edge enhancement: vortex filter

A vortex filter is an interesting case for study and provides an equivalent of a derivative operation uniformly in all directions. We define the vortex filter as:

$$H(\rho, \phi) = \exp(i\phi). \quad (14.13)$$

A physical vortex filter plate has unit amplitude everywhere and a spirally varying phase which changes uniformly from 0 to 2π . For 1D signal a derivative like operation is provided by the Hilbert transform (or equivalently a $\text{sgn}(\nu)$ filter) which converts a cosinusoidal signal to a sinusoidal one and vice versa with a sign change. The sine-cosine pair is commonly known by the name quadrature pair since the two signals are out of phase by $\pi/2$. This idea is often used in the $\exp(i\omega t)$ or complex representation in the study of wave phenomena. There is no straightforward generalization of the Hilbert transform concept in two or higher dimensions. The vortex phase as an isotropic Hilbert transform filter was first suggested by Larkin and co-workers 2001. The spiral phase function behaves like a sign function along any radial line passing through the origin of the (f_x, f_y) plane. We illustrate the effect of the spiral phase filter in enhancing the edges in an image isotropically. Figure 14.6(a) and (b) show an amplitude object and its corresponding image using a 4F system when a vortex phase filter is placed in the Fourier transform

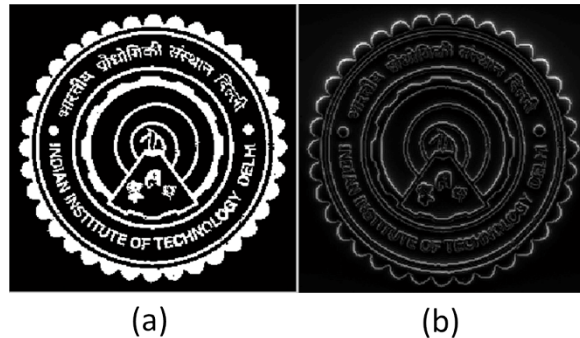


Figure 14.6: Simulation of the effect of vortex phase filter on an image: (a) amplitude object, (b) effect of vortex phase filter.

plane of the system aligned with the optic axis. The unit amplitude of the filter implies that the energy in the input plane is not lost but preferentially re-distributed near the points of high magnitude derivative in the object function.

14.4.4 Apodization filters

The coherent impulse response of a 4F imaging system may have side-lobes analogous to the Gibbs oscillations discussed in Chapter 2, particularly when the Fourier plane aperture has hard edges at the boundaries. Such side-lobes can create ringing artifacts in the resultant image. For example the impulse response corresponding to a rect-function aperture is a sinc-function which has long tail and side-lobes. A suitable window function used along with the filter function significantly reduces the side lobes - an effect known as apodization. We will illustrate this effect with an example of a low pass rect-filter for which a Gaussian apodization window is applied. The effect of a Gaussian window used with the rect-filter will be to convolve the corresponding sinc-impulse response with the Fourier transform of the window function (another Gaussian). This averaging effectively reduces the side-lobes of the sinc impulse response. In the illustration in Fig. 14.7(a) we show a test image which is low-pass filtered using a simple rec-filter and a Gaussian weighted rect-filter as in Fig.

14.7(b), (c) respectively. The side-lobes of the sinc function are seen to create ringing or ghost-like artifacts near sharp edge features after filtering. These artifacts are seen to be mitigated in the Gaussian apodized low-pass filter.

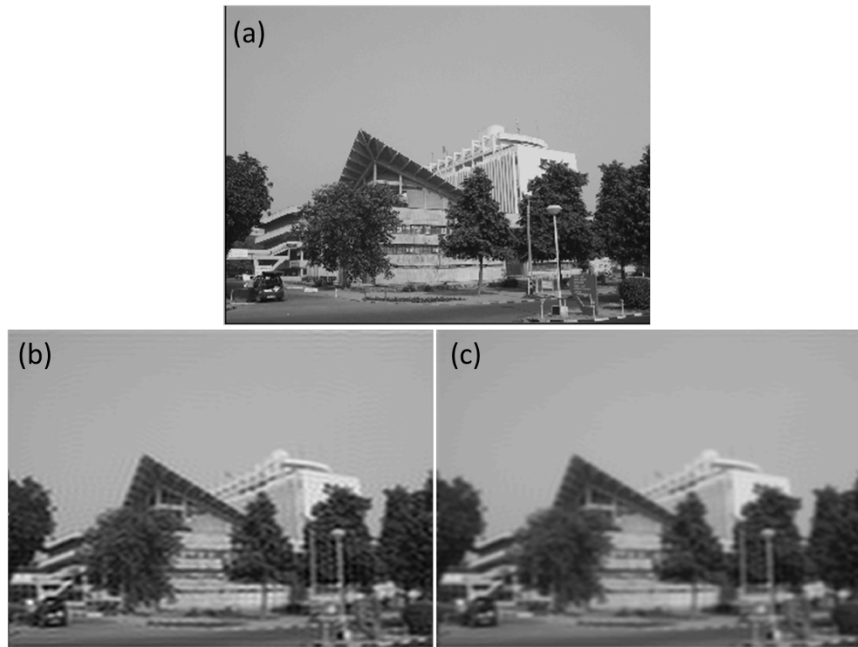


Figure 14.7: Simulation for illustrating apodization: (a) test image, (b) test image filtered using a low-pass rect filter, (c) test image filtered using a Gaussian weighted low-pass rect filter.

14.5 Frequency response of optical imaging systems: coherent and incoherent illumination

Having studied the effects of various Fourier plane filters we now require a formal way to compare the performance of different imaging systems from the perspective of their frequency response. Once again based on our discussion on the 4F system, we have already

noted in Eq. (14.9) that the coherent impulse response of a system is related to the aperture $P(u, v)$ by a Fourier relationship. We define the coherent transfer function $H(f_x, f_y)$ of the imaging system as the Fourier transform of $p(x, y)$ as follows:

$$\begin{aligned} H(f_x, f_y) &= \int_{-\infty}^{\infty} \int_{-\infty}^{\infty} dx dy p(x, y) \exp[-i2\pi(f_x x + f_y y)] \\ &= \int_{-\infty}^{\infty} \int_{-\infty}^{\infty} du dv P(u, v) \delta(f_x - \frac{u}{\lambda F}, f_y - \frac{v}{\lambda F}) \\ &= P(\lambda F f_x, \lambda F f_y). \end{aligned} \quad (14.14)$$

Here we have omitted some inconsequential constant factors in the last step. While we have concentrated on the coherent imaging case so far, several commonly used imaging systems like cameras operate with illumination that is virtually spatially incoherent. In order to arrive at the input-output relation for such systems, we start by relating the two point correlation function in the object and image planes. The correlation function is given by:

$$\begin{aligned} &< u^*(x_1, y_1) u(x_2, y_2) > \\ &= \int \int \int \int dx'_1 dy'_1 dx'_2 dy'_2 < u^*(x'_1, y'_1) u(x'_2, y'_2) > \times \\ &\quad p^*(x_1 - x'_1, y_1 - y'_1) p(x_2 - x'_2, y_2 - y'_2). \end{aligned} \quad (14.15)$$

The function $p(x, y)$ under the integral sign is the coherent impulse response of the system. For incoherent illumination, the two-point correlation in the input plane is given by a delta function:

$$< E^*(x'_1, y'_1) E(x'_2, y'_2) > = I(x'_1, y'_1) \delta(x'_1 - x'_2, y'_1 - y'_2). \quad (14.16)$$

Further setting $x_1 = x_2$ and $y_1 = y_2$ in the output plane gives a relation between field intensities in the input and output planes.

$$\begin{aligned} I(x_1, y_1) &= \int \int dx'_1 dy'_1 I(x'_1, y'_1) |p(x_1 - x'_1, y_1 - y'_1)|^2 \\ &= I(x_1, y_1) * |p(x_1, y_1)|^2. \end{aligned} \quad (14.17)$$

For incoherent illumination case, the function $|p(x, y)|^2$ takes the role of the system's impulse response. The impulse response $|p(x, y)|^2$

is referred to as the incoherent impulse response or the point spread function of the imaging system. Since $p(x, y)$ is related to the aperture of the system by a Fourier transform relation, the frequency response of the system for incoherent case is somewhat more involved. The frequency response for the incoherent case is known by the name of Optical Transfer Function (OTF) defined as:

$$\begin{aligned} & OTF(f_x, f_y) \\ &= \frac{\mathcal{F}\{|p(x, y)|^2\}}{\mathcal{F}\{|p(x, y)|^2\}_{f_x=0, f_y=0}} \\ &= \frac{\int \int dudv P(u + \frac{\lambda F f_x}{2}, v + \frac{\lambda F f_y}{2}) P^*(u - \frac{\lambda F f_x}{2}, v - \frac{\lambda F f_y}{2})}{\int \int dudv |P(u, v)|^2}. \end{aligned} \quad (14.18)$$

Here we have used the auto-correlation theorem in the last step and the two terms under integral sign in the numerator have been symmetrized. In this form the OTF is similar to the ambiguity function defined in Eq. (2.96). The absolute magnitude of the OTF is known as the Magnitude Transfer Function (MTF). . For illustration of the concepts above, we will consider a one-dimensional 4F system with rectangular aperture $P(u) = \text{rect}(u/(2w_x))$. The coherent cutoff frequency of the system is obtained by replacing the variable u with $\lambda F f_x$ so that the highest spatial frequency passed by the system is given by: $f_{cc} = (w_x)/(\lambda F)$. The coherent impulse response of the system is given by $p(x) = 2w_x \text{sinc}(2w_x x)$ and the OTF is given by convolution of two rect-functions which is a triangle function:

$$OTF(f_x) = \Lambda\left(\frac{\lambda F f_x}{2w_x}\right). \quad (14.19)$$

The incoherent cut-off frequency is thus given by $f_{ic} = (2w_x)/(\lambda F)$ which is twice that of the coherent cutoff frequency. This result does not necessarily imply that incoherent systems are capable of resolving better. For example, suppose that in the above example, a coherently illuminated system can just resolve a signal $g(x) = \cos(2\pi f_0 x)$ with $f_0 = f_{cc} = (w_x/\lambda F)$. When incoherent illumination is used, only intensities are of concern so that the input to the system that can just be resolved is now $|g(x)|^2$ which has twice the extent in Fourier space as compared to $g(x)$.

The aberrations in an imaging system may be modeled as phase errors in the Fourier plane relative to an open aperture. For example defocus may be modeled by inserting a quadratic phase mask in the Fourier plane. Figure 14.8 shows the MTF of the system for a rect-function aperture and a rect-function aperture with quadratic phase mask to mimic defocus aberration. The effect of aberrations on OTF is to typically produce a response that shows smaller values compared to the triangle function response of the aberration-free Fourier plane aperture. The cut-off frequency for aberrated and non-aberrated systems is however same since the cut-off is decided by the aperture size. The effect of Gaussian apodization window on a diffraction limited system is also illustrated where the system performance is seen to be better compared to the diffraction limited system for low frequency range. The magnitude of the OTF is referred to

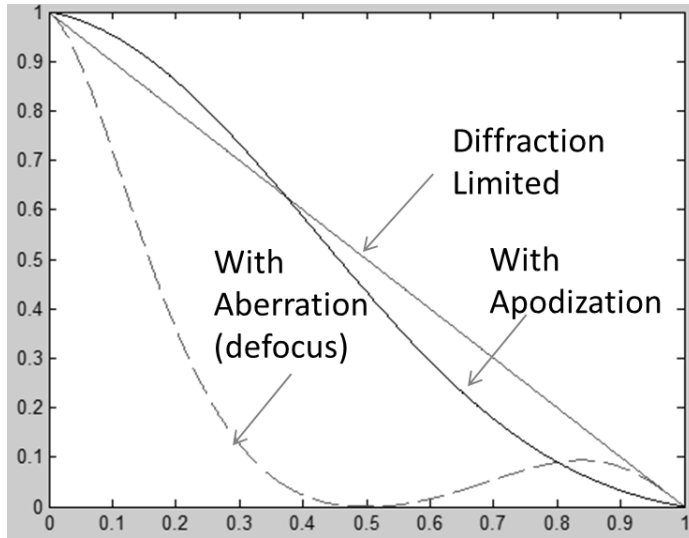


Figure 14.8: Illustration of aberrations and apodization on system MTF: The dotted curve represents the MTF for 0.5 wavelengths of defocus aberration.

as the modulation transfer function (MTF) and is very important for design considerations. The effect of amplitude and phase of OTF on two specific spatial frequency components is illustrated in Fig. 14.9 for clarity. We observe that the effect of MTF is to reduce the am-

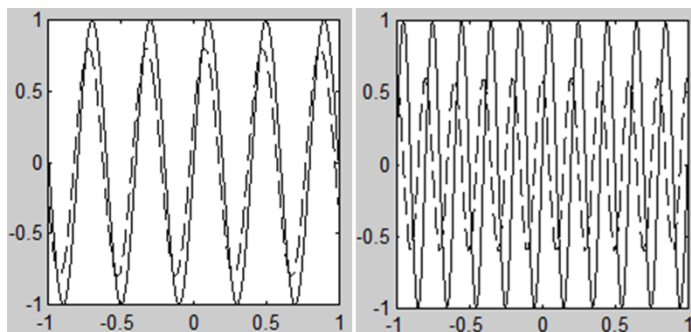


Figure 14.9: Illustration of system OTF on two sinusoidal signals. Input: solid curve, Output: dotted curve. The MTF values reduce the modulation of the particular frequency component and the phase of the OTF creates a relative phase shift in the input sinusoidal signal.

plitude modulation in the input signal and the effect of the phase of OTF at a given spatial frequency is to cause a relative phase shift in the input and output pattern. Since any realistic input image can be decomposed into Fourier components, the overall effect on the image is a combination of spatial frequency dependent amplitude and phase modulation which typically blurs and distorts a given image.

References and suggested reading

1. M. Born and E. Wolf, *Principles of Optics: Electromagnetic Theory of Propagation, Interference and Diffraction of Light*, (Ed. 7) Cambridge Univ. Press (1999).
2. J. W. Goodman, *Introduction to Fourier Optics*, (Ed. 2), McGraw-Hill (1996).
3. K. Iizuka, *Elements of Photonics*, (vol. 1 and 2), John Wiley & Sons (2002).
4. J. W. Goodman, *Statistical Optics*, Wiley-Interscience (2000).

15. Imaging from information point of view

In view of the general framework of computational imaging systems combining optical hardware and algorithms for image recovery as outlined in Chapter 1, we need a mathematical framework for comparison, analysis and possibly synthesis of novel imaging system concepts. As novel optical components (e.g. aspherics, freeform optics, binary/multi-level phase masks, etc.) get incorporated in imaging system design, the conventional metrics for imaging system quality (e.g. Strehl ratio) become difficult to use. This is because image formation process does not end at the image detection stage. The image recovery algorithms have an important role to play as well.

A central question one may study is the quantification of information that an image recovery algorithm may be able to retrieve after light waves carrying this information travel from object through the imaging system aperture and get detected at the imaging sensor. The problem of quantifying information in light waves was first addressed by Gabor in 1950's and subsequently by many researchers as listed in references at the end of this chapter. The treatment in this chapter is presented in terms of the canonical or 4F system as it can effectively mimic a large number of imaging systems and diffraction phenomena. The focus of our analysis will be on basic elements of information that are transmitted by a canonical 4F imaging system. Once such basic elements or system specific modes are determined, they can be used to treat the information propagation through an imaging system. Additional important aspect in this study is the signal-to-noise ratio which will also be seen to limit the information

that may be transmitted by a system.

15.1 Eigenmodes of a canonical imaging system

In this section we will present a brief analysis of the 4F imaging system, and in particular, the information carrying capacity of the system from the object to the image plane. In this context we will discuss the eigenfunction analysis of the 4F imaging systems as presented in [Khare and George 2005 and Khare 2007]. This formulation is on the lines of the discussion on the prolate spheroidal functions as in Section 3.6. For simplicity a one-dimensional notation will be used here. We have already seen in Eq. (14.9) that the impulse response $p(x)$ of a 4F system is related to its aperture $P(u)$ by a Fourier transform relationship. Since the aperture of any practical imaging system is finite in extent, the impulse response $p(x)$ is a bandlimited function and therefore has a sampling expansion. Assuming the bandwidth of the impulse response to be $2B$ we have:

$$p(x) = \sum_{m=-\infty}^{\infty} p\left(\frac{m}{2B}\right) \text{sinc}(2Bx - m). \quad (15.1)$$

Further assuming that the input object extends to a length $x : (-L, L)$ we will study the possibility of finding the eigenmodes $\psi_n(x)$ of the systems that obey the following eigenvalue equation:

$$\mu_n \psi_n(x) = \int_{-L}^L dx' p(x - x') \psi_n(x). \quad (15.2)$$

Here μ_n refers to the eigenvalue corresponding to the eigenfunction $\psi_n(x)$. The eigenvalue μ_n and the eigenfunction $\psi_n(x)$ may be complex valued in general depending on the nature of $p(x)$. To maintain consistency with the analysis on prolate spheroidal functions in Section 3.6 we have used the impulse response $p(x - x')$ above instead of $p(x + x')$ as is expected from Eq. (14.8). This sign change only refers to inversion of the resultant image and is therefore inconsequential for the present discussion. We note that in the discussion of

prolate functions in Section 3.6, a similar eigenvalue equation was studied for the case when $p(x) = \text{sinc}(2Bx)$. The analysis there solely depended on the fact that the sinc-function has a sampling expansion. A similar analysis for the present problem gives rise to a discrete eigenvalue problem that is equivalent to the continuous eigenvalue problem in Eq. (15.2). The discrete eigenvalue problem may be stated as:

$$A\mathbf{u}_n = \mu_n \mathbf{u}_n, \quad (15.3)$$

where the elements of the matrix A are defined as:

$$A_{mk} = \int_{-L}^L dx' p\left(\frac{m}{2B} - x'\right) \text{sinc}(2Bx' - k), \quad m, k = -\infty, \dots, 0, \dots, \infty. \quad (15.4)$$

The vector \mathbf{u}_n is defined as:

$$\mathbf{u}_n = [\dots \psi_n\left(\frac{m}{2B}\right) \dots]^T, \quad (15.5)$$

and is seen to be made up of the Nyquist samples of the eigenfunction $\psi_n(x)$. We further note an interesting connection between the matrix A and the matrix $A^{(0)}$ in Eq. (3.23) that was defined in the analysis of the prolate spheroidal functions. The impulse response $p(m/(2B) - x')$ in the definition of matrix A above may be further expressed as a sampling expansion with respect to the variable x' to get:

$$\begin{aligned} A_{mk} &= \sum_{l=-\infty}^{\infty} p\left(\frac{m-l}{2B}\right) \int_{-L}^L dx' \text{sinc}(2Bx' - l) \text{sinc}(2Bx' - k) \\ &= \sum_{l=-\infty}^{\infty} p\left(\frac{m-l}{2B}\right) A_{lk}^{(0)}. \end{aligned} \quad (15.6)$$

The matrix A is therefore simply a product of the matrix $p_{ml} = p((m-l)/(2B))$ that is formed using the Nyquist samples of the impulse response and the matrix $A^{(0)}$ that was defined in Eq. (3.23) in the analysis of the prolate spheroidal functions. The solution of the discrete eigenvalue problem above gives the eigenvectors that may be sinc-interpolated to get the eigenfunctions $\psi_n(x)$. As an illustration of this sampling theorem based procedure we show in Fig.

15.1(a) the the relative fall-off of eigenvalues for the four impulse responses $p(x) = \text{sinc}(2Bx)$, $\text{sinc}^2(Bx)$, $\text{sinc}^3(2Bx/3)$, $\text{sinc}^4(Bx/2)$ all of which have the same bandwidth. The relative fall-off in the absolute magnitude of the Fourier transform $P(f) = \mathcal{F}\{p(x)\}$ is plotted in Fig. 15.1(b) for comparison. It is interesting to note that there is a striking similarity in the behaviour of the eigenvalue plots and $|P(f)|$. The numerical values of $L = 2$, $B = 2$ and a matrix A of size 101×101 was used for this illustration [Khare 2007]. With a reasoning similar to that for the prolate function case in Section 3.6, we note that the number of significant eigenvalues for a bandlimited impulse response $p(x)$ is approximately equal to the space-bandwidth product $(2L)(2B)$ of the system, although in detail the fall-off in eigenvalues depends on the specific functional form of $p(x)$. The set of eigenfunctions $\{\psi_n(x)\}$ may now be considered as the modes or the fundamental elements of information that may be transmitted by the 4F system from the input to the output plane. The function set is specific to the system impulse response. If the input to the system is represented as a linear combination of the eigenfunctions (at least in the sense of uniform convergence),

$$g_{in}(x) = \sum_n a_n \psi_n(x), \quad (15.7)$$

then the output of the system is easy to determine and is given by:

$$g_{out}(x) = \sum_n \mu_n a_n \psi_n(x). \quad (15.8)$$

The modes with index $n \gg 4BL$ are thus transmitted with very small eigenvalues and may get lost in any detection noise at the output end. Further for a given noise level in detection at the output end, one may compare different systems in terms of their information carrying capacity based on the nature of eigenvalue fall-off. We observe that the analysis presented in this section does not rely on any symmetry properties of the impulse response function $p(x)$ and as a result general cases involving system aberrations (represented by phase variations in Fourier plane) may also be handled using the same procedure. Such analysis typically leads to complex valued eigenfunctions and eigenvalues. We may refer to such complex valued eigenfunctions as the eigenwavefronts associated with the imaging system [Khare and George 2005].

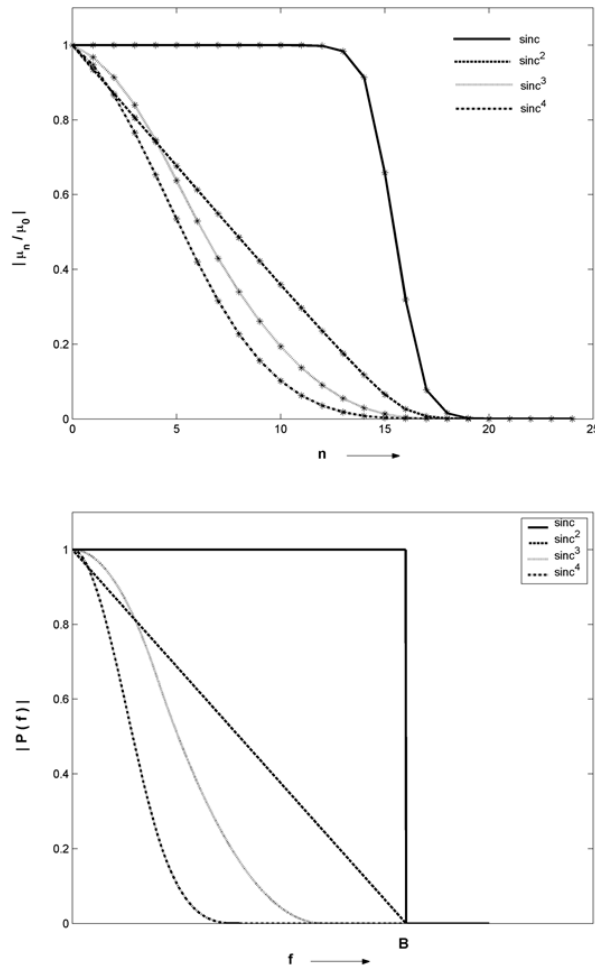


Figure 15.1: Eigenfunction analysis of 4F system: (a) eigenvalues corresponding to the impulse responses $p(x) = \text{sinc}, \text{sinc}^2, \text{sinc}^3, \text{sinc}^4$ all having the same bandwidth, (b) Corresponding magnitudes of the aperture functions $|P(f)|$. The numerical values $L = 2, B = 2$ are used in these illustration. [Adapted with permission from Inverse Problems 23, 1395 (2007)]

15.1.1 Eigenfunctions and inverse problems

The eigenmodes of a general 4F imaging system as may be determined using the procedure shown in the previous section are po-

tentially useful for treating the inverse or image deblurring problems. Suppose that the measured output to a 4F system is denoted by $\tilde{g}_{out}(x)$ which includes the noise at the detection end. We may represent the the measured output as a linear combination of the eigenmodes $\psi_n(x)$ as:

$$\tilde{g}_{out}(x) = \sum_n b_n \psi_n(x). \quad (15.9)$$

While the eigenmodes may not in general be orthogonal to each other, the representation above may be understood as a projection onto the space spanned by the eigenmodes. In other words, the coefficients b_n are selected such that the squared L2-norm error

$$||\tilde{g}_{out}(x) - \sum_n b_n \psi_n(x)||_2^2$$

is minimized. Having represented the output in terms of the eigenmodes, the estimated solution for the input is:

$$\tilde{g}_{in}(x) = \sum_n \frac{b_n}{\mu_n} \psi_n(x). \quad (15.10)$$

We observe that the coefficients b_n contain the effect of noise in the measured data $\tilde{g}_{out}(x)$. As the index n of the terms in Eq. (15.10) increases beyond $(2B)(2L)$ we are in effect dividing the noisy coefficients b_n by small numbers. Division of the noisy coefficients by small numbers in general amplifies the noise in the inverse solution. A simple regularization method to avoid this is to truncate the series solution to a finite number of terms thus effectively reducing the information transmitted from object to image space. The noise at the image detection plane is thus seen to be the fundamental limiting factor in terms of information retrievable by means of an inverse solution as in Eq. (15.10). We illustrate these ideas with a specific example of the inverse problem with the eigenfunctions of the $\text{sinc}^4(Bx/2)$ impulse response. The first ten eigenfunctions for this impulse response for the parameters $L = 2, B = 2$ are shown in Fig. 15.2.

A raised triangle object and the corresponding output blurred by the sinc^4 impulse response with 1% random additive noise are shown in Fig. 15.3 (a) and (b) respectively.

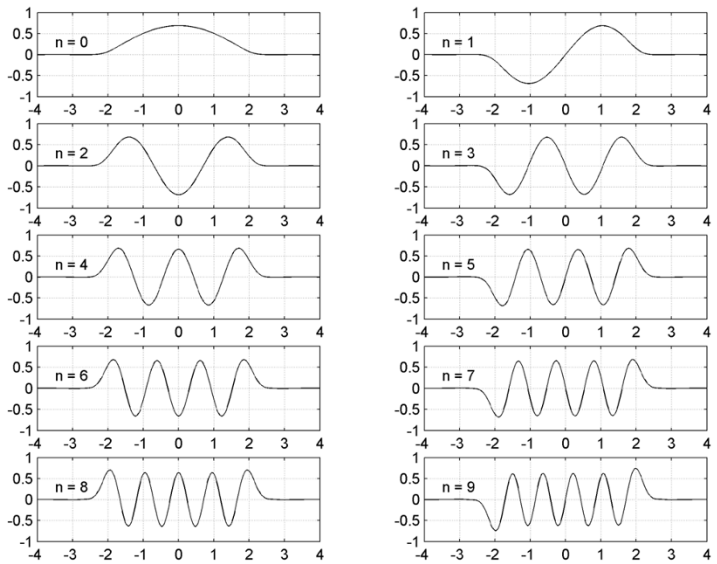


Figure 15.2: First ten eigenfunctions corresponding to the sinc^4 impulse response. The numerical parameters used are $L = 2$, $B = 2$. [Adapted with permission from Inverse Problems 23, 1395 (2007)]

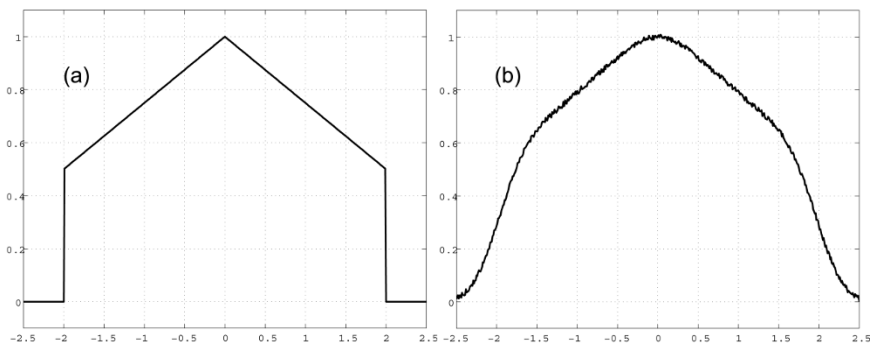


Figure 15.3: (a) Raised triangle object, (b) Object blurred with sinc^4 impulse response with 1% additive random noise. [Adapted with permission from Inverse Problems 23, 1395 (2007)]

The reconstruction of the object using 10, 14 and 18 eigenfunctions is shown in Fig. 15.4 (a), (b) respectively. The solid curves in this Figure show the recovery whereas the dotted curves show the test object. The illustration shows that adding terms with index $N > 4BL$ causes noise amplification due to division by small eigenvalues as discussed above. The noise therefore limits the number of terms that can be included in the series solution thereby limiting the achievable resolution.

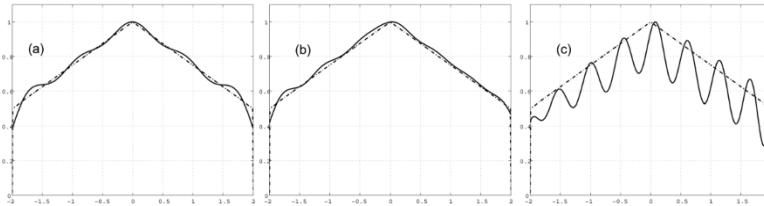


Figure 15.4: Estimation of inverse solution with eigenfunctions for 1% noise. (a),(b) show recoveries using 10, 14 and 18 eigenfunctions respectively. Solid curevs: recovery, Dotted curves: test object. [Adapted with permission from Inverse Problems 23, 1395 (2007)]

While we did not discuss it here, one may further incorporate prior constraints on the solution g_{in} to determine an inverse solution with desired characteristics on the lines of discussion in Chapter 6. The eigenmode analysis of a generic imaging system was provided for a scalar component of light field that is propagated from object to image space was presented here. Additional degrees of freedom including polarization and spectrum of the light waves may be used further to understand the full electromagnetic degrees of freedom available to an imaging system. We will not explore this topic further in this book.

References and suggested reading

1. D. Gabor, "Light and Information", *Progress in Optics*, vol. 1 (ed E. Wolf), pp. 109-153 (North-Holland, Amsterdam) (1961).

2. C. K. Rushforth and R. W. Harris, "Restoration, resolution and noise", J. Opt. Soc. Am., vol. 58, pp. 539-545 (1968).
3. G. Toraldo di Francia, "Degrees of freedom of an image", J. Opt. Soc. Am., vol. 59, pp. 799-804 (1969).
4. M. Bendinelli, A. Consortini, L. Ronchi and B. R. Frieden, "Degrees of freedom and eigenfunctions for the noisy image", J. Opt. Soc. Am., vol. 64, pp. 1498-1502 (1974).
5. M. Bertero and E. R. Pike, "Resolution in diffraction limited imaging, a singular value analysis I, the case of coherent illumination", Opt. Acta, vol. 29, pp. 727-746 (1982).
6. M. Bertero, P. Boccacci and E. R. Pike, "Resolution in diffraction limited imaging, a singular value analysis II, the case of incoherent illumination", Opt. Acta, vol. 29, pp. 1599-1611 (1982).
7. M. Bertero, P. Brianzi, P. Parker and E. R. Pike, "Resolution in diffraction limited imaging, a singular value analysis III, The effect of sampling and truncation of the data", Opt. Acta., vol. 31, pp. 181-201 (1984).
8. cox I. J. Cox and C. J. R. Sheppard, "Information capacity and resolution in an optical system", J. Opt. Soc. Am. A, vol. 3, pp. 1152-1158 (1986).
9. lohmann A. W. Lohmann, R. G. Dorsch, D. Mendlovic, Z. Zalevsky and C. Ferreira, "Space-bandwidth product of optical signals and systems", J. Opt. Soc. Am. A, vol. 13, pp. 470-473 (1996).
10. D. A. B. Miller, "Spatial channels for communicating with waves between volumes", Opt. Lett., vol. 23, pp. 1645-1647 (1998).
11. R. Piestun and D. A. B. Miller, "Electromagnetic degrees of freedom of an optical system", J. Opt. Soc. Am. A, vol. 17, pp. 892-902 (2000).

12. K. Khare and N. George, "Sampling theory approach to eigen-wavefronts of imaging systems", *J. Opt. Soc. Am. A*, vol. 22, pp. 434-438 (2005).
13. K. Khare, "Sampling theorem, bandlimited integral kernels and inverse problems", *Inverse Problems*, vol. 23, pp. 1395-1416 (2007).

Part 3:

Selected Computational

Imaging Systems

16. Digital Holography

Phase measurement is one of the most important problems in Optics. When light waves are scattered by an object, the information about the object is encoded in the scattered waves in the form of amplitude as well as phase variations (apart from possible changes in polarization, spectrum, etc.). The phase information is often much more valuable compared to the amplitude information. While ordinary photography can record amplitude information, holography is an interferometric technique that records both amplitude as well as phase information. Holographic imaging was first demonstrated by Gabor (1949) and a major advance in the form of off-axis hologram was demonstrated by Leith and Upatnieks (1961). There are several excellent resources that discuss the history and development of holography as provided in references to this chapter. The main idea behind the possibility of holographic imaging was already discussed in the context of Rayleigh-Sommerfeld-Smythe diffraction theory in Chapter 10. In particular we obtained the important result that if the tangential E-field is specified in a particular plane (say $z = 0$), then all the components of the E-field are completely determined in the right half space. Consider an object that on illumination by a coherent beam of light produces a certain tangential field $O(x, y, z = 0)$ in the plane $z = 0$ as shown in Fig. 16.1. Now suppose that the same field can be generated in the $z = 0$ plane by some other means so that an observer in the $z > 0$ region receives the same diffracted field as before. In that case even if the original object is not physically present to the left of the screen, the viewer of the scene will perceive its presence. It is clear that the field $O(x, y, z = 0)$ has both amplitude as well as phase in general which needs to be recorded and then re-created. One of the simplest means to generate the same field

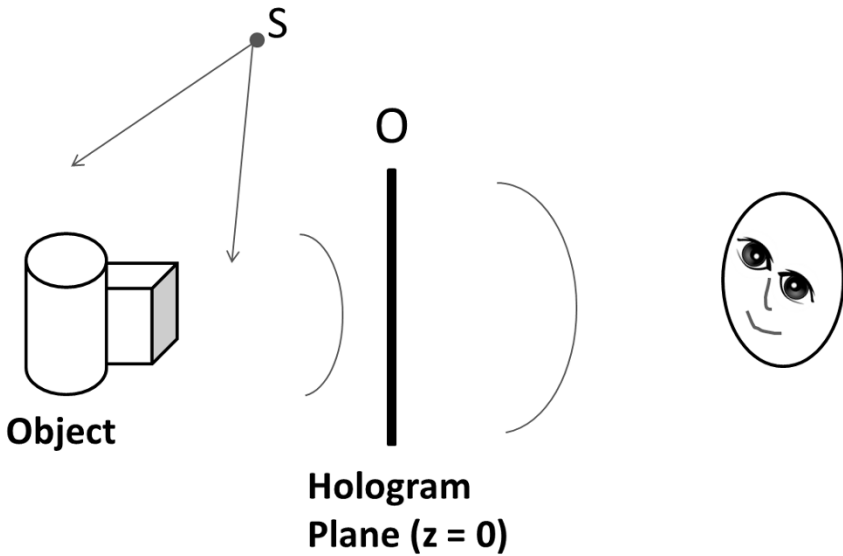


Figure 16.1: Spatially coherent wavefront from source S illuminates an object to produce scattered field whose tangential component in the hologram plane is given by $O(x, y, 0)$. If this field component can be recorded and generated in the hologram plane again, then the viewer on the right hand side will get the same perception as if the object was present in its original location.

$O(x, y, z = 0)$ is to record it interferometrically. As we have already studied in Chapter 12, an interference pattern with good fringe contrast (or visibility) may be recorded if the two interfering beams are mutually coherent. Typically a reference beam R is derived from the same source by means of a beam-splitter device and is interfered with the object beam O at the $z = 0$ plane which we will now refer to as the hologram plane. The interference pattern H recorded on a square-law area detector is described as:

$$H = |R + O|^2 = |R|^2 + |O|^2 + R^*O + RO^*. \quad (16.1)$$

The phase information about the object wave O is recorded in an encoded form in the last two terms of the above equation. The object beam may be recorded this way using multiple configurations.

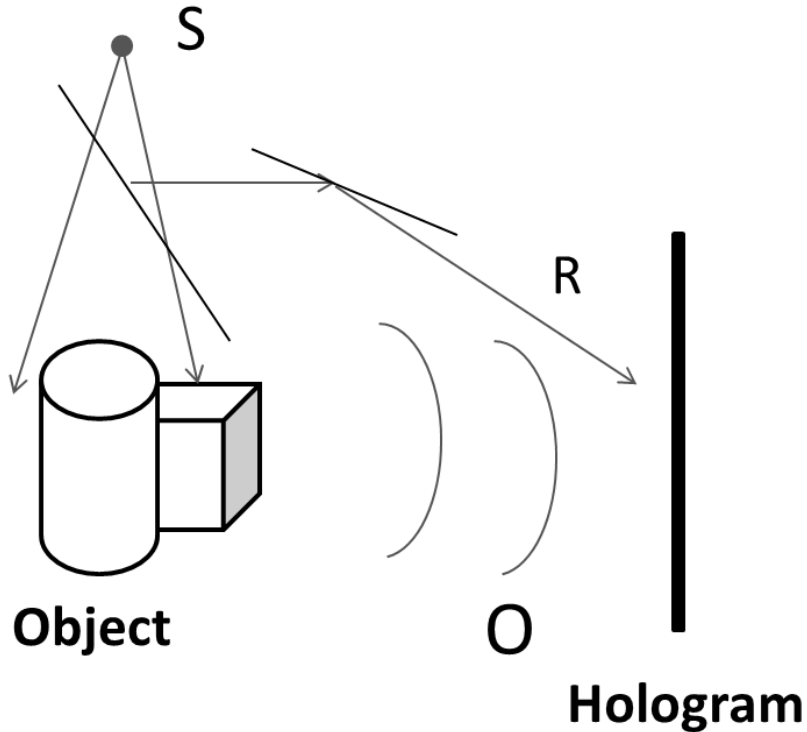


Figure 16.2: Recording of a hologram to store amplitude and phase information in object wave O .

For example, if the field $O(x, y)$ at the hologram plane represents the Fraunhofer or Fresnel diffraction pattern corresponding to the object being imaged, we may term the hologram as Fourier transform hologram or Fresnel hologram. If on the other hand the object field $O(x, y)$ corresponds to the image of the object, the hologram is termed as the image plane hologram.

In traditional film-based holography, the hologram pattern H is recorded on a high resolution photographic film and the replay of the hologram is achieved by physical re-illumination of the hologram with a counter-propagating or conjugate beam R^* . Assuming that the transmission function of the developed film is linearly proportional to the hologram intensity pattern H , the re-illumination

process of the hologram with the R^* beam creates a field profile R^*H in the hologram plane:

$$R^*H = R^*|R|^2 + R^*|O|^2 + R^{*2}O + |R|^2O^*. \quad (16.2)$$

The cross terms in the above equation (third and fourth terms on right hand side) are important as they are proportional to the complex object waves O and O^* . These two terms evolve via diffraction and form real and virtual images of the original object. From early days of holography till mid-1990's holographic imaging continued to be performed preferentially using high resolution photographic films.

Our goal in this chapter is to concentrate on the topic of digital holography which has become a popular computational phase imaging modality over the last 20 years or so after the availability of high quality CCD/CMOS sensors. We will not consider the formalism where a physical illumination beam is employed for replay of the hologram but assume that the hologram H as above is available as a sufficiently sampled 2-dimensional array of numbers that are read out from an array sensor. We will discuss some of the traditional methods for processing digital holograms (holograms recorded on array sensors) that are in-principle similar to the traditional film-based hologram replay. We will also present a brief discussion of some recent developments of using an optimization approach to complex object wave recovery from holograms. This new optimization approach will be seen to overcome the important limitations of the traditional digital processing methods that mimic film based hologram replay numerically.

16.1 Sampling considerations for recording of digital holograms

Throughout this chapter we will simply assume that the hologram H in Eq. (16.1) has been recorded on an array sensor such as CCD or CMOS. It then becomes important to understand some sampling issues in recording of the hologram on an array sensor. When two plane waves with a nominal angle 2θ between their k-vectors interfere, it can be shown that the fringe period is given by $\lambda/(2 \sin \theta)$.

Clearly as per the Nyquist criterion, we must have at least two sam-

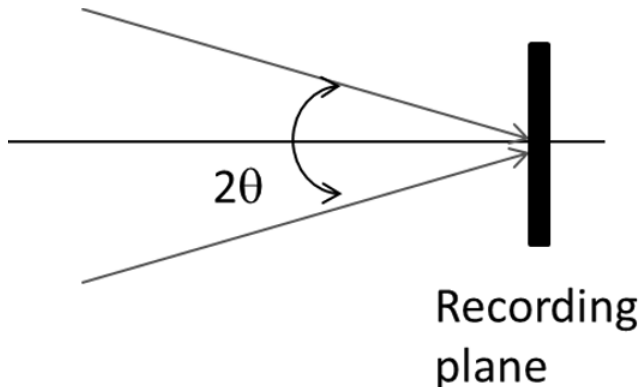


Figure 16.3: Recording of a hologram/interference pattern resulting from two plane waves with an angle 2θ between them.

ples of the interference pattern per fringe period. In practice it is suitable to have 3-4 pixels span one fringe period. For sensor pixel size of $5 \mu m$ and $\lambda = 0.5 \mu m$, the nominal angle between two beams cannot be very large (1-2 degrees) when recording a digital hologram. In this respect digital holography differs from film based holography as high resolution films readily allow much larger angle (30-40 degrees) between two interfering beams.

16.2 Complex field retrieval in hologram plane

In this section we will consider three different approaches to retrieval of complex object wave information from recorded hologram pattern(s), which is an important first step in processing of digital holograms. The retrieved object field can then be numerically propagated using diffraction formalism for final image formation in case the hologram is a Fresnel or Fourier transform hologram. In case of image plane hologram the retrieved complex field directly corresponds to the required complex image.

16.2.1 Off-axis digital holography

Off-axis digital holography as first proposed in the work of Leith and Upatnieks uses a plane wave reference beam at a nominal angle θ relative to the object wave $O(x, y)$. The reference beam may be described as $R = R_0 \exp(i2\pi f_0 x)$ where $f_0 = \sin \theta / \lambda$ and the resulting interference pattern can be described as:

$$H = |R_0|^2 + |O(x, y)|^2 + 2|R_0||O(x, y)| \cos[2\pi f_0 x - \arg(O(x, y))]. \quad (16.3)$$

The amplitude $|R_0|$ of the plane reference beam is essentially con-

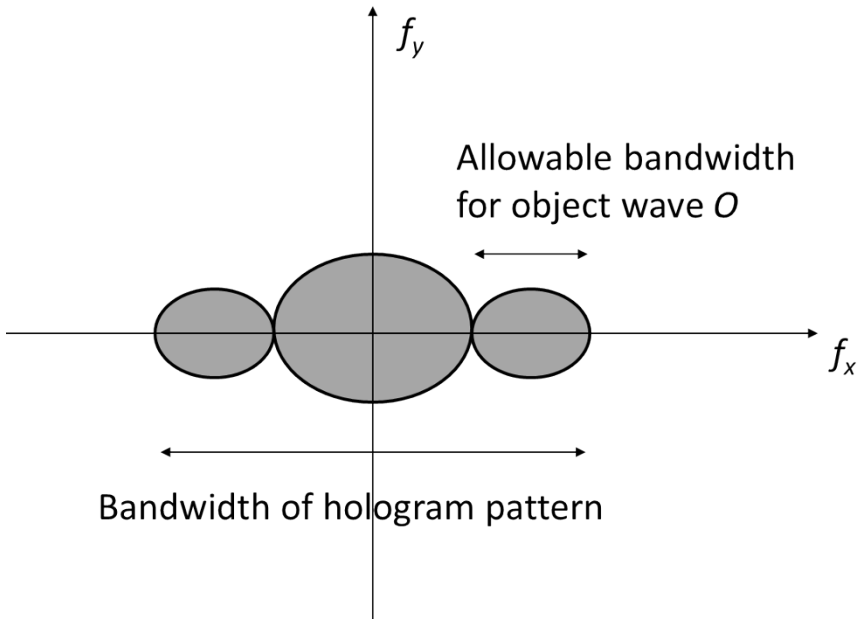


Figure 16.4: Fourier transform representation of the off-axis hologram showing dc and cross-terms.

stant across the hologram. The Fourier transform structure of the off-axis hologram is as shown in Fig. 16.4 and consists of three main lobes. The first two term $|R_0|^2$ and $|O(x, y)|^2$ are located near the center of the (f_x, f_y) plane and are known as the dc terms. The cosine term in Eq. 16.3 can be split into two terms that are located at spatial frequency locations $(f_0, 0)$ and $(-f_0, 0)$. The information of

interest about the complex object wave $O(x, y)$ is contained in one of the side lobes in the Fourier plane. If this lobe is filtered out, the object wave may be recovered. In a single shot operation, one must make sure that the three different lobes do not overlap with each other substantially. Suppose the expected bandwidth of the object wave is $2B$ along the x-direction, the width of the central lobe in the Fourier transform plane corresponding to the term $|O(x, y)|^2$ is $4B$ and the transform of $|R_0|^2$ is a delta function located at the zero frequency. In order to make sure that the dc and the crosss term do not overlap, we must therefore have:

$$f_0 = \frac{\sin \theta}{\lambda} \geq 3B. \quad (16.4)$$

The reference beam angle is thus selected carefully to avoid overlap of terms in Fourier space and subsequent loss of information about the object wave. We observe that the allowable object wave bandwidth is much smaller than the total hologram bandwidth along the x-direction due to the non-overlap condition. In single shot op-

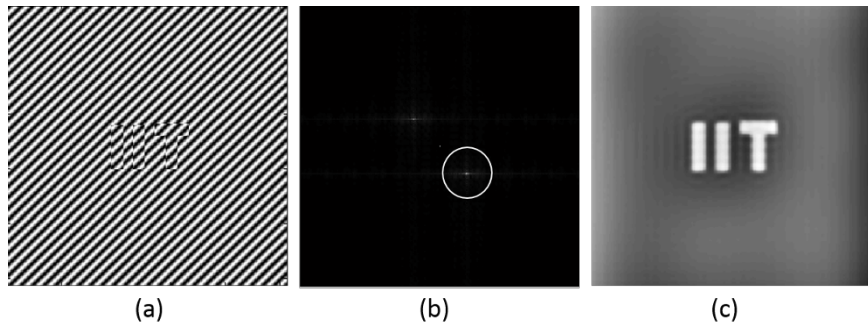


Figure 16.5: Steps in complex object wave retrieval for the Fourier transform method. (a) Hologram, (b) 2D Fourier transform of the hologram. The region shown by circle centered on the cross-term peak is the filtered and brought to the center of the Fourier space. (c) Recovery of object wave (phase shown here) by inverse Fourier transformation.

eration, one may process the digitally recorded hologram signal in following steps :

1. Compute the 2-dimensional Fourier transform of the off-axis hologram,
2. locate the carrier-frequency peak and filter out appropriate region of the Fourier transform plane near the carrier-frequency peak,
3. shift the filtered region to zero frequency (or dc) in Fourier transform plane,
4. compute inverse Fourier transform of the dc shifted field to obtain the complex object field $O(x, y)$ in the hologram plane.

The sequence of steps above is shown diagrammatically in Fig. 16.5. If a hologram is sampled just adequately on an array sensor, then the detector bandwidth is approximately same as the total hologram bandwidth shown in Fig. 16.4. The allowable object bandwidth is however much smaller than what the detector is capable of resolving when the Fourier transform method is used due to the overlap consideration of Fourier bands of the hologram signal. For the image plane hologram of the IITD phase object we see that the single shot hologram followed by Fourier transform method loses resolution due to Fourier domain filtering.

16.2.2 Phase shifting digital holography

Phase shifting is a technique used to regain the lost resolution in Fourier transform method. Multiple digital holograms are recorded on a digital array sensor with known phase shifts in the reference beam. For example if the R beam gets four pre-determined phase shifts $0, \pi/2, \pi$, and $3\pi/2$, the corresponding digital holograms as per Eq. (16.1) are given by:

$$\begin{aligned} H_1 &= |R|^2 + |O|^2 + 2|R||O| \cos(\phi_O - \phi_R), \\ H_2 &= |R|^2 + |O|^2 - 2|R||O| \sin(\phi_O - \phi_R), \\ H_3 &= |R|^2 + |O|^2 - 2|R||O| \cos(\phi_O - \phi_R), \\ H_4 &= |R|^2 + |O|^2 + 2|R||O| \sin(\phi_O - \phi_R). \end{aligned} \quad (16.5)$$

In the above equation, the terms ϕ_O and ϕ_R denote the 2-dimensional phase functions corresponding to the object and reference beams respectively at the hologram plane. Known phase shifts can be added to the reference beam in several ways, e.g. introducing appropriate combination of wave retarder plates in the reference beam, introducing a QHQ (Q=quarter wave plate, H= half wave plate) geometric phase shifter in the reference beam, using a piezo-electric transducer to shift the location of an optical component like a mirror in the reference beam path, etc. By adding the known reference phase shifts to the reference beam, it is now possible to obtain both the sine and cosine quadratures of the unknown phase. If the reference phase ϕ_R is known, we can obtain the object beam phase as:

$$\phi_O(x, y) = \phi_R(x, y) + \arctan\left(\frac{H_4 - H_2}{H_1 - H_3}\right). \quad (16.6)$$

Observe that unlike off-axis holography, the reference beam does not have to be an off-axis plane wave but can in general have any known phase profile. In Fig. 16.6 we diagrammatically show the complex object recovery for a phase object using the phase shifting method. For illustration a plane reference wave is used as can be seen from the fringes. Illustration in Fig. 16.6 shows the steps in the recovery of the IIT phase object with four hologram frames and we clearly see the high resolution phase object recovery. At the cost of recording multiple frames the phase shifting digital holography regains the full detector resolution. It is required that during the recording of the multiple hologram frames, the object remains stationary. Also it is important to remember that while recording the four data frames as in Eq. (16.5) in the laboratory, each data frame contains noise (e.g. detector readout noise and photon noise), and as a result by processing the four frames as above there is a noise penalty to pay in terms of accuracy of the measured phase. The noise part while not considered here is considered to limit the phase measurement accuracy ultimately to the shot-noise or \sqrt{N} level where N is the average number of photon events recorded in a single digital hologram pixel.

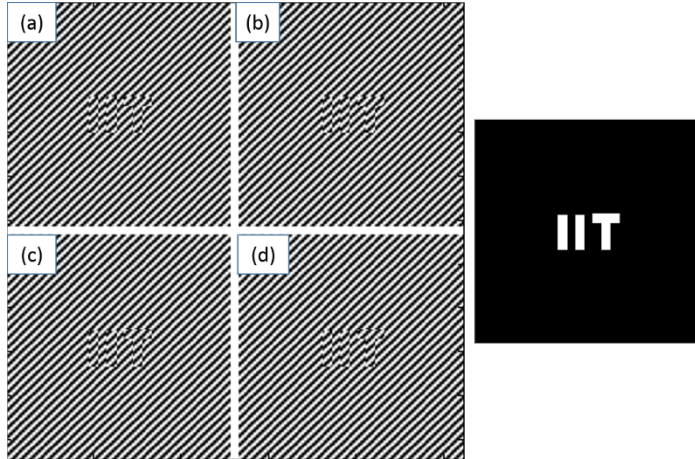


Figure 16.6: Phase shifting digital holography, (a)-(d): Four holograms for the IIT phase object with reference beam phase shifts given by $0, \pi/2, \pi, 3\pi/2$ respectively. (e) Recovery of object phase using Eq. (16.6).

16.2.3 Optimization method for complex object wave recovery from digital holography

The Fourier transform method, the phase shifting method and their variations are well-established, however, they have certain limitations due to the nature in which the information recovery from a digital hologram is understood. For example while Fourier transform method can perform single shot holographic imaging, it by default achieves lower resolution than what the digital detector array is capable of. Due to sampling considerations, the allowable reference beam angle for off-axis hologram is already quite small and the non-overlap requirement for the dc and cross term lobes in Fourier domain further reduces the attainable object resolution. The phase shifting method regains the detector resolution, however, multiple hologram frames have to be recorded. The optical system has to be stable during the multiple recordings and further the object needs to be stationary during the recording process. There is also a noise penalty to be paid when recording multiple hologram frames. The optimization method as proposed recently by the present author

and co-workers provides a way to address some of these limitations. Early results using the optimization method are very interesting and we outline this method briefly. The Fourier transform method and the phase shifting method rely on linear processing of the hologram data and are in some sense equivalent to replay of the film based holograms. With the digitally recorded data in hand, a new framework for hologram data processing may be evolved. In particular the problem of complex object wave recovery from a hologram may be modeled as an optimization problem such that we minimize a cost function of the form:

$$C(O, O^*) = \|H - (|R|^2 + |O|^2 + R^*O + RO^*)\|^2 + \alpha\psi(O, O^*). \quad (16.7)$$

The first term above is the least square or L2-norm squared error that represents consistency of the solution O with the hologram data H . The reference beam is assumed to be known as is the case with the Fourier transform method or the phase shifting method. The second term is the constraint term that models some desired property of the solution O depending on the Physics of the problem. For example if we are recording a Fresnel hologram, we expect the solution for object wave $O(x, y)$ to have a smooth profile whereas in case of an image plane hologram, the solution $O(x, y)$ is expected to retain information about sharp edges in the object to be imaged. The optimization problem above is peculiar in that the cost function to be minimized is real and positive valued but the solution of interest $O(x, y)$ is complex valued. For optimization purpose it is necessary to evaluate the functional gradient of the cost function to find the descent direction in which the solution is to be propagated starting with some initial guess. We have already studied one such problem in Chapter 6 and recall that direction of steepest descent for δC is obtained when the variation δO is in the direction of $\nabla_{O^*}C$. A gradient descent iteration may now be written as:

$$O^{(n+1)} = O^{(n)} - t[\nabla_{O^*}C]_{O=O^{(n)}}, \quad (16.8)$$

where $O^{(n)}$ denotes the guess solution for O at the n -th iteration. The step size “ t ” may be selected using standard backtracking line search. The off-axis image plane hologram shown in Fig. 16.5(a) of the IITD phase object is processed with the gradient descent iteration above and a Total Variation penalty is used for $\psi(O, O^*)$.

The recovered object phase is shown in Fig. 16.7. We observe that the penalty function $\psi(O, O^*)$ effectively models the redundancy in the expected solution and provides high quality image recovery even though the single shot hologram data is considered incomplete from the perspective of traditional methods for processing of digital hologram. The present author and co-workers have recently demonstrated both resolution and noise advantage of the optimization technique. In particular, it has been shown that high resolution image recovery is possible even if the dc and the cross terms overlap substantially. Further the single shot phase imaging capability of the optimization method provides a significant noise advantage over the traditional methods like phase shifting that treat individual pixels in hologram data as independent of each other.

As of now the optimizations method has not been studied in its full detail. Initial results indicate that practical computational holographic imaging systems with superior performance are realizable if we employ this technique.

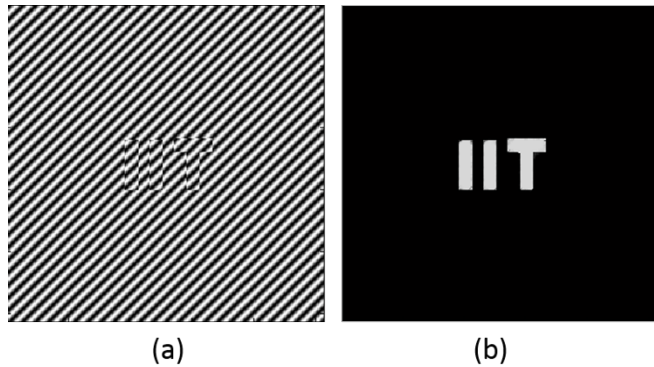


Figure 16.7: Recovery of IIT phase object from single digital hologram frame using constrained optimization method. The Total Variation penalty is used here as a constraint. (a) Holohram, (b) Phase recovery.

16.3 Digital holographic microscopy

Digital holography can be adapted appropriately for microscopy applications where it is important to image transparent objects such as label-free cell samples. At present the traditional brightfield microscopy does not provide good depth information. The depth information is recoverable if phase change in the light beam as it passes through the sample is recorded. The modalities such as phase contrast do respond to phase change but do not provide any quantitative phase information. The quantitative phase information can readily be obtained by interferometric means. The 3D scanning microscopy options such as laser scanning confocal microscopes are too costly for routine microscopy work, say in pathology labs. Digital holographic microscopes have a potential in this regard that they can allow single shot high resolution 3D imaging of cells. The design and performance of such microscopes depends critically on the algorithmic approach used for image recovery. A digital holographic micro-

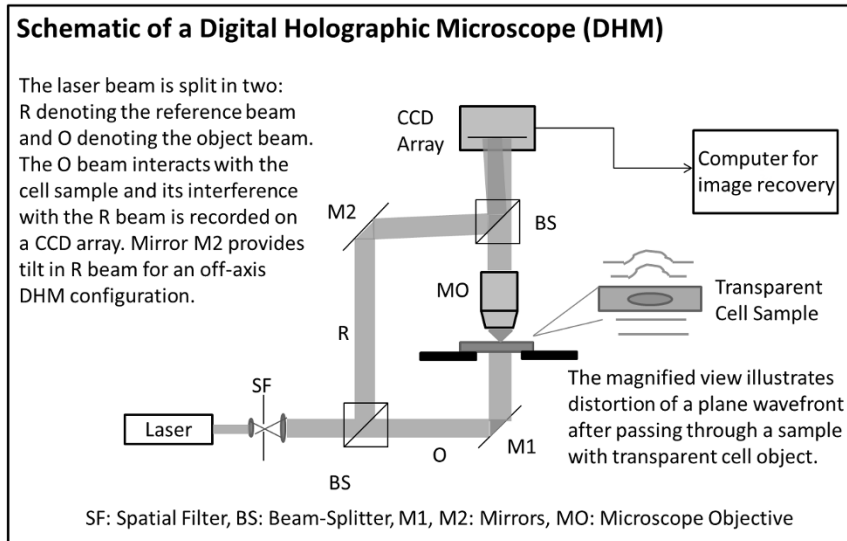


Figure 16.8: Schematic of a Digital Holographic Microscope system.

scope system is shown schematically in Fig. 16.8 where a Mach-

Zehnder interferometer configuration is used for recording a digital hologram of transparent cell samples. The microscope objective is used here in order to provide magnification. The phase information obtained with a digital holographic microscope corresponds to the local optical path difference suffered by light waves by the relation:

$$\phi(x, y) = \frac{2\pi}{\lambda} (n_{cell} - n_{medium}) L(x, y). \quad (16.9)$$

Here n_{cell} and n_{medium} denote the local refractive index inside the cell and the surrounding medium and $L(x, y)$ denotes the cell thickness. The phase map thus effectively contains the information about the refractive index distribution inside the cell which can be ultimately related to its chemical composition. If high resolution low noise recovery of cell images is made, digital holography can potentially provide diagnostic information from cell images since in addition to the usual amplitude image, information about a third dimension (phase) is also available. Fig. 16.9 shows the holograms of transparent cell samples and the corresponding phase recovery shown as a 3D surface plot. The phase image may be recovered using any of the three methods discussed above. An interesting aspect of imaging using a holographic microscope is that the complex object wave in the hologram plane may be used to obtain a focused image in a plane that is typically not accessible due to limited depth of focus of a high NA microscope objectives. The propagation of the field may be performed using the angular spectrum or the Fresnel diffraction method and the sharp features in the image after propagation may be considered as focused objects in the new plane.

16.4 Summary

Digital holography is an important computational imaging modality that provides amplitude as well as phase information and thus has several interesting applications in bioimaging, metrology, etc. We have discussed some standard linear methods for processing of digital holograms and also provided a brief discussion of a novel optimization based procedure for recovering complex object wave information from digital holograms. Several other forms of digital

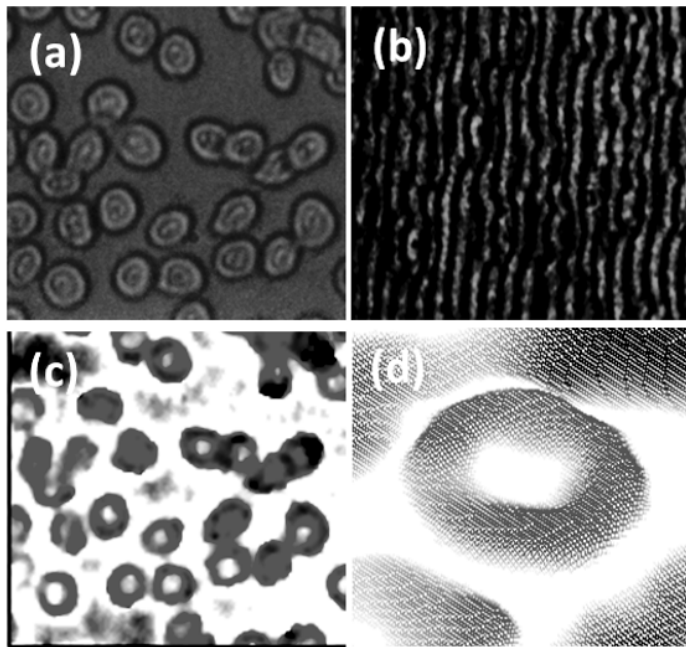


Figure 16.9: Cell imaging using Digital holographic microscope: (a) Brightfield image of Red Blood Cells, (b) Digital hologram of the cell sample, (c) Phase image recovered from the hologram, (d) 3D rendering of single cell. Each blood cell is approximately 8-10 μm in lateral dimension.

holography, e.g. low coherence (broadband light) digital holography, parallel phase shifting digital holography, Fresnel incoherent digital holography, etc. have not been discussed here but the reader can easily follow literature on these recent developments after studying the material provided in this chapter.

References and suggested reading

1. D. Gabor, “A new microscopic principle, Nature 161, 177-178 (1948).
2. E. N. Leith and J. Upatnieks, “Reconstructed wavefronts and communication theory, J. Opt. Soc. Am. 52, 1123-1128

- (1962).
3. J. W. Goodman and R. W. Lawrence, “Digital image formation from electronically detected holograms, *Appl. Phys. Lett.* 11, 77-79 (1967).
 4. M. Takeda, H. Ina, S. Kobayashi, “Fourier transform method of fringe pattern analysis for computer based topography and interferometry”, *J. Opt. Soc. Am.* 72, 156-160 (1982).
 5. H. Chen, M. Shih, E. Arons, E. N. Leith, J. Lopez, D. Dilworth, and P. C. Sun, “Electronic holographic imaging through living human tissue,” *Appl. Opt.* 33, 3630-3632 (1994)
 6. U. Schnars and W. P. Juptner, “Direct reconstruction of holograms by a CCD target and numerical reconstruction, *Applied Optics* 33, 179-181 (1994).
 7. I. Yamaguchi and T. Zhang, “Phase shifting digital holography”, *Opt. Lett.* 22, 1268-1270 (1997).
 8. E. Cuche, F. Bevilacqua, and C. Depeursinge, “Digital holography for quantitative phase contrast imaging, *Opt. Lett.* 24, 291-293 (1999).
 9. E. Cuche, P. Marquet, and C. Depeursinge, “Simultaneous amplitude-contrast and quantitative phase-contrast microscopy by numerical reconstruction of Fresnel off-axis holograms, *Appl. Opt.* 38, 69947001 (1999).
 10. M. Liebling, T. Blu, M. Unser, “Complex-wave retrieval from a single off-axis hologram”, *J. Opt. Soc. Am. A* 21, 367-377 (2004).
 11. L. Yaroslavsky, *Digital holography and digital image processing*, Kluwer Academic (2010).
 12. M. K. Kim, “Principles and techniques of digital holographic microscopy, *SPIE Reviews* 1, 018005-1 -018005-50 (2010).
 13. K. Khare, Samsheerali P. T., J. Joseph, “Single shot high resolution digital holography”, *Opt. Express* 21, 2581-2591(2013).

14. Samsheerali P. T., K. Khare, J. Joesph, “Quantitative phase imaging with single shot digital holography”, Opt. Communications 319, 85-89 (2014).
15. M. Singh, K. Khare, A. K. Jha, S. Prabhakar, R. P. Singh, “Accurate multipixel phase measurement with classical light interferometry”, Phys. Rev. A 91, 021802(R) (2015).
16. Rosen J. and Brooker G. “Digital spatially incoherent Fresnel holography, Optics Lett. 32, 912-914 (2007).

17. Phase retrieval from intensity measurements

Phase retrieval from intensity measurements is one of the most challenging computational imaging problems. In Chapter 11 we already discussed the Transport of Intensity Equation (TIE) technique which relates the longitudinal intensity derivative of a diffraction field (in Fresnel zone) to the transverse phase gradient. The solution of the problem was studied in that case with a direct Fourier transform based method. In Chapter 16, we discussed interferometric approach to phase measurement. There are however practical situations (e.g. X-ray imaging, imaging through turbulent atmosphere) where setting up an interferometer is not always easy. In this chapter we will describe non-interferometric iterative techniques that allow one to reconstruct an object from the absolute magnitude of its Fourier transform when some additional constraints are imposed on the object. Some well known algorithms such as the Gerchberg-Saxton method and the Fienup hybrid input-output algorithm will be discussed.

The phase retrieval problem may be stated as follows:

Determine an unknown object function $g(x, y)$ from the magnitude $|G(f_x, f_y)|$ of its Fourier transform.

Clearly any randomly selected phase function when associated with the magnitude $|G|$ will correspond to a solution. However the challenging task in this problem is to find a solution that satisfies physically meaningful constraints. The iterative solution thus sequentially enforces the magnitude constraint in the Fourier transform domain

and constraints representing any physically desirable properties of the solution $g(x, y)$ in the image domain.

The phase problem occurs naturally in study of Fraunhofer diffraction where the measured diffraction intensity pattern $|G(f_x, f_y)|^2$ is not sufficient to reconstruct object due to lack of phase information. Another case where the phase retrieval problem occurs is that of astronomical imaging through turbulent atmosphere. For example, in the technique known as speckle interferometry, the short exposure images of a star object $o(x, y)$ are recorded sequentially for multiple realizations of atmospheric turbulence. The resultant set of images may be described by:

$$g_k(x, y) = o(x, y) * p_k(x, y), \quad (17.1)$$

where $p_k(x, y)$ denotes the combined PSF of the telescope system and the atmosphere turbulence effects. The name speckle interferometry arises from the fact that the individual short exposure images have a speckle-like structure due to the atmosphere induced random phase changes in system aperture. If the images $g_k(x, y)$ are averaged, the averaged image will simply be equivalent to long-time averaging over atmospheric turbulence and the resultant image will have a large blur. Instead as first proposed by Labeyrie (1970), the averaging is performed in the Fourier domain as:

$$\langle |G_k(f_x, f_y)|^2 \rangle = |O(f_x, f_y)|^2 \langle |P_k(f_x, f_y)|^2 \rangle. \quad (17.2)$$

The quantity $\langle |P_k(f_x, f_y)|^2 \rangle$ may be measured separately by imaging a nearby unresolved (delta function like) start object that sees similar atmospheric turbulence statistics. The result is that one obtains the Fourier transform intensity $|O(f_x, f_y)|^2$ corresponding to the object $o(x, y)$ of interest. Another example of Fourier transform intensity measurement is X-ray diffraction studies, where the recorded intensity pattern is proportional to the absolute squared magnitude of the Fourier transform of the electronic density in the crystal structure under investigation. Phase retrieval is valuable in these and allied problems.

17.1 Gerchberg Saxton algorithm

We will discuss some of the main ideas in phase retrieval starting with the Gerchberg-Saxton (GS) method which is also known by the name of error-reduction method. The basic structure of the GS method may be described by means of the flowchart in Fig. 17.1. Given the data corresponding to measurement of the modulus

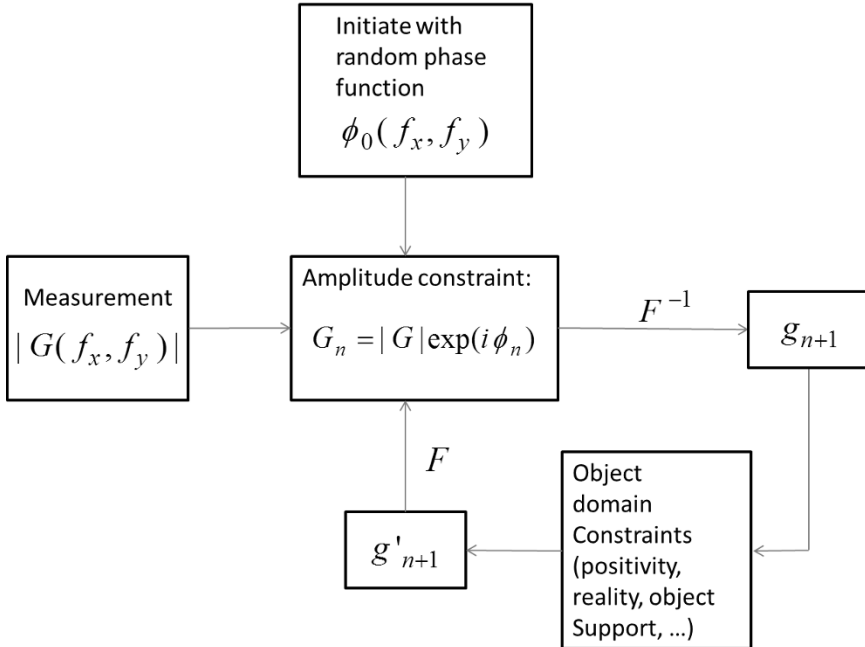


Figure 17.1: Schematic diagram showing steps in Gerchberg-Saxton method for phase retrieval.

$|G(f_x, f_y)|$ of the Fourier transform, an initial guess for the function $G(f_x, f_y)$ is made using a phase function $\phi_0(f_x, f_y)$ where the values of the phase function are selected from a random distribution in $[-\pi, \pi]$. Steps in the n -th iteration of the algorithm are as follows:

1. The function $G_n(f_x, f_y)$ is inverse Fourier transformed to obtain a guess solution $g_{n+1}(x, y)$.
2. Any prior information about the object is applied to the guess solution $g_{n+1}(x, y)$ to obtain a modified guess solution $g'_{n+1}(x, y)$.

The constraints of interest may include positivity of the solution $g(x, y)$, information about object support, etc. The image pixels not satisfying the desired constraint are set to zero.

3. The modified solution is Fourier transformed to obtain the next guess $G_{n+1}(f_x, f_y)$ for the Fourier transform $G(f_x, f_y)$. The function $G_{n+1}(f_x, f_y)$ is then modified such that its amplitude is replaced by the known modulus $|G(f_x, f_y)|$ and its phase is left unchanged.

As an illustration we show the recovery of an image from its Fourier transform magnitude 17.2(a) using 5, 10, 100 iterations of the GS method in Fig. 17.2(b)-(d) respectively. For this illustration we have used the positivity and object support (or size) as constraints in object domain.

17.2 Fienup's hybrid input-output algorithm

While GS method works well for simple objects as used in the illustration in Fig. 17.2, it is known to have stagnation problems with more complex greyscale objects. An important advance over the GS method which is far superior in terms of the stagnation issues is the Fienup hybrid input-output (HIO) algorithm. The algorithm treats the solution update step as a negative feedback process. For example, as shown in Fig. 17.3, consider the process that enforces the Fourier domain magnitude constraint. The image $g(x, y)$ is Fourier transformed and the amplitude of the resultant transform is replaced by the known modulus $|G|$. On inverse Fourier transforming we get a new function $\hat{g}(x, y)$. The pixels in the new image may be divided into two sets: (i) set Γ : those satisfying the object domain constraints (e.g. positivity) and (ii) those which do not obey the object domain constraints. While the pixels of \hat{g} that obey the object domain constraints are retained as is, the pixels that do not obey the object domain constraints can be used to provide a negative feedback to the previous guess solution. With this idea, the update step

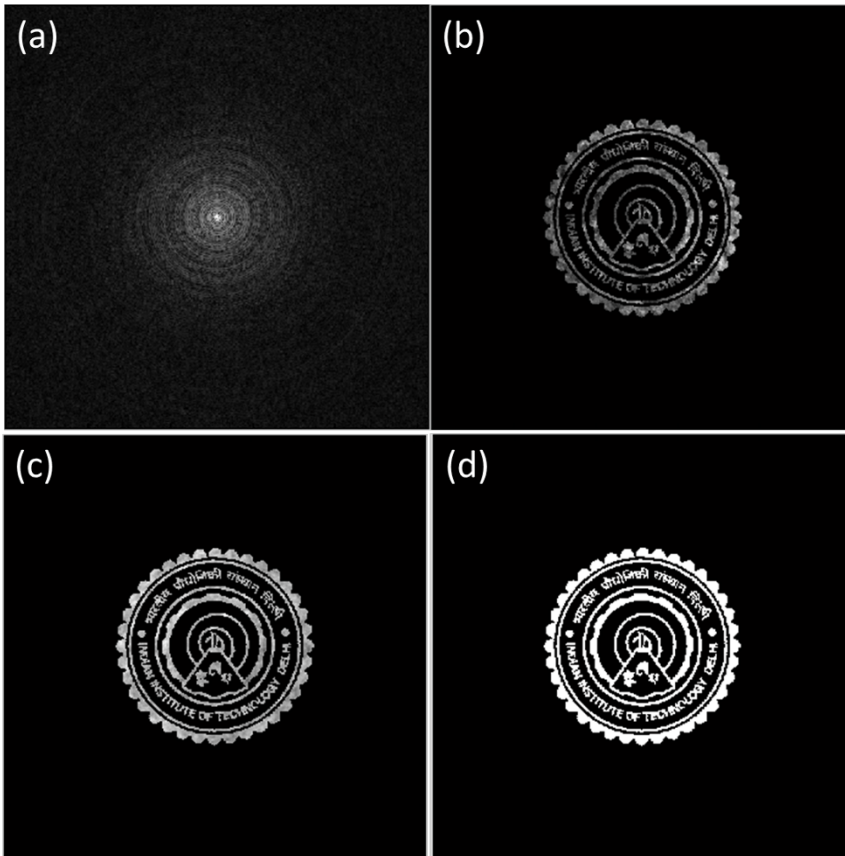


Figure 17.2: Illustration of the Gerchberg-Saxton method for phase retrieval: (a) Modulus $|G|$ of Fourier transform of an object, recovery of image with (b) 5, (c) 10, and (d) 100 iterations of the GS method. The object domain constraints used are positivity and object support.

for the hybrid input-output algorithm is:

$$\begin{aligned} g_{n+1}(x, y) &= \hat{g}_n(x, y), & (x, y) \in \Gamma \\ &= g_n(x, y) - \beta \hat{g}_n(x, y), & (x, y) \notin \Gamma. \end{aligned} \quad (17.3)$$

Here β is some positive parameter whose value is selected in range $(0, 1)$. The effectiveness of the Fienup method for the more complicated Lena object is illustrated in Fig. 17.4. Using the modulus of

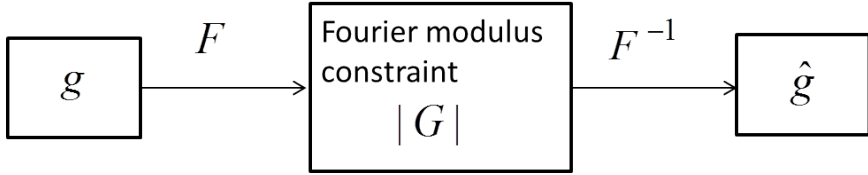


Figure 17.3: Operation enforcing Fourier domain magnitude.

Fourier transform in (a), image reconstructions after 500 iterations of the GS and Fienup methods are shown in (b) and (c) respectively. It is a general practice to use iterative schemes consisting of a combination of HIO and GS iterations (e.g. 90 HIO iterations followed by 10 GS iterations). Several new ideas such as iterated map algorithm due to Elser (2006) for phase retrieval generalize the HIO algorithm further, however, we will not discuss these advanced ideas here. Interested readers may refer to references at the end of this chapter. At present one of the most challenging problem for phase retrieval from single intensity measurement is the problem of recovering complex valued objects. Since an object $g(x, y)$ and $g^*(-x, -y)$ have the same Fourier transform magnitude, the solution to iterative phase retrieval is known to stagnate such that features of both the solutions are present in the final image recovery. A prominent solution for avoiding this twin-image problem is to use a truncated non-symmetric object support for initial iterations followed by full object support in further iterations.

17.3 Phase retrieval with multiple intensity measurements

17.3.1 Phase retrieval with defocus diversity

While GS and Fienup methods were developed for phase retrieval problem associated with single intensity measurement, the ideas find application in more general framework known as phase diversity imaging. In this framework, two or more intensity measurements are made such that the transformation undergone by light field

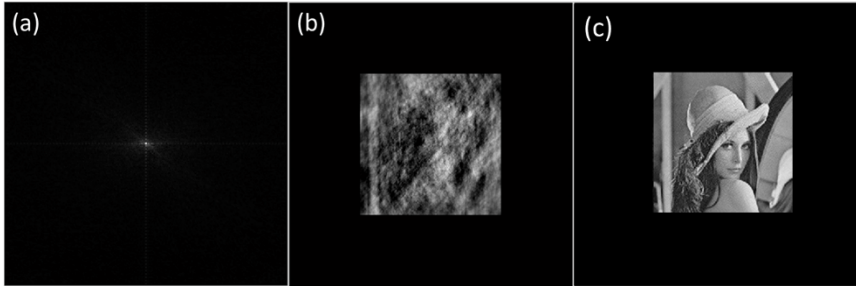


Figure 17.4: Comparison of GS and Fienup methods for a greyscale object: (a) Modulus of Fourier transform, (b),(c): image reconstructions with 500 iterations of GS and Fienup methods. The positivity and object support constraints are used in this algorithm.

between the two measurements is well-known. Defocus based diversity for intensity measurements has been a popular choice in the literature. As shown in Fig. 17.5 multiple intensity measurements are made by moving the detector in longitudinal (or z) direction. The iterative phase recovery is carried out as follows:

1. Initiate the field associated with first measurement by assigning a random phase function and amplitude equal to the square root of the intensity.
2. Propagate this field by a distance $(z_2 - z_1)$. The propagation may be implemented for example by Fresnel or angular spectrum methods.
3. In the second plane, enforce the measurement constraint by replacing the propagated field amplitude with square root of the measured intensity data leaving the phase part unchanged.
4. Continue this process over all intensity measurements iteratively.

The illustration in Fig. 17.6 shows recovery of the IITD phase object with two intensity measurements near the back focal plane of a lens in a Fourier transform configuration. It is important to select the defocus distance such that the two intensity measurements have

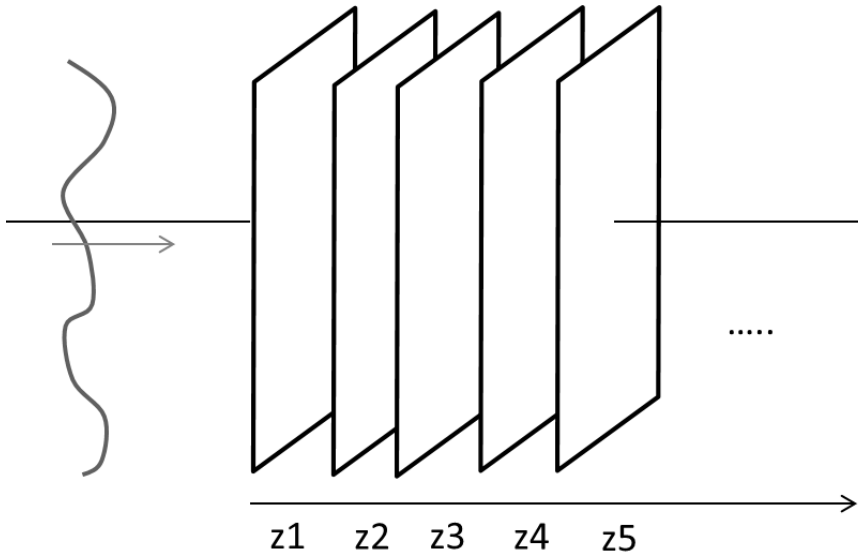


Figure 17.5: Phase diversity imaging by multiply intensity measurements related by defocus. An unknown wavefront is travelling in $+z$ direction and intensity measurements are made using an area sensor at different locations along z -axis.

sufficient diversity for robust convergence in practice. In our simulation, a lens with focal length 30 cm and aperture 8 mm is assumed. The intensity patterns are assumed to be sampled with sampling interval of $10\mu\text{m}$. The intensity measurements are simulated in the focal plane and at a plane defocused 4 mm from the focal plane. Experiments with such configurations have to be performed preferably with high bit-depth digital sensors (typically 12 bit or more) so that two defocused patterns provide sufficiently non-redundant information. Two intensity measurements with small defocus distances will otherwise be difficult to distinguish due to pixel value quantization and readout noise of the sensor. This type of algorithms have been successfully employed and it has been observed that in the Fresnel zone setup the robustness of iterative phase recovery improves with number of measurements. We remark here that such defocus based measurements are somewhat inefficient in that they record highly redundant information. In particular two fields related by a small

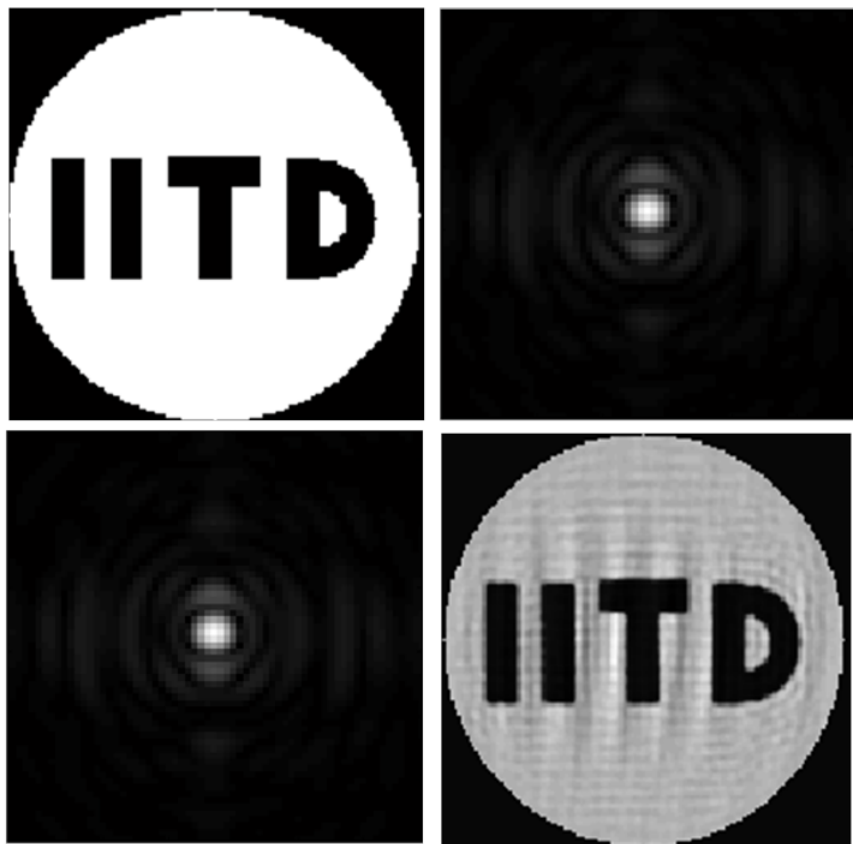


Figure 17.6: Phase retrieval with defocus diversity near Fourier transform plane. (a) Phase object, Central portion of intensity pattern in (b) Fourier transform plane and (c) a plane 4 mm defocused with respect to the Fourier transform plane, (d) Iterative phase recovery with 500 iterations of the defocus diversity method.

defocus are highly correlated in their spatial detail. In the following discussion we describe a new approach based on the recent work of the present author and co-workers which naturally provides diversity in the two intensity measurements.

17.3.2 Phase retrieval by spiral phase diversity

When estimating an unknown field in the form $\exp[i\psi(x, y)]$, the best form of non-redundant information is contained in the two quadrature components $\cos[\psi(x, y)]$ and $\sin[\psi(x, y)]$ or their equivalent. If the amplitude of the two quadratures can be measured then it is conceivable that such non-redundant information may be used to derive the unknown phase iteratively. The problem of defining a quadrature transform for 2D signals is however not a straightforward problem. Larkin and co-workers made a detailed analysis of the idea of spiral phase transform as an appropriate quadrature transform for 2D signals. The present author has shown that this choice is actually optimal in the sense of Mandel's theorem as discussed in Chapter 7. In recent times several researchers have shown that the Fraunhofer diffraction pattern of an aperture has a distinct character when the illumination beam is a plane wave or a beam with spiral phase structure. As we show here this diversity may be utilized for addressing the non-interferometric phase retrieval problem. For a signal $G(f_x, f_y)$ the spiral phase transform is defined as:

$$\hat{G}(f_x, f_y) = \int \int dx dy \ g(x, y) \exp(i\theta) \exp[-i2\pi(f_x x + f_y y)]. \quad (17.4)$$

Here $\theta = \arctan(\frac{y}{x})$ is the polar angle. The spiral phase is a generalization of the sign filter which is used for defining the quadrature or Hilbert transform in one-dimension. For an unknown wavefront $g(r, \theta)$ we study the possibility of making two Fourier plane intensity measurements of the form:

$$I_1(\rho, \phi) = |F\{g(r, \theta)C(r, \theta)\}|, \quad (17.5)$$

$$I_2(\rho, \phi) = |F\{g(r, \theta) \exp(i\theta)C(r, \theta)\}|^2. \quad (17.6)$$

As we have already studied in Chapter 14, the Fourier transform of an object function $g(r, \theta)$ may be generated physically in the back focal plane of a thin convex lens. In the above equations, $C(r, \theta)$ denotes the aperture of the Fourier transforming lens. We may obtain the two intensity measurements as above using a system shown in Fig. 17.7. The iteration for phase retrieval may be carried out in the following steps:

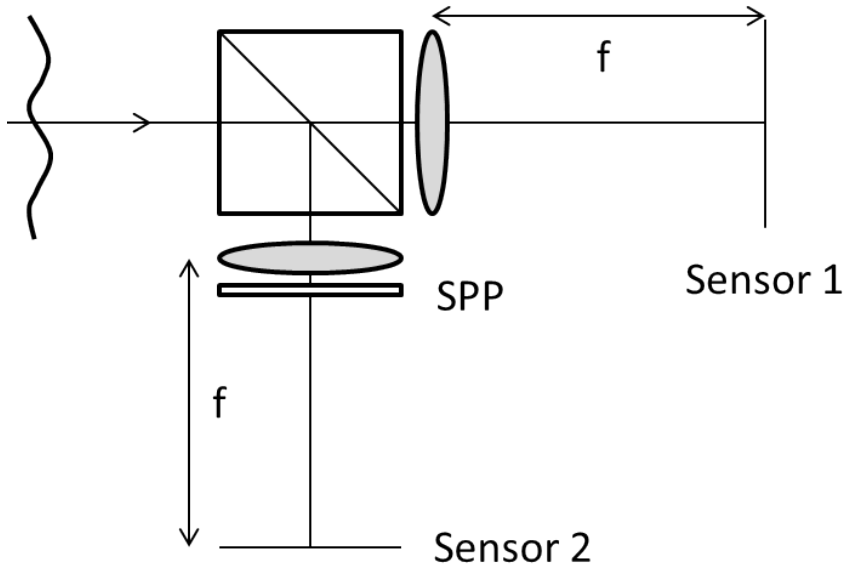


Figure 17.7: System for phase retrieval using spiral phase diversity. An incoming wavefront is split with a beam-splitter and two sensors record Fourier transform intensity measurements. Sensor 1 records usual Fourier transform and Sensor 2 records Fourier transform with a spiral phase plate (SPP) mask in the lens aperture.

1. Begin the iteration by assigning a random phase function at the sensor plane 1. Amplitude at sensor 1 is assumed to be equal to $\sqrt{I_1(\rho, \phi)}$.
2. Perform inverse Fourier transform operation to get to the lens plane. Apply lens aperture support constraint.
3. Multiply the field by spiral phase $\exp(i\theta)$ and perform Fourier transform operation to obtain field corresponding to Sensor 2 plane. Update the amplitude of Sensor 2 field with $\sqrt{I_2(\rho, \phi)}$ leaving the phase unchanged.
4. Perform inverse Fourier transform operation on the updated Sensor 2 field, multiply by conjugate spiral phase $\exp(-i\theta)$ and once again apply lens aperture constraint.

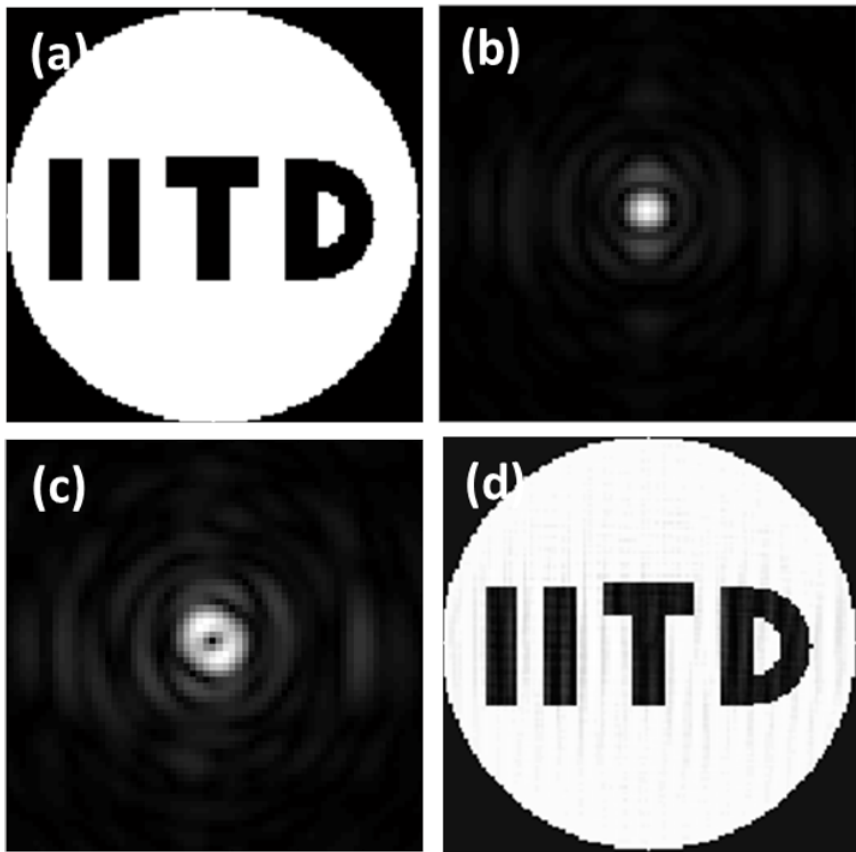


Figure 17.8: Illustration of spiral phase diversity technique for IITD phase object. (a) Phase object, (b)-(c): Two Fourier transform intensity measurements without and with spiral phase mask in the lens aperture plane, (d) phase image recovery.

The above iterative process is continued back and forth between the two sensor plane till a stable phase solution is obtained.

In Fig. 17.8 (b), (c) we show an illustration of the two intensity measurements $I_1(\rho, \phi)$ and $I_2(\rho, \phi)$ corresponding to the IITD phase image. The non-redundant quadrature nature of these two measurements is clear from the observation that the positions of maxima and minima in the two measurements are complementary. This complementary nature of the two intensity images readily provides suffi-

cient diversity suitable for experimental measurements and subsequent iterative phase recovery. Phase image recovery using 500 iterations of the spiral phase diversity method is shown in Fig. 17.8 (d). We note that this iteration does not require any constraints on the solution such as positivity. The only constraint used is the lens aperture constraint which is fully dependent on the system geometry. We also note improved quality of image recovery in comparison to the defocus diversity method as in Fig. 17.6. In principle, two measurements connected by spiral phase diversity can be made simultaneously, thus allowing phase sensing of dynamic wavefronts.

At a more fundamental level phase diversity technique suggests that phase measurement may not be performed by physically interfering two fields as in optical interferometry. Instead two or more coded intensity measurements corresponding to the unknown field are sufficient to infer the phase of the unknown wavefront computationally. Phase sensors based on the phase diversity based ideas can be potentially much simpler compared to interferometric systems.

17.4 Gerchberg-Papoulis method for bandlimited extrapolation

In this section we will study the closely related problem of band-limited extrapolation which we formulate as reconstruction of an image $g(x, y)$ of known support from the knowledge of a limited section of its Fourier transform $G(f_x, f_y)$. For a finite support object the transform $G(f_x, f_y)$ extends all over the (f_x, f_y) plane in principle, however, practically it may be possible to measure the transform over a finite region. We have already encountered this problem in case of extrapolating property of prolate spheroidal functions. Here we describe an iterative framework for extrapolation as first studied independently by Gerchberg and Papoulis. The transform $G(f_x, f_y)$ is assumed to be known on a low-pass support window $W(f_x, f_y)$. With the knowledge of object support window $C(x, y)$ in the image domain, initial guess for the object $g(x, y)$ may be set as

$$g^{(0)}(x, y) = C(x, y)\mathcal{F}^{-1}[G(f_x, f_y)W(f_x, f_y)] \quad (17.7)$$

The steps for the iterative algorithm are described below and are

seen to be similar to the Gerchberg-Saxton phase retrieval method. For the $(n + 1)$ -the iteration we proceed as follows:

1. Calculate forward Fourier transform $G'(f_x, f_y) = \mathcal{F}[g^{(n)}(x, y)]$ and modify it as

$$G^{(n+1)} = G(f_x, f_y)W(f_x, f_y) + G'(f_x, f_y)[1 - W(f_x, f_y)]. \quad (17.8)$$

In other words, the new Fourier transform is obtained by replacing the part of $G'(f_x, f_y)$ in the support window $W(f_x, f_y)$ by the known Fourier transform $G(f_x, f_y)$. The values of the transform $G'(f_x, f_y)$ beyond the window $W(f_x, f_y)$ are left unchanged.

2. Calculate inverse transform $g'(x, y) = \mathcal{F}^{-1}[G^{(n+1)}(f_x, f_y)]$ and get an updated guess $g^{(n+1)}(x, y)$ by applying suitable image domain constraints on $g'(x, y)$.

As an illustration of the Gerchberg-Papoulis extrapolation, we consider the case of a two point object as in Fig. 17.9(a). The transform of the object (magnitude shown) as in Fig. 17.9(b). A blurred object corresponding to a truncated transform in Fig. 17.9(d) is shown in Fig. 17.9(c). The recovered object and its transform as per 1000 iterations of the extrapolation procedure above are shown in 17.9(e),(f). In this illustration we used positivity and support constraints and additionally total variation minimization in the object domain. While exact recovery of the object may be difficult for an extrapolation problem of this nature, we observe a reasonably good recovery of the original object in this illustration.

References and suggested reading

1. R. W. Gerchberg and W. O. Saxton, “A practical algorithm for the determination of the phase from image and diffraction plane pictures”, *Optik* 35, 237-246 (1972).
2. R. W. Gerchberg, “Super-resolution through error energy reduction”, *Optica Acta* 21, 709-720 (1974).

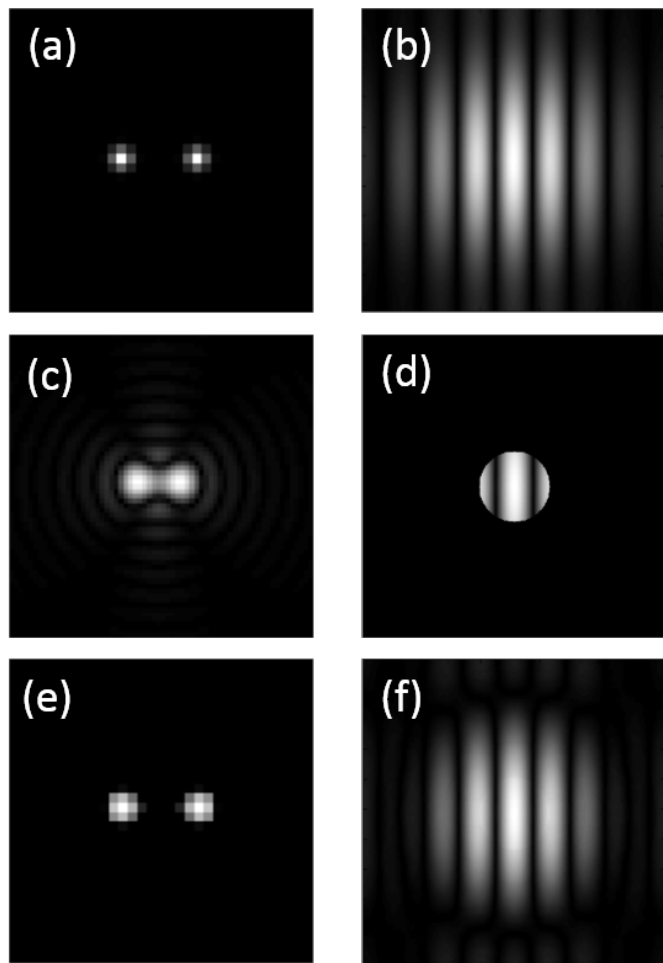


Figure 17.9: Illustration of Gerchberg-Papoulis extrapolation method for a two-point object. (a),(b) Original object and magnitude of its Fourier spectrum, (c), (d) Blurred version of the object corresponding to a truncated Fourier transform, (e),(f) Recovered object and its Fourier transform showing that the transform values beyond truncation in (d) are approximately filled.

3. A. Papoulis, “A new algorithm in spectral analysis and band-limited signal extrapolation”, IEEE Trans. Circuits Syst. 25, 735-742 (1975).

4. J. R. Fienup, “Reconstruction of an object from the modulus of its Fourier transform”, *Opt. Lett.* 3, 27-29 (1978).
5. J. R. Fienup, “Phase retrieval algorithms: a comparison”, *Appl. Optics* 21, 2758-2769 (1982).
6. J. R. Fienup and C. C. Wackerman, “Phase retrieval stagnation problems and solutions”, *J. Opt. Soc. Am. A* 3, pp. 1897-1907 (1986).
7. A. Labeyrie, “Attainment of diffraction limited resolution in large telescopes by Fourier analysing speckle patterns in star images”, *Astron. and Astrophys.* 6, 85-87 (1970).
8. V. Elser, I. Rankenburg, and P. Thibault, “Searching with iterated maps”, *Proc. Natl. Acad. Sci.* 104, 418-423 (2007).
9. A. Anand, G. Pedrini, W. Osten, P. Almoro, “Wavefront sensing with random amplitude mask and phase retrieval”, *Opt. Lett.*, 32 1584-1586 (2007).
10. P. Almoro, G. Pedrini, and W. Osten, “Complete wavefront reconstruction using sequential intensity measurements of a volume speckle field”, *Appl. Opt.* 45, 8596-8605 (2006).
11. P. Gao, G. Pedrini, and W. Osten, “Phase retrieval with resolution enhancement by using structured illumination”, *Opt. Lett.* 38, 5204-5207 (2013).
12. P. Gao, G. Pedrini, C. Zuo, and W. Osten, “Phase retrieval using spatially modulated illumination”, *Opt. Lett.* 39, 3615-3618 (2014).
13. R. A. Gonsalves, “Phase retrieval by differential intensity measurements”, *JOSA A* 4, 166-170 (1987).
14. K. G. Larkin, D. J. Bone, M. A. Oldfield, “Natural demodulation of two-dimensional fringe patterns I: General background of spiral phase quadrature transform”, *JOSA A* 18, 1862-1870 (2001).

15. K. Khare, “Complex signal representation, Mandel’s theorem and spiral phase quadrature transform”, *Appl. Opt.* 47(22) E8 E12 (2008).
16. L. Mandel, “Complex representation of optical fields in coherence theory”, *JOSA* 57, 613-617 (1967).
17. D. P. Ghai, P. Senthilkumaran and R. S. Sirohi, “Single-slit diffraction of an optical beam with phase singularity”, *Opt. & Lasers in Engg* 47, 123-126 (2009).
18. J. Hickmann, E. Fonseca and S. Chavez Cerdá, “Unveiling a truncated optical lattice associated with a triangular aperture using lights orbital angular momentum”, *Phys. Rev. Lett.* 105, 053904 (2010).
19. S. Singh, A. Ambuj and R. Vyas, “Diffraction of orbital angular momentum carrying optical beams by a circular aperture”, *Opt. Lett.* 39, 5475-5478 (2014).
20. M. K. Sharma, C. Gaur, P. Senthilkumaran, K. Khare, “Phase imaging using spiral phase diversity”, *Appl. Opt.* 54, 3979-3985 (2015).

18. Compact multi-lens imaging systems

Digital imaging has become a widespread technology with miniature cameras getting embedded in devices such as mobile phones. While digital array (CCD or CMOS) sensors have virtually overtaken film based cameras for most imaging applications, the Physics of image formation in these systems has largely remained same. It is only in the last decade that novel system concepts are emerging that use unconventional optical design followed by image recovery algorithms.

In this chapter we will discuss on some specific computational imaging systems that have received much attention in literature in recent times. The examples chosen here represent systems or ideas that truly bring out the advantages of integrating computational methods with unconventional optical system design to achieve superior imaging performance. The first system that we will discuss is the compact form factor multi-lens camera followed by the plenoptic or lightfield camera that allows retrospective computational focusing. Both the systems offer practical advantages that cannot be achieved through purely hardware or purely image processing approaches thus highlighting the importance of the computational imaging framework.

18.1 Compact form factor computational camera

Easy availability and manufacturability of miniature optical components has made it possible to realize compact optical imaging

systems . Suppose we consider an ordinary digital camera and set out to miniaturize it, all components may be reduced proportionately except for the sensor pixels that have typical dimensions in the range $1\text{-}5 \mu\text{m}$. Suppose a microlens with the same F-number as an ordinary camera is used, reduction in lens aperture size implies that proportionately smaller number of pixels are available for recording the image with the same field of view. One interesting solution to this problem is to use multiple microlenses (typically a periodic microlens-array). The image recorded behind each of the microlenses is a low-resolution image but all the low-resolution images may be combined digitally to produce a single full resolution image. The model for this computational camera relies on the idea of generalized sampling which may be explained as in the schematic diagram shown in Fig. 18.1.

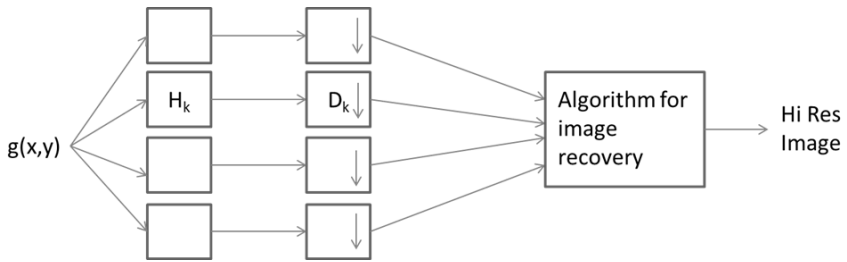


Figure 18.1: Computational camera model from the viewpoint of generalized sampling. A given high resolution scene is imaged using multiple imaging systems (denoted by H_k). Recording the output of these multiple imagers with limited number of pixels behind each microlens involves downsampling (denoted by D). All the low resolution images are then combined by numerical processing to obtain a single high resolution image.

A given picture $g(x, y)$ is seen by multiple microlens imagers with individual impulse responses given by $h_k(x, y)$. The recorded image behind an individual microles may be given by a downsampled and translated version of $g_k(x, y) = g(x, y) * h_k(x, y)$. Even if all the individual impulse responses $h_k(x, y)$ are identical, a diversity in recorded images is possible due to relative fractional pixel shifts between the individual images. This diversity may be ex-

ploited algorithmically to combine all the low resolution images into a single high resolution image. Formally the k -th recorded sub-image may be represented as:

$$g_k = DH_k S_k g. \quad (18.1)$$

Here the operators D, H_k, S_k denote the operations of downsampling, blurring due to system impulse response and shift (or translation) respectively. Note that the downsampling operator is assumed to be the same for all elemental sub-images. The inversion problem of reconstructing the full high resolution image may be expressed as constrained optimization problem of minimizing a cost function:

$$C(g) = \sum_k ||g_k - DS_k H_k g||^2 + \alpha\psi(g). \quad (18.2)$$

Here the first term represents the data consistency and the second term represents any desirable constraint on the final image, e.g. minimal Total Variation or other appropriate penalty functions. When solving the optimization problem iteratively, a transpose (or adjoint) of the forward system operator for the k -th system

$$A_k = DH_k S_k \quad (18.3)$$

is required. The transpose operator is readily represented as

$$A^\dagger = S_k^- H_k^\dagger U, \quad (18.4)$$

where S_k^-, H_k^\dagger, U denote negative shift, convolution with inverted impulse response $h_k(-x, -y)$ and upsampling operations respectively. The downsampling and upsampling operations may be performed by any standard interpolation routine. In Fig. 18.2 we show an example of high resolution image recovery with a compact system consisting of 25 element microlens array. The elemental images, interpolated version of the central image in the 5×5 elemental image array, and the recovered high resolution image are shown. The total variation penalty function was used for the constraint term $\psi(g)$. We observe that the final reconstruction has higher resolution as well as lower noise background. The reconstruction is typically an iterative procedure as described in Chapter 6. If the system is modeled cor-

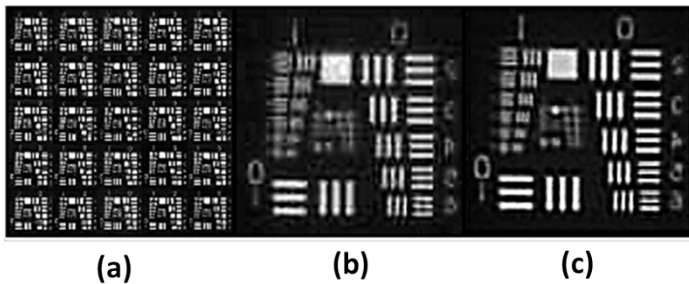


Figure 18.2: Illustration of image recovery for a multi-lens thin camera system, (a) 25 elemental low resolution images, (b) upsampled interpolated version of the central sub-image in the 5×5 low resolution image array in (a), (c) Reconstructed high resolution image. The reconstruction was performed using the total variation penalty. [Multi-lens image data courtesy Dr. G. Unnikrishnan, Instruments Research Development Establishment, Dehradun, India].

rectly, it may be possible in general to get a good final image quality even without high quality microlens array. We note once again that a compact form factor system is possible here through a combination of system design and image recovery algorithms. Any amount of lens design sophistication or image processing done stand alone cannot easily achieve this goal in general.

18.2 Lightfield cameras

In traditional camera designs, typically a multi-element lens is placed in front of a sensor and focusing is achieved by changing the distance between the sensor and the lens. Plenoptic imaging systems record information in such a way that a single recorded frame allows retrospective focusing of images. The image recorded at the sensor is not directly meaningful visually. An image reconstruction algorithm applied to the recorded data enables focusing at various depths. In this section we will explain the working principle of lightfield systems with the help of some simple simulations. We will first discuss the concept of lightfield and how plenoptic systems record the light-

field using a microlens array. Image reconstruction algorithm for retrospective computational refocusing will be discussed next.

18.2.1 The concept of lightfield

In typical camera systems every sensor pixel records a signal proportional the total integrated light energy arriving at the pixel area. The information about the directional distribution of this energy is lost. Referring to Fig. 18.3 the lightfield function $L(u, v; x, y)$ represents the distribution of energy reaching the image plane at the point (x, y) from an elemental area located at coordinates (u, v) in the lens aperture plane. Conceptually the lightfield function may be considered to have complete information about the directional distribution of light entering the imaging system. The plenoptic systems aim to record this complete information (the name “plenoptic” refers to complete information). The image intensity recorded as a func-

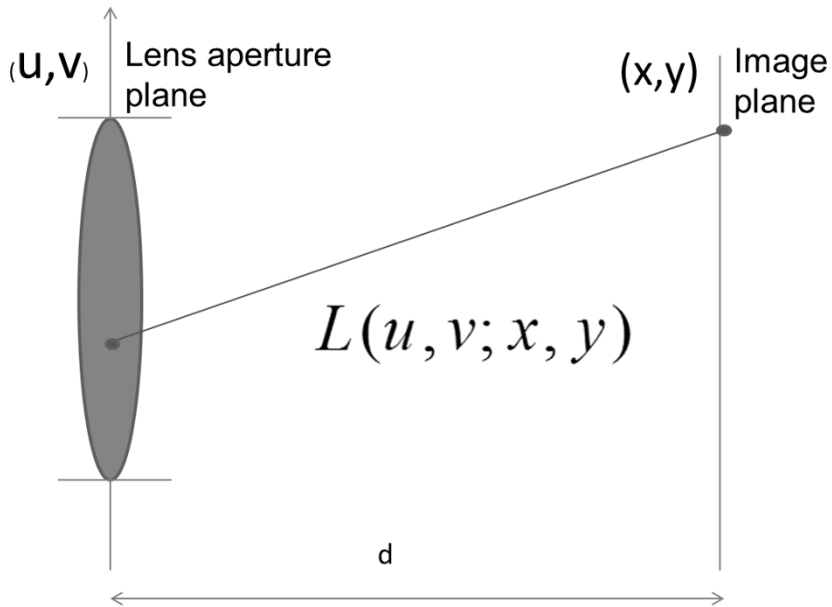


Figure 18.3: Schematic of an imaging system. The lightfield function $L(u, v; x, y)$ represents the energy distribution from lens aperture plane to the image plane.

tion of image plane coordinates (x, y) is obtained by integrating the lightfield function over the lens aperture coordinates:

$$I(x, y) = \int \int dudv L(u, v; x, y). \quad (18.5)$$

We note that if the lightfield function is known between the lens aperture plane and an image plane, then it is possible to calculate the lightfield function between the lens aperture plane and any other defocused plane. As shown in Fig. 18.4 the ray of light representing optical energy flow between points $A(u, v)$ and $P(x, y)$ also cuts another plane at a point $P'(x', y')$. The coordinates (x', y') of the new

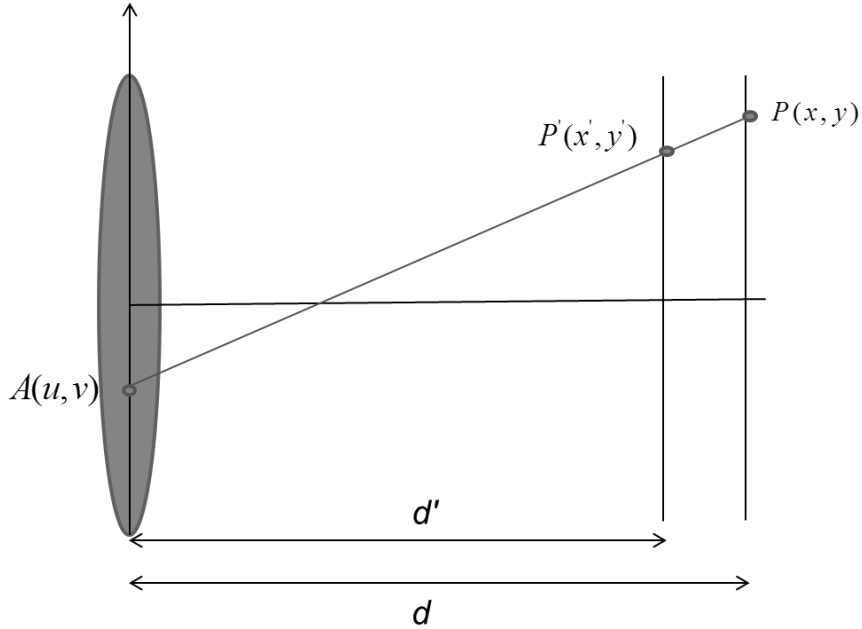


Figure 18.4: Knowledge of the lightfield function $L(u, v; x, y)$ allows one to calculate the lightfield function $L(u, v; x', y')$ between lens aperture and another plane.

plane are related to the coordinates (x, y) by a simple geometrical

relation:

$$x' = \alpha x + \beta u, \quad (18.6)$$

$$y' = \alpha y + \beta v. \quad (18.7)$$

Here the parameters α and β are given by:

$$\alpha = \frac{d'}{d}, \quad (18.8)$$

$$\beta = 1 - \frac{d'}{d}. \quad (18.9)$$

We may therefore obtain the lightfield function $L(u, v; x', y')$ as:

$$L(u, v; x', y') = L(u, v; \alpha x + \beta u, \alpha y + \beta v). \quad (18.10)$$

Further when integrated with respect to (u, v) the new lightfield function gives us a new image $I(x', y')$ formed in the new plane without any physical focusing requirement.

18.2.2 Recording the lightfield function with microlens array

In the last section we have seen that the knowledge of the lightfield function between two planes is sufficient for computational refocus. The recording of the lightfield function is therefore the first aim of a lightfield imaging system. The lightfield function may be recorded by introducing a microlens array between the main lens aperture and the sensor array. The microlens array is positioned such that each microlens in the array images the main lens aperture on the sensor plane. The configuration is shown schematically in Fig. 18.5 (a). Figure 18.5(b) shows part of the pattern recorded on the sensor array. Care must be taken to turn down the lens aperture so that the images behind the individual microlenses do not overlap. As shown in Fig. 18.5 (b), the pattern recorded behind an individual microlens is a map of the lens aperture as seen from the corresponding microlens position. Representing the microlens center coordinates as (x_j, y_j) , the pattern behind a single microlens may be denoted as $L(u, v; x_j, y_j)$. The collection of all individual images thus forms the complete lightfield function.

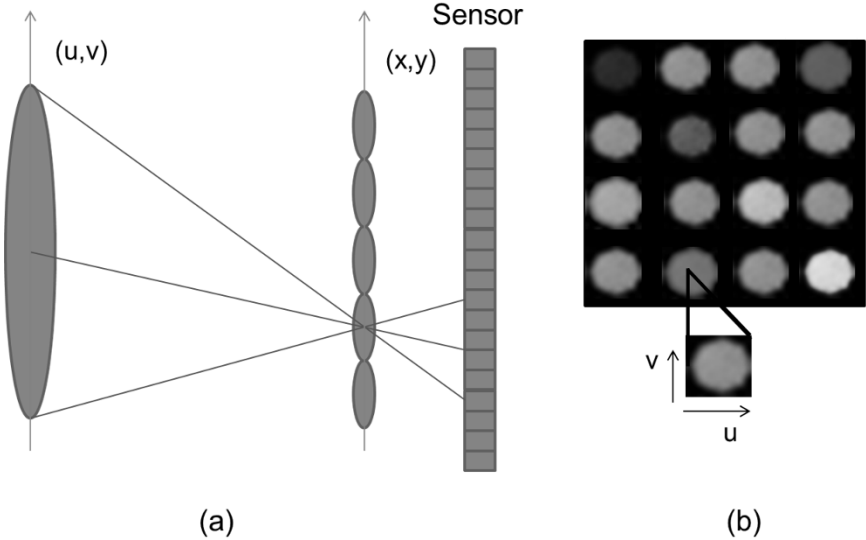


Figure 18.5: (a) Schematic of a lightfield imaging system. The lenses in the microlens array are positioned to image the main lens aperture on the sensor. (b) Part of a typical sensor pattern. The pattern behind an individual microlens is a map of the lens aperture ((u, v) coordinates) as seen from the corresponding microlens position.

In Fig. 18.6 we show a simulation for image data recorded by a plenoptic camera for on-axis point sources. For the simulation we assumed 31×31 lens array with an array of 32×32 pixels behind each microlens. While these parameters are far from the realistic commercial systems, they are sufficient to provide a basic understanding of the plenoptic system. When the point source is located such that the source is imaged in the microlens plane, the raw detector data as shown in Fig. 18.6 (a) is observed. We see that only the image area behind the on-axis microlens is illuminated. For a defocused on- axis source located farther away from the plenoptic camera, a focused image is formed somewhere between the main lens and the microlens array. As a result the microlens array is illuminated by a cone of light rays covering a number of microlenses depending on the defocus distance. The eventual pattern appearing

on the detector is shown in Fig. 18.6(b). Note that a source located on the system optical axis is on optical axis of the central microlens but is an off-axis source for other microlenses. The peaks in the detector pattern as in Fig. 18.6(b) are thus shifted relative to the microlens centers (except for the central microlens). The next task is to process this data to form an image of the point source. Note that the number of (x, y) samples available is the same as the number of microlenses and as a result nominal image resolution obtained is equal to the number of microlenses (which is much less than the number of sensor pixels).

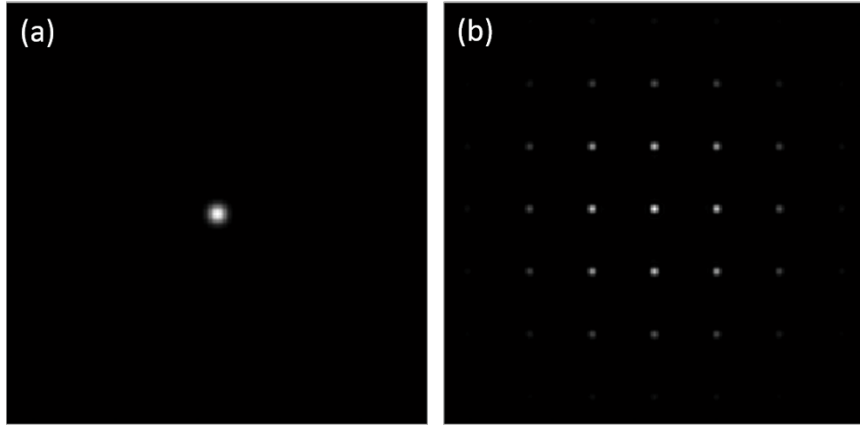


Figure 18.6: Central portion of simulated data frame as recorded by a plenoptic camera for on-axis point sources. For simulation, we used a 31×31 microlens array with 32×32 pixels behind each microlens. (a) Nominal on axis point source which is imaged by main camera lens on microlens array plane, (b) on-axis point source imaged by main lens in a plane defocused with respect to microlens plane.

For the data in Fig. 18.6(a), image formation is a trivial task since only the central sub-image contains non-zero data and thus contributes to image formation. The lightfield function is a collection of all the sub-images. Since the microlens plane is the nominal image plane, a focused image is obtained as:

$$I_1(x, y) = \int \int dudv L(u, v; x, y). \quad (18.11)$$

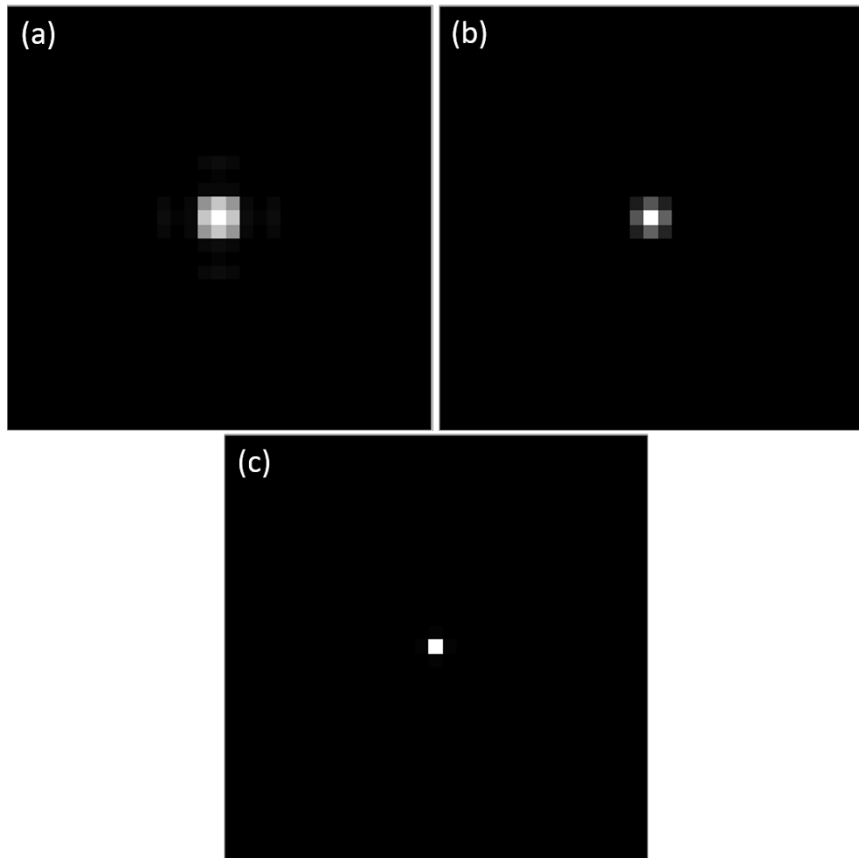


Figure 18.7: Image reconstruction corresponding to raw data in Fig. 18.6(b) at various depths between the main lens and the microlens array plane. (a),(b) reconstruction for on-axis point source at defocused planes, (c) focused image of the point source when appropriate values of α and β as in Eq. (18.10) are used.

The reconstructed image in this case is essentially obtained by integrating the total energy in the central image and putting it in the central image pixel. All the other reconstructed pixel values are zero. For the data in Fig. 18.6(b), we observe that the cone of light due to an on-axis point source is seen to reach several lenses and the corresponding sub-images on the detector have non-zero regions. The pixels from the sub-images obtained from the raw detector data

are first re-arranged such that for a fixed (u, v) we get a 2D image $L(u, v; x, y)$ by appropriately sampling the pixel locations behind each microlens. These images are shifted and scaled as per Eq. (18.10) to obtain the components $L(u, v; x', y')$ of the lightfield for fixed (u, v) . Integration over main lens aperture plane for calculating image

$$I_2(x', y') = \int \int dudv L(u, v; x', y'), \quad (18.12)$$

amounts to adding up all the individually transformed lightfield components. Figure 18.7(a)-(c) show reconstructions of the image of the on-axis point source (corresponding to data in Fig. 18.6(b)) at various depths. The scaling and shifting operations above may be implemented easily using any of the standard 2D interpolation schemes available in commonly used software packages. For photography in ambient light a general object/scene to be imaged may be considered to be a collection of point sources at various depths. The raw data in that case may not be easy to interpret by visual inspection, however, the processing of the data is similar to the above case of on-axis point sources.

Another class of multi-lens systems which have been studied in detail are known as integral imaging systems which rely on the multiple perspectives provided by a lenslet array for 3D imaging. A similar approach in principle has also been studied recently in microscopy where 3D images of samples are generated by using a single microscope objective which is illuminated sequentially in multiple illumination directions. The methodology is commonly known as ptychography. We will not discuss these systems in this book. The interested reader can however refer to further references on these topics.

References and suggested reading

1. A. Papoulis, “Generalized sampling expansion”, IEEE Trans. Circuits Syst. 24, 652-654 (1977).
2. J. L. Brown, “Multi-channel sampling of low pass signals”, IEEE Trans. Circuits Syst. 28, 101-106 (1981).

3. J. Tanida, T. Kumagai, K. Yamada, S. Miyatake, K. Ishida, T. Morimoto, N. Kondou, D. Miyazaki and Y. Ichikoa, “Thin observation module by bound optics (TOMBO): concept and experimental verification”, *Appl. Opt.* 40, 1806-1813 (2001).
4. M. Elad and A. Feuer, “Super-resolution reconstruction of image sequences”, *IEEE Trans. Pattern Anal. and Machine Intell.* 21, 817-834 (1997).
5. P. Milanfar (Ed.), “Super Resolution Imaging”, CRC Press, Boca Raton (2011).
6. K. Nitta, R. Shogenji, S. Miyatake, and J. Tanida, “Image reconstruction for thin observation module by iterative backprojection”, *Appl. Opt.* 45, 2839-2900 (2006).
7. K. Choi and T. J. Schultz, “Signal processing approaches for image resolution restoration for TOMBO imagery”, *Appl. Opt.* 47, B104-B116 (2008).
8. M. Shankar, R. Willett, N. Pitsianis, T. Schultz, R. Gibbons, R. Te Kolste, J. Carriere, C. Chen, D. Prather and D. Brady, “Thin infrared imaging systems through multichannel sampling”, *Appl. Opt.* 47, B1-B10 (2008).
9. A. D. Portnoy, N. Pitsianis, X. Sun, and D. Brady, “Multichannel sampling schemes for optical imaging systems”, *Appl. Opt.* 47, B76-B85 (2008).
10. E. H. Adelson and J. Y. A. Wang, “Single lens stereo with a plenoptic camera”, *IEEE Trans. Pattern Anal. Machine Intell.* 14, 99-106 (1992).
11. R. Ng, M. Levoy, M. Bredif, G. Duval, M. Horowitz, and P. Hanrahan, “Light field photography with a hand-held plenoptic camera”, Computer Science Stanford Technical Report CSTR 2, 1-11 (2011).
12. G. Wetzstein, I. Ihrke, D. Lanman, and W. Heidrich, “Computational plenoptic imaging”, *Computer Graphics Forum* 30, 2397-2426 (2011).

13. S. A. Shroff and K. Berkner, "Image formation analysis and high resolution image reconstruction for plenoptic imaging systems", *Appl. Opt.* 52, D22-D31 (2013).
14. Commercial Lightfield system and literature at www.lytro.com
15. X. Xiao, B. Javidi, M. Martinez-Corral, and A. Stern, "Advances in three-dimensional integral imaging: sensing, display and applications", *Appl. Opt.* 52, 546-560 (2013) and references therein.
16. X. Ou, R. Horstmeyer, G. Zheng, and C. Yang, "High numerical aperture Fourier ptychography: principle, implementation and characterization", *Opt. Express* 23, 3472-3491 (2015).

19. PSF Engineering

In Chapter 18 we have described the concept of lightfield and how it allows one to recover images at different depths. One of main the limitations of the lightfield or plenoptic system is that the raw image resolution is same as number of lenses in the microlens array and is thus lower compared to the diffraction limited resolution of the system. In this chapter we will describe the concept of wavefront coding which allows near diffraction limited imaging with extended depth of field performance. In the following discussion we will study three important wavefront coding designs that allow extended depth of field. It is well-known that for a typical imaging system, the depth of field is given by $\lambda/(NA)^2$ where λ is the nominal wavelength of illumination and NA is the numerical aperture. The designs we will discuss here give performance that is an order of magnitude higher than this typical depth of field value. The main aim of the designs to be discussed here is to make the system point spread function invariant with respect to defocus. This feature allows a simple image deblurring process (like Wiener filter) to bring all the object planes in focus simultaneously.

19.1 Cubic phase mask

Usage of cubic phase mask for extending depth of field was first proposed by Cathey and Dowski (1995). This is one of the early computational optical imaging systems that combined optical design with image recovery to obtain superior imaging performance. As we will discuss here the cubic phase mask function may be arrived at by considering the behavior of the optical transfer function (OTF) of an imaging system for variable defocus. We will assume the system

aperture function to be separable in x and y dimensions and limit our discussion to a one dimensional case. Further we will present the discussion in terms of a 4F or canonical optical processor. The OTF of the 4F system is given by:

$$OTF(u) = \frac{\int dx P(x + u/2)P^*(x - u/2)}{\int dx |P(x)|^2}. \quad (19.1)$$

In terms of the symbols in Chapter 14, Section the variable $u = \lambda F f_x$ and $P(\dots)$ denotes the system aperture function. For an on-axis point source defocused with respect to the object or input plane of a canonical optical processor, the aperture function may be suitably represented as:

$$P(x) = P_0(x) \exp(i\alpha x^2). \quad (19.2)$$

Here $P_0(x)$ represents the system aperture (with any suitable phase mask) and the quadratic phase factor arises due to defocus of an object point from the nominal object plane. The parameter α controls the magnitude of defocus. The idea here is to design the aperture $P_0(x)$ such that the system OTF becomes almost independent of α . The OTF may now be expressed as:

$$OTF(u) = A \int dx P_0(x + u/2)P_0^*(x - u/2) \exp(i\alpha xu), \quad (19.3)$$

where we have included the normalization in the constant A . Assuming a trial polynomial form for the aperture phase:

$$P_0(x) = \exp(i\beta x^\gamma), \quad (19.4)$$

the OTF may be expressed as:

$$OTF(u) = A \int dx \exp(i\theta(x)), \quad (19.5)$$

where

$$\theta(x) = [\beta(x + \frac{u}{2})^\gamma - \beta(x - \frac{u}{2})^\gamma] + \alpha xu. \quad (19.6)$$

The integrals with reasonably fast phase variation as above can be approximated by stationary phase method. The idea behind the stationary phase method is that the integrand oscillates slowest near the

stationary points of the phase function and these regions on x -axis contribute to the overall integral the most. Denoting the stationary point of $\theta(x)$ by x_0 , the integral may be approximated as:

$$A \int dx \exp(i\theta(x)) \approx \frac{A}{2} \sqrt{\frac{2\pi}{\theta''(x_0)}} \exp[i\theta(x_0)]. \quad (19.7)$$

If we want the amplitude term in the approximation above to be independent of the defocus parameter α , it is required that the second derivative of $\theta(x)$ is independent of α . Since the stationary point x_0 is determined using:

$$\theta'(x_0) = \alpha u + \gamma \beta [(x_0 + \frac{u}{2})^{\gamma-1} - (x_0 - \frac{u}{2})^{\gamma-1}] = 0, \quad (19.8)$$

it is required that x_0 be linear in α . We see that this can be achieved if $\gamma = 3$ which will result in a cubic phase mask. For $\gamma = 3$ we observe that the stationary point is given by:

$$x_0 = -\frac{\alpha}{6\beta}. \quad (19.9)$$

The system OTF is thus obtained as per Eq. (19.7):

$$OTF(u) \approx \frac{A}{2} \sqrt{\frac{\pi}{3\beta u}} \exp[-i\frac{\alpha^2 u}{12\beta} + i\frac{\beta u^3}{4}]. \quad (19.10)$$

We observe that the MTF of the system which is equal to the magnitude of the OTF, is independent of the defocus parameter α . The phase part of OTF has two terms one of which is independent of α . The first term in phase function is linear in u and will thus cause translation or shift in point spread function (PSF) of the system with changing defocus. The effect of this α -dependent term may however be made negligible by selecting the phase mask function with large value of β . In the illustration in Fig. 19.1(d)-(f) we show the PSF of a cubic phase mask system for three distinct values of the defocus parameter $\alpha = 0, 4, 8$ respectively with $\beta = 25$. For comparison the system PSFs for a system without the cubic phase mask is shown for the same values of α in Fig. 19.1 (a), (b), (c). We seen that the PSF for cubic phase mask system has remained almost same over the range of α values. Objects at different depths relative to the nominal

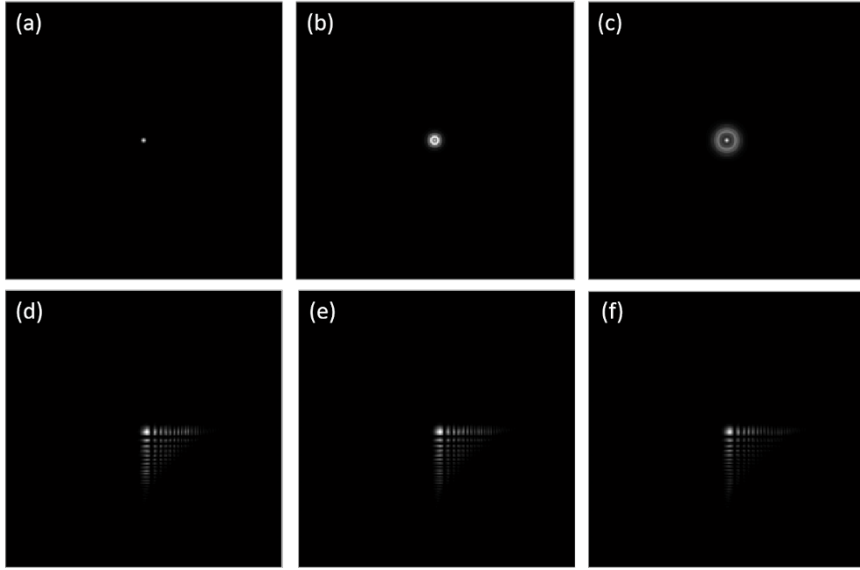


Figure 19.1: Effect of cubic phase mask on system PSF. (a)-(c) PSF for systems with defocus parameter $\alpha = 0, 4, 8$ and no cubic mask. (d)-(f) System PSF for same values of α where a cubic phase mask $\beta(x^3 + y^3)$ has been introduced in the system aperture with $\beta = 25$.

object plane are therefore blurred similarly. The advantage of having almost similar PSF for varying object depth (denoted by changing values of α parameter) is that objects at varying depths are blurred in almost similar manner by the system. All objects may then be recovered by a single inverse filter that typically corresponds to the average PSF over the range of values of α of interest. Combination of hardware design and digital processing thus makes it possible to have an extended depth of field of the imaging system.

The cubic phase function as discussed here for extending the depth of field is also known in the context of the so-called non-diffracting solutions of free space diffraction problem that are known as the Airy beams. Airy beams have found several recent applications in manipulation and trapping of microparticles in liquids. We will not discuss the topic of Airy beams further but refer the reader to references at the end of this chapter.

19.2 Log-asphere lens

In this section we will discuss an alternate model for obtaining distance invariant PSF using a circularly symmetric lens design as first suggested in the work of Chi and George (2001). The basic idea behind this design is explained in Fig. 19.2. The lens element can be

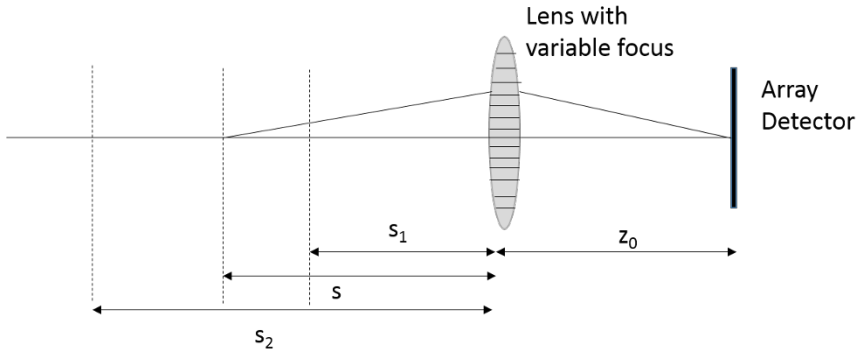


Figure 19.2: Extended depth of field using variable focus lens: concept.

broken into concentric rings such that an elemental annular ring with radius r is designed to form an image of an object point at distance s from the lens. The resultant image of an object point as recorded on the array detector consists of focused image due to one annular lens ring and defocused images due to other annular rings. As shown in Fig. 19.2 a lens element may be designed to have a depth of field ranging over distances s_1 to s_2 along the system optic axis. An annular ring of radius r can be considered to focus point $s(r)$ given by:

$$s(r) = s_1 + (s_2 - s_1) \frac{r^2}{R^2}, \quad (19.11)$$

where R is the radius of the lens element. The phase delay function for the lens may be derived using Fermat's principle. The optical path length for a point at s imaged at the point Q on the detector is given by:

$$L = \sqrt{s^2 + r^2} + \frac{\lambda}{2\pi} \phi(r) + \sqrt{z_0^2 + r^2}. \quad (19.12)$$

Further, solving for $\partial L/\partial r = 0$ as per the Fermat's principle provides a solution for the phase function of the desired lens given by:

$$\begin{aligned}\phi(r) = & -\frac{2\pi}{\lambda}(\sqrt{r^2 + z_0^2} - z_0) \\ & - \frac{\pi}{\lambda} \frac{1}{\gamma} \left[\log(2\gamma\{\sqrt{r^2 + (s_1 + \gamma r^2)^2} + (s_1 + \gamma r^2)\}) + 1 \right. \\ & \left. - \log(4\gamma s_1 + 1) \right].\end{aligned}\quad (19.13)$$

Here the parameter γ is defined as:

$$\gamma = \frac{s_2 - s_1}{R^2}, \quad (19.14)$$

and z_0 is the distance between the lens and the detector. It may be noted that the first term in expression for $\phi(r)$ may be identified with a phase function for point-to-point imaging and the second term is an additional logarithmic term which may be called as a log-asphere phase mask. In Fig. 19.3(a)-(c) we show the PSFs for the log-asphere lens at variable depths corresponding to the defocus values in Fig. 19.1(a)-(c) respectively. The PSFs are seen to be almost

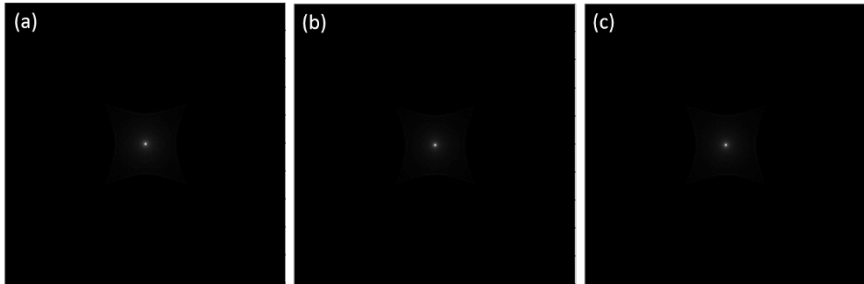


Figure 19.3: (a)-(c) PSF for log-asphere lens for object points at variable depths corresponding to the defocus values in Fig. 19.1(a)-(c).

same when the object points are at variable depths. Further since the PSFs have a form of a symmetric blurring function, the inverse filter required for recovery is very similar to edge sharpening filter. More sophisticated approaches to image recovery are also possible

and give further enhancement in image quality. We refer the interested reader to the references at the end of the chapter for further details on these topics.

We remark that the cubic phase or the log-asphere are possible to realize in practice due to several advances in optical surface manufacturing capabilities in recent decades.

19.3 Rotating point spread functions

Rotating point spread functions is another important development in the context of pupil function engineering. The pupil functions in this case as first studied in the work of Schechner, Piestun and Shamir are linear combinations of the Laguerre-Gaussian (LG) functions . The LG functions are eigensolutions of the para-axial wave equation in a cylindrical coordinate system. An LG mode is defined by means of two indices (l, p) such that the function $LG_{l,p}$ is defined as:

$$LG_{lp}(r, \phi, z) = \frac{C_{lp}}{w(z)} \left(\frac{r\sqrt{2}}{w(z)} \right)^{|l|} \exp\left(\frac{r^2}{w^2(z)} - i \frac{\pi r^2}{\lambda R(z)}\right) \times \\ L_p^{|l|}\left(\frac{2r^2}{w^2(z)}\right) \exp[i l \phi + i(2p + |l| + 1)\psi(z)]. \quad (19.15)$$

Here C_{lp} is a normalization constant. Other parameters in the above equation are beam waist

$$w(z) = w_0 \sqrt{1 + \left(\frac{\lambda z}{\pi w_0^2}\right)^2}, \quad (19.16)$$

with w_0 being the initial ($z = 0$) spot size,

$$R(z) = z[1 + (\frac{\pi w_0^2}{\lambda z})^2] \quad (19.17)$$

is the radius of curvature of the beam and

$$\psi(z) = \arctan\left(\frac{\lambda z}{\pi w_0^2}\right) \quad (19.18)$$

is the Gouy phase. The functions $L_p^{[l]}$ are the generalized Laguerre polynomials. It was shown in the early work of Schechner, Piestun and Shamir that if wave fields are generated by coherent superposition of LG_{lp} modes such that mode labels (l_j, p_j) ($j = 1, 2, 3, \dots, N$) satisfy

$$\frac{p_{j+1} - p_j}{l_{j+1} - l_j} = \text{constant.} \quad (19.19)$$

the resultant intensity PSF patterns approximately retain their functional form over a distance such that the whole pattern rotates continuously with defocus. In Fig. 19.4 we show the behaviour of intensity PSF obtained by linear superposition of the LG modes denoted by indices $(1, 1), (2, 2), (3, 3), (4, 4), (5, 5)$ with equal energy in each mode. The intensity PSF at three distinct planes is shown to illus-

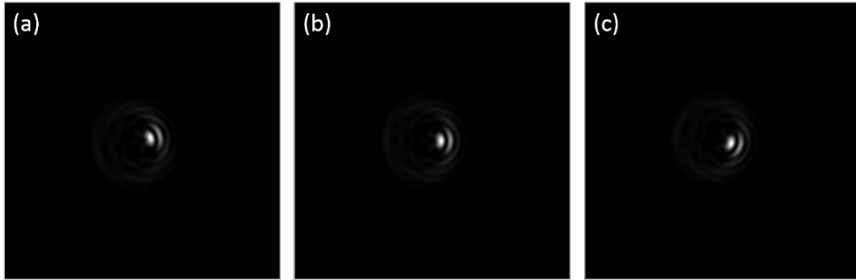


Figure 19.4: (a)-(c) Illustration of rotating PSF with defocus. The PSF is generated by a mask which corresponds to a linear superposition of LG modes denoted by (l, p) indices $(1, 1), (2, 2), (3, 3), (4, 4)$, and $(5, 5)$. It is observed that the PSF retains its functional form but rotates continuously with defocus.

trate the rotation of the pattern. If a mask representing such linear combination of LG modes is placed in the pupil plane of an imaging system, then distinct object planes at varying depths are blurred by such rotating PSFs. Such pupil plane masks may be designed to produce PSF rotation of say 180-degrees over a desired depth. The PSF rotation in a sense provides depth encoding along with extended depth of field feature. For example when the recorded blurred image is deblurred using a PSF with a particular orientation, the recovered image corresponds to a particular slice in the object along the depth

dimension. Such optical sectioning capability can be important for microscopy applications.

References and suggested reading

1. G. Hausler, “A method to increase the depth of focus by two step image processing”, Optics Communications 6, 38-42 (1972).
2. J. Ojeda-Castaneda, P. Andres and A. Diaz, “Annular apodizers for low sensitivity to defocus and to spherical aberration”, Optics Letters 11, 487-489 (1986).
3. J. Ojeda-Castaneda, R. Ramos and A. Noyola-Isgleas, “High focal depth by apodization and digital restoration”, Applied Optics 27, 2583-2586 (1988).
4. J. Ojeda-Castaneda and L. R. Berriel-Valdos, “Zone plate for arbitrarily high focal depth”, Applied Optics 29, 994-997 (1990).
5. E. R. Dowski Jr. and W. T. Cathey, “Extended depth of field through wavefront coding”, Applied Optics 34, 1859-1866 (1995).
6. M. V. Berry and N. L. Balazs, “Nonspreadng wave packets”, American J. of Physics 47, 264-267 (1979).
7. G. A. Siviloglou, J. Broky, A. Dogariu and D. N. Christodoulides, “Observation of accelerating Airy beams”, Physical Review Letters 99, 213901 (2007).
8. I. Kaminer, R. Bekenstein, J. Nemirovsky, M. Segev, “Non-diffracting accelerating wave packets of Maxwell’s equations”, Physical Review Letters 108, 163901 (2012).
9. W. Chi and N. George, “Electronic imaging using a logarithmic asphere”, Optics Letters 26, 875-877 (2001).

10. N. George and W. Chi, “Extended depth of field using a logarithmic asphere”, *J. of Optics A: Pure and Applied Optics* 5, S157-S163 (2003).
11. W. Chi and N. George, “Computational imaging with logarithmic asphere: theory”, *J. Opt. Soc. Am. A* 20, 2260-2273(2003).
12. W. Chi, K. Chu, N. George, “Polarization coded aperture”, *Optics Express* 14, 6634-6642 (2006).
13. Y. Y. Schechner, R. Piestun and J. Shamir, “Wave propagation with rotating intensity distributions”, *Physical Review E* 54, R50-R53 (1996).
14. R. Piestun, Y. Y. Schechner and J. Shamir, “Propagation invariant wavefields with finite energy”, *J. Opt. Soc. Am. A* 17, 294-303 (2000).
15. A. Greengard, Y. Y. Schechner and R. Piestun, “Depth from diffracted rotation”, *Optics Letters* 31, 181-183 (2006).
16. S. R. P. Pavani and R. Piestun, “High efficiency rotating point spread functions”, *Optics Express* 16, 3484-3489 (2008).
17. S. Prasad, “Rotating point spread function via pupil function engineering”, *Optics Letters* 38, 585-587 (2013).
18. G. P. J. Laporte, D. B. Conkey, A. Vasdekis, R. Piestun, and D. Psaltis, “Double helix enhanced axial localization in STED-nanoscropy”, *Optics Express* 21, 30984-30992 (2013).

20. Structural illumination imaging

As we have discussed so far in this book, computational imaging systems aim at breaking traditional system limits by combining novel optics hardware and image recovery algorithms. Structural illumination is an important concept in this regard and structural illumination based microscopy systems are now commercially available for obtaining resolution beyond diffraction limit. Structural illumination typically refers to high frequency modulation of the illumination pattern in imaging applications. As we will see in this chapter the knowledge of the high frequency modulation pattern allows one to computationally recover images with resolution higher than the diffraction limited resolution offered by optics alone. The term “diffraction limited resolution” itself needs to be looked at once again in view of the development of such computational imaging systems.

We will first explain this super-resolution concept with a simple picture of a microscope objective as in Fig. 20.1 (a) where a point object is illuminated by light beam. For a usual microscope objective the diffraction limited resolution is decided by the numerical aperture which is related to the the cone of acceptance angle of the light rays. This is similar to the case of the 4F or canonical processor where the resolution is decided by the extent of the Fourier plane aperture. The light rays scattered from the point source at large angles are not captured by the imaging system and hence do not contribute to image resolution. The idea behind structural illumination is to modulate the illumination pattern with high spatial frequency. The modulation of illumination pattern may be achieved by placing

a structure like grating near the object to be imaged. The role of this structure as shown in Fig. 20.1 (b) is to scatter some of the high frequency components in the scattered light (that were previously not captured by the optical system aperture) back into the aperture of the system. The computational problem now is to recover this high frequency information in a visually suitable form using the knowledge of the modulation pattern. Typically multiple modulation patterns are used for capturing one high resolution image beyond the diffraction limited resolution capability of the imaging system. In

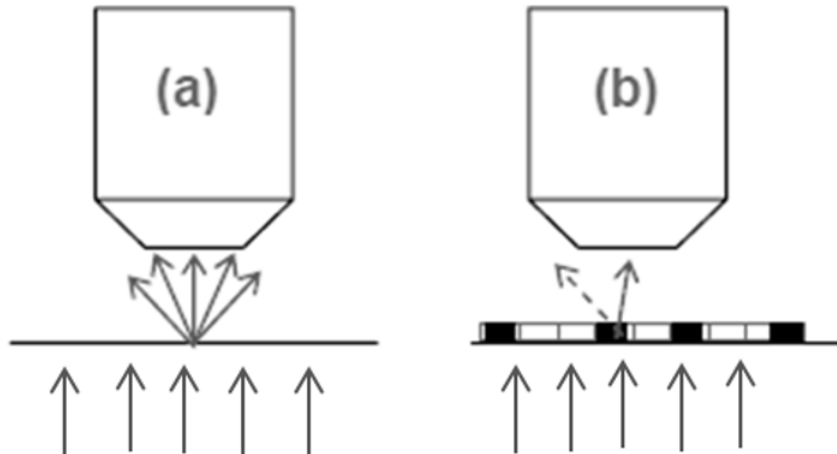


Figure 20.1: Schematic diagram for understanding the basic principle behind structural illumination imaging. (a) When a point object scatters light, some of it is not captured by the imaging system due to its limited aperture. (b) When a structure is present near the object, some of the light which would not have entered the aperture (dotted arrow) is now scattered by the high frequency structure into the system aperture. The aim of computational imaging algorithm is to recover this high frequency information from the coded image data with the knowledge of the modulation pattern.

Fig. 20.2 (a) we show a sine-wave object whose Fourier transform magnitude is shown in panel (b). Figure 20.2(c) shows the system OTF $O(f_x, f_y)$ in Fourier transform domain. Since the system response is low-pass in nature, the sine wave oscillations cannot be

resolved by the system and the resultant output is a flat image as shown in Fig. 20.2(d).

20.1 Forward model and image reconstruction

We will state the forward problem in structural illumination imaging as follows. Consider a modulation pattern $m_k(x, y)$ that effectively multiplies the object $g(x, y)$ to be imaged. Here k denotes the index of the modulation pattern used. If the imaging system point spread function (PSF) is denoted by $o(x, y)$ then the k -th recorded image may be represented as a convolution:

$$q_k(x, y) = o(x, y) * [m_k(x, y)g(x, y)]. \quad (20.1)$$

Note that the recorded raw image has limited resolution due to the convolution with the PSF $o(x, y)$ since the corresponding OTF has a low frequency cut-off in the Fourier space. For usual imaging systems that we have studied so far the modulation pattern is typically $m_k(x, y) = 1$ across all pixels. The data $q_k(x, y)$ recorded with modulation however contains high frequency information in a coded form which is to be recovered computationally. While more general coding patterns are possible, in this chapter we will consider simple high-frequency cosinusoidal modulation patterns to explain high resolution image recovery in structural illumination imaging. In particular we will start by considering a code of the form:

$$m_1(x, y) = \frac{1}{2}[1 + \alpha \cos(2\pi f_0 x + \Phi_1)], \quad (20.2)$$

where α is a positive number in $(0, 1)$. It is instructive to look at the corresponding recorded image $q_1(x, y)$ in Fourier space:

$$\begin{aligned} Q_1(f_x, f_y) &= \frac{1}{2}O(f_x, f_y)[G(f_x, f_y) + \frac{\alpha}{2}G(f_x - f_0, f_y)e^{i\Phi_1} \\ &\quad + \frac{\alpha}{2}G(f_x + f_0, f_y)e^{-i\Phi_1}]. \end{aligned} \quad (20.3)$$

We see that the Fourier space extent of $Q_1(f_x, f_y)$ is limited by that of the system OTF as there is an overall multiplication by the

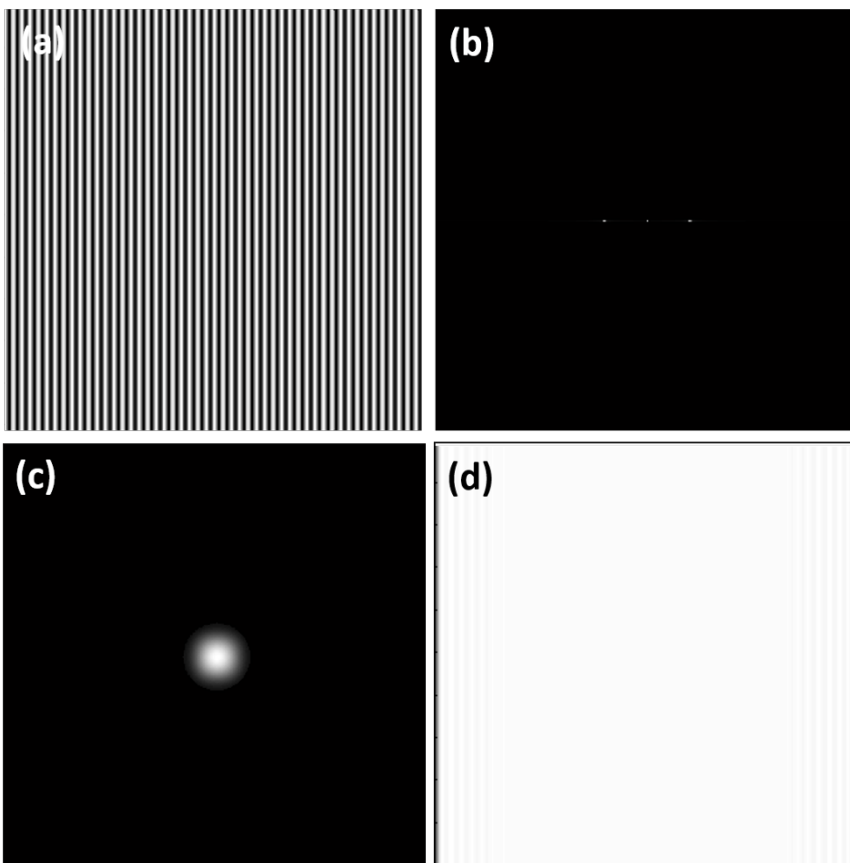


Figure 20.2: (a) Sinusoidal object (b) Fourier transform magnitude for object in (a), (c) System OTF, (d) Recorded data showing flat image due to the low-pass nature of system response relative to the frequency of sine-wave input.

function $O(f_x, f_y)$. At each location (f_x, f_y) in the Fourier domain the data consists of three terms corresponding to $G(f_x, f_y)$ and its shifted versions. By introducing three codes corresponding to three distinct values of Φ_k with $k = 1, 2, 3$ we can resolve this ambiguity. In particular we can write a system of equations:

$$\begin{pmatrix} Q_1(f_x, f_y) \\ Q_2(f_x, f_y) \\ Q_3(f_x, f_y) \end{pmatrix} = \frac{1}{2} \begin{pmatrix} 1 & e^{i\Phi_1} & e^{-i\Phi_1} \\ 1 & e^{i\Phi_2} & e^{-i\Phi_2} \\ 1 & e^{i\Phi_3} & e^{-i\Phi_3} \end{pmatrix} \times \begin{pmatrix} O(f_x, f_y)G(f_x, f_y) \\ \frac{\alpha}{2}O(f_x, f_y)G(f_x - f_0, f_y) \\ \frac{\alpha}{2}O(f_x, f_y)G(f_x + f_0, f_y) \end{pmatrix}. \quad (20.4)$$

For every point (f_x, f_y) this system may be inverted to obtain the 2D Fourier transform $O(f_x, f_y)G(f_x, f_y)$ and its folded versions $O(f_x, f_y) \times G(f_x \pm f_0, f_y)$. We notice that the folded versions of the transform products $O(f_x, f_y)G(f_x \pm f_0, f_y)$ contain the high frequency information that the system cannot record in the absence of the structural illumination. The modulation of the illumination thus offers new information that can now be utilized to get high resolution image using low resolution optics. In Fig. 20.3 (a)-(c) we show three recorded images $q_k(x, y)$ with $k = 1, 2, 3$ of the object in Fig. 20.2(a) when the reference phase values $\Phi = 0, 2\pi/3, 4\pi/3$ are used. The recorded data contains low frequency fringes in this case that may be associated with the well-known Moire effect.

One may apply a Wiener filter (see Chapter 5) corresponding to the system OTF $O(f_x, f_y)$ to the products $O(f_x, f_y)G(f_x, f_y)$ and $O(f_x, f_y)G(f_x \pm f_0, f_y)$ to recover the Fourier transform $G(f_x, f_y)$ and its folded versions and fill the Fourier space beyond the low-pass extent of the OTF. The recovered high resolution object is shown in Fig. 20.3 which is comparable to the original object. In the illustration above the object had variation only along the x -direction. For a more general object, typically the structural illumination may be generated in three directions to fill the Fourier space beyond the extent of OTF in all directions. This point is illustrated in Fig. 20.4(a), (b) which show Fourier space extent of the data recorded by an imaging system without and with structural illumination. We observe that by carefully selecting the modulation frequency relative to bandlimit of the system OTF, image resolution higher by a factor of

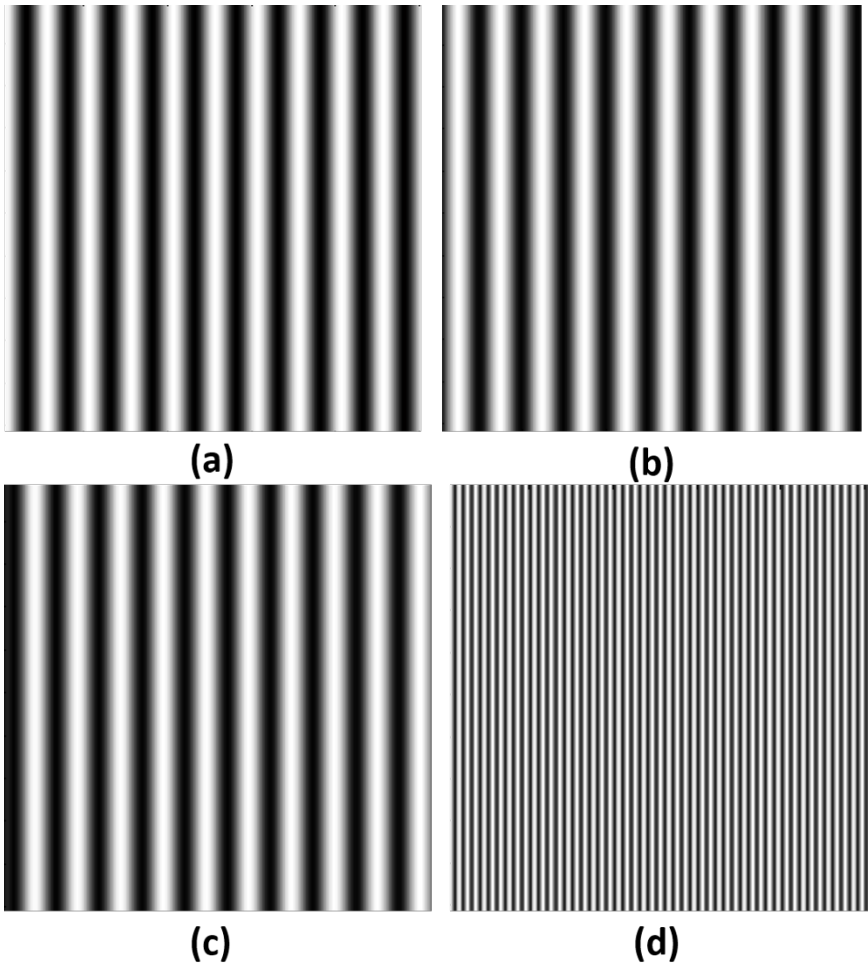


Figure 20.3: (a),(b),(c) Three recorded data images for $\Phi = 0, 2\pi/3, 4\pi/3$ respectively. (d) Recovered high resolution image.

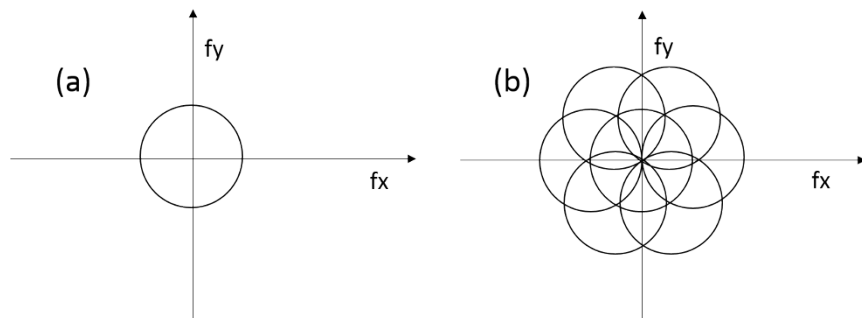


Figure 20.4: (a),(b) Diagrams illustrating Fourier space filling for system without and with structural illumination. The circle in (a) shows the extent of system OTF.

2-3X over the diffraction limited resolution is achievable. For a microscope using high NA objectives (e.g. oil objectives with $NA = 1.25$) and using structural illumination, remarkably high image resolution of 100-150 nm is achievable with visible light. Structural illumination ideas therefore provided significant resolution gain for optical microscopes and are proving to be valuable for basic Bio-sciences and materials research. Structural illumination is one of the several modalities such as Stimulated Emission Depletion (STED) microscopy, Photoactivated localization microscopy etc. that have in recent times demonstrated sub-diffraction limited performance by combining optical and computational tools. We will not discuss these techniques here but refer the interested reader to list of further references.

References and suggested reading

1. M. G. Gustafsson, “Surpassing the lateral resolution limit by a factor of two using structured illumination microscopy”, *J. Microscopy* 198, 82-87 (2000).
2. S. A. Shroff, J. R. Fienup and D. R. Williams, “Phase-shift estimation in sinusoidally illuminated images for lateral superresolution”, *J. Opt. Soc. Am. A* 26, 413-424 (2009).

3. P. Kner, B. B. Chun, E. R. Griffis, L. Winoto and M. G. Gustafsson, “Super-resolution video microscopy of live cells by structured illumination”, *Nature Methods* 6, 339-342 (2009).
4. S. W. Hell and J. Wichmann, “Breaking the diffraction resolution limit by stimulated emission: stimulated emission depletion fluorescence microscopy”, *Optics Letters* 19, 780-782 (1994).
5. E. Betzig, G. H. Patterson, R. Sougrat, O. W. Lindwasser, S. Olenych, J. S. Bonifacino, M. W. Davidson, J. Lippincott-Schwartz, H. F. Hess, “Imaging intracellular fluorescent proteins at nanometer resolution”, *Science* 313, 1642-1645 (2006).
6. M. Rust, M. Bates and X. Zhuang, “Sub-diffraction-limit imaging by stochastic optical reconstruction microscopy (STORM)”, *Nature Methods* 3, 793-796 (2006).
7. B. Huang, S. Jones, B. Brandenburg and X. Zhuang, “Whole cell 3D STORM reveals interactions between cellular structures with nanometer-scale resolution”, *Nature Methods* 5, 1047-1052 (2008).

21. Image reconstruction from projection data

In this chapter we will briefly describe computational imaging using projections of the object of interest. Projection based imaging naturally occurs in diagnostic healthcare systems, e.g. X-ray based imagers, Positron Emission Tomography (PET), Magnetic Resonance Imaging (MRI), Single-photon Emission Computed Tomography, and to some extent ultrasound imaging to some approximation. These minimally invasive computational imaging systems have made tremendous difference to healthcare practices by providing suitable tools for imaging of internal body parts of human patients for diagnostic purposes and for carrying out image guided surgeries. In addition to healthcare systems, the projection based ideas also find usage in radio-astronomical imaging using large antenna arrays where correlations between signals recorded at distant antennas provide Fourier space information about the source star structure as per the van Cittert-Zernike theorem. Recently projection based imaging has also been applied to optical tomography of Biological samples. We have already developed some background on projection based imaging in Chapter 2 where we discussed the Fourier slice theorem that connects a projection with the Fourier transform of the object to be imaged. In this chapter we will revisit the topic in more detail. The discussion in the following sections will be limited to 2D image reconstruction from projection data. Currently used medical X-ray Computed Tomography systems use a cone-beam X-ray configuration. The image reconstruction algorithms in this case are more involved, however, their basic principles can be traced back to the ideas discussed in the following sections.

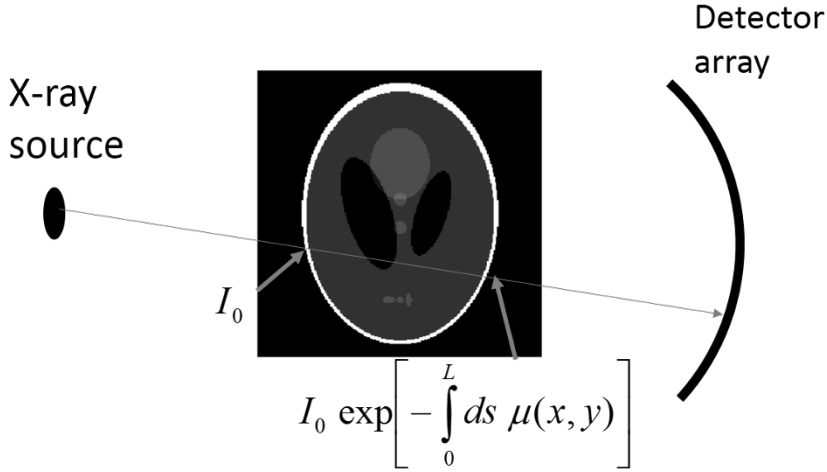


Figure 21.1: Schematic representation showing mechanism of recording X-ray projection data through an object.

21.1 X-ray projection data

When X-rays pass through an object such as a human patient, they get attenuated due to the absorption of the X-rays at each location within the object. Further for energies over 40 keV or so and in typical clinical settings, the diffraction effects if any are negligible and the X-ray propagation can be treated with a ray or geometrical optics model. Attenuation through a material can be modeled as follows. Referring to Fig. 21.1 we observe that if the incident X-ray beam intensity before entering the object is denoted by I_0 , the intensity I after passing through the object can be approximately represented by the well-known Beer-Lambert law:

$$I = I_0 \exp\left[- \int ds \mu(\vec{r})\right]. \quad (21.1)$$

Here ds is an elemental length along the ray and $\mu(\vec{r})$ is the position (and hence material) dependent X-ray absorption coefficient. For example, in case of a human patient, the absorption coefficient is higher for bones as compared to soft tissue. Following the notation

in Section 2.12 the quantity

$$-\log\left(\frac{I}{I_0}\right) = \int ds\mu(\vec{r}) \quad (21.2)$$

may be associated with a line integral through the image $\mu(x, y)$ of the absorption coefficient at some angle θ represented as:

$$p_\theta(t) = \int \int dx dy \mu(x, y) \delta(x \cos \theta + y \sin \theta - t). \quad (21.3)$$

The projection data thus has two dimensions: the rotation angle θ and the location along the t or the projection direction. The projection data for a point object located at (x_0, y_0) is given by:

$$p_\theta(t) = \delta(x_0 \cos \theta + y_0 \sin \theta - t). \quad (21.4)$$

As a function of t and θ and for constant (x_0, y_0) the projection data for a point object is a sinusoidal curve in the $t - \theta$ space. The projection data $p_\theta(t)$ is thus often referred to as a sinogram. As an illustration we show the sinograms for a two-point object and a phantom object. Both the sinograms are plotted for parallel set of projections with 500 samples on the t axis and 1000 angular samples around the circle. While the sinogram for a two-point object is fairly easy to decipher, for a more complex object the sinogram does not provide much information about the object on simple visual inspection.

21.2 Image reconstruction from projection data

In Section 2.12 we have already studied the Fourier slice theorem which states that the Fourier transform of $p_\theta(t)$ with respect to t provides a slice of the transform $M(f_x, f_y) = \mathcal{F}\{\mu(x, y)\}$ through the center of the Fourier space in the projection direction. In other words,

$$\mathcal{F}_t\{p_\theta(t)\} = M(\nu \cos \theta, \nu \sin \theta). \quad (21.5)$$

As shown in Fig. 21.3 the projection along one direction denoted by θ thus fills the Fourier space data along one line through the center of

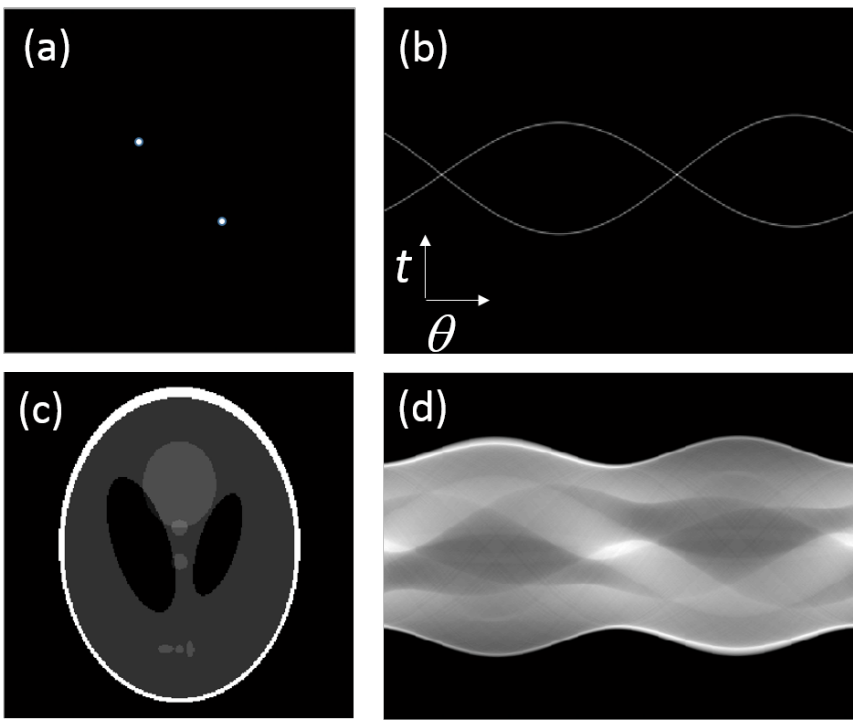


Figure 21.2: Illustration of sinogram data. (a) Two point object, (c) phantom object, (b),(d) Sinograms corresponding to (a), (c).

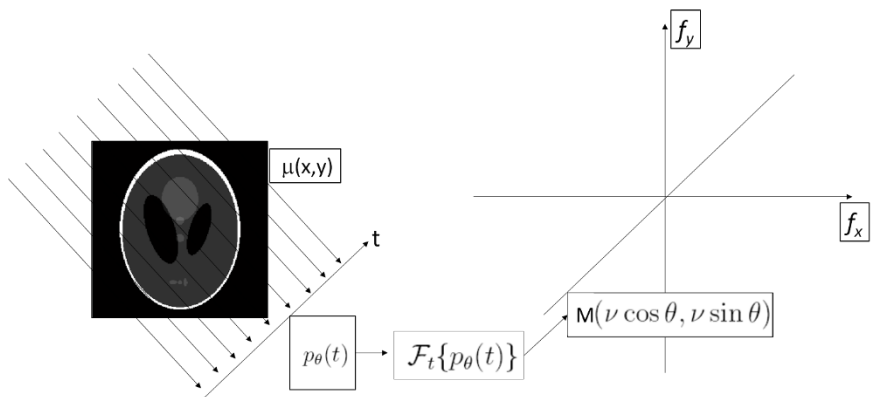


Figure 21.3: Schematic representation showing the use of Fourier slice theorem for image reconstruction from projection data.

Fourier space. Projections along multiple θ directions therefore fill the whole 2D Fourier space densely. We further rewrite the Fourier expansion of $\mu(x, y)$ in order to relate the resulting expression to the Fourier slice theorem. We have:

$$\begin{aligned}\mu(x, y) &= \int \int df_x df_y M(f_x, f_y) e^{i2\pi(f_x x + f_y y)} \\ &= \int_0^{2\pi} \int_0^\infty \nu d\nu d\theta M(\nu \cos \theta, \nu \sin \theta) e^{i2\pi\nu(x \cos \theta + y \sin \theta)} \\ &= \int_0^\pi \int_{-\infty}^\infty |\nu| d\nu M(\nu \cos \theta, \nu \sin \theta) e^{i2\pi\nu(x \cos \theta + y \sin \theta)}.\end{aligned}\tag{21.6}$$

Using the Fourier slice theorem and the above equation, we immediately see the steps required for reconstructing the image $\mu(x, y)$ as follows:

1. Take 1D Fourier transform of the projection data $p_\theta(t)$ along the $t-$ direction. This transform is equal to a slice through the 2D Fourier transform as represented by $M(\nu \cos \theta, \nu \sin \theta)$ for angle θ denoting the projection direction.
2. Multiply the 1D Fourier transform by the filter $|\nu|$ which is known as the ramp-filter.
3. Take inverse 1D Fourier transform.
4. Integrate over all angles θ to calculate the contribution of each projection to a given image point $\mu(x, y)$.

The last step of integrating over all angles is known as back-projection and this operation is mathematically equivalent to the adjoint or transpose of the forward projection operation. The procedure outlined above is known as the filtered backprojection method and it was first suggested by G. N. Ramachandran and A. V. Lakshminarayanan. In their honour the ramp filter is sometimes referred to as “Ram-Lak” filter. The filtered-backprojection method and its variants are used regularly in almost all current medical Computed Tomography (CT) scanners for 2D (slice) and 3D imaging of human

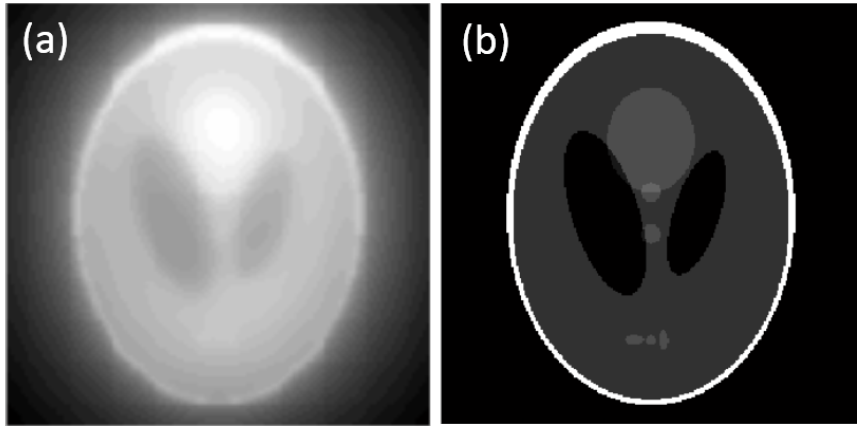


Figure 21.4: Image reconstruction from sinogram data using (a) simple backprojection and (b) filtered backprojection. The illustration uses 1000 views around a circle.

patients. In Fig. 21.4 we show the result of un-filtered and filtered backprojection of the data in Fig. 21.2(d). We observe that simple (unfiltered) backprojection is not an inverse operation and typically gives rise to a blurred image and the full high resolution is provided when the ramp filter is employed. The ramp filter may also be interpreted in an alternative way by writing:

$$|\nu| = i\text{sgn}(\nu)\nu. \quad (21.7)$$

The filter function $i\text{sgn}(\nu)$ may be associated with Hilbert transformation and the term ν may be associated with a derivative operation. The ramp filtering can then also be thought of as a derivative of each projection (along $t-$ axis) followed by a directional Hilbert transform in the image domain. We will not discuss this topic in further detail but mention that the derivative operation being a local operation, this method has some advantages in relation to memory access pattern in a practical system.

In this chapter we have provided a very brief introduction to image reconstruction from projection data. The interested reader may refer to further references at the end of the chapter. While we have ignored any noise issues in this discussion, noise in detection of X-rays is highly important aspect of reconstruction, particularly since

there is a lot of emphasis on reducing X-ray dose to the human patient. In recent times, there is extensive ongoing research on exploring efficient iterative algorithms that are more suitable at handling noise as compared to the direct filtered backprojection based methods. The problem of image reconstruction in iterative methods reduces to a constrained optimization problem which may be stated as follows. Minimize the cost function $C(\mu)$ given by:

$$C(\mu) = ||p - A\mu||^2 + \Psi(\mu). \quad (21.8)$$

Here p refers to the projection data, A refers to the forward projection operation and $\Psi(\mu)$ refers to the set of constraints on the image $\mu(x, y)$. The first term is a data matching term and instead of L2-error, this term can have other forms like weighted L2-norm or maximum-likelihood that can model the noise statistics much better. The constraints can be, e.g. positivity of the image, minimum Total Variation or other edge preserving penalties. The projection and back-projection (or A^T) operations are computationally expensive and specialized hardware is required for their accurate implementation on commercial medical scanners. It is likely that iterative image reconstruction will become more widespread in medical CT scanners in the coming years due to its image quality advantages at low X-ray dose.

References and suggested reading

1. G. N. Ramachandran and A. V. Lakshminarayanan, “Three-dimensional reconstructions from radiographs and electron micrographs: Application of convolution instead of Fourier transform”, Proc. National Academy of Sciences 68, 2236-2240 (1971).
2. A. C. Kak and M. Slaney, *Principles of Computerized Tomographic Imaging*, Society for Industrial and Applied Mathematics (2001).
3. F. Natterer, *The Mathematics of Computerized Tomography*, Wiley (1986).

4. P. Suetens, *Fundamentals of Medical Imaging*, Cambridge University Press (2009).
5. L. A. Feldkamp, L. C. Davis and J. W. Kress, “Practical cone-beam algorithm”, *J. Opt. Soc. Am. A* 1, 612-619 (1984).
6. A. Katsevich, “Theoretically exact filtered-backprojection type inversion algorithm for spiral CT”, *SIAM J. Applied Mathematics* 32, 681-697 (2002).
7. F. Noo, R. Clackdoyle, J. Pack, “A two step Hilbert transform method for 2D image reconstruction”, *Phys. Med. Biol.* 49, 3903-3923 (2004).
8. Y. Zou and X. Pan, “Exact image reconstruction on PI-lines from minimum data in helical cone-beam CT”, *Physics in Med. Biol.* 49, 941-959 (2004).
9. B. DeMan, J. Nuyts, P. Dupont, G. Marchal, P. Suetens, “An iterative maximum likelihood polychromatic algorithm for CT”, *IEEE Trans. Medical Imaging* 20, 999-1008 (2001).
10. I. Elbakri and J. Fessler, “Statistical image reconstruction for polyenergetic X-ray computed tomography”, *IEEE Trans. Medical Imaging* 21, 89-99 (2002).
11. E. Sidky and X. Pan, “Image reconstruction in helical cone-beam computed tomography by constrained total variation minimization”, *Physics in Med. Biol.* 53, 4777-4807 (2008).
12. J. Nuyts, B. DeMan and J. Fessler, W. Zbijewski and F. J. Beekman, “Modelling the physics in the iterative reconstruction for transmission computed tomography”, *Phys. Med. Biol.* 58, R63-R96 (2013).

22. Ghost Imaging

In this chapter we will consider a computational image formation technique that has attained popularity in the last decade. The technique is referred to as “ghost imaging” since the specialty of this method is that it uses a bucket detector or a single pixel detector to collect light that has interacted with the object of interest to form its image. There is extensive literature on this topic by now. One of the aims of this chapter is to provide a simple signal processing based explanation of image formation in this modality so as to make this topic more accessible. The point of view presented here is also amenable to newer and more efficient ways of utilizing this computational imaging modality.

22.1 Schematic of a ghost imaging system

A ghost imaging system may be schematically described as shown in Fig. 22.1. As proposed initially, a source of light producing correlated photon pairs (e.g. parametrically down-converted photons in a non-linear optical process) is employed. One of the photons in this pair is detected by a photon counting array detector while the other photon interacts with the object $T(x, y)$ to be imaged. The photon that has interacted with the object is detected with complete disregard to its spatial location by an area integrating single pixel (or bucket) detector. The detector signal in the first arm is a function of the position (x, y) where an event is detected as well as the time when the event occurred. We will denote this detector current as $i_1(x, y, t)$. The bucket detector signal has no position dependence and we will denote it as $i_2(t)$. The estimated image of the object is

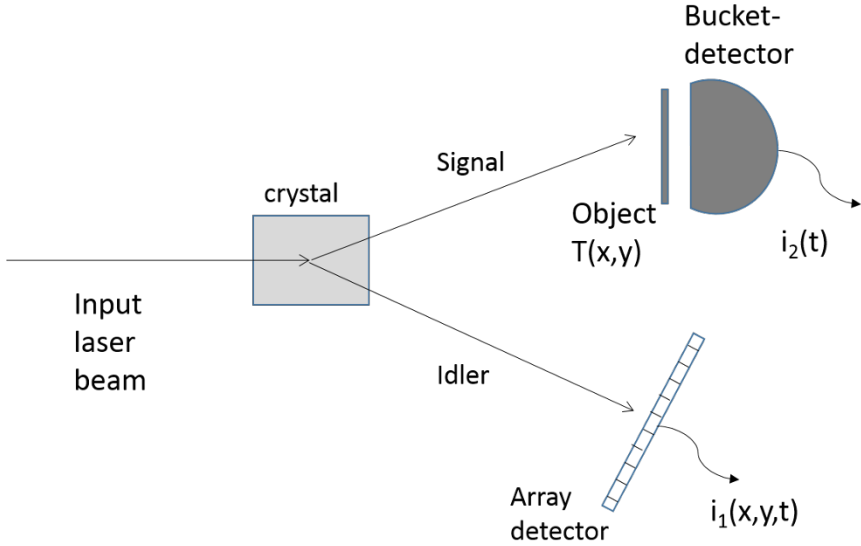


Figure 22.1: Ghost imaging setup schematic using correlated photon pair from parametric down-conversion process.

then formed by correlation of the two signals $i_1(x, y, t)$ and $i_2(t)$.

$$\tilde{T}(x, y) = \langle i_1(x, y, t) i_2(t + \tau) \rangle. \quad (22.1)$$

The time delay τ is adjusted appropriately according to the optical path difference in the two arms of the interferometer. The correlation above is performed either by an electronic circuit or by numerically multiplying the time-dependent image recorded on the array sensor with the photo-current $i_2(t)$ from the bucket detector and averaging over multiple image frames. The image formation is possible due to the time and position correlation of down-converted photon pair. In the early days of ghost imaging research it was generally considered that a quantum source of light producing correlated photons is required for implementing a ghost imaging system. However it was soon clear that classical light can also give rise to required correlations. For example, consider a system schematic as shown in Fig. 22.2 where a thermal-like source is produced by a laser spot focused on a rotating glass diffuser. A beamsplitter is used in a Hanbury Brown Twiss setup where the array detector in one reference arm

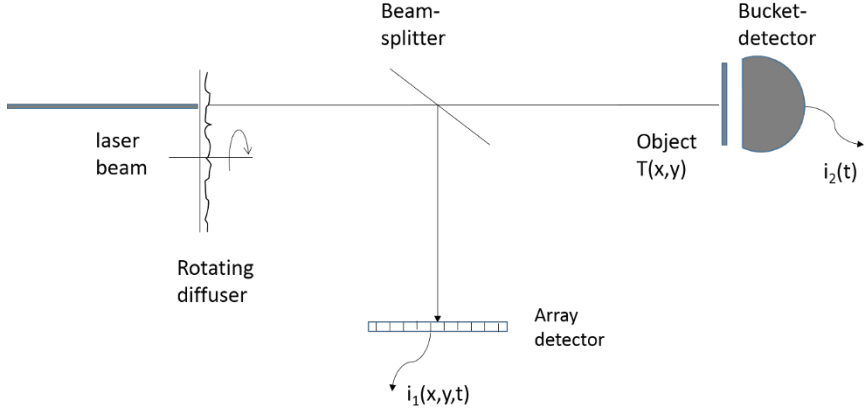


Figure 22.2: Ghost imaging setup schematic using speckle from rotating diffuser as a thermal-like source.

records an image of the speckle intensity pattern $i_1(x, y, t)$ and at the same time a bucket detector records a scalar product:

$$i_2(t) = \int \int dx dy T(x, y) i_1(x, y, t), \quad (22.2)$$

between the speckle intensity pattern and the transmission function $T(x, y)$ of the object of interest. The correlation between the signals from the array and bucket detectors as above gives rise to:

$$\begin{aligned} & \langle i_1(x, y, t) i_2(t + \tau) \rangle \\ &= \int \int dx' dy' T(x', y') \langle i_1(x', y', t) i_1(x, y, t + \tau) \rangle \\ &= \int \int dx' dy' T(x', y') \langle i_1(x', y') \rangle^2 [1 + |\gamma(x - x', y - y', \tau)|^2]. \end{aligned} \quad (22.3)$$

The intensity-intensity correlation above for the thermal-like source has been factorized using the Gaussian moment theorem. The first term in the above equation integrates out to a constant background while the second term is a convolution of the absolute square of the coherence function $|\gamma(x - x', y - y', \tau)|^2$ with the image $T(x, y)$ to be estimated. The form of the coherence function can be controlled

by selecting appropriate size for laser spot on the diffuser and the diffuser velocity, so that $|\gamma|^2$ can have a very narrow spread. Further if the form of $|\gamma|^2$ is known, the image $T(x, y)$ can be recovered by any of the suitable image de-convolution algorithms as discussed in Chapters 5 and 6 applied to the correlation function. The correlation above thus helps in forming the image. In the following illustration we use a 100×100 pixel “IITD” object and perform the speckle based averaging described above numerically. The reconstructed images after averaging over $N = 10^4$ and 10^6 realizations of speckle patterns are shown in Fig. 22.3(a), (b) respectively. We remark that the resolution of the resultant image is guided by the speckle size at the object transparency $T(x, y)$. The ghost imaging system may

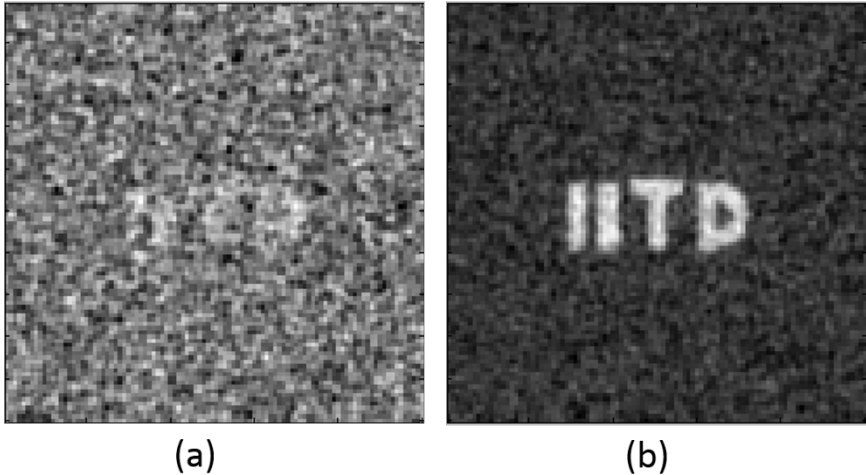


Figure 22.3: Ghost images obtained by (a) 10^4 and (b) 10^6 speckle intensity frames for ensemble averaging. The IITD object has 100×100 pixels.

be simplified further if instead of the rotating glass diffuser a spatial light modulator screen is used to generate the speckle patterns. In such cases the speckle intensity patterns at the object can be numerically calculated and the array detector is then not necessary.

22.2 A signal processing viewpoint of ghost imaging

The speckle based averaging for image formation as suggested above is not very intuitive especially when a large number of photons are being detected in a single speckle intensity frame almost simultaneously in a realistic ghost imaging experiment. Further the large number of speckle realizations (as compared to number of pixels in the image), required for image formation makes the overall image formation process somewhat inefficient from information content point of view. A question one may further ask is whether the thermal-like source is an absolute necessity for ghost imaging to work. We will answer these issues by providing a signal-processing approach to image formation in ghost imaging.

We will denote the sequence of speckle patterns used for correlation purpose as $\{\phi_n(x, y)\}$ with $n = 1, 2, \dots, N$. It is clear that the correlation of the bucket detector signal with the signal at the array detector amounts to the following process for formation of the estimated image $\tilde{T}(x, y)$:

$$\tilde{T}(x, y) = \sum_{n=1}^N c_n \phi_n(x, y), \quad (22.4)$$

where the coefficients c_n 's are given by the scalar product between $\phi_n(x, y)$ and $T(x, y)$:

$$c_n = \int \int dx dy T(x, y) \phi_n(x, y). \quad (22.5)$$

Clearly the speckle pattern realizations $\phi_n(x, y)$ are simply being treated as random keys and the image is being formed by their linear combination. Since the functions $\phi_n(x, y)$ representing the speckle intensity patterns are not orthogonal to each other, the process of simple linear combination above is inefficient. In fact since $\phi_n(x, y)$ are likely to be linearly independent functions, one should require no more speckle pattern realizations than the number of pixels in the image to be reconstructed. Further if the expected sparsity in the object $T(x, y)$ is accounted for appropriately in image reconstruction process, number of speckle realizations much less than the

number of pixels in the image should also allow for good estimation of $T(x, y)$. In the illustration below we model the ghost image formation problem as an optimization problem where we minimize the cost function of the form:

$$C[T(.)] = \|g - ST(\cdot)\|^2 + TV[T(\cdot)]. \quad (22.6)$$

Here g is a vector formed by the sequence of bucket detector signals, matrix S consists of random keys (speckle patterns) arranged as row vectors and $T(\cdot)$ denotes the required estimated image matrix arranged as a single column vector. Figure 22.4 shows the ghost image recovery with 5000 realizations of speckle patterns using the optimization based solution which is much better compared to the image formed by simplistic averaging as in Fig. 22.3. The results



Figure 22.4: Ghost image obtained 5000 speckle intensity frames for ensemble averaging and optimization based reconstruction. The IITD object has 100×100 pixels.

above once again highlight the power of the sparsity constrained optimization procedure, this time for the ghost imaging modality.

References and suggested reading

1. T. B. Pittman, Y. H. Shih, D. V. Strekalov and A. V. Sergienko, “Optical imaging by means of two-photon quantum entangle-

- ment”, Phys. Rev. A 52, R3429-3432 (1995).
2. R. S. Bennink, S. J. Bentley and R. W. Boyd, “Two-photon coincidence imaging with a classical source”, Phys. Rev. Lett. 89, 113601 (2002).
 3. A. Gatti, E. Brambilla and L. A. Lugiato, “Correlated imaging, quantum and classical”, Phys. Rev. A 70, 013802 (2004).
 4. A. Gatti, E. Brambilla, M. Bache and L. A. Lugiato, “Ghost imaging with thermal light: comparing entanglement and classical correlation”, Phys. Rev.Lett. 93, 093602 (2004).
 5. B. I. Erkmen and J. H. Shapiro, “Ghost imaging: from quantum to classical to computational”, Adv. Opt. Photon. 2, 405-450 (2011).
 6. J. H. Shapiro and R. W. Boyd, “The physics of ghost imaging”, Quantum Inf. Process. 11, 949-993 (2012).
 7. M. F. Duarte, M. A. Davenport, D. Takhar, J. N. Laska, T. Sun, K. F. Kelly and R. G. Baraniuk, “Single pixel imaging via compressive sampling”, IEEE Signal Proc. Mag. 25, 83-91 (2008).
 8. O. Katz, Y. Bromberg and Y. Silberberg, “Compressive ghost imaging”, Applied Phys. Letters 95, 131110 (2009).
 9. J. Cheng, “Ghost imaging through turbulent atmosphere” Opt. Express 17, 7916-7921 (2009).
 10. B. I. Erkmen, “Computational ghost imaging for remote sensing”, J. Opt. Soc. Am. A 29, 782-789 (2012).

23. Appendix: Suggested Exercises

1. (a) Prove the generalized form of the energy or Parseval theorem shown below.

$$\int_{-\infty}^{\infty} dx g(x) h^*(x) = \int_{-\infty}^{\infty} df_x G(f_x) H^*(f_x).$$

In the above equation, G and H denote the Fourier transforms of g and h respectively and the $*$ denotes the complex conjugation operation.

- (b) Evaluate the integrals below:

$$\int_{-\infty}^{\infty} dx \left(\frac{\sin \pi x}{\pi x} \right)^2, \quad \int_{-\infty}^{\infty} dx \left(\frac{\sin \pi x}{\pi x} \right)^4.$$

2. Plot the function $q(x)$ defined below as x varies along the real line.

$$q(x) = \int_{-\infty}^x dt \delta(t - 100).$$

3. (a) The rect function is defined as:

$$\text{rect}(x) = \begin{cases} 1 & |x| < 1/2 \\ 1/2 & |x| = 1/2 \\ 0 & |x| > 1/2 \end{cases}$$

Evaluate the Fourier transform $\mathcal{F}\{\text{rect}(x)\}$.

- (b) A two-dimensional function $g(x, y)$ is shown in the Fig. 23.1 below. The function takes a value equal to 1 in the shaded region and is equal to zero elsewhere. Evaluate the Fourier transform $\mathcal{F}\{g(x, y)\}$.

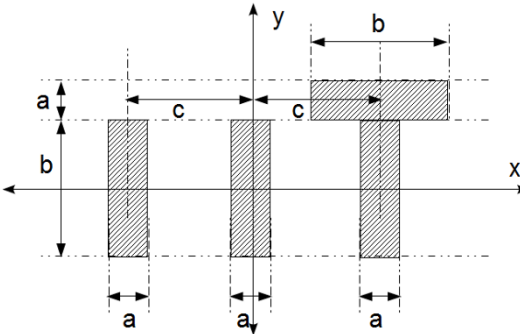


Figure 23.1: Function $g(x, y) = 1$ in the shaded region, $= 0$ elsewhere.

4. Plot the following function:

$$f(x) = \text{rect}(x) * \Lambda(x),$$

where $*$ denotes convolution.

5. State whether the following statements are TRUE or FALSE, giving appropriate reasoning.
(a)

$$\sum_{n=-\infty}^{\infty} \text{sinc}(2Bx - n) \text{sinc}(2Bx' - n) = \text{sinc}[2B(x - x')].$$

(b) In the Shannon sampling formula, the sample at $x = 1/(2B)$ makes a non-zero contributions to the signal at other sampling locations given by $x = n/(2B)$ with $n \neq 1$.

6. The angular resolution of a typical human eye is 1 arc minute. Estimate the minimum number of pixels (order of magnitude estimate is sufficient) needed for a smartphone screen of size 2 inch x 4 inch.
7. A barcode scanner for reading barcodes on books or packages is to be designed. A typical barcode is shown in Fig. 23.2 and has a width of 1 inch (2.54 cm). The smallest feature in the code is approximately 0.5 mm wide. The scanner device



Figure 23.2: Typical barcode of width = 1 inch.

has a lens which images the barcode onto an array of detector pixels with suitable de-magnification. Estimate the minimum number of pixels needed in the linear detector array for proper functioning of the barcode scanner.

8. The spot of Arago:

(a) Consider the first Rayleigh-Sommerfeld solution:

$$U(x, y, z) = \int \int dx' dy' U(x', y', 0) \frac{\exp(ikR)}{2\pi R} \left(-ik + \frac{1}{R}\right) \frac{z}{R},$$

where, $R = \sqrt{(x - x')^2 + (y - y')^2 + z^2}$. Express this result in the form:

$$U(x, y, z) = \frac{\partial}{\partial z} [...].$$

(b) A plane wave $\exp(ikz)$ is incident on a thin opaque circular disk of radius a much larger than wavelength λ , located in $z = 0$ plane and centered at $x = y = 0$. Calculate the on-axis diffraction field intensity as a function of z .

9. The first Rayleigh-Sommerfeld solution for the tangential field component $E_x(x, y, z)$ in terms of the field in the $z = 0$ plane is given by:

$$E_x(x, y, z) = \int \int dx' dy' E_x(x', y', 0) \frac{\exp(ikR)}{2\pi R} \left(-ik + \frac{1}{R}\right) \frac{z}{R},$$

where R is the distance between two points (x, y, z) and $(x', y', 0)$.

- (a) An object transparency with coherent transmission function $t(x, y)$ and placed in $z = 0$ plane is illuminated with spatially incoherent illumination from an LED source which has a narrow bandwidth with central wavelength λ_0 . Write an expression for the intensity of light observed at point (x, y, z) .
- (b) Is the input-output equation relating the intensity at point (x, y, z) to the transmission function $t(x, y)$ linear and space invariant ?
10. Using Fresnel approximation, show that the Helmholtz equation takes the para-axial form given by:

$$[i\frac{\partial}{\partial z} + \frac{\nabla_{xy}^2}{2k} + k] u(\vec{r}) = 0.$$

You may find the following relation useful: $H_{Fresnel}(f_x, f_y) = \exp[ikz - i\lambda z(f_x^2 + f_y^2)]$.

11. **Pseudo-Eigenfunctions of Fresnel transform** The set of angular prolate spheroidal functions of order zero $\{\phi_n(x)\}$ have the self finite Fourier transform property:

$$\int_{-1}^1 dx \phi_n(x) \exp(-i2\pi xx') = \alpha_n \phi_n(x'),$$

where α_n 's are constants. Show that a prolate function multiplied by a quadratic phase function on Fresnel transform gives the same prolate function multiplied by another quadratic phase function. For simplicity you may assume Fresnel diffraction over an aperture of size $x : (-1, 1)$.

12. The transfer function for free-space diffraction in terms of the angular spectrum is given by:

$$H(f_x, f_y; z) = \exp(i\alpha z).$$

- (a) Starting with the Helmholtz equation $(\nabla^2 + k^2)U(x, y; z) = 0$ find the value of α .
- (b) Describe the nature of the transfer function when $k^2 \geq 4\pi^2(f_x^2 + f_y^2)$ and $k^2 < 4\pi^2(f_x^2 + f_y^2)$.

- (c) Show that a plane wave $\exp(ikz)$ at $z = 0$ will always remain a plane wave after propagation to arbitrary distance z .
 (d) A diffraction grating with a transmission function:

$$t(x, y) = \frac{1}{2}[1 + \cos(2\pi \frac{x}{a})],$$

Show that a more accurate expression for the Talbott (or self-imaging) distance corresponding to the grating is given by:

$$z_T = \frac{\lambda}{1 - \sqrt{1 - \lambda^2/a^2}}.$$

13. A computer simulation for a diffraction problem using the angular spectrum is to be performed where only the propagating components are of interest. Determine the sampling interval Δf_x and Δf_y in the 2D Fourier transform domain that is appropriate for representing the angular spectrum transfer function. If the aperture is specified within a square window of size $L \times L$, find the corresponding sampling intervals Δx , Δy that correspond to your choice of Δf_x and Δf_y .
14. An image is printed on a transparency using a printer with resolution M dots per mm and the transparency is used as an object in a F-Lens-F Fourier transform setup. The transparency is illuminated using a plane wave of wavelength λ traveling along the optical axis of the system. Estimate the size of an array sensor (in terms of number of pixels) that is required to observe the highest detail in the object transparency. Assume square pixels of dimension $p \mu\text{m}$.
15. An ultra-thin annular (ring-like) slit of radius r_1 is placed in the input plane of the F-Lens-F Fourier transforming system. For illumination using a monochromatic (wavelength = λ) plane wave beam traveling along the optic axis of the system, find an expression for the resultant scalar field in the back focal plane of the lens. Find an expression for the field for propagation by a distance z_0 beyond the back-focal plane and show that the beam intensity profile has not changed due to propagation.

16. The Lena image is placed at the input plane of a 4F optical processor and the output images corresponding to three different filters in the Fourier transform plane are shown in Figures 23.3 (a),(b),(c) respectively. Describe the form of the filter functions (with appropriate reasoning) that may have resulted in these three different outputs.

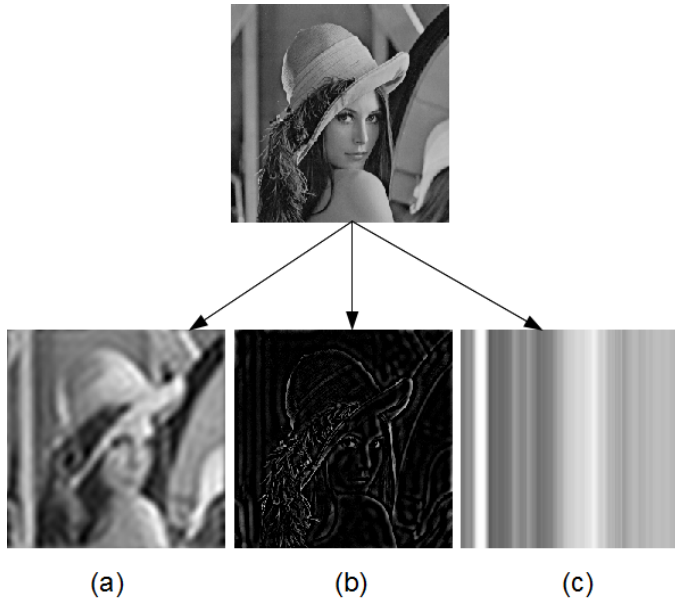


Figure 23.3: The effect of three different filters on the Lena object function is shown in Figures (a),(b),(c) respectively.

17. Consider an F-Lens-F optical Fourier transform system that you wish to setup in the laboratory. A phase only transmissive liquid crystal SLM is to be placed at the input of the system and the Fourier transform output is recorded on a CCD camera. The SLM pixel size is $10 \mu\text{m}$ and the CCD camera pixel size is $5 \mu\text{m}$. Both the SLM and CCD have 1000×1000 pixels. The illumination is with a plane laser beam which fully illuminates the SLM active area and is blocked outside the SLM area. The phase function displayed on the SLM is such that the alternate columns of the SLM have phase values 0 and π .

- (a) What focal length F would you choose for the lens so that the diffraction peaks are well separated on the CCD camera ?
 (b) Write a computer program to model this system in a computer and show the output image.
18. A 4F imaging system has a rectangular Fourier plane aperture of size $(2B_x \times 2B_y)$.
 (a) Find the coherent impulse response of the system.
 (b) Find the OTF of the system and sketch the MTF along the x -dimension.
 (c) What is the incoherent cut-off frequency for this system ?
 (d) Sketch the approximate system MTF when the system has aberrations.
19. An imaging system has a centrally obscured square aperture of size $a \times a$. The central $a/3 \times a/3$ square part of the aperture is opaque. Sketch (approximately) the MTF curve for the system along the x -axis.
20. A resolution test target - a bar chart with $(1,0)$ periodic amplitude transmission function - as shown in Fig. 23.4 serves as an input to a 2F-lens-2F imaging setup. The period of the input pattern is $1/f_o$ mm. Spatially incoherent illumination with wavelength λ is used in this experiment.
 (a) You have two lenses with aperture diameters $D_1 = (\lambda F f_0 / 2)$

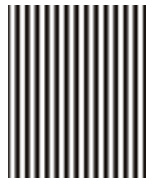


Figure 23.4: Resolution test chart.

and $D_2 = (3\lambda F f_0)$ and same focal length F available to you in the lab. Assuming a imaging system configuration with 1:1 magnification, which lens would you use for imaging the bar chart object and why?

(b) A pixelated digital detector is to be used for recording the

image in this experiment. What is the maximum permissible pixel size that can produce a meaningful image ?

21. A hologram is recorded by using two unit amplitude waves at the hologram plane: (1) a quadratic phase wavefront given by $\exp[i\alpha(x^2 + y^2)]$ and (2) a spiral phase wavefront given by $\exp(i \arctan(y/x))$. Write an expression for the hologram intensity pattern and find the curve(s) that describe the location of intensity minima in the hologram pattern. Can you determine whether the quadratic phase front is converging or diverging by using a single hologram intensity pattern?
22. A hologram of a plane wave traveling at angle θ with respect to z -axis and a object wave traveling in $+z$ direction is recorded in plane $z = 0$.
 - (a) Draw a diagram showing the Fourier space representation of the hologram pattern associating appropriate terms in the hologram intensity pattern with corresponding energy peaks/lobes in 2D Fourier transform plane.
 - (b) If this hologram is to be recorded on a CCD array, find the optimal CCD pixel size that you will need.
 - (c) Derive an expression for the maximum resolution for object beam achievable from a single hologram pattern using linear filtering methods.
23. Spherical waves from an on axis point source located at $z = 0$ and an in-line plane wave traveling in the $+z$ -direction (assume that the two sources are derived from the same laser beam and thus have required coherence properties) are used to form a hologram in plane $z = z_0$. The hologram was recorded using illumination wavelength λ_1 nm but for reconstruction purpose, a plane wave traveling in negative z direction and having a wavelength λ_2 nm is used. Obtain an expression for the hologram intensity pattern and draw a rough sketch showing the fringes. Find the location of the reconstructed real image.
24. (a) A quadratic phase wavefront traveling in $+z$ direction

$$\exp[i\alpha(x^2 + y^2)]$$

is interfered with its laterally shifted replica (wavefront shifts in x, y directions: $\Delta x, \Delta y$) in plane $z = 0$. Find the period of the resultant fringe pattern.

(b) **Earthquake hologram:** A satellite carrying a radar beam



Figure 23.5: Radar interference pattern generated from two consecutive passes of a satellite over an earthquake site.

travels on the same trajectory over an earthquake site before and after the incidence of an earthquake event. The complex reflectivity radar image patterns recorded by the satellite on its two visits are interfered numerically to generate a hologram as shown in Fig. 23.5. The figure scale is tens of kilometers. Using a slightly more complicated model than in part (a), explain how you will interpret the interference pattern.

25. **Multi-pinhole camera** A pinhole camera is to be operated at low-light conditions at night-time and so in order to gather more light, N pinholes randomly placed at points (x_j, y_j) with $j = 1, 2, \dots, N$ are used. For example, the image recorded by a 3-pinhole camera is shown in Fig. 23.6 for illustration. Suggest a method by which you will numerically process this image data (available as a 2D matrix of pixel values) in order to recover a non-overlapped image.



Figure 23.6: Image recorded by a three-pinhole camera

Index

- angular spectrum method, 145
aperture stop, 130
apodization, 198

bandlimited extrapolation, 247
bandpass sampling theorem, 54
Baye's rule, 108
Bessel function, 43
blind deconvolution, 95

canonical optical processor, 193
Cauchy principal value, 34, 35
central limit theorem, 115
central moment, 110
characteristic function, 112
chief ray, 131
chirp phase function, 37
circ function, 42
coherent transfer function, 200
comb function, 36
compact form factor camera, 254
compressive imaging, 97
computational imaging, 16
correlation coefficient, 111
cubic phase mask, 267

dc blocking filter, 194
defocus diversity, 240
degree of polarization, 186
delta function, 29, 30, 32
diffraction, 133

digital holographic microscopy, 229
Dirichlet sufficiency conditions, 21, 28

eigenfunction analysis of imaging systems, 206
ergodic process, 118
evanescent waves, 150
expectation value, 110
extended depth of field, 267

Fast Fourier transform, 67
Fermat's principle, 127
Fienup hybrid input-output algorithm, 238
filtered backprojection, 289
Fourier series, 21
Fourier slice theorem, 43
Fourier transform, 28
Fourier transform method, 223
fractional Fourier transform, 162
Fraunhofer diffraction, 164
Fresnel diffraction, 153

Gaussian, 36
Gaussian distribution, 114
Gaussian moment theorem, 116
generalized functions, 29
generalized sampling, 254
geometric phase shifter, 185
Gerchberg-Saxton algorithm, 237

- ghost imaging, 293
Gibbs phenomenon, 23
Green's theorem, 137
half wave plate, 185
Hanbury Brown Twiss interferometer, 173
Helmholtz equation, 136
Helmholtz-Kirchhoff theorem, 136
ill-posedness, 79
image de-convolution, 91
image denoising, 87
interference law, 169
inverse filter, 80
jinc function, 43
joint probability, 108
Jones matrix, 183
Jordan's lemma, 34
Karhunen-Loeve expansion, 121
Kirchhoff diffraction, 141
L1-norm solution, 101
Laguerre-Gaussian function, 273
lightfield camera, 256
linear systems, 75
magnitude transfer function, 201
Mandel's photon counting formula, 175
Mandel's theorem, 123
marginal ray, 131
Maxwell equations, 135
Michelson stellar interferometer, 171
moments, 110
Nyquist rate, 51
off-axis digital holography, 222
optical transfer function, 201
optimization method for digital holography, 226
phase contrast, 195
phase diversity imaging, 240
phase shifting digital holography, 224
Poisson summation formula, 50
polarization, 183
probability, 107
propagating waves, 149
properties of Fourier transform, 40
quarter wave plate, 185
ramp filter, 289
random process, 117
random variable, 109
ray transfer matrix, 127
Rayleigh-Sommerfeld diffraction solution, 144
rect function, 28
rotating diffuser, 180
rotating point spread function, 273
sampling theorem, 49
self-imaging, 160
sign function, 33, 35
sinogram, 287
Slepian functions, 56
Sommerfeld radiation condition, 141
space-frequency representation, 171
space-invariance, 77
spatial and temporal coherence, 167

speckle, 177
speckle interferometry, 236
spectral density, 119
spiral phase diversity, 244
standard deviation, 111
stationary phase method, 268
stationary process, 118
statistically independent events, 108
step function, 33
structural illumination, 277

total variation, 89
transport of intensity equation, 156

uniform convergence, 24

van Cittert-Zernike theorem, 169
variance, 110
vortex phase filter, 197

Wiener filter, 82
Wiener-Knintchine theorem, 120
Wigner distribution, 45